Purdue University

Steel Bridge Research, Inspection, Training, and Engineering (S-BRITE) Center

August 2018

Member-Level Redundancy of Built-up Steel Axially-Loaded Members

Jason B. Lloyd,
Purdue University, lloyd1@purdue.edu

Francisco J. Bonachera Martin,
Purdue University, fbonache@purdue.edu

Cem Korkmaz,
Purdue University, ckorkmaz@purdue.edu

Robert J. Connor,
Purdue University, rconnor@purdue.edu

RECOMMENDED CITATION

Lloyd, J. B., Bonachera Martin, F.J., Korkmaz, C., and R. J. Connor: *Member-level Redundancy of Built-up Steel Axially-Loaded Members*, Purdue University, West Lafayette, Indiana, 2018.

AUTHORS

Jason B. Lloyd, Ph.D., P.E.
Research Engineer
Purdue University
lloyd1@purdue.edu

Francisco Javier Bonachera Martin, Ph.D.
Research Engineer
Purdue University
fbonache@purdue.edu

Cem Korkmaz, Ph.D.
Research Engineer
Purdue University
ckorkmaz@purdue.edu

Robert J. Connor, Ph.D.
Professor of Civil Engineering
Director of S-BRITE Center
Purdue University
(765) 496-8272
rconnor@purdue.edu
Corresponding Author

ACKNOWLEDGEMENTS

This project was funded by the Transportation Pooled Fund (Study Number TPF-5(253)). Participating agencies include: Federal Highway Administration, Indiana Department of Transportation, Iowa Department of Transportation, Minnesota Department of Transportation, New York State Department of Transportation, Oregon Department of Transportation, Wisconsin Department of Transportation, Wyoming Department of Transportation, and the Army Corps of Engineers. This project benefitted from substantial material and fabrication donations provided by Steel Dynamics Inc., Hirschfeld Industries Bridge Division, Nucor Fastener Division, SSAB Americas, and Nucor Plate. In addition, we acknowledge the essential contributions from staff professionals and graduate students at Purdue University throughout this research.

Contents

List of Figures

List of Tables

1. INTRODUCTION & MOTIVATION

1.1. Redundancy in Bridges

AASHTO (2014) defines a fracture-critical member (FCM) as a, "Component in tension whose failure is expected to result in the collapse of the bridge or the inability of the bridge to perform its function." In other words, in order for a primary steel tension member to be a FCM, it must be considered non-redundant. I.e., it cannot redistribute load around the failed member, or component, in order to continue to perform its function. Therefore, if it is shown that a member, or component, *is* redundant, it should *no longer* be designated as fracture-critical. A redundant bridge member is one whose failure does not result in the failure of the bridge. Simply put, it is a member that the bridge can safely operate without for a particular function or load scenario; or in other words at a required level of reliability. Redundancy in a bridge can exist in multiple forms, such as Load Path Redundancy, Structural Redundancy, and Internal Member Redundancy. These three forms of redundancy are defined by Lwin (2012), as:

- *Load Path Redundancy* is when the bridge has multiple main supporting members, such as girders or trusses, meaning more than two such members.
- *Structural Redundancy* is provided by continuity of main members over interior supports or by other three-dimensional mechanisms born from secondary members providing lateral load redistribution.
- *Internal Member Redundancy* refers to a built-up member detailed using mechanical fasteners, such as bolts or rivets, which limit fracture propagation across the entire member cross section.

Interestingly, other industries, such as the aircraft industry, address the issue of redundancy of an individual member by exploiting internal member redundancy. Specifically, ensuring that complete member failure is not a plausible failure mode since it is comprised of separate isolated components designed and detailed such that should any one of the components fail, the overall member still possesses sufficient strength to safely carry dead load and some portion of live load. This is often referred to as "fail-safe" design or "damage tolerant design". Damage Tolerant Design (DTD) uses design approaches to create a structure that can sustain defects safely until repair can be made. It is based on the assumption that flaws exist in any structure and that these flaws will propagate over time. DTD is coupled with a maintenance program that will result in detection and repair of the damage before it reduces the capacity of the structure to an unacceptable limit. Such limits could be strength and fatigue, for example. These

strategies are routinely employed in oil, aircraft and ship structures. Built-up members that use mechanical fasteners to connect multiple elements would typically qualify as "fail-safe" members, or Internally Redundant Members (IRMs). Identifying IRMs and estimating rational inspection intervals for them is a DTD approach to the asset management of existing fastener built-up steel axial members.

1.2. Brief History of Built-up Members in Bridges

Built-up member bridge construction practices using wrought iron can be traced to as early as the late 18th Century. From the 1840's onward, construction of long-span wrought-iron bridges in the UK continued the advancement of riveted connections and use of built-up member construction (Collette, 2014). The dawn of rolled steel mills in the late 19th Century and early 20th Century further progressed the use of built-up construction, making it the most widely used form of building and bridge construction (Collette, 2014; Hebdon, 2015). Hot-driven rivets were predominantly used to fasten multiple components, such as plates and angles, together until the 1950's to 1960's when high strength bolts and welding processes became preferred methods of construction. Today, thousands of bridges possessing built-up members continue to serve the highway and railway industries. They remain a vital part of the US and international infrastructure systems, and in many cases have become historic and iconic structures.

1.3. Background on Development of Fracture Critical Inspection Requirements

Currently, in the United States (U.S.), the maximum time interval between FCM inspection is mandated to be twenty-four months (23 CFR §650.311, 2017). This inspection frequency was first defined in the *Recording and Coding Guide for the Structure Inventory and Appraisal of the Nation's Bridges* in December 1995 (FHWA, 1995). The Federal-Aid Highway Act of 1968 (Pub. L. 90-495, 82 Stat. 815) originated a requirement for the Secretary of Transportation to establish the National Bridge Inspection Standards (NBIS) to ensure the safety of the nation's bridges. This legislation followed the well-documented collapse of the Point Pleasant Bridge in 1967. Later, the Federal-Aid Highway Act of 1970 (Pub. L. 91-605, 84 Stat. 1713) limited the NBIS to bridges on the Federal-Aid highway system. However, the Surface Transportation Assistance Act of 1978 (Publ. L. 95-599, 92 Stat. 2689) extended the NBIS requirements to all bridges greater than 20 feet on public roads. Later the Surface Transportation and Uniform Relocation Assistance Act of 1987 (Pub. L. 100-17, 101 Stat. 132) expanded the scope of bridge inspection programs to include special inspection procedures for fracture critical members.

1.4. Motivation for this research

Since the legislation of 1987, bridges containing FCMs have been required to receive a "hands-on" inspection, meaning the inspector must be within an arm's length of any fracture critical component (*The Manual for Bridge Evaluation Second Edition*, 2011; NBIS, 1988). The cost of hands-on inspections can be strenuous on state transportation budgets due to the time required to get at an arm's length of all FCMs in the bridge, traffic control during inspections, and specialized equipment required (Connor, Dexter, & Mahmoud, 2005). Furthermore, while hands-on inspections of FCMs are intended to improve public safety, a study carried out for Indiana interstates revealed that overall congested crash rates increased by 24.1 times over uncongested crash rates and that 90% of the congested crashes in 2014 occurred with a traffic queue duration of ≥ 5 minutes (Mekker et. al., 2015). Traffic queues of this magnitude can result from several things, including closed lanes on bridges due to inspections. Thus, protecting the safety of the traveling public is multi-faceted. It is not necessarily as simple as requiring more bridge inspection, particularly when one considers the low probability of detection for very small defects intended to be found. The approach to the nation's bridge inspection program must be rational while taking into account the economic *and* safety factors from all facets of the program.

A current search of the National Bridge Inventory (NBI) reveals that there are about 13,000 bridges with riveted and bolted built-up-members in the national inventory. Approximately 56% of the steel bridges in the United States possess FCMs and about 35% of them are trusses. Due to their status as bridges possessing FCMs, many owners are reluctant to retain them in inventory and expend disproportionate amounts of resources on inspection programs until they can be replaced. Further, the term "Fracture Critical Member" inherently raises the concern or even expectation that the entire non-redundant member will eventually fail leading to collapse.

Generally speaking, many structural engineers recognize that built-up members can possess internal redundancy, and even non-engineers typically grasp the concept when it is explained to them. However, there has been relatively limited research on the subject to corroborate the concept and satisfy the academic rigor needed for codified specifications. The available literature contains a few field experiments performed to observe post-fracture capacity of superstructures possessing built-up FCMs. However, the most comprehensive investigation was recently completed by Hebdon (2015) at Purdue University focusing on the member-level redundancy of build-up steel girders (flexural members).

Based on the work by Hebdon and the additional research described in this report, in June of 2018 the AASHTO Subcommittee on Bridges and Structures voted to adopt the guide specifications that codify methods to determine member-level redundancy for mechanically-fastened built-up members and set rational special inspection intervals. Thus, FHWA policy changes are expected to occur fueled by this acceptance of the research results by the individual state departments of transportation that make up the T-14 committee.

Prior to completion of this research, documented experimental and analytical research on the member-level redundancy and post-fracture fatigue life of built-up *axial* members remained incomplete. The data and analysis garnered from the current project has been used to develop complete, rational guidelines for assessing the redundancy of steel built-up axial members, traditionally classified as fracture critical.

2. PRIOR RESEARCH AND BACKGROUND

There are few documented cases of partially failed built-up fracture critical members in service, meaning that only one component is completely cracked, while the other components of the member are not. Additionally, member level redundancy research is also limited in the literature. Hebdon *et al*. (2015) reports a few projects, including the Milton Madison bridge field test, which is of enough consequence to this research that it is worth repeating here. The research performed by Hebdon *et al*. (2015) is easily the most comprehensive in member-level redundancy and being directly related to this research, is also discussed below.

2.1. Empirical Evidence from Bridges in Service

In-service failures can be edifying for industry, showing areas where further understanding is required to design and build more resilient structures. There is only one known case of a bridge in service that has experienced failure of a single component of a built-up axially-loaded FCM that can be found in the literature; it is the Hastings Tied Arch Bridge discussed below. While there certainly is anecdotal evidence that is sometimes cited, none appear to be documented and reported in detail. This could mean that they rarely occur, or that they simply are not usually documented. Load shedding to adjacent components during fatigue cracking of built-up components as observed by Hebdon *et al*. (2015) may also help explain why it could be rare. The lack of documented cases could also suggest that mechanically-fastened built-up members are performing better than industry tends to recognize. More broadly speaking, historical performance of any bridge with FCM failures is very insightful, especially if one is expecting partial or full collapse of the structure following failure of the FCM. The following bridges did not have built-up members, but they each experienced complete or partial failure of a FCM, *without* full or partial collapse; Lafayette St. Bridge, U.S. 422 Bridge over Schuylkill River, Neville Island Bridge over Ohio River, Hoan Bridge, Dan Ryan Expressway (cross girder fracture), Diefenbaker Bridge, and the SR-46 over Eel River (Cha *et al.*, 2014). In the case of the Hoan Bridge in Milwaukee, WI, all but a single bottom flange plate of the three girders supporting the approach span failed in brittle fracture; however, the structure did not collapse due to structural redundancy. More recently, a barge impact in September 2013 severed a FCM (bottom chord) of the Matthews Bridge in Florida (Judy, 2013) and in January 2017 the Delaware River Bridge deck truss approach span experienced a full depth fracture of one of its FCMs (Rice, 2017). Neither of these two bridges collapsed, but instead continued to carry traffic loads until they

could be closed for emergency repairs. Connor *et al.* (2005) reported that since 1960, no bridge with built-up members classified as a fracture critical member is known to have failed due to the fracture of a single component propagating a fracture to an adjacent component.

2.1.1. Hastings Bridge, Minnesota

Two separate arms-length inspections revealed two partial member fractures on the Hastings Bridge in Minnesota in 1997 and 1998. The bridge was a tied-arch through truss bridge built in 1949 with riveted built-up members (see Figure 2.1). Both fractures occurred in the same plate of the same tie girder. While the first fracture arrested in adjacent rivet holes, the second fracture propagated through the entire tie girder web plate (see Figure 2.2). Initiating, at a tack weld the second fracture ran the entire length of the web plate. Investigations later determined that a single plate used in the fabrication of the tie girder erroneously had very low toughness causing each of these fractures to occur (Niemann, 1999). The internal member redundancy of the built-up tie girder prevented the fracture from propagating into adjacent components.

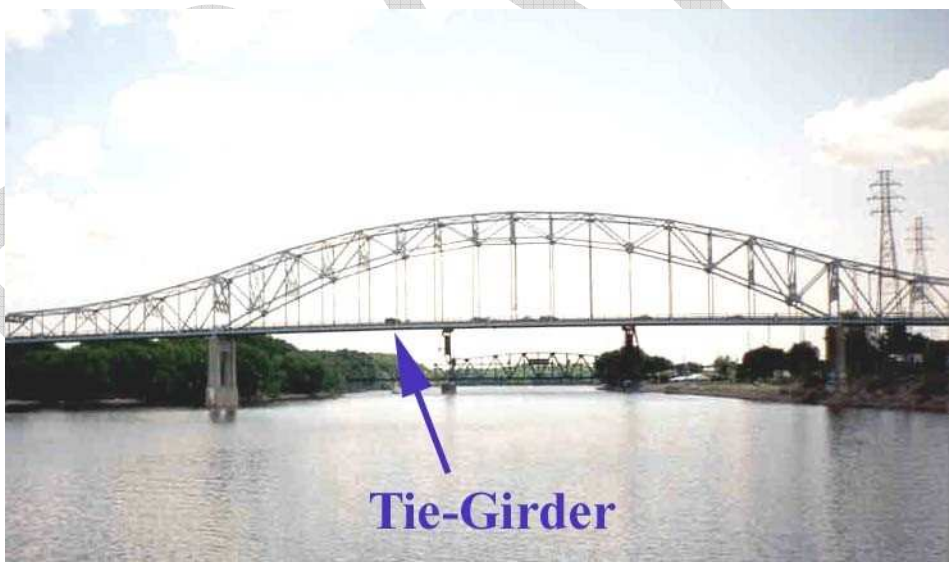

Figure 2.1 Hastings Bridge, Minnesota (Niemann, 1999)

Figure 2.2 Fractured tie girder plate, Hastings Bridge (Niemann, 1999)

2.2. Review of Laboratory & Field Research

Extensive fatigue testing of riveted members has been performed over the last several decades, including full and small-scale specimens for both flexural and axial tension members. However, few experimental studies have been performed investigating fracture resistance of built-up members focused on quantifying member-level redundancy. A few pertinent previous research projects are discussed below, listed in chronological order.

2.2.1. Fisher, Yen, and Wang (1990)

As part of NCHRP Report 302, Fisher *et al.* (1990) compiled fatigue test data for more than 1,200 full-scale riveted members and reported that the type of riveted detail did not significantly affect fatigue resistance. Consistent with current fatigue category designations for riveted details, they reported that when the net section stress range exceeded 7 ksi (the constant amplitude fatigue limit of AASHTO Category D), and that "first" cracking could be expected in one or more components. However, the total fatigue strength of riveted details was best characterized by the AASHTO Category C curve due to the inherent redudnacy provided by the multiple components requiring new cracks to initiate in individual components Fisher *et al.* (1990) reported three more interesting conclusions:

1. Fatigue cracks developed in riveted members favor inspection due to the "significant remaining life" that existed between development of a crack in a component and failure of the section.
2. It was not possible to develop brittle fractures from small fatigue cracks in full-scale test members.
3. All of the built-up members tested possessed sufficient member-level redundancy, "retaining their structural adequacy when one or two components of the tension-carrying components cracked". The sections were all able to redistribute the applied loads without adverse effects.

These three conclusions were all consistent with findings reported by Hebdon *et al*. (2015) discussed below.

2.2.2. DiBattista and Kulak (1995)

DiBattista and Kulak (1995) investigated full-scale riveted members in shear splice connections. Perhaps the most unique aspect of this research was that it focused on the fatigue resistance of axially loaded specimens that were taken from a bridge. While some fatigue data for riveted shear splices existed prior to this research (Fisher *et al.*, 1987), some of which was reported to come from in-service bridges, as well. This is interesting simply because most full-scale fatigue test data were obtained from flexural girder tests within a region of constant moment. The nuance offered by uniaxial testing (or flexural testing in three-point bending) is the inclusion of bearing stresses on the fatigue resistance of built-up riveted members, but these only occurss if a portion of the axial member is attached to loading points or there is a splice within the member where shear loads would be transferred. Whereas, hypothetically no bearing effects would be captured in a constant moment region of zero shear stress of a four-point bending flexural specimen. Fisher *et al.* (1987) also discussed the bearing ratio variable suggesting that a bearing ratio of less than 1.5 (nominal stress of the rivet to the nominal tensile stress in the plate) had little effect on the fatigue life, but when it exceeded 1.5 combined with a reduced clamping force, the fatigue life was notably affected (less than Category D).

DiBattista and Kulak (1995) argue that results from the constant moment region tests may give unconservative results for predicting fatigue life of riveted details that are in bearing. Furthermore, in order to supplement the existing database of fatigue test results for riveted details, the specimens were subjected to low stress ranges. The experimental program consisted of fatigue tests of full-scale gusset plate end connections from four riveted tension diagonals taken from the Miette River Bridge. It was

determined prior to testing that any existing fatigue damage from service loads was negligible because strain measurements and historical records indicated that the stress ranges in the diagonals never exceeded the Category D CAFL. Four diagonals were obtained from the bridge and then cut in half producing eight total specimens (only seven were tested due to damage of one during removal from the bridge). The diagonals consisted of four angles riveted to a web plate forming a built-up I-section using a single row of aligned rivets (versus a staggered rivet pattern). A loading plate was attached to the cut end of the specimens, and using a fulcrum with bearing pins to release moment due to rotation of the lever arm, the specimens were loaded in uniaxial tension with a single hydraulic actuator. A minimum stress of 1.4 ksi was maintained and several stress ranges were tested ranging from 8.4 ksi to 10.6 ksi. The failure criteria defined was complete failure of one angle and a crack detected in a second component of the built-up member. *Typically, the second component to crack was the web plate, which was the adjacent component to the cracked angle.*

They concluded that the fatigue test results exceeded the fatigue strength predicted by Category D, and were close to Category C in some cases. Other specimens, however, resulted in fatigue strength less than that predicted by Category D. These poorer performing specimens all had two unique characteristics in common with each other, however, that were suggested as the cause for lower fatigue resistance. First, each had relatively large gaps between the plies indicating lower clamping forces in the rivets. Second, each had sets of rivet holes that were very close to each other near the points of cracking suggesting the net section stress range may not have been accurately estimated using a straight net section plane. Literature review discussed by DiBattista and Kulak (1995) included two reports on fatigue tests carried out on axial members that seemed to corroborate that the fatigue strength of riveted axial members is at least Category D and in some cases exceeded Category C. These references are Reemsnyder (1975) and Baker and Kulak (1982).

2.2.3. Diggelmann, Connor, and Sherman (2013)

A destructive field test was performed on the Milton-Madison Bridge prior to demolition. This bridge was built in 1921 to carry US-421 across the Ohio River connecting Milton, KY, with Madison, IN. The bridge was comprised of 19 spans, including several deck truss approach spans on the Madison side (north end) and multiple through-truss main spans and approach spans on the Milton side (south end) (Diggelmann *et al.*, 2013). The superstructure was built-up riveted construction, which was common in the 1920's.

In April 2012, researchers at Purdue University instrumented the first deck truss approach span on the Indiana side of the bridge, seen in Figure 2.3. The center three panels of the span were then loaded with 145 kips of sand (approximately 2/3 of the original design live load). The center of the bottom chord was rigged with explosives and severed in two stages. The first blast severed one of the two built-up channels that made up the tension chord, as shown shortly after the explosion in Figure 2.4. The channel was severed by the blast about six feet from the gusset plate connection. Cutting just one (the interior) of the two channels was performed to observe the member level redundancy of the built-up tension chord. The second blast minutes later severed the rest of the fracture-critical tension chord, revealing the structural redundancy of the span.

Figure 2.3 Approach span of Milton Madison Bridge tested for redundancy

Figure 2.4 Partially severed FCM, Milton Madison Bridge approach span

2.2.3.1. Summary of Results for Milton Madison Bridge Partial FCM Fracture

Focusing on the portion of the Milton Madison Bridge test that rendered the bottom chord partially failed (the first blast), the following summarizes pertinent results from that test, as reported by Diggelmann *et al.* (2013):

- Note from Figure 2.4 that the remaining component of the FCM (after the first blast), had been damaged by the demolition contractor prior to the blast. They removed the flanges of the angles with a torch, which can be seen in the figure by the blackened member near the first blast location. Severing half of the FCM did not result in the complete member failure or structural collapse, even with a severely damaged remaining component. The bridge maintained sufficient member level redundancy for the applied loads.
- The component failure was a worst-case scenario since the angles and both plates that comprised the built-up channels were all severed simultaneously. In a real-word scenario, only one of these four components would have been able to fail since a crack would not have been able to propagate across component boundaries.

- Deflections resulting from the first blast were very small, between 0.08 and 0.12 inches, which were near the limits of what could be detected using the equipment and crew size used for the deflection measurements.

2.2.4. Hebdon et al. (2015), Hebdon et al. (2017a), and Hebdon et al. (2017b)

Phase I of this pooled fund research project investigated the behavior of built-up flexural members in a partially failed state. Fifteen full-scale built-up steel girders were tested in the following manner. First, each specimen had a component, such as a flange angle or cover plate, notched and loaded in fatigue (four-point bending) to help control and accelerate fatigue crack growth at a particular location. Next, the specimens were cooled to embrittle the material making it more vulnerable to fracture. Fracture of a single component was then attempted or induced by several methods. And finally, the specimen was cycled again in constant amplitude fatigue in the faulted condition until another component of the damaged built-up girder failed in fatigue. Following the experimental program, an analytical program investigated multiple parameters of typical built-up girder construction to characterize how they affect the behavior of the girders in the partially failed state. The results of the parametric study were used to determine factors to calculate after-fracture net section stresses, which are necessary to determine the remaining fatigue life of built-up girders with a component failure. Several pertinent conclusions resulted from this research. They are:

- Brittle fracture of a component from a built-up girder is highly unlikely due to the constraint created by adjacent fasteners and redistribution of load into adjacent components. Hebdon *et al*. (2015) pointed out that traditional linear elastic fracture mechanics calculations, which assume a single plate with a crack, did not accurately predict the critical crack length of a cracked component for these reasons. In fact, in order to induce fracture for the experiments, they had to perform all three of the following steps:
    - Load the specimen to the full design load resulting in an original net-section stress greater than the calculated critical stress for a given crack length.
    - Adjacent fasteners were removed from near the intended fracture plane to reduce constraint and allow the crack to open.
    - Hydraulically driven wedges were forced into notches in line with the fatigue cracks to escalate stress intensity at the crack tip.
- Forced fracture of a component was performed without the fracture propagating into adjacent components. Cracks were found in other components of the built-up tension flange in which

hydraulically-driven wedges were not used to force brittle fracture; however, these were due to fatigue, i.e., were not form as a result of brittle failure of an adjacent component.

- Significant fatigue life remained after fracture of a component in built-up girders. Using the calculated net stress range for the partially failed girder section, the AASHTO Category D fatigue curve was found to be a reasonable lower bound for girders with drilled or reamed holes. When the stress amplification factor discussed below was used, however, the category was increased to Category C. And finally, the AASHTO Category E' fatigue curve was found to be a reasonable lower bound for girders with holes punched full size for the partially failed girder section and stress amplification factor.
- Stress redistribution during fatigue crack growth of the built-up girders revealed the following:
    - Non-symmetry resulting from a partially cracked component, such as a cover plate, substantially increased stress in the adjacent component(s) when the cracked component had lost 60% or more of its section. However, it was concluded that this was not of significance and could be ignored simply because the remaining section of the partially cracked plate would fatigue out quickly and the small number of higher stress range cycles due to the partial crack were negligible on overall member fatigue life.
    - The majority of load redistribution from a cracked component transferred into immediately adjacent components (60% - 80%). The percent stress increase in adjacent components was found to be reduced when the member possessed multiple cover plates.
    - Resulting stress in an adjacent component to the fully failed component was found to be 20% - 25% larger than that calculated using linear elastic beam theory based on the remaining net section. Thus, Hebdon *et al*. (2015) developed an amplification factor, β_{AF}, to account for this behavior, shown in Equation (2.1).

$$\sigma_{net-AF} = \beta_{AF} \frac{M}{S_{x-net-AF}} \tag{2.1}$$

Where:

$\sigma_{net\text{-}AF}$ = after-failure net section stress

β_{AF} = 1 + 0.2(1+N/4) = after-failure net section amplification factor (*Note: this was later changed to $\beta_{AF} = 1 + 0.25(1+N/4)$ to account for additional secondary effects, which were discovered during additional parametric studies that considered even more extreme geometries.*)

M = applied moment based on the AASHTO fatigue truck (AASHTO 2014, Article 3.6.1.4)
N = the number of cover plates
$S_{x\text{-}net\text{-}AF}$ = after-fracture section modulus

- Finally, Hebdon *et al*. (2015) described a method to determine the remaining fatigue life of a built-up girder with a single component failed using the Palmgren Miner's Rule of linear damage accumulation accounting for fatigue damage prior to the single component failure and an adjusted net-section stress range to account for damage accumulation after a single component failure.

The remaining fatigue life could then be used to set a rational arms-length inspection interval for the member. It is worth noting that the inspection interval assumes that the moment the inspectors evacuate the bridge, a component fractures and the adjacent components accumulate fatigue damage at a higher stress range. However, testing by Hebdon *et al.* (2015) and Fisher *et al.* (1987) showed that brittle fracture in built-up members is very unlikely due to inherent load redistribution as a component slowly fatigues. Thus, the method proposed by Hebdon *et al*. (2015) to set an extended inspection interval holds another level of conservatism in that sudden fracture is not the likely failure mode. Rather it is more likely the component would slowly crack in fatigue.

2.3. Summary of Current Specifications

2.3.1. AREMA Chapter 15

The American Railway Engineering and Maintenance-of-Way Association (AREMA) Chapter 15 (Commentary Article 9.7.3.3.2 (3)) contains a paragraph that briefly describes the potential for member-level redundancy inherent in built-up members. It states that due to multiple components, the immediate consequence of fatigue cracking may not be as serious as in welded structures. It states further:

> "*Riveted construction often has built-up members and connections, so that if one element fails there is normally sufficient capacity and redundancy for the force to be redistributed. The members will usually survive long enough for the crack to be detected by routine inspection thereby permitting corrective action before more serious damage develops. If no immediate repair action is to be taken, the probable time between first detectable cracking and uncontrolled propagation should be taken into account when setting up inspection frequency*."

This brief paragraph describes the essence of this research. The AREMA section, however, does not provide specifics on how to determine if "sufficient capacity" does exist, meaning not only strength, but fatigue resistance, and how exactly to set up the inspection frequency. These very things are among the objectives of this research.

2.3.2. AASHTO Manual for Bridge Evaluation

The AASHTO Manual for Bridge Evaluation contains a short commentary in Section C7.2.1 which states, "For new design, the base metal at net sections of riveted connections is specified to be Category D. This represents the first cracking of a riveted member, which is highly redundant internally." It further suggests that due to the internal redundancy, Category C is more accurate for the crack to grow to "critical size". It ends by stating, "This increase in fatigue life for evaluation purposes is appropriate due to the redundancy of riveted members."

The principle of this commentary is that longer fatigue life can be counted on for built-up riveted members due to internal member redundancy that allows for load redistribution and crack tolerance. This could possibly be interpreted to mean what the AREMA specifications more explicitly states. A critical crack size is one that can be found by inspectors before more severe damage occurs, relying upon member-level redundancy to maintain service loads until then. The MBE commentary appears to be suggesting that Category C fatigue resistance is more accurate for riveted built-up members because Category D is based upon "first cracking", suggesting that the extended fatigue life gained by evaluating as Category C is due to fatigue crack growth beyond first cracking, perhaps to cracking of a second component within the cross section. Evaluating mechanically built-up members in this way would mean that inspectors are not intended to identify small cracks growing from beneath rivets heads, but rather they are intended to identify a component that is fully cracked through.

2.3.3. Current Federal Highway Administration Policy

Lwin (2012) clarified requirements for, and definitions of, redundant and non-redundant members in bridges. Along with defining modes of redundancy, Lwin states the policy of the time, which is that FHWA cannot accept the approach of using internally redundant detailing to demonstrate that non-load path redundant members are not fracture critical. However, the memorandum concludes stating that implications of IRMs are the subject of ongoing research, leaving the policy open to change pending results of pertinent research.

3. EXPERIMENTAL RESEARCH PROGRAM

The experimental research program conducted in this portion of the research consisted of five brittle fracture tests of full-scale built-up axial members and two load redistribution tests of continuous truss chords. Table 3.1 contains the list of fracture specimens that were tested, indicating the failed component, the type of fasteners, and the result of the tests. The five fracture specimens were fabricated from modern materials. However, as is discussed below, all specimens were tested at temperatures that placed them into lower shelf fracture toughness removing any advantage in toughness offered by modern steels. Four of the five fracture specimens were made up of three plates, including two 1/2-inch thick outer plates (referred to as redundancy plates) and one 1-1/2-inch thick center plate. The fifth fracture specimen was composed of a 3/4-inch thick center plate and four 5x3-1/2x1/2 inch redundancy angles. The two load redistribution specimens were obtained from two 65-ft. long tension chord sections removed from the Winona Bridge deck truss span when the bridge was replaced. Additional background information on the Winona Bridge is provided in Section 3.1.7. The purpose of the load redistribution tests was to observe after-fracture load redistribution behavior of a partially failed cross section, such as would be the case if a single channel failed in a two-channel member. The results of the load redistribution tests were used to calibrate finite element models for a two-channel member parametric study and validate the simplified method of analysis that resulted.

3.1. Experimental Tests

Five specimens were tested in order to prove the resistance of built-up axial members to fracture propagation across component interfaces, herein referred to as cross-boundary fracture resistance (CBFR). This type of test was also performed by Hebdon *et al*. (2015) for flexural members in four-point bending. Similar to the flexural tests, each axial specimen was notched and cycled in fatigue to sharpen a crack tip at the edge of one of the components. Next, the specimens were cooled using a cooling chamber and liquid nitrogen to at least the AASHTO Temperature Zone 3 Minimal Service Temperature (MST) of -60°F, and then axially loaded. If the toughness of the modern steel required a cooler temperature than Zone 3 in order to achieve single-digit ft-lbs toughness, then a colder temperature was applied during the test. As was observed by Hebdon (2015), initiating brittle fracture in mechanically fastened built-up members was challenging. If the notched component did not fracture at the peak test load, then

hydraulically-driven wedges were applied at the notches to increase the stress intensity factor and force brittle fracture propagation without overloading the specimen.

A few different fasteners were included in the CBFR tests. These included snug tightened high strength bolts (shown to mimic the clamping force of a hot-driven rivet; Bowman *et al.*, 2012), finger-tightened (no wrench used) A307 bolts (shear stiffness of the A307 bolt is similar to a modern A502 hot-driven rivet; Ocel, 2013), and one case where snug tightened high strength bolts were combined with a tack weld aligned with the fracture path.

The load redistribution specimens obtained from the Winona Bridge deck truss were riveted built-up members constructed with 3/4-inch diameter hot-driven rivets. Due to the length of these specimens, a second test frame was required, which is described below.

3.1.1. Test Matrix for Experimental Work

The fracture test matrix included five CBFR specimens and two two-channel member specimens. The specimens and tests associated with each specimen are listed in Table 3.1. The cross-boundary fracture resistance of built-up members has been adequately demonstrated for flexural members (Hebdon *et al.*, 2017b). It was desired to observe if axial members possessed similar fracture resistance. Some have suspected that the extreme demands put on the edges of fastener holes due to potentially large bearing stresses during fracture could initiate ductile tearing or brittle fracture in components adjacent to the failing component, thereby propagating the fracture through the entire cross section. Additionally, it was expressed by some that frictional forces between components could possibly propagate the fracture, as well. It was critical to this research to see if the cross-boundary fracture resistance observed in flexural members would also be observed in axial members.

Four specimens were designed and fabricated with exaggerated proportions favoring a high energy release rate and load transfer during the fracture event. This is discussed more in the following section. The fifth fracture resistance specimen was unique from the first four fracture resistance specimens in that instead of two small plates providing redundant load paths, four angles were used, one of which had a tack weld connecting it to the fracture component. The objective with this specimen was to observe the effect of the tack weld on the fracture resistance. Specimen fabrication drawings are provided in Appendix D.

Table 3.1 Experimental Specimen Test Matrix

Specimen ID	Specimen Type	Targeted Parameter	Component Failed	Fastener Type	Fracture Jumped?
1	New	Fracture resistance	Center plate	Snug A325	No
2	New	Fracture resistance	Center plate	Snug A325	No
3	New	Fracture resistance	Center plate	Loose A307	No
4	New	Fracture resistance	Center plate	Snug A325	No
5	New	Fracture resistance with tack weld	Center plate	Snug A325	No
6	Removed from Service	Multi-Component Behavior	Cover Plate at mid-panel	Rivet	N/A
		Two-channel behavior	Channel near Gusset	Rivet	N/A
7	Removed from Service	Two-channel behavior	Channel at mid-panel	Rivet	N/A

Specimen 6 and 7 were removed from the Winona Bridge. They were primarily used to observe behavior of two-channel, continuous built-up axial members that extended beyond a single span, or a single panel length. These specimens served to obtain data on the behavior of the two-channel members once a single channel has failed. This included continuity benefits that could exist. They were also used to calibrate finite element models to carry out a parametric study that was used to develop a simplified method of internal redundancy evaluation for two-channel members, which is discussed further in Section 4.5.1. Although the Winona Bridge members were not specifically two-channel members (they had a redundant cover plate, as can be seen in Figure 3.26), the two-channel member behavior could be studied by simply severing one entire half of the tension chord (cover plate and rolled channel) allowing the collection of data on the load redistribution that occurred when one half of the member was failed. In addition, Specimen 6 was used to observe behavior when a single cover plate was failed, helping to support the investigation of load redistribution behavior of multi-component members.

3.1.2. Design of CBFR Specimens 1 - 4

Cross-boundary fracture resistance (CBFR) was tested using Specimen 1, 2, 3, and 4. Figure 3.1 shows a sketch of the specimens, having two 1/2-inch thick redundancy plates that narrow at the middle portion in order to reduce the cross section and one 1-1/2-inch thick center plate. The proportions were not typical of in-service built-up axial members for the distinct purpose of intensifying the strain energy released and redistributed load during fracture. By testing a very extreme case of fracture resistance it

stands to reason that less extreme proportionality differences between components found in-service would exhibit similar fracture resistance. In this case, the center plate made up 66% of the total cross section. A hole was machined at each end of the specimens for the loading and reaction pins. Two lubricated eight inch diameter high strength, quenched and tempered pins were used to load the specimen to help reduce bending moment in the specimen that could possibly result from test assembly or loading imperfections, etc. The three plates were bolted together using 80 bolts located at the center in four columns spaced four inches apart and twenty rows spaced three inches apart.

Each specimen was instrumented with strain gages and thermocouples. Gage plans showing exact locations of the sensors are provided in Appendix C. Load was measured using a calibrated pressure transducer between the hydraulic pump and the ram manifold.

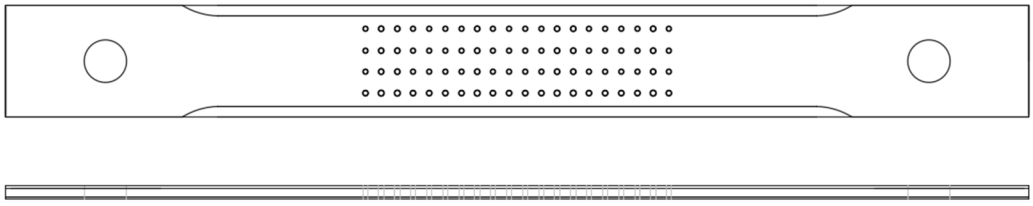

Figure 3.1 Sketch of CBFR Specimens 1, 2, 3, and 4

Figure 3.2 shows the specimen in the test frame, cooled (indicated by the white frost formed on the surface), and having small hydraulic rams with wedges inserted into the notches, all being held by two self-reacting frames. Hebdon *et al*. (2015) observed that brittle fracture would most often not initiate without the aid of the wedges, which were used to increase the stress intensity at the fatigue crack tip by increasing crack tip opening, without applying additional load to the specimen. Once the specimen was brought up to peak test load, the hydraulic wedges were driven into the notches. Notice that the self-reacting frames used to hold the small hydraulic jacks were constructed such that they vertically hinge and could not carry axial load, meaning they did not provide an additional load path for the redistributed load resulting from fracture of the center plate.

Figure 3.2 Fracture specimen with hydraulic rams and wedges in place

3.1.3. CBFR Test Setup and Specimen Preparations

Two test setups were required for the CBFR test matrix. The first was the fatigue station used to grow a sharpened fatigue crack at the edge(s) of the fracture components. Several steps were taken to prepare the fracture component prior to fatigue cycling. First, the component intended to be fractured was notched at one or more edges, developing a stress concentration to accelerate fatigue crack growth and control where the crack initiated. Figure 3.3 shows an example of one of these specimens after it had been notched.

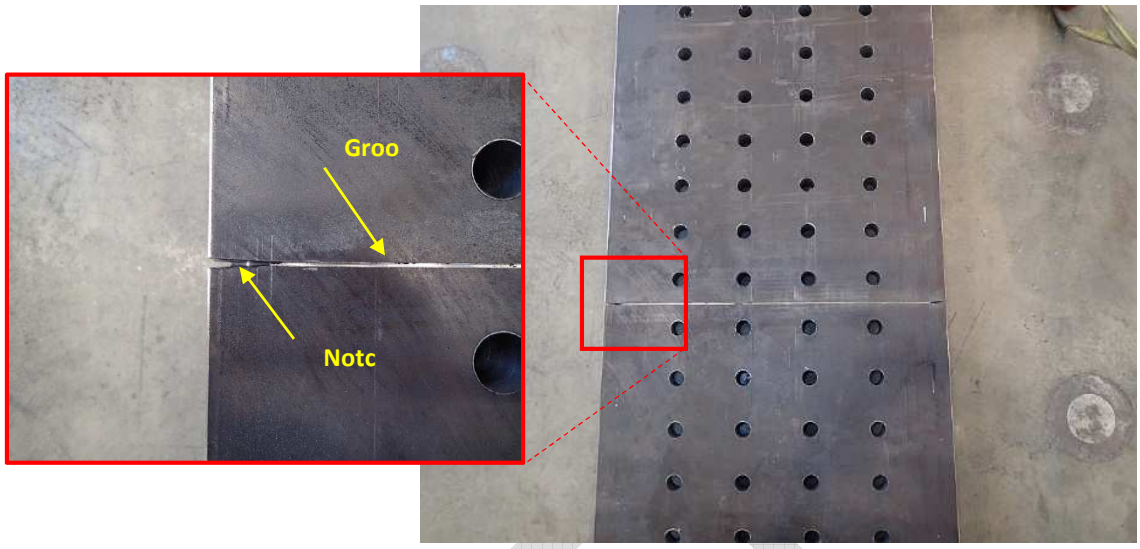

Figure 3.3 Edge notch & groove for fatigue crack growth on fracture specimens

Following notching, a shallow groove was cut across the entire transverse direction of the component intended to be fractured. The groove has been labeled on the inlet of Figure 3.3. The purpose of the groove was to help increase stress concentration across the component to guide the fracture away from a fastener hole, ensuring a complete fracture of the entire component cross section. This was done because the stress pattern due to shear transfer through bolts or rivets tends to guide an advancing crack front towards a fastener hole resulting in crack arrest. However, the goal of the test was to achieve a complete fracture of the component. After notching and grooving, the fracture components were placed in the fatigue station shown in Figure 3.4 and Figure 3.5. The notched plate was stood on its edge and braced at four locations along its length, then cycled in tension-only sinusoidal fatigue loading with about a 10 ksi stress range. Once the crack had grown just beyond the notch, the plate was flipped and the other side of the plate was fatigue cracked in a similar fashion. Most of the specimens required about 300 – 400 thousand cycles per side for the crack to initiate and grow to the desired length. After completion of the fatigue crack growth, the specimens were assembled in the large-scale axial test frame.

Figure 3.4 Fatigue station setup

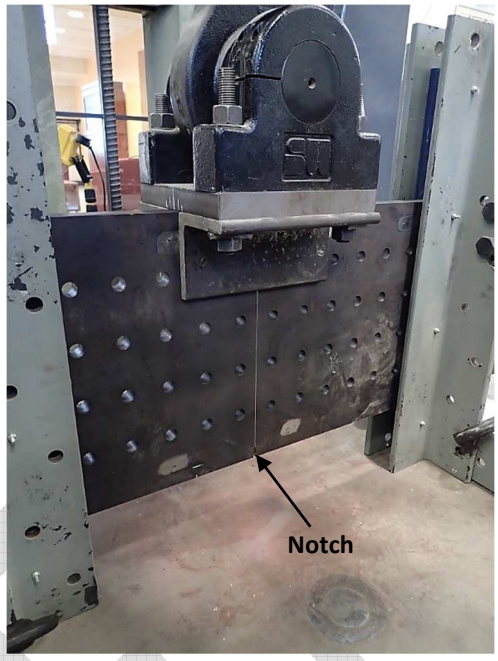

Figure 3.5 Fatigue loading of a fracture plate

The second CBFR test setup is shown in Figure 3.6. It was a vertically-oriented self-reacting frame designed for a maximum tensile capacity of 2,000 kips. This frame was used for all of the fracture tests completed during this research. Once the specimens were inserted into the frame (one at a time), they were bolted together, instrumented with strain gages and thermocouples, and then cooled using a cooling chamber and liquid nitrogen. The fracture specimens were cooled to a temperature that ensured lower shelf fracture toughness of the redundancy components. The cooling chamber is shown in Figure 3.7, being constructed of rigid foam insulation and wood with copper plumbing that utilized low pressurized tanks to blow the liquid nitrogen inside the chamber. The cooling process typically took about 1.5 hours, with the target temperature being achieved on the surface of the specimens within the first 20 minutes, followed by another hour of "soaking" to ensure the plates were fully cooled through the thickness.

Figure 3.6 Large-scale axial test frame

Figure 3.7 Cooling chamber used to reduce specimen toughness

3.1.4. CBFR Specimen 1 - 4 Test Results

3.1.4.1. CBFR Specimens 1 - 4 Material Testing Results

Specimens 1 - 4 were made up of Grade 50 steel. The center plates were cut from new plate material. The two redundancy plates installed on either side of the center plate were also cut from modern materials. However, they first served as web plate material for two specimens from research completed by Hebdon *et al*. (2015). The web plates were cut out of the built-up girder webs, machined, and reused for these tests. All four redundancy plates were made from two web plates. The first set of redundancy plates were tested in Specimen 1. The second set of redundancy plates were used for Specimens 2, 3, & 4. This statement is significant in that the same plates resisted all three fracture events without any detectable sign of damage resulting. The redundancy plates were ASTM A709-Gr 50 steel plates. Table 3.2 provides the strength and Charpy V-notch impact test data for the redundancy plates and Figure 3.8 plots the entire energy vs. temperature curve, obtained from Hebdon *et al*. (2015). Single digit toughness values were expected at the test temperature targeted for each fracture event. Hence, the fact that all of the redundancy plates resisted fracture cannot be a result of superior toughness. Interestingly, it appears that the impact energy results for these plates would not pass for *fracture-critical* Zone 3 material, being less than the required 25 ft-lbs at 10°F. Regardless, the tests were performed at -60°F, putting the toughness of the redundancy plates in single-digit ft-lbs.

Table 3.2 Material properties for the 1/2-inch redundancy plates (Hebdon et al., 2015)

Specimen ID	Avg. CVN @ -30°F (ft-lbs)	Avg. CVN @ -60°F (ft-lbs)	Yield Strength (ksi)	Tensile Strength (ksi)
1, 2, 3, 4	12	7	59	80

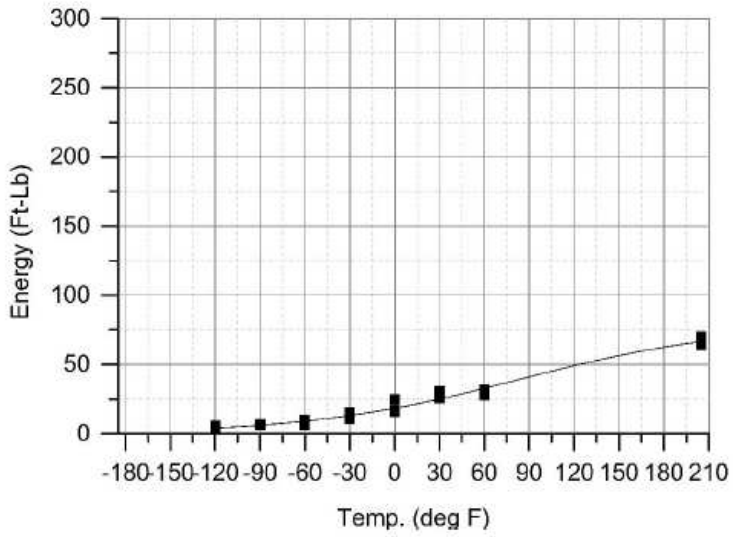

Figure 3.8 CVN impact energy for 1/2-inch redundancy plates (Hebdon et al., 2015)

3.1.4.2. CBFR Specimens 1 – 4 Fracture Test Results

Table 3.3 summarizes the test data for CBFR Specimens 1 - 4. The first test performed revealed that upon fracture of the center plate, the load significantly dropped due to a prompt change in axial stiffness that could not be matched by the ability of the hydraulic system to maintain the load. What resulted was a quick reduction in load, as well. Table 3.3 lists the load at fracture and the load after fracture, meaning the load that was sustained by the redundancy plates once the hydraulic system equalized again. For tests 1, 2 and 4, the load reduced approximately 26 – 30%. The load dropped 39% for test 3.

Table 3.3 Fracture test results for CBFR Specimens 1 - 4

Specimen ID	Redundancy Plate Set	Load at Fracture (kips)	Steel Temp. at Fracture (°F)	Load after Fracture (kips)	Calculated Net Section Stress (ksi)
1	1	657	-60	480	36.2
2	2	1015	-30	758	57.2
3	2	994	-65	614	46.3
4	2	1000	-70	705	53.2

Anticipating the drop in load, the fracture load for tests 2, 3, and 4 was increased about 30% such that upon fracture of the center plate, the redundancy plates would be required to sustain a load approaching their nominal yield strength of 50 ksi. This also meant that they needed to briefly resist a load approaching 30% greater than their nominal yield strength.

Table 3.1 lists the type of fastener used and how it was tightened for each test. Tests 1, 2 and 4 used ASTM F3125 Grade A325 high strength bolts. The bolts were installed in a snug-tight condition, which is defined as the full effort of one ironworker using an ordinary spud wrench to bring the plies into *firm* contact (RCSC, 2014). This was done attempting to simulate the average clamping force of a hot-driven rivet (Bowman *et al.*, 2012) making a shear/bearing joint, which was considered to be the most demanding shear load transfer mechanism at the bolt holes of the redundancy plates.

Figure 3.9 provides a sample of data for Test 4 from two strain gages that were located on opposite sides of the specimen (one on each of the redundancy plates), centered directly over the fracture plane. Data were sampled at a rate of 10 kHz. The instant of fracture is evident on the plot from the large spike in stress going from the upper 20's ksi to a peak of 62 ksi. This response was similar between tests 1, 2, and 4 where snug-tight bolt conditions existed.

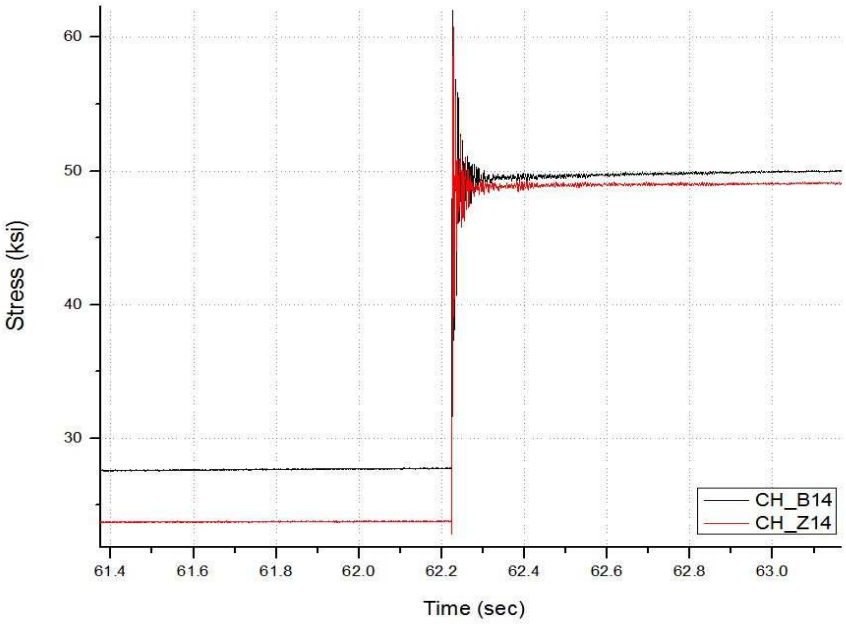

Figure 3.9 Sample of stress data from Test 4 using snug-tight bolts

Knowing the variability in bolt clamping forces that can result from snug-tight conditions (Bowman *et al.*, 2012; Kulak *et al.* 2001), fracture test 3 was performed using finger-tight conditions with ASTM A307

bolts to ensure all load was transferred through bearing in the bolt and bolt hole and effectively no load could be transferred through friction. In this context, "finger-tight conditions" means no wrenches were used to tighten the bolts; rather, the three plates were brought into contact by simply turning the nut using the strength of a worker's own hands. This left no perceivable gaps between plates while ensuring the lowest possible clamping force in each bolt. Figure 3.10 plots stress data from two strain gages located at the same locations as the strain gages in Figure 3.9. The data were collected at a rate of 10 kHz. The measured fracture load for test 3 was within 6% of the fracture load for test 4. However, the measured peak stress reached 79.4 ksi in both central gages before the load dropped off (the load was sustained for approximately 1/100th second). This means the redundancy plates sustained an impulse loading that was equal to their measured tensile strength of 80 ksi. Once the load dropped off, the sustained stress in the redundancy plates exceeded their nominal yield strength of 50 ksi, slightly below the measured yield strength, 59 ksi. Upon removal from the test frame, the redundancy plates were examined for any damage, such as elongated holes or cracks. No damage could be detected.

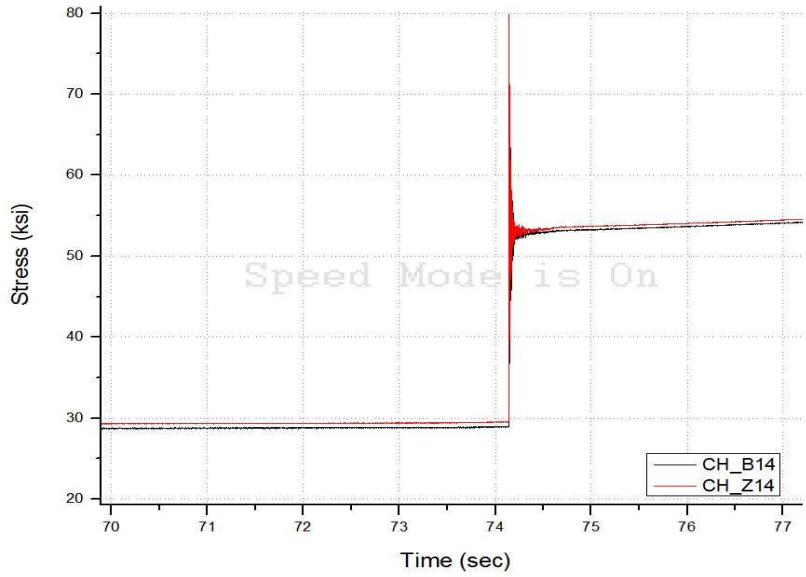

Figure 3.10 Sample of stress data from Test 3 using finger-tight bolts

The fracture tests were purposefully harsh and extreme cases with low material toughness and disproportionate components that resulted in large load redistribution into redundant components. No running fractures propagated beyond a single component unequivocally demonstrating that mechanically

built-up axial members possess internal member redundancy through cross-boundary fracture resistance. Furthermore, this conclusion is conservative when considering that brittle fracture of a component in a mechanically built-up member is extremely unlikely (Fisher *et al*., 1987; Hebdon *et al*., 2015).

3.1.5. Design of CBFR Specimen 5: Tack Weld Specimen

The objective for Specimen 5 was to observe if a tack weld would affect the cross-boundary fracture resistance of the built-up member. The layout of Specimen 5 is shown in Figure 3.11. Fabrication drawings with greater detail are provided in Appendix D. The net section of the four redundancy angles combined was approximately equal to the net section of the center plate. Thus, unlike for fracture specimens 1 – 4, fracturing the center plate resulted in approximately half of the cross section severed. The redundancy angles were attached to the center plate using a single column of 20 bolts each. 5/8-inch thick reinforcement plating was welded to both sides of the ends of the center plate near the loading and reaction pins to increase bearing capacity.

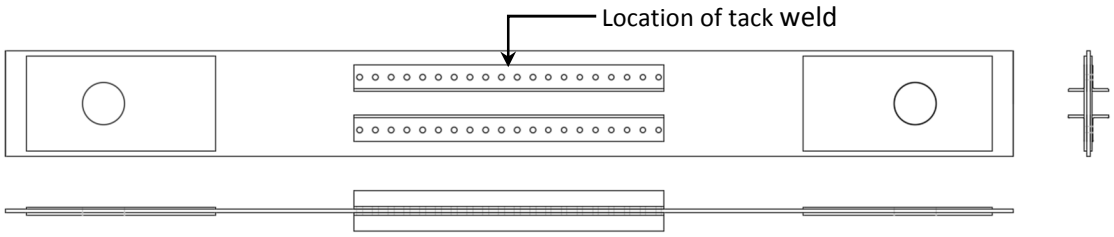

Figure 3.11 Specimen 5 fabrication drawing

Historically, tack welds were used by fabricators to hold geometry during fit-up, drilling or punching, and riveting of members together. At that time, the fatigue resistance of tack welds was not understood and removal of the small welds was not considered necessary. The current AWS D1.5 requires the same quality of weld for tack welds as for final welds, and that if the tack welds are not incorporated into final welds, that they be removed without leaving nicks or gouges (AWS, 2015). However, for decades this was not the case and so many bridges are currently in service having built-up members with tack welds from fabrication.

This test was designed to be an improbable worst-case scenario. A long tack weld was placed directly in line with the notch and fatigue crack, forcing the running fracture to intercept it. While fatigue cracking of tack welds in service is not unheard of, it also is not very common. Bowman *et al.* (2012) showed that the fatigue resistance is that of AASHTO Category C or better. When they do crack, they generally crack in a relatively benign throat failure or simply become unfused to the base metal (Connor & Lloyd, 2017). It is possible, though, for a tack weld to crack at the toe into the base metal, this was the cause of the Hastings Bridge component failure. In any of these cases, however, the fatigue crack would have no path into an adjacent component. Instead, the built-up member would need to develop a fatigue crack at a plate edge, away from the tack weld. This could be very unlikely, unless there is some kind of damage, such as a gouge or nick present. Making this scenario even less likely is that the edge crack would also need to align with a tack weld. These are the only plausible cases for this scenario to occur in service. That said, this test was designed to demonstrate built-up member CBFR in the event that it did occur.

3.1.6. CBFR Specimen 5 Test Results

3.1.6.1. CBFR Specimen 5 Material Testing Results

CBFR Specimen 5 required several attempts before successfully fracturing the center plate. The plate was modern ASTM A709 steel for nonfracture-critical applications. The redundancy angles were also modern steel, meeting ASTM A36 chemistry requirements, while possessing grade 50 nominal yield strength. Single digit CVN energy values were expected at the test temperature targeted for the fracture event. Hence, the fact that the redundancy angles resisted fracture, once again, was not the result of superior toughness. Table 3.4 provides the CVN energy averages at -30 and -60°F. Notice that at -60°F, the average CVN energy was 5 ft-lbs. Due to the challenges of forcing brittle fracture in the center plate, however, the final fracture test was performed close to -150°F to better ensure brittle behavior. Figure 3.12 plots all CVN energy values measured for the redundancy angles.

Table 3.4 Material properties for the 1/2-inch redundancy angles

Specimen ID	Avg. CVN @ -30°F (ft-lbs)	Avg. CVN @ -60°F (ft-lbs)	Yield Strength (ksi)	Tensile Strength (ksi)
5	21	5	55	70

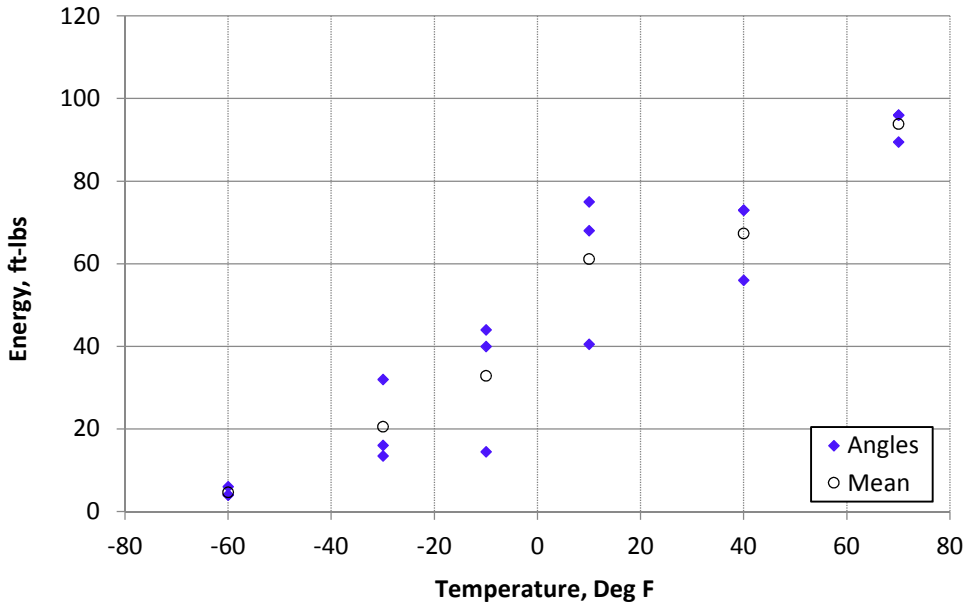

Figure 3.12 CVN impact energy for 1/2-inch redundancy angles

3.1.6.2. CBFR Specimen 5 Fracture Test Results

The targeted fracture load was 820 kips, putting the redundancy angles close to net section rupture when the center plate fractured. The center plate material, even at temperatures as cold as -80°F, locally yielded out-of-plane when the wedge was driven into the notch during the initial fracture attempts making the wedge ineffective at opening the crack. In an effort to prevent the local yielding at the notch, two steel tabs were welded to the center plate directly above and below the notch along the plate edge in order to constrain the material through the thickness. The tabs can be seen in Figure 3.13 to the right side of the image. During the final fracture attempt, the specimen was cooled to -150°F, the cooling chamber was removed and the hydraulic wedge installed. Once the specimen was loaded to 820 kips, the wedge was driven forcing brittle fracture of the center plate.

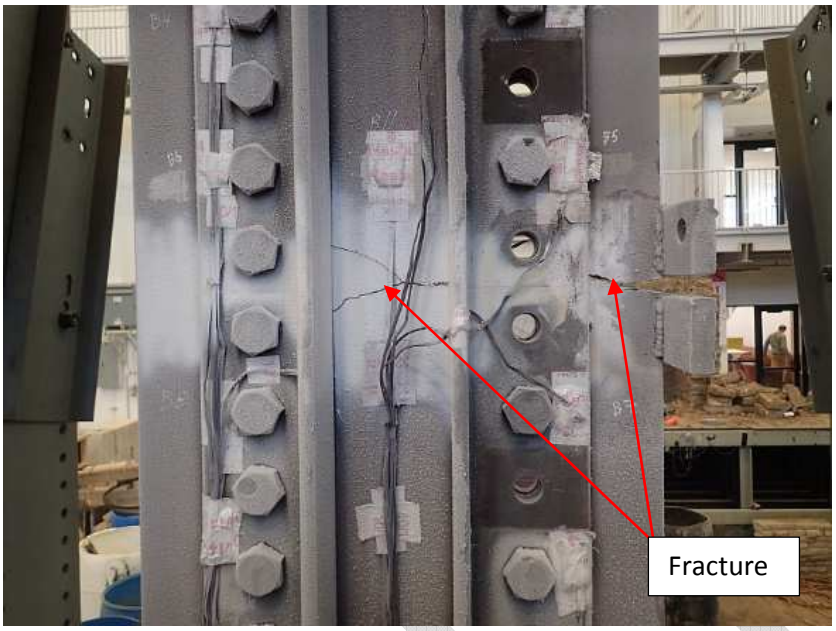

Figure 3.13 CBFR Specimen 5 following fracture of the center plate

Figure 3.14 Fractured tack weld and center plate

Upon fracture, the hydraulic load suddenly decreased to 630 kips, and slowly rose to 720 kips before being shut off. The redundancy angles survived their design tensile rupture load during the fracture event, as well as their gross yield load after. Yielded fastener holes in the angles and center plate were observed upon removal of the components from the load frame.

Figure 3.13 shows the specimen following completion of the fracture test. The fracture traveled directly through the tack weld, bifurcated at the center of the plate, and arrested in the two bolt holes on the opposite side of the plate. The fracture did not jump into the angles, including the angle that was tack welded to the center plate. Figure 3.14 shows a closer image of the fractured tack weld. High speed video captured at 14,000 fps showed in 30 frames (i.e., about 2 milliseconds) the entire fracture pop-in and arrest. The first several frames show the fracture pass through the tack weld and the tack weld shear open with the separation of the plate halves. Fusion of the tack weld to both the angle and plate was confirmed following the test. It is believed that the fracture was not able to run into the angle due to the shear failure of the weld. However video evidence appears to show the fracture beyond the tack weld by the time it begins to shear. This cannot be conclusively determined, however, due to the quality of the image. It is also worth noting that this was the only fracture specimen where a saw cut groove was not placed across both sides of the fractured component, oriented transverse to the longitudinal axis of the plate. This was done on specimens 1 – 4 in order to help increase the tensile stress concentration and guide the fracture across the entire cross section without turning into a bolt hole and arresting. In this case, it was desired to observe if the fracture would arrest in a fastener hole after intercepting the tack weld. It did, which stopped the fracture from completely severing the center plate. The tensile stress concentrations at the edges of fastener holes transferring load through shear in the fastener tends to draw fractures into the faster holes. In service, it is anticipated that if an unlikely brittle fracture in a mechanically built-up member did occur, it would arrest in another fastener hole before severing the entire component, such as it did for the Hastings Bridge discussed previously.

Results for CBFR Specimen 5 supported those of Specimens 1 – 4 showing that a running fracture cannot jump across component boundaries, even when a tack weld falls within its path. Therefore, structures possessing tack welds need not be screened from the evaluation process to determine internal member redundancy of mechanically-fastened built-up members.

3.1.7. Design and Condition of Specimens 6 & 7

Specimens 6 and 7 were members that had previously been in service for an extended period of time, removed from approach span 16 of the Winona Bridge that was built in 1940 and carried traffic over the Mississippi River near Winona, MN. The Minnesota Department of Transportation (MNDOT) donated the specimens as part of a related study. Following completion of the other testing the specimens were adapted for the IRM research. Figure 3.15 and Figure 3.16 show the general condition of the specimens as they were delivered. The condition of the rolled channels was generally clean with some minor section loss resulting from corrosion. Significant pack rust was evident between the channels and the cover plates along the top of the chords, being the cover plated the components with the greatest section loss. The gusset connections for the mid-span tension chord sections were also in good condition with some slight corrosion damage. Figure 3.17 shows a sketch of the specimen cross section at one of the stay plates, which makes the appearance of a box section, however the stay plates were intermittent along the lengths spaced at a distance of 43 inches center-to-center (28 inch clear distance). The channels were C15x40 rolled channels sections, continuous through the gussets. The cover plates were 14-3/4 inches tall by 3/8 inches thick and were discontinuous at the gussets.

Figure 3.15 Winona Bridge specimens as they arrived

Figure 3.16 View of corrosion damage resulting in section loss and pack rust

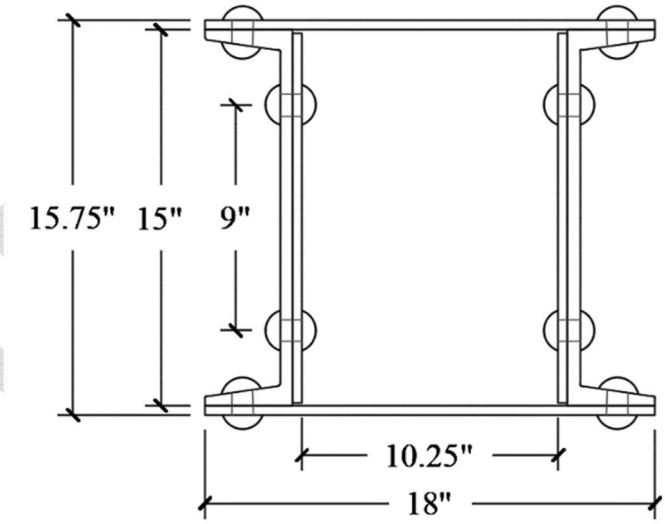

Figure 3.17 Cross section of Specimen 6 & 7 (shown with stay plates)

3.1.8. Specimen 6 & 7 Test Setup and Specimen Preparations

A horizontally-oriented self-reacting load frame was designed with capacity for 1.5 million pounds. Two 60-foot long W24x146 rolled wide flange beams were used as compression elements in this frame, which were sized and braced to ensure the frame possessed sufficient axial stiffness and buckling capacity.

Figure 3.18 shows the two wide flange columns with hydraulic jacks mounted on cap plates prior to placement of the specimen between them.

Load and reaction boxes were fabricated, along with connection and splice plate components, and bracing components. Figure 3.19 shows the specimen placed between the reaction columns with the loading box attached. Figure 3.20 shows a top-down perspective of this area. The four hydraulic jacks pushed against the loading box, reacting against the reaction columns putting the specimen into axial tension. A reaction box identical to the loading box was connected to the opposite end of the specimen providing a load path between the specimen and the reaction columns, seen in Figure 3.21. In this way the load was contained entirely within the load frame. Steel rollers can be seen along the length of the load frame in Figure 3.18 on which the specimen was rested. Smaller rollers were also placed along the length of the two reaction columns allowing the entire frame and specimen to effectively float without transferring load into the floor. This allowed the specimens to strain under tension and the reaction columns to strain under compression without preventing their relative movements. This aspect of the load frame was important because displacements of the long specimens were significant. For example, at the peak test load the specimens approached one inch of axial extension.

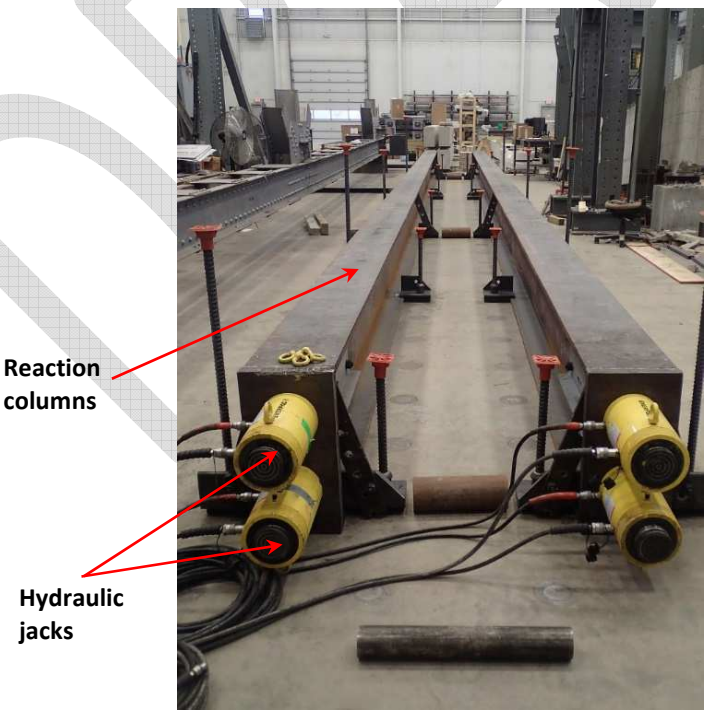

Figure 3.18. Self-reacting load frame with 4 hydraulic jacks

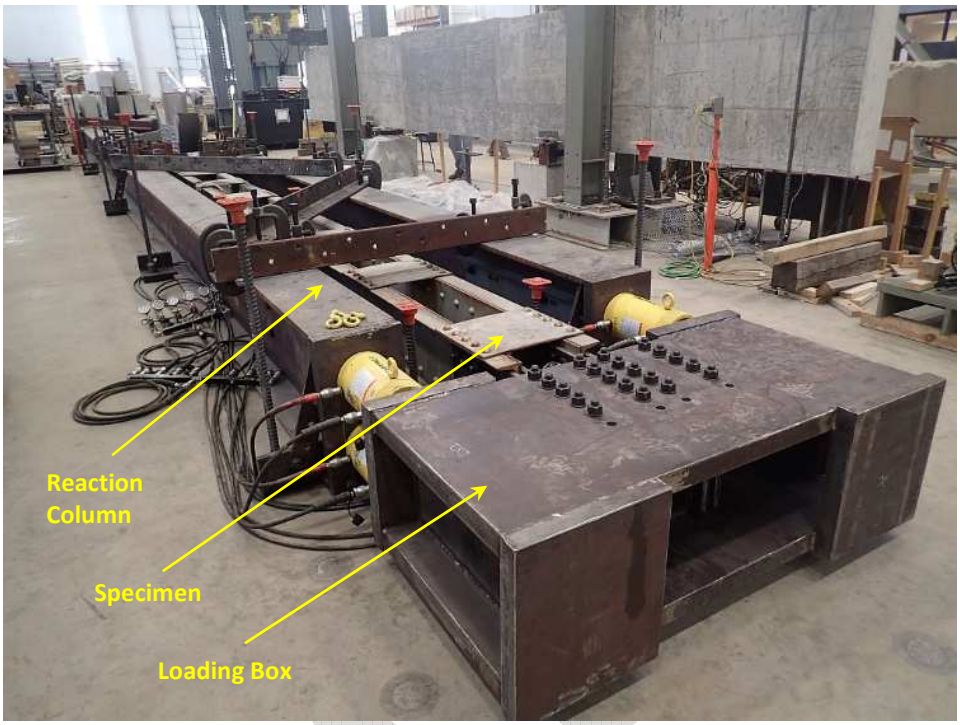

Figure 3.19. Load frame with specimen placed and ready for testing

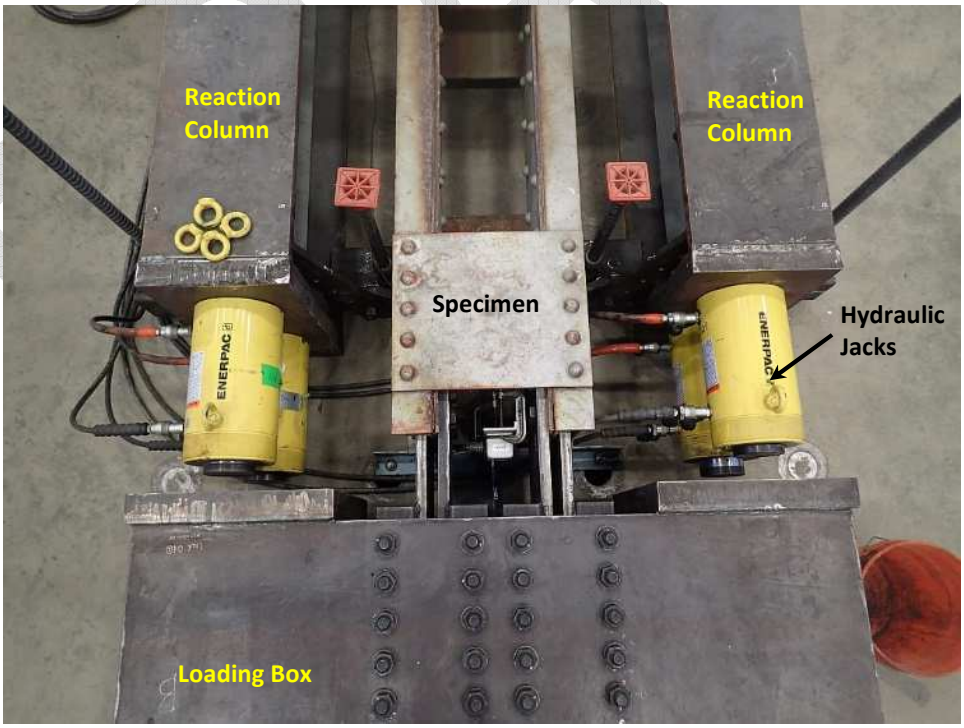

Figure 3.20. Top view of loading mechanism and specimen connection

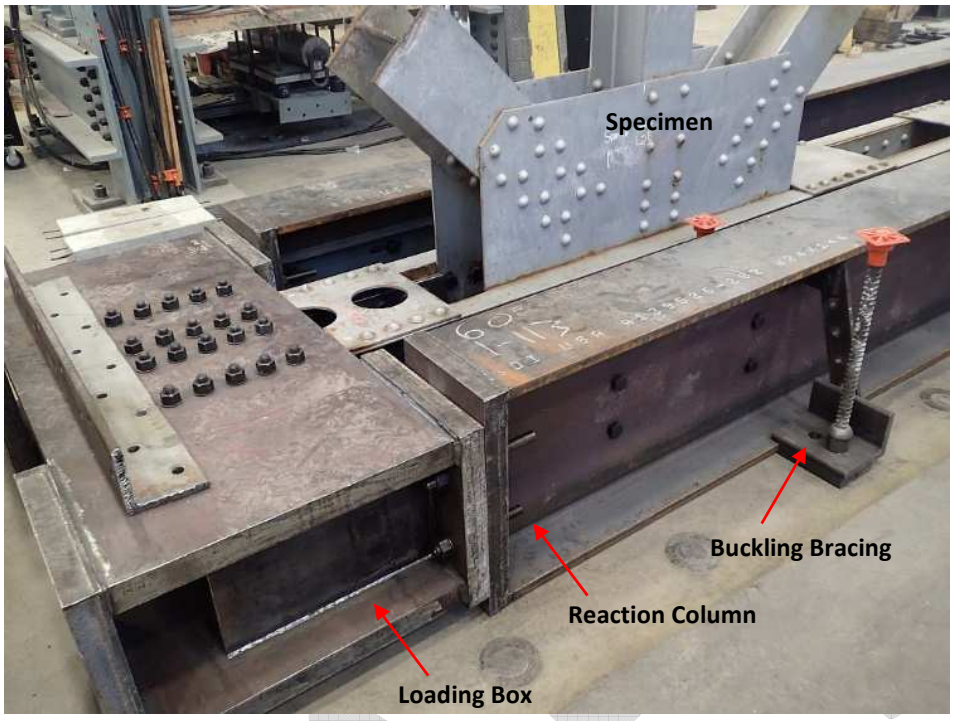

Figure 3.21. Reaction box connection to the reaction columns

As previously described, Specimen 6 and 7 were removed from Winona Bridge Span 16, as indicated in Figure 3.22 with the dashed red rectangle. Specimen 6 was from the east truss line chord and Specimen 7 was from the west truss line chord. The specimens were approximately 65 feet long upon arrival. Preparation of the specimens for testing included trimming each end to the right length to make a connection to the load frame. The final length of each of the specimens was 740.5 inches (61.7 feet). Rivets were removed at each end and bolt holes were drilled for connection to the loading beams. The member cross-sectional area between joint L1 and L2 reduced to only the rolled channel, thus, to be able to test the full capacity of the larger cross section between joint L2 and L6, A992 Grade 50 splice plates were installed near the L2 gusset plate and connection into the reaction box. A strengthening plate can be seen in Figure 3.23 where it is shown shortly after installation and prior to placing the specimen inside the load frame. All connections were bearing-type connection using 1-inch diameter ASTM F3125 Grade A325 high strength bolts. This significantly reduced the number of required bolts, which in turn reduced the size of the loading and reaction boxes. It also made “shake down”, explained later, an important part of the loading sequence.

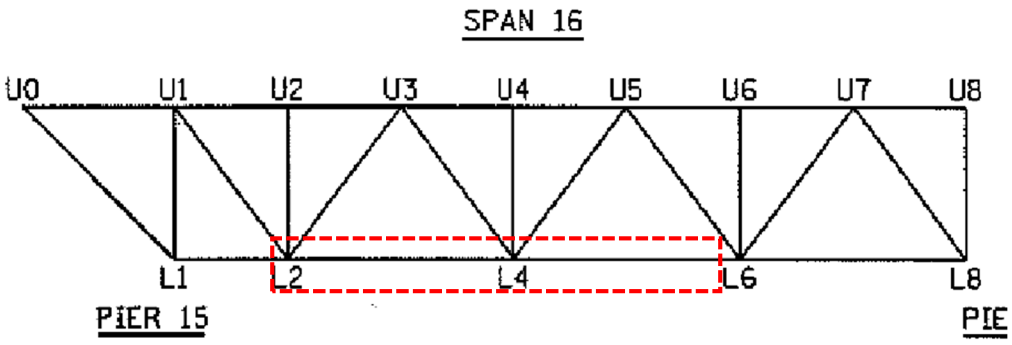

Figure 3.22. Winona Bridge Span 16 framing elevation. Specimens removed from area shown by the dashed line

Figure 3.23. Connection at the reaction end of the specimen showing the additional plate

The fracture test results section of this report shows that it is not possible for a fracture of one component of a built-up member to propagate to an adjacent component. This is a characteristic of mechanically-fastened built-up members referred to as cross-boundary fracture resistance. Thus, for the internal redundancy testing of the Winona Bridge members, half of the chord was severed using a flame cutting torch. Then the specimen was statically loaded. The propagation of a brittle fracture was not only not a possibility for this specimen, due in part to its length and in part to the fact that it was a multi-

component built-up member, but was also not necessary for the targeted objectives of these tests, which were focused on the post-fracture redundant strength.

First, one of the cover plates for Specimen 6 was cut at location "A", centered between the two gusset plates (see Figure 3.24). The specimen was only tested within the linear-elastic range. Next, the remainder of one half of the specimen was cut at the same location, similar to what is shown in Figure 3.26, and the specimen was once again loaded several times within the linear-elastic range. Then, the cut at location "A" was spliced back together and the same specimen was cut near the gusset plate at location "B", as can be seen in Figure 3.25, severing an entire half of the member. The specimen was loaded into the non-linear range leading to plastic deformation of the intact built-up channel and adjacent stay plate. Specimen 7 was cut at location "A", which is shown in Figure 3.26. This data was used to calibrate finite element models allowing for parametric studies of two-channel, truss-type built-up members, which is discussed further in Section 4.5.1. Gage plans showing exact locations of sensors for each specimen are provided in Appendix C.

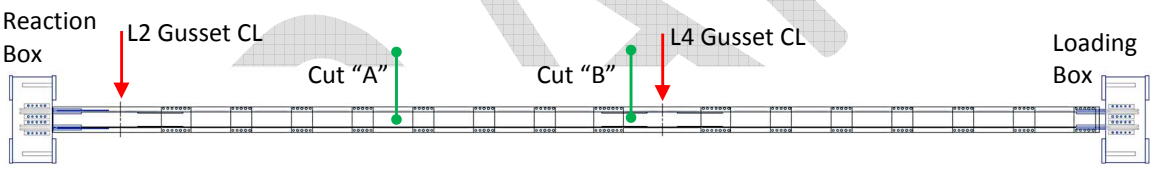

Figure 3.24 Plan view sketch of two-channel member specimens showing locations of the member cuts

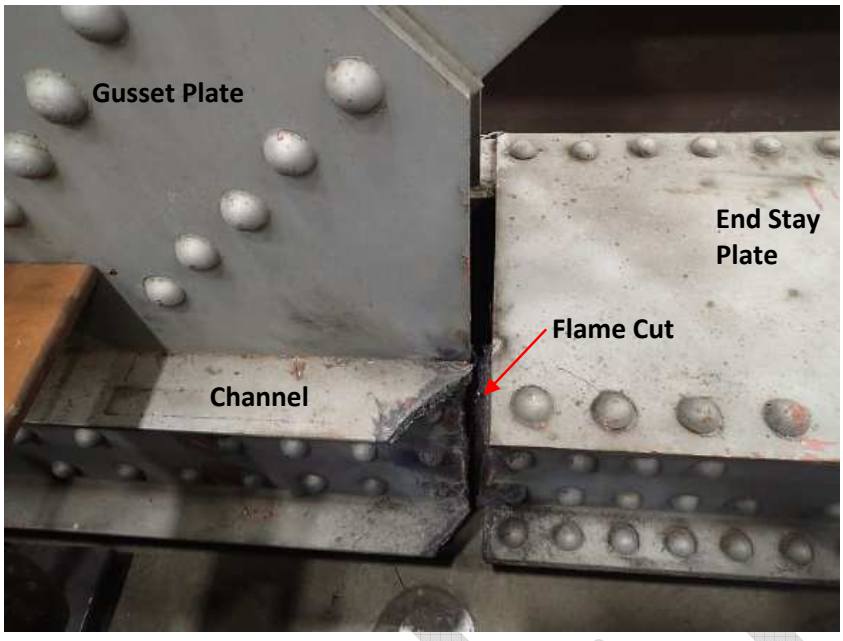

Figure 3.25 Component cut "B" on Specimen 6 (indicated in Figure 3.24)

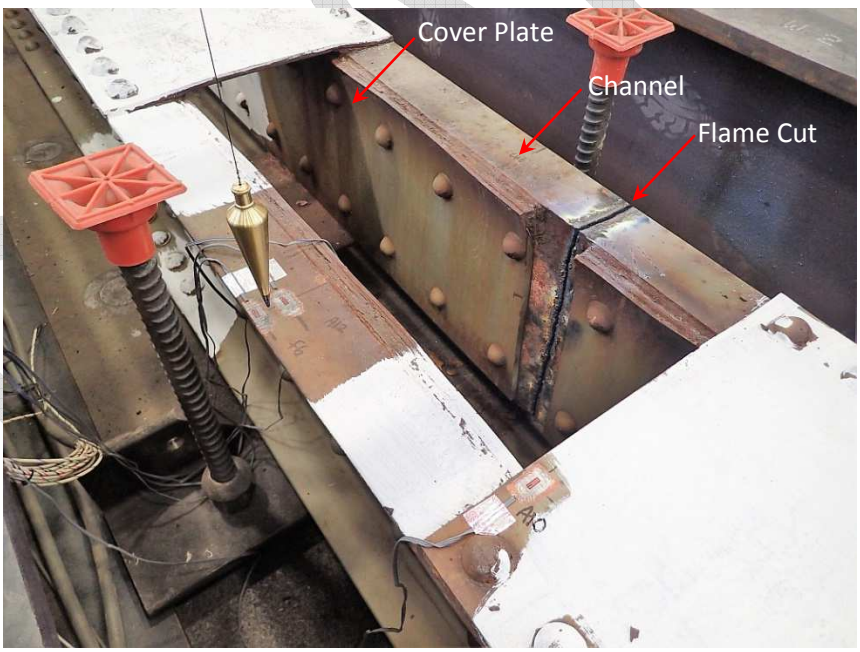

Figure 3.26 Component cut "A" on Specimen 7 (indicated in Figure 3.24)

3.1.9. Specimen 6 & 7 Test Results

3.1.9.1. Specimens 6 & 7 Material Testing Results

Material was removed from a cover plate, a channel web, and two gusset plates in order to test for Charpy V-notch energy (for estimation of the material toughness), yield strength, tensile strength, and chemical composition. All material testing was performed according to requirements of ASTM E415, ASTM E8, and ASTM E23. Table 3.5 provides the results of the chemistry test showing element percentages that were within the relatively loose standards of ASTM A7 steel that likely would have been specified at the time of the construction of the Winona Bridge in the late 1930's. ASTM A36 standard did not become a dominant steel in construction until the early 1960's. The mechanical properties shown in Table 3.6 are also consistent with minimums standardized by ASTM A7, diverging with considerably more elongation in 2" than minimally required, suggesting higher ductility. ASTM A7 required a minimum 24% elongation in 2-inches, a minimum yield strength of 33 ksi, tensile strength of 60 to 75 ksi for shapes of all thicknesses, and tensile strength of 60 to 72 ksi for plates up to 1.5 inches thick. Two samples were taken from each of two gusset plates. One sample was oriented parallel with the longitudinal axis of the tension chord ("Horizontal") and one same was oriented perpendicular to the longitudinal axis of the tension chord ("Vertical"). This was done in order to observe whether differences in the material properties existed between the perpendicular directions since often times the rolling direction of gusset plates cannot be visually detected. With one exception, differences of less than 2% were measured between opposing directions suggesting uniform, orthotropic mechanical properties. The one exception was the *Elongation in 2"* for the two directions of Gusset Plate 2, where a difference of 13% was measured.

Table 3.5. Chemical composition of the Winona Specimens

Element	Channel Web	Cover Plate	Gusset Plate 1	Gusset Plate 2
Carbon	0.23%	0.24%	0.25%	0.26%
Manganese	0.49%	0.5%	0.42%	0.63%
Phosphorus	0.016%	0.016%	0.009%	0.024%
Sulfur	0.015%	0.016%	0.030%	0.046%
Silicon	0.05%	0.05%	0.02%	<0.005%
Nickel	0.04%	0.04%	0.03%	0.03%
Chromium	0.05%	0.05%	0.02%	0.04%
Molybdenum	0.01%	0.01%	0.01%	0.01%
Copper	0.04%	0.04%	0.02%	0.03%

Table 3.6. Mechanical properties of the Winona Specimens

	Channel Web	Cover Plate	Gusset Plate 1: Horizontal Orientation	Gusset Plate 1: Vertical Orientation	Gusset Plate 2: Horizontal Orientation	Gusset Plate 2: Vertical Orientation
Tensile Strength (ksi)	66.1	69.6	63.7	64.0	70.7	69.9
Yield Strength @ 0.2% Offset (ksi)	38.6	40.5	36.1	35.2	41.4	42.6
Elongation in 2"	37.5%	31.2%	34.3%	33.5%	30.2%	26.7%

Although some limited chemical specifications and tensile capacity minimums were typically provided in early steel specifications, toughness was not. Toughness is a material property that quantifies the ability of a material to resist fracture in the presence of a crack. Direct measurement of toughness requires costly testing and relatively large piece of material. As a result, an economical alternative often used is the Charpy V-notch Impact (CVN) test. These tests are not a direct measure of toughness, rather a measure of energy absorption. Using accepted correlation methods, such as the Master Curve Method, fracture toughness can be estimated from CVN data.

Eighteen CVN specimens were obtained from a rolled channel web and from a cover plate (36 specimens, total) to allow testing of at least three specimens at each of the desired temperatures and to allow development of a complete CVN energy vs temperature curve (see Figure 3.27). However, the more data for each test temperature, the more reliable the estimate of toughness becomes. Therefore, more specimens were tested at selected temperatures, such as 40°F and 70°F. Due to the single-digit energy measurements observed at 10°F, it was determined unnecessary to test at cooler temperatures.

As noted in the figure, the specimens from the cover plate were "sub-size". A standard CVN specimen is 10 mm x 10 mm x 40 mm long. However, because the cover plate was only 3/8" thick (9.5 mm), a full-size CVN could not be machined and thinner, or sub-size specimens, measuring 7.5 mm x 10 mm x 40 mm long were required. Standardized testing of sub-size CVN specimens can be performed. The smaller thickness dimension of a sub-size specimen can influence the results in two ways. First, the thinner material has a reduced cross sectional area, which reduces its ability to absorb energy. This means the absorbed energy of a sub-size specimen will be less than that of a standard size specimen. Second, the reduced thickness of a sub-size specimen reduces the tri-axial constraint against plastic flow. This means that the sub-size specimen will be more ductile making cleavage fracture less likely to occur. This effect results in fracture mode transition temperatures that are lower for sub-size specimens than for standard size specimens. As a result, the American Petroleum Institute (API) Fitness-For-Service manual

(API 579-1/ASME FFS-1, 2007) provides guidance for the adjustment of the measured CVN energy absorbed and the test temperature at which the sub-size specimens are tested. These adjustments account for the two effects of the sub-size specimen making the results relatively comparable to that of standard sized specimens. The adjustments to the sub-size results are incorporated into the data plotted in Figure 3.27 and listed in Table 3.7.

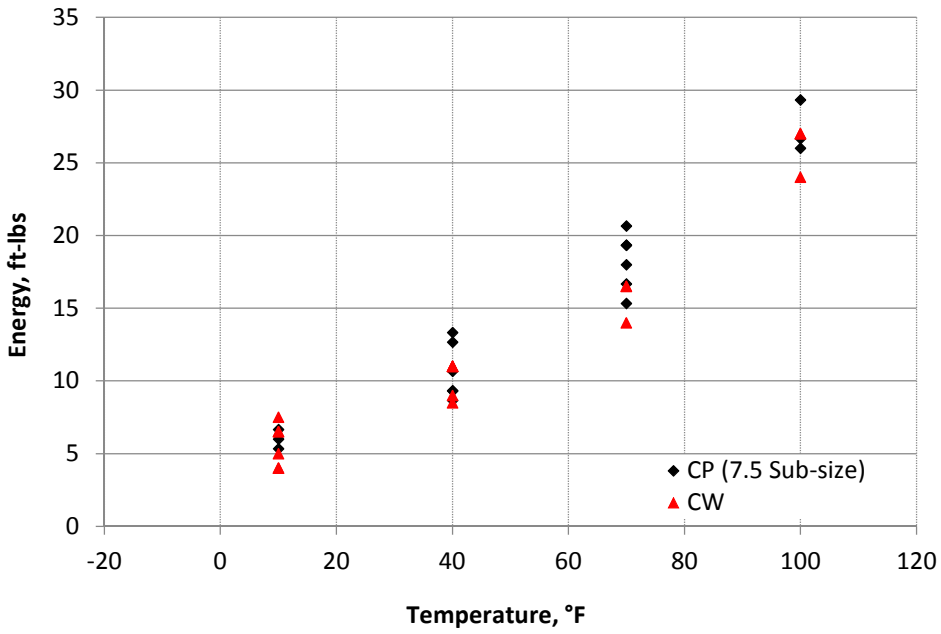

Figure 3.27. Plot of CVN Impact Energy vs. Temperature: Cover plate (CP) and Channel web (CW)

As a point of interest, Table 3.7 compares the modern CVN impact energy requirements from Section 6 of the *AASHTO LRFD Bridge Design Specification* with the average CVN impact energy test results for the Winona Bridge specimens at the service temperature indicated. As can be seen, the only category for which the historic steel would meet the modern specification is Zone 1 Nonfracture-critical.

Table 3.7. Comparison of CVN Impact Energy for Grade 36 Steel

Service Temperature (°F)	AASHTO Fracture-Critical (ft-lbs)	AASHTO Nonfracture-Critical (ft-lbs)	Average for Winona Channel (ft-lbs)	Average for Winona Cover Plate (ft-lbs)
70 (Zone 1)	25	15	16.0	18.2
40 (Zone 2)	25	15	10.0	10.7
10 (Zone 3)	25	15	6.8	6.0

3.1.9.2. Specimens 6 & 7 Testing Results

Prior to cutting Specimen 6, it was loaded in the "as-delivered" (i.e., non-faulted) condition over several load cycles to ensure test setup and sensors were operating correctly. Data for the first several load cycles were discarded as part of the "shakedown" of the specimen. This is a term used to describe the settling of the specimen and load frame connections until fully seated. This process helps to remove excess displacements that could be wrongfully attributed to specimen elongation, particularly when the connections are designed as bearing connections and inevitably some of the fasteners go into bearing before others. Shakedown load cycles were performed within the elastic range of the specimen. Sensor locations can be seen in the gage plans in Appendix C.

Figure 3.28 shows a load-displacement plot for Specimen 6 prior to being cut. The vertical axis is load and the horizontal axis is longitudinal displacement. The peak load was 1150 kips. The solid blue line is the estimated, or nominal, load-displacement curve based on a simple mechanics of materials equation for displacement of an axially loaded body (i.e., $\delta = PL/AE$). The measured curves correlated well with the nominal estimation and indicated a linear-elastic response to the applied load. The peak load of 1150 kips surpassed the original design load for the member by 222% and effectively reached the capacity of the hydraulic jacks. This portion of the testing helped confirm proper loading and unloading cycles were being performed and that sensors were operating as desired. Next, load was removed and then Specimen 6 was torch cut between the end stay plate and the L4 (center) gusset plate (location "B" as indicated on Figure 3.24) leaving only half of the original cross section intact. Several load cycles were applied, including a final cycle up to 800 kips, as plotted in Figure 3.29. An estimated, or nominal, load-displacement curve has also been plotted for the linear-elastic range, which does not take into account the loss of half the cross section. This curve is based on the equation for elastic displacement of an axially loaded body (i.e., $\delta = PL/AE$), as shown above. However, in this case it may not be an appropriate comparison because the measured curve represents the member in the faulted condition with only half of its cross section at location "B" where localized slip reduced axial stiffness. As would be expected, the nominal calculation in the unfaulted condition estimated a stiffer axial displacement than was measured. The difference in this case was about 18%. In a real world application the loss of axial stiffness would result in the member shedding some load to adjoined members, such as cross members, diagonals, etc. This behavior was observed by Diggelmann *et al.* (2013) where when the first blast severed half of the built-up channel member on the Milton-Madison deck truss, the load measured in cross members, as well

as in the truss line opposite the severed member were observed to increase. This is an important observation simply because all evaluation methods developed in this research conservatively assume that all of the load originally carried by the faulted member remains in the faulted member. Some limited load shed from the damaged member will help improve performance of the member in the faulted condition.

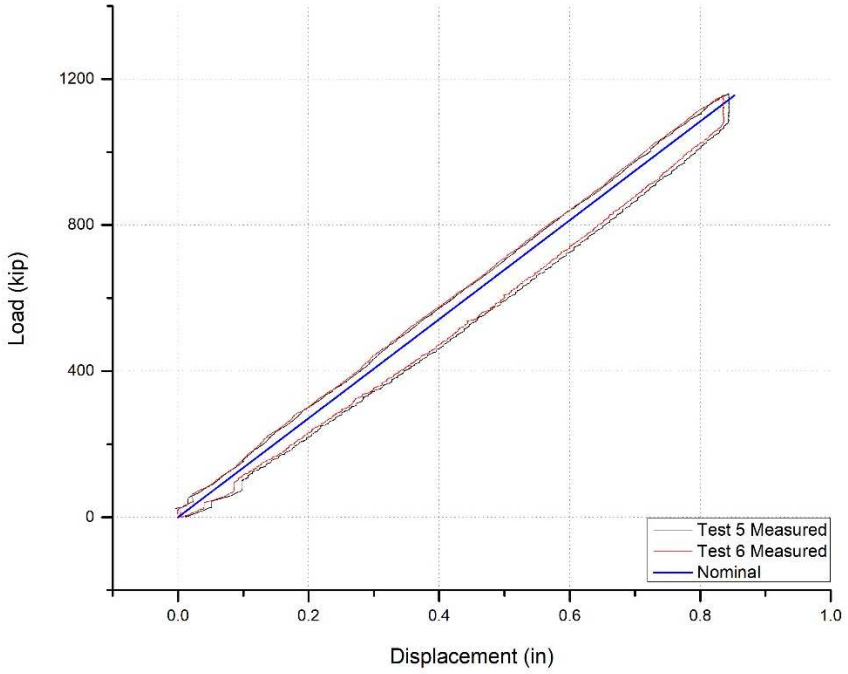

Figure 3.28 Load vs. displacement curve for Specimen 6 prior to severing half of the cross section showing predictable elastic behavior

Table 3.8 provides the nominal and actual section capacity calculations for the specimen in the faulted state. The area calculations for Specimen 6 assume the cross section included the 1/2" splice plate and the rolled channel. This is because the channels were continuous through the joint, but the cover plates terminated at the gusset plate where splice plates were used to carry the load across the discontinuity. This left the smallest area near the gusset plate comprised of only the splice plate and rolled channel. It can be seen in Figure 3.29 that the onset of localized yielding occurred at around 600 kips. This was notably less than the actual gross section yield calculated to be 754 kips. However, the net section yield load, which is not typically considered in strength calculations, was calculated to be approximately 625 kips. This would suggest that the specimen began to yield at fastener holes, most likely the first set of rivets shared by the splice plate and cover plate or gusset plate. What is most important

to notice, however, is that the faulted specimen exceeded the original design load of 517 kips by 15 – 20% before the onset of yielding and was able to reach about 1.5 times the design load before gross section yielding began to shed load. This is remarkable considering that the specimen was in the faulted state with only half of the original cross section intact. Furthermore, the specimen reached the load while also resisting additional flexural stress resulting from after-fracture second order moments at the location of the failure.

Table 3.8 Specimen 6 & 7 cross-sectional area and capacity calculations

	Specimen 6 (@ Location "B")	**Specimen 7 (@ Location "A")**
Gross Area (in^2)	19.2	17.3
Net Area (in^2)	15.9	14.5
Nominal Gross Section Yield (kip)	632	571
Actual Gross Section Yield (kip) [with φ_y = 0.95]	754 [716]	679 [645]
Nominal Net Section Fracture (kip)	954	870
Actual Net Section Fracture (kip) [with φ_u = 0.8]	1073 [858]	972 [778]
Peak Test Load (kip)	800	647

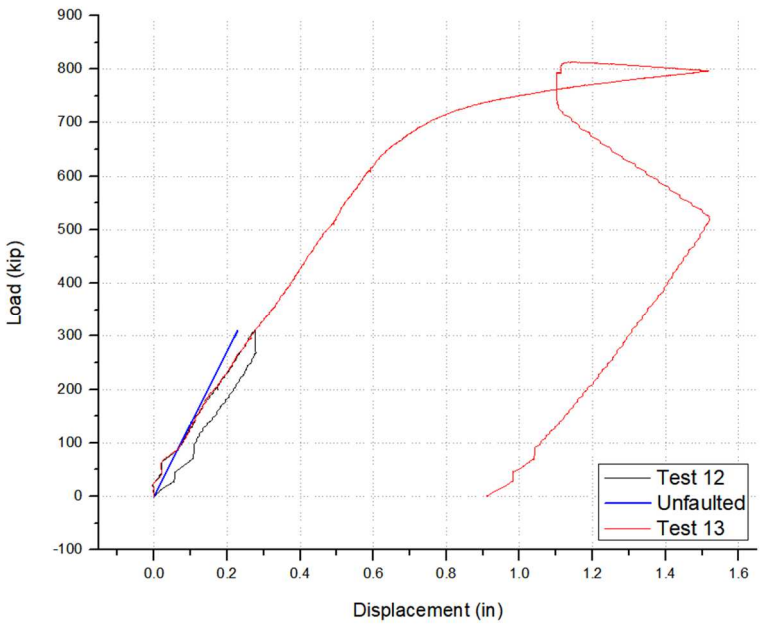

Figure 3.29 Load vs. displacement curve for Specimen 6 with severed section at location "B" (near gusset plate, see Figure 3.24)

Specimen 7 was also loaded several times in order to perform a “shakedown” on the connections and ensure the specimen was seated into the load frame properly. Several additional static load cycles were applied up to a peak load of 647 kips. A few of these have been plotted in Figure 3.30 where cycles up to 300 kips remained linear-elastic and later cycles reaching loads of 600 kips or more produced permanent plastic deformation. The estimated nominal load-displacement curve of the member in the unfaulted condition has also been plotted as reference. In this case, the axial stiffness of the specimen in the faulted condition was reduced by 45% within the elastic range of loading, which would have resulted in load shed to adjoined members in an actual structure. Similar to Specimen 6, Specimen 7 experienced onset of what was likely net section yielding at about 500 to 550 kips, which is less than the calculated gross section yielding load of 679 kips. The 550 kip load closely corresponded with a calculated net section yielding load of 565 kips. Once again, the faulted specimen was able to achieve loads in excess of the original design load, in this case by just over 25%, in addition to resisting the after-fracture second order moments induced by resdistribution of loads around the failure.

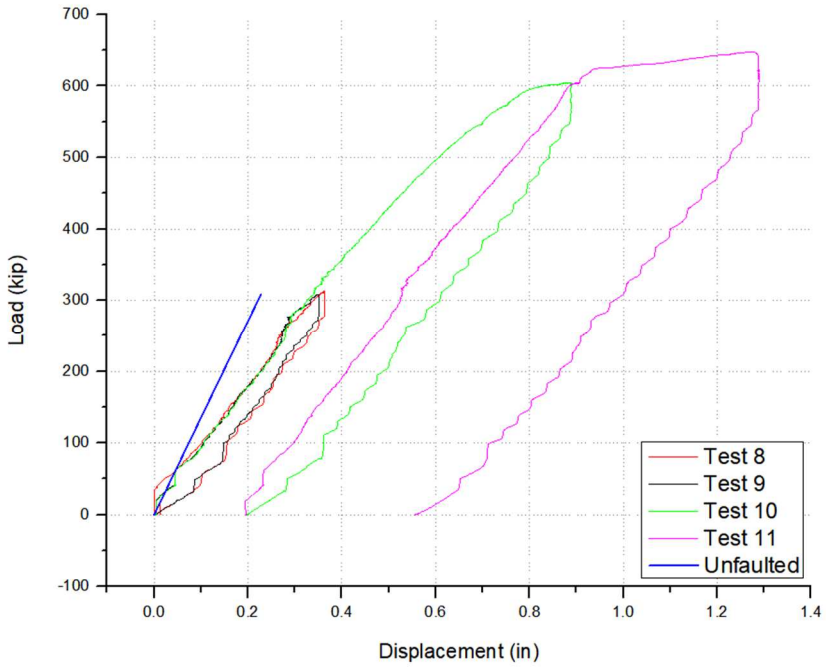

Figure 3.30 Specimen 7 load-displacement curves with severed section at location “A” (mid-panel, see Figure 3.24)

In both cases, the stay plates, also known as batten plates, showed no sign of permanent deformation at the peak loads. This was surprising, particularly when considering that both specimens

possessed considerable amounts of pack rust that had initiated out-of-plane deformation of the stay plates that would reduce their buckling capacity. An example of this is shown in Figure 3.31, which was taken prior to testing. The deformation has been highlighted with dashed lines. Figure 3.32 shows Specimen 6 after testing has been completed where it can be seen that the channel flange buckled, slip occurred at the rivets, and the end stay plate rotated in-plane. The in-plane rotation was indicated at the corner of the end stay plate where a small unpainted section of the channel was exposed. The stay plates resisted opening of the severed channel through a horizontal in-plane shear action. This put part of the stay plate in tension and part of the plate in compression, the capacity of which would theoretically be controlled by the buckling capacity of the plate. However, in both experimental cases, and as was later confirmed in the parametric study, the faulted member capacity was not limited by the stay plate thickness (and thus buckling capacity), which was found to have non-appreciable effects on the internal redundancy analysis. The plates for Specimen 6 and 7 were 3/8-inch thick – a common thickness for riveted built-up members.

Figure 3.31 Specimen 6 end stay plate <u>prior to testing</u> showing pack rust-induced bending of the stay plate

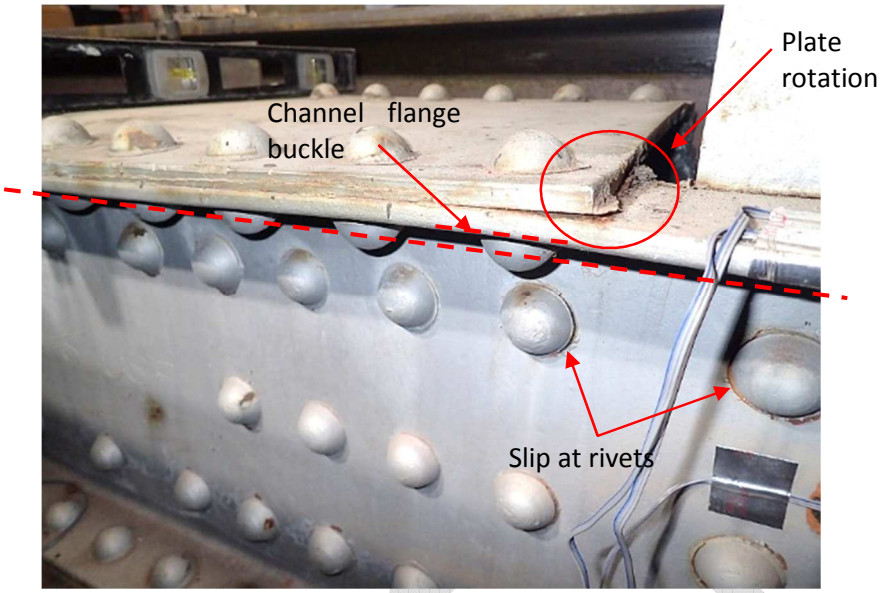

Figure 3.32 Specimen 6 <u>after testing</u> was completed showing buckled channel flange, slip at the rivets, and rotated end stay plate

4. ANALYTICAL RESEARCH PROGRAM

The majority of axial built-up members found in truss bridges can be classified into three categories: multi-component type, angle-only type, and two-channel type. In this research, several finite element analysis parametric studies were performed investigating these three types. All finite element models were generated and solved using the Abaqus finite element software suite. Benchmark models were calibrated using experimental data obtained from the experimental tests described in Chapter 3. Solid element models were used to analyze cases of multi-component and angle-only type members where localized stress concentrations were necessary for the solution. The two-channel type members were evaluated using shell element models where the findings were focused on global stresses and secondary moments, providing significant computational savings.

4.1. Methods Used for Parametric Study of Multi-Component Members

Localized behavior resulting from a single failed component was examined in a finite element analysis parametric study using the Abaqus software suite. Several three-dimensional member geometries were created and evaluated using linear elastic, static implicit analysis in which large deformation effects (finite strain theory) were included. Prior to performing the parametric study, the finite element models (FEMs) were calibrated to experimental data obtained from CBFR Specimens 1 and 2.

4.1.1. Multi-component Member FEM Calibration and Specifications

Data collected during the laboratory testing of Specimen 1 and 2 were compared to several benchmark finite element models in order to calibrate the model parameters and ensure accurate results consistent with experimental work. Strain and load sensors used during the experimental testing provided data for comparison. The benchmark models were quarter symmetry models. 8-node linear continuum hexahedral (brick) elements with reduced integration and hourglass control (Abaqus designation C3D8R) were used with a structured hexahedral mesh. The global size of the mesh was 1/2 inch with higher density around the fastener holes and a minimum of four elements through the thickness of each component. The global mesh size used for the fastener was 1/8 inch. This mesh size at the fastener hole edges approximately matched the mesh

size of the fastener stem in contact with the edge of the holes ensuring similar computational stiffness. Figure 4.1 shows typical mesh for the members and fasteners.

A linear elastic-isotropic plastic material model was defined for the fasteners and plates having a modulus of elasticity of 29,000 ksi and Poisson's Ratio of 0.3, although strains never reached yield. Preload clamping force was assigned for each rivet of 5 kips, when needed. Based on work by Bonachera Martin (2014) which also served as background to [INSERT REFERENCE TO HEBDON'S], the model was assigned general hard contact normal behavior and penalty tangential behavior with a friction coefficient of 0.25. It was realized that due to the uniform bearing of the fasteners, the results were insensitive to preload and friction parameters, but they did occasionally assist with model convergence by disallowing rotation and slippage of the rivets. Hence, friction and fastener preload were utilized when needed to ease convergence of the analysis.

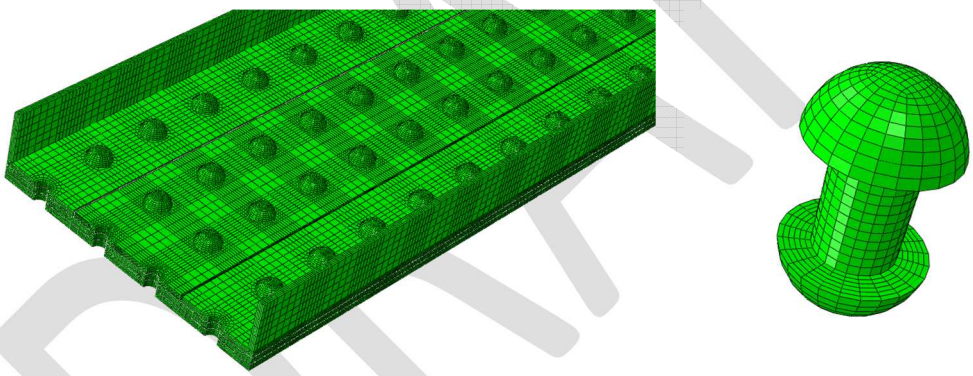

Figure 4.1 (Left) Typical member mesh; (Right) Typical fastener mesh

All fasteners were modeled as rivets, being sized to fill the entire hole, which was 7/8-inch in diameter. Thus, the dominant load transfer mechanism between components was fastener bearing. Following completion of the calibration process described below, initial parametric models were created full size using a seam to model the fracture in a particular component. Later models were created using half-symmetry boundary conditions at the location of the failure saving significant computational cost.

Figure 4.2 and Figure 4.3 show stress curves for Specimen 2 compared to results obtained from the benchmark FEMs. The curves were obtained by subtracting the results at a load of 300 kips from the results at a load of 700 kips, or an equivalent 400 kip load amplitude. Each plot contains an inset image of the FEM with longitudinal normal stress contours and the rivets removed to expose the stress contours of the plates. The failure plane of the center plate is labeled, as well as the path along which the stresses from the FEMs were obtained. The stresses shown in Figure 4.2 were obtained along a path centered between the columns of fasteners along the surface of the exterior, or redundancy, plate. The stresses shown in Figure 4.3 were obtained along a path passing through the center of the third row of fasteners, transverse along the surface of the redundancy plate. The discontinuity of the curves indicates the location of the fastener holes. The laboratory data plotted are also the difference between measurements at 300 and 700 kip loads. The plots include the actual data, as well as the average for each data set. Figure 4.2 plots data from four FEMs referred to as Trial 1 through Trial 4. Figure 4.3 plots data from three of the four, excluding Trial 2. The trials were among several attempts to calibrate the FEMs. Trial 1 was the first attempt, which matched the measured stresses well at the first row of fasteners (at 1.5 inches from the failure plane), but diverged significantly at the third row of fasteners underestimating measured stresses by 30% — such that the FEM was over predicting load transfer out of the redundancy plates and back into the fractured center plate. Trial 2 softened the rivets by changing the modulus of elasticity to 15,000 ksi in an effort to reduce the load transfer. This made marginal improvements. It was obvious that the FEM was transferring load back into the center plate more quickly than was occurring in the experiment. This was primarily due to a fundamental difference in the fasteners used in the FEM as compared to the laboratory test. In the experiment, the fasteners were high strength bolts that were snug tightened using the effort one worker with a standard wrench, a process used to simulate the clamping force of hot-driven rivets while testing with bolts. Snugging the bolts put all plies into firm contact, but did not fully tension the bolts. As is standard practice for bolted connections, the holes were oversized 1/16 inch, which left small gaps between the bolts and plate at random locations that could not be predicted, meaning that some bolts most likely were in bearing earlier in the loading cycle than others. This would change the way load was transferred out of the redundancy plates and back into the failed center plate because the bolts that were not in bearing would only be able to transfer limited load through friction until they came into bearing. The FEM was generated using rivets that filled each fastener hole completely allowing predictable, uniform

load transfer back into the failed plate through bearing at every fastener. In an effort to adjust for this discrepancy and ensure the FEMs were otherwise providing acceptable results, Trial 3 FEM was generated in which the first row of fasteners was arbitrarily removed to slow load transfer. This made notable improvements at the second row of fasteners coming to within about 8% of the average measured stress. The final attempt was Trial 4, which took the concept of Trial 3 FEM a step further by removing one more row of fasteners at the third row. The results for this model matched experimental results exceptionally well. The results show therefore show that the FEA methodology utilized adequately models load transfer among mechanically fastened components.

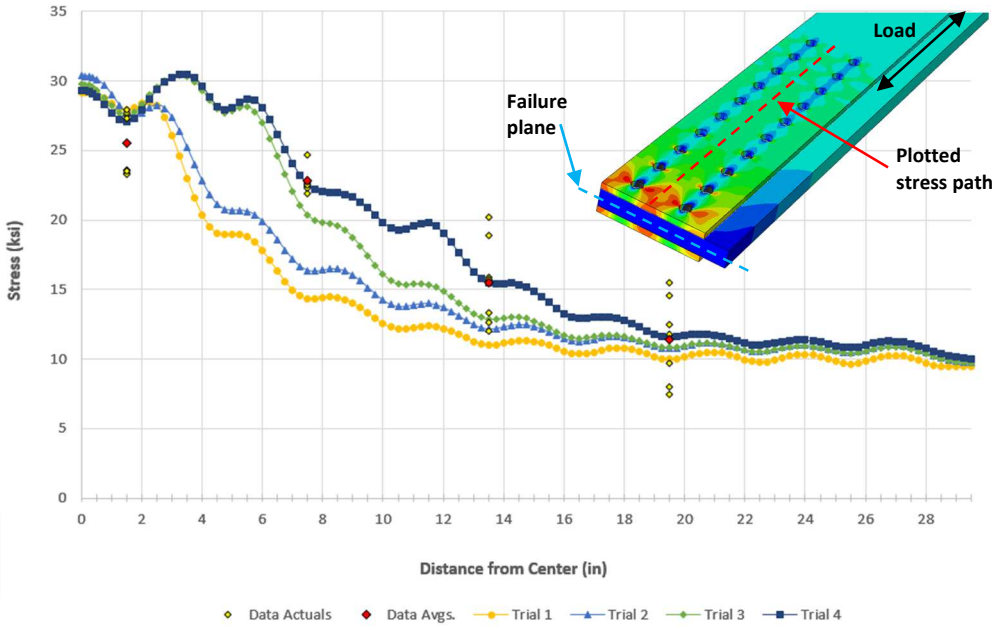

Figure 4.2 Experimental data compared to FEA results – plotted along longitudinal dimension

This same exercise was performed comparing results for stress at a transverse position across the redundancy plates located at the net section of the third row of rivets up from the fracture plane (or center of the specimen). This is shown in Figure 4.3 where results were plotted for FEMs Trial 1, Trial 3, and Trial 4. Outcomes were similar for the longitudinal stress path described above. Trial 1 under predicted stress in the redundancy plate suggesting once again that load transfer was occurring more quickly in Trial 1 than in the experiment. Results improved markedly for Trial 3 and Trial 4, coming to within a few percent of the average measured stress.

A mesh convergence study was also performed quadrupling the mesh density at the fastener holes. While the stresses at the edge of the fastener holes were not replicated among the models with different meshes, convergence was achieved within 1/8 inch. 20-noded quadratic brick elements increased results approximately 5% over the linear bricks, however in light of other sources of conservatism in the analysis results, which are discussed in later sections, it was not considered significant enough to justify the substantial computational cost increase it required. Further, the stress value computed at the edge of the hole is a localized effect that does not bear a significant impact on the quality of the computational solution.

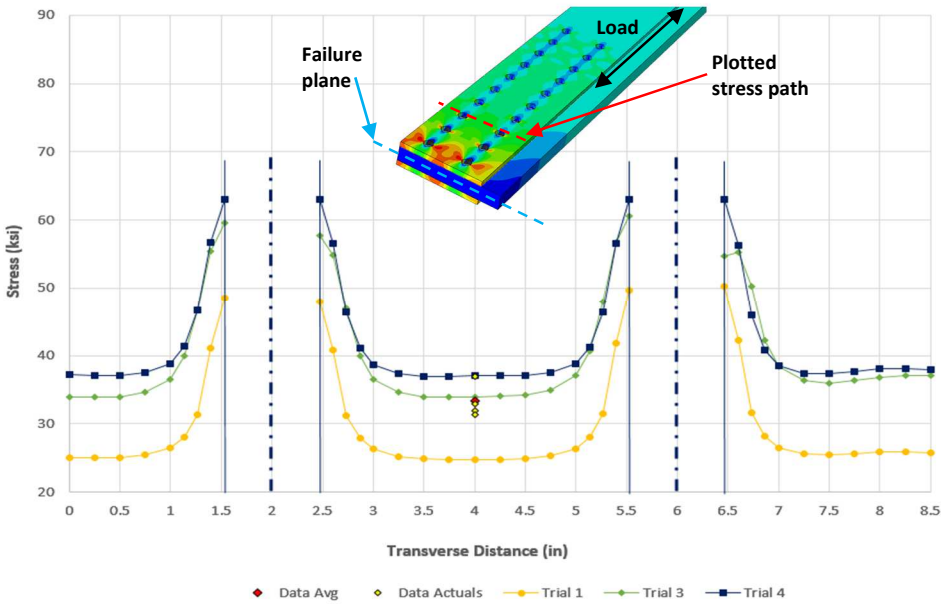

Figure 4.3 Experimental data compared to FEA results – plotted along transverse dimension

The benchmark linear brick element model, as described above, was found to be acceptably accurate. Arbitrary removal of fastener rows was required to match the experimental results. This was a consequence of the small oversize (1/16”) of the fasteners’ holes in the specimen that resulted in some bolt rows not being engaged as they were not fully preloaded, while the fastener modeled in the FEM occupied the entirety of the hole and in order to “disengage” them removal from the FEM was necessary. Setting this difference aside, the FEMs were able to predict results to within a few percent and acceptably captured after-fracture load redistribution behavior of the

test specimens and therefore set the standard for finite element models used in the parametric study of multi-component and angle-only members.

4.1.2. Geometric Parameters Varied for Multi-component Members

A number of parameters were varied widely in order to study localized stress effects in multi-component members following failure of a single component. All geometries were subjected to a gross-section axial tensile stress of 2 ksi away from the failure site using surface traction on the undeformed cross-section. The parameters included in the study were:

- Fixed and pinned end boundary conditions
- Fastener shear stiffness
- Web plate depth
- Web plate thickness
- Angle thickness
- Adjacent angle leg length
- Number of web plates in the member
- Position of the failed web plate within the member
- Fastener spacing (including a staggered or zig-zag pattern)
- Fastener position within the web plate

Due to the innumerable combinations that could exist in service, as well as unknown boundary stiffness characteristics that likely vary from bridge to bridge, many of the parameters were evaluated by bounding the problem. That is, if a parameter was determined to have an effect, it was explored further, if it did not, it was removed from further consideration. The study included several geometries with a failed web plate, others with a failed angle, and numerous models specifically looking at the shear lag effect in web plates following failure of an angle. The first several failed web plate models were identical to the failed angle models, changing only the component that failed. It was soon realized that nearly all cases were governed by assuming failure of the web plate due to the amount of load in the plates, as compared to the angles. Hence, more geometries with failed plates were generated for the study. However, two cases were found to be controlled by failure of an angle. This lead to development of what is referred to as the "40-over-fastener" rule discussed in Section 4.2.3, which is a check made for these cases. This portion of the parametric study focused on built-up channel, I-section, and box geometries that ranged from 18 to 42 inches deep, between 1 and 4 plates per web, and from 3/8-inch to 1-inch thick components. Table 4.1 provides the geometric specifications evaluated.

Table 4.1 Geometries for models with a failed web plate (all dimensions are in inches)

Model ID	Type	Angle Thickness	Adj. Angle Leg Size	Web Height	No. of Plates in Web	Web Thickness	Fastener Spacing	Failed Component
A1	**Channel**	3/8	5	18	-	1/2	4	Angle
A2		3/8	5	18	-	1/2	4	
A3		3/8	5	36	-	1/2	4	
A4		3/4	5	18	-	1	4	
A5		3/8	5	18	-	1/2	4	
A6		3/8	5	18	-	1/2	2-1/2	
A7		3/8	5	18	-	1/2	8	
A8		3/8	8	18	-	1/2	4	
A9		3/4	5	36	-	1/2	3	
A10		3/4	5	36	-	1/2	6	
A11	**Box**	3/8	5	18	-	1/2	4	Angle
A12		3/8	5	18	-	1/2	4	
A13	**I-section**	3/8	5	18	-	1/2	5x2[1]	Angle
W1	Channel	3/8	5	18	1	1/2	4	Web plate
W2		3/8	5	18	1	1/2	4[2]	
W3		3/8	5	36	1	1/2	4	
W4		3/4	5	18	1	1/2	4	
W5		3/8	5	18	1	1	4	
W6		3/8	5	18	1	1/2	2-1/2	
W7		3/8	5	18	1	1/2	8	
W8		3/8	8	18	1	1/2	4	
W9		3/4	5	36	1	1/2	3	
W10		3/4	5	36	1	1/2	6	
W11		3/8	5	18	2	1/2, 3/8	4	1/2” Full-depth web plate
W12		3/8	5	18	1	1/2	5x2[3]	Web plate
W13		1/2	5	26	2	1/2, 3/8	4[4]	1/2” Full-depth web plate
W14		1/2	5	26	2	1/2, 3/8	4[5]	1/2” Full-depth web plate
W15		3/8	5	18	3	1/2, 3/8, 3/8	4	3/8” Exterior web plate
W16		3/8	5	18	3	1/2, 3/8, 3/8	4	1/2” Interior web plate
W17		1/2	5	26	2	1/2, 3/4	4	3/4” Partial-depth web plate
W18[6]		3/8	5	18	1	1/2	4	Web plate
W19		3/8	5	18	3	1/2, 3/8, 3/8	4	1/2” Exterior web plate
W20		3/8	5	18	3	3/8, 3/8, 3/8	4	3/8” Interior web plate
W21		3/8	5	18	3	3/8, 3/8, 3/8	4	3/8” Exterior web plate
W22		3/8	5	18	2	3/8, 3/8	4	3/8” Interior web plate
W23		3/8	5	18	3	3/4, 3/8, 3/8	4	3/4” Exterior web plate
W24		C15x40[7]	-	15	2	3/8	6	Rolled channel
W25		3/8	5	18	4	1/2, 3/8, 3/8, 3/8	4	1/2” Exterior web plate
W26		5/8	8	42	4	13/16, 13/16, 5/8, 11/16	8x3[2]	13/16” Exterior web plate
W27	Box	3/8	5	18	2	1/2, 1/2	4	Web plate
W28[8]		3/8	5	18	2	1/2, 1/2	4	
W29	I-section	3/8	5	18	1	1/2	5x2[3]	Web plate

Notes: 1. Staggered fastener pattern spaced five inches longitudinally and two inches transversely, 2. Fastener shear stiffness reduced by factor of two, 3. Staggered fastener pattern (longitudinal x transverse), 4. Modeled with two fasteners transversely across partial-depth web plate, 5. Modeled with three fasteners transversely across partial depth web plate, 6. Modeled 2x longer than base model W1 to observe effect of location of fracture relative to applied boundary condition, 7. Model geometry comprised of a rolled channel similar to C15x40 with additional web plate, 8. Model geometry reversed orientation of the angles to ensure consistent behavior with model W26.

Finally, this section refers to “interior” and “exterior” web plates throughout the discussion when reporting on members having multiple plates per web. The following is provided to help clarify what is meant by these terms in the context of the research, as it may not be intuitive. An interior web plate on an axial member refers to a full-depth plate with components, either plates (full or partial-depth) or angles, on *both* sides of it. Note that a member may have more than one interior plate. An exterior web plate is a full-depth plate that has at least one surface entirely exposed. Figure 4.4 illustrates a couple of typical examples. The sketch on the left contains plates that are “exterior” plates even though they are positioned toward the center of the box. However, notice that the plates positioned towards the outside of the box are also considered “exterior” plates. The right side of the figure shows interior plates on the built-up channels, which have angles on one side and a full-depth exterior plate on the other side. The interior plates shown on the right side figure would still be interior plates even if the partial-depth web plate were not there. Recall that for a plate to be considered “exterior”, it must have one side *completely* exposed, having no angles or plates attached to one side.

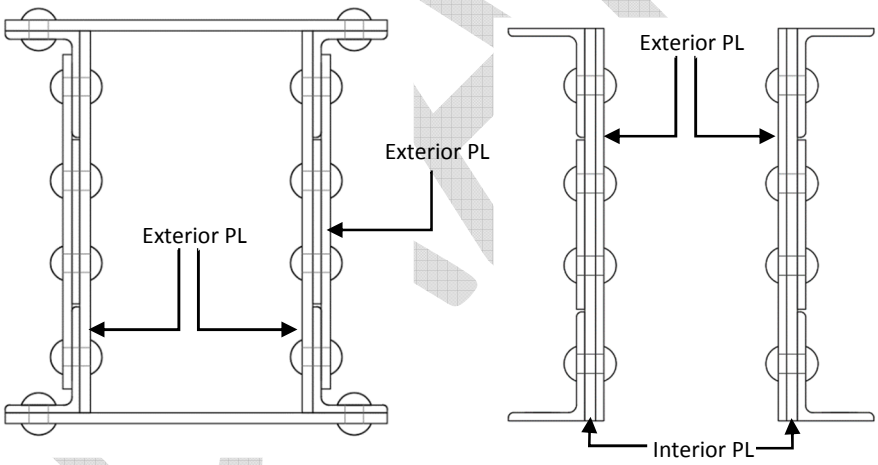

Figure 4.4 Illustrations of typical built-up members (Left) box member with all exterior plates, (Right) channel member (lattice removed) with interior and exterior plates

4.1.3. Net Section Stress through Integration of Nodal Forces

Each model was created requesting element nodal forces (NFORC) outputs allowing integration of element nodal forces in selected elements with the Abaqus free body cut tool. The integrated nodal forces were simply divided by the gross or net areas, as necessary, to obtain an equivalent nominal stress.

Results of models were compared using this method, which accounted for large stress gradients, such as near the edges of fastener holes. All net section stress values in the present paper were calculated this way.

4.2. Results for Parametric Study of Multi-Component Members

The following sections provide discussion and results for the finite element analysis (FEA) parametric study that focused on multi-component members. The analysis revealed that a majority of the load coming from a failed component was redistributed into the adjacent components over a short length producing a localized stress amplification. Similar behavior was observed by Hebdon *et al*. (2015) for flexural members. Figure 4.5 provides an illustration of this localized behavior. A cross-section is shown from a built-up channel comprised of two angles, two full-depth web plates, and a partial-depth web plate. The image plots longitudinal stress in the cross-section (in and out of the page). Any value at or below the remotely applied stress of 2 ksi is blacked out to help highlight stress amplifications. Red indicates a location of highest tensile stress concentration and blues are the lowest magnitude tensile stresses. It can be seen that stresses are highest at the fastener holes and through the thickness, nearest the failed component. In this particular case, the full-depth web plate adjacent to the failed plate collected 86% of the load from the failed plate. Stress amplification above the theoretical axial stress of the remaining cross-section was found to be caused by shear lag in the load transfer and local bending near the failure plane. These effects are discussed in greater detail in the following sections.

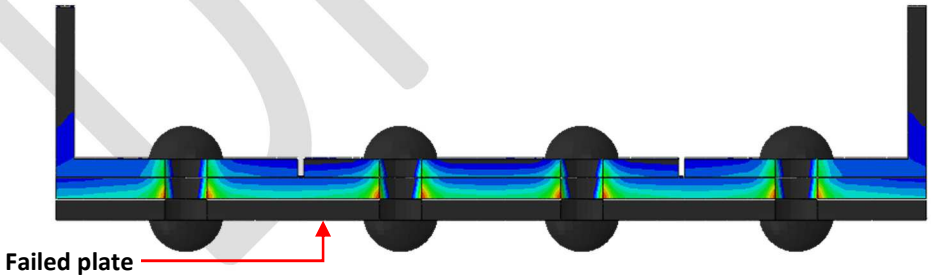

Figure 4.5 Example of localized load redistribution

4.2.1. *Effect of Boundary Conditions on Multi-Component Members*

The effect of boundary conditions for built-up members with a failed component was addressed by applying fixed and pinned boundary conditions on models of identical geometry. All degrees of freedom were constrained at the fixed boundary plane, whereas the pinned boundary plane released rotational degrees of freedom while constraining displacements. Figure 4.6 plots longitudinal (or axial) stresses on the surface of the web plate at the transverse location of the first fastener row away from the failure plane (as indicated by the red dashed cut line shown on the inset image) on two of the models analyzed. The curves are discontinuous at the locations of the two fastener holes. These two models were comprised of two angles and a single web plate. The failed component was one of the angles. The figure indicates that fixed boundary conditions provided a more conservative solution, but the overall difference in output was not significantly dissimilar. Several geometries were analyzed this way, with both fixed and pinned end boundary conditions. In all cases, the differences among outputs were negligible or the fixed boundary condition resulted in a slight stress increase. Due to the difficulty determining the level of boundary constraint that may exist on any one bridge, let alone all possible bridges, as well as the similar results, it was decided that fixed boundary conditions should be conservatively used moving forward with the parametric study.

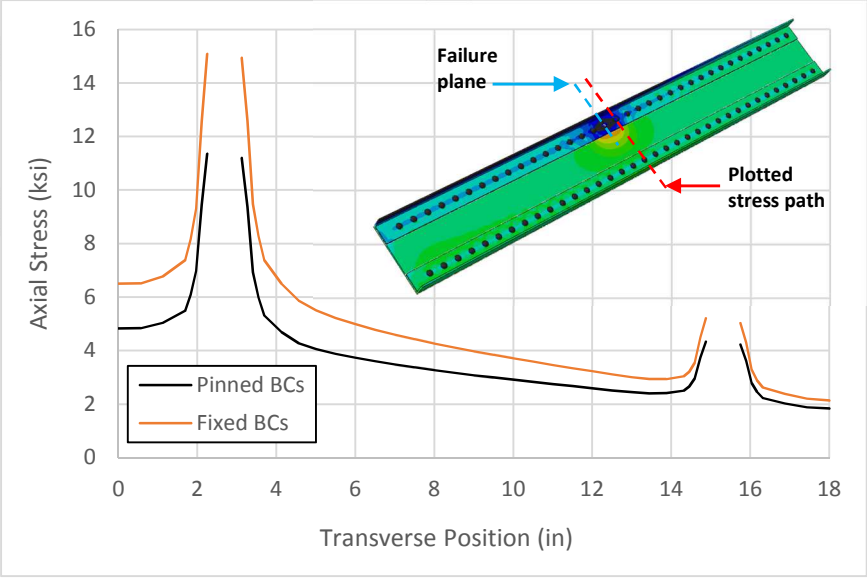

Figure 4.6 Effect of boundary conditions

4.2.2. Effect of Fastener Shear Stiffness on Multi-Component Members

Fastener shear stiffness was also considered for the parametric study. The primary load transfer mechanism across failure planes in the built-up members was shear through fastener bearing. Components adjacent to the failed component effectively functioned as shear splices redistributing load out of the failed component, around the failure, and back into it. The lab testing and finite element analysis (FEA) confirmed that upon the initial fracture event, some local yielding may occur at the bolt holes. However, live load stresses due to fatigue would still remain elastic since they are much smaller. Therefore, because this study was focused on determining elastic fatigue stresses resulting from a failed component, all loads were conservatively maintained well below the elastic limits of the material and the benefits of load redistribution due to non-linear redistribution were ignored for the majority of models. It was found that fastener stiffness did not have an effect on the results, even when the fastener stiffness was reduced by a factor of 2. This effectively means that fastener stiffness will not need to be considered in the analysis of candidate IRMs; therefore, the resulting analysis is applicable to riveted and bolted memebrs.

4.2.3. Effect of Web Depth, Web Thickness, Fastener Position & Spacing on Multi-Component Members

A parametric study was performed to understand the stress amplification effect in web plates resulting from load redistribution of an adjacent failed angle. A range of complete member models showed several similarities in the load redistribution behavior and revealed that a very simplified approach could be developed to evaluate the load redistribution. Figure 4.7 shows three illustrative examples where web plate depths and angle sizes have been varied. It can be seen that although the geometries vary widely, the redistributed load from the failed angle (the failed angle has been removed to show stress contours in the web plate) remains primarily in the top few inches of the adjacent web plate. In short, it was learned that the load redistributed into the adjacent plate at the first engaged fastener was:

- Not distributed through the entire depth of the web plate;
- Distributed over a nearly constant depth, regardless of web plate geometry (*i.e.*, depth & thickness);
- Not influenced by geometry of the other components within the member;
- Affected by the edge distance and spacing of the fasteners.

Based on these observations, simplified sub-models were created to evaluate the effects of fastener edge distance and spacing. First, however, web plate depth and thickness were varied in the sub-models to confirm that results were consistent with the complete member models. The finite element models used to study the web parameters were consistent with that described in Section 4.1. except that quadratic brick elements (Abaqus designation C3D20) were used instead of linear brick elements. Figure 4.8 shows the schematic for variables listed in Table 4.2, which contains the geometries studied.

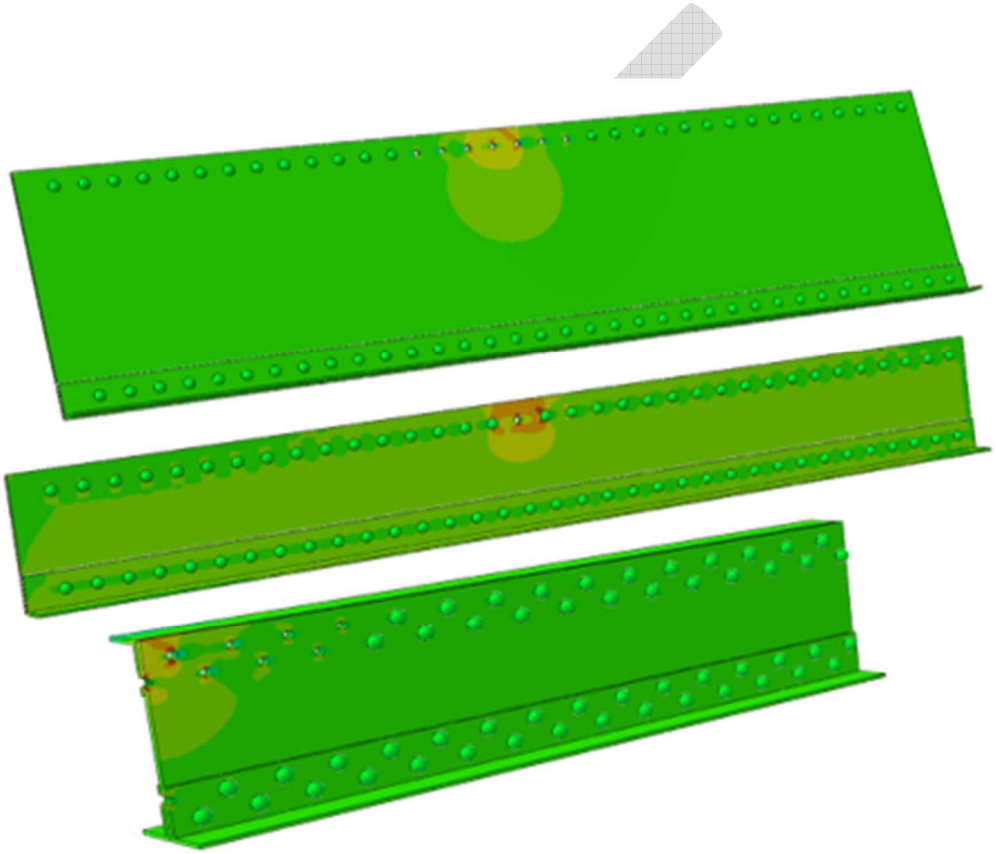

Figure 4.7 Examples illustrating similar load redistribution characteristics despite differing geometries (failed angles removed for clarity)

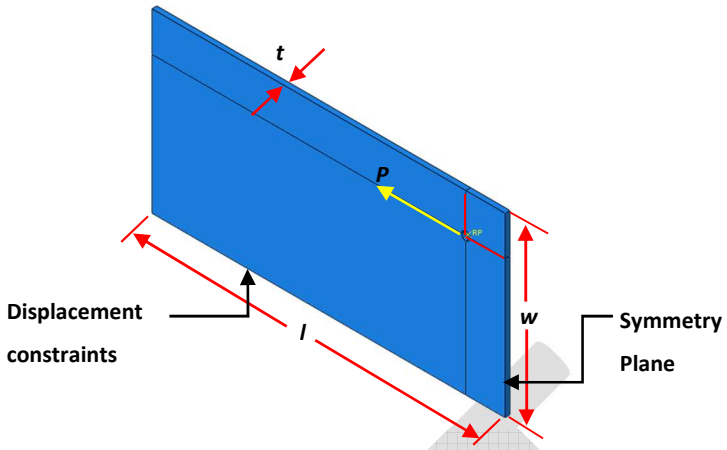

Figure 4.8 Schematic for web plate shear lag FEMs

Table 4.2 Geometries for web plate shear lag analysis (all dimensions in inches)

Model ID	*a*	*b*	*w*	*t*	*l*	Notes
SL1	2-1/2	2-1/2	10	1/2	36	
SL2	4	4	18	1/4	36	
SL3	2-1/2	2-1/2	18	1/2	36	
SL4	4	4	18	1/2	36	
SL5	4	4	18	1/2	36	Z
SL6	4	4	18	1/2	36	Y
SL7	4	4	18	1/2	36	X
SL8	4	4	18	1/2	36	X, Z
SL9	4	4	18	1	36	
SL10	4	4	18	2	36	
SL11	4	4	36	1/2	36	
SL12	4	2	18	1/2	36	
SL13	4	8	18	1/2	36	

Notes:
X = Plasticity added to the material definition.
Y = Global mesh size refined to 1/2 typical mesh size.
Z = Applied load increased by factor of 10.

As shown in Figure 4.8, a single fastener hole was modeled. A concentrated force, *P*, was applied at a reference point that was centered in the fastener hole and coupled to a surface on the interior of the fastener hole simulating the load application of a fastener in bearing without explicitly modeling the fastener. Mesh size and material plasticity were also considered, as noted in Table 4.2, to ensure solution convergence. The length of the plates was kept constant. Symmetry boundary conditions were applied at the vertical surface of the plate just behind the fastener hole. Out-of-plane displacements were restrained along the bottom longitudinal surface of the plates of all models. Each model was also evaluated adding in-plane displacement constraint at the same surface. This parameter was found to have no effect on the results. Web depth, web thickness, fastener position in the web relative to the edge, as well as fastener spacing were studied. Web depths ranged from 10 to 36 inches, web thickness

ranged from 1/4 to 2 inches, fastener spacing ranged from 5 to 16 inches, transverse edge distance ranged from 2-1/2 to 4 inches, as well as models having varying combinations of fastener spacing and edge distances.

Figure 4.9 & Figure 4.10 plot results for the web parameters. All plots have percent of applied load on the vertical axis and depth position in the plate along the horizontal axis. The depth position is the dimension taken from the top surface of the plate nearest the fastener hole, moving down toward the bottom surface of the plate following the path of the variable *w* shown in Figure 4.8. Position "0" indicates the depth of the center of the fastener hole. Forces along the depth position were integrated and normalized by the magnitude of the applied load to obtain the percent of applied load. Figure 4.9(a) & (b) clearly indicate that there is no effect resulting from web thickness, magnitude of the load in the fastener, mesh size in the model, or material plasticity (Note that curves overlap in the figure for both plots). Figure 4.10(a) & (b) show a minimal effect caused by the depth of the web and the position and spacing of the fastener hole. Most notably these plots show that the load transferred out of the failed angle and into the adjacent plate was not distributed across the full-depth of the plate. Rather it was concentrated toward the edge of the plate near the first engaged fastener in the angle due to shear lag effects. Interestingly, all cases considered in the study converged at or within a few percentage points of 40% of the applied load being distributed into the web plate at a depth equal to the fastener position. The deviation ranged from one to five percent, which provided a reasonable method for calculating the shear lag effect in a web plate of any geometric combination.

Knowing that approximately 40% of the load was being distributed into the first few inches of the web plate, it was important then to understand the relationship between the amount of load in the web plate and the area of the plate in which the load was carried (or distributed into) in order to accurately estimate the largest fatigue stress range that would result from a failed angle. Nodal forces were integrated at increments equal to the element size and then divided by the unit area of the web plate equaling a position-dependent unit stress that was independent of the thickness of the web plate. Figure 4.11 plots percent of maximum unit stress versus depth position in the plate for the models that had the greatest effect on shear lag (Note: refer to Figure 4.8 for meaning of dimensions "a" and "b"). Stress along the depth position were normalized by the magnitude of the maximum stress to obtain the percent of maximum unit stress. Position "0" was the location of the center of the fastener hole. The plot shows that there was minor variance of depth into the plate to reach maximum unit stress, typically occurring at a depth coincident with the position of the fastener.

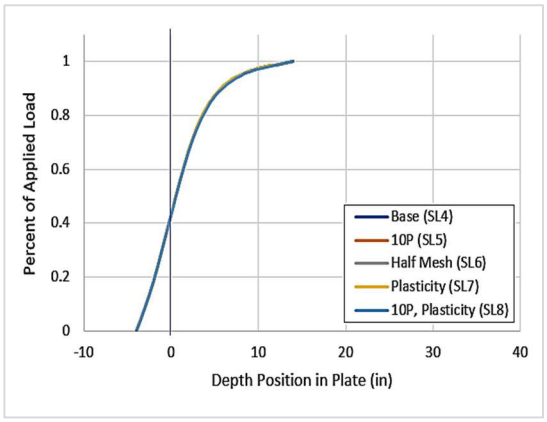

(a) Load, Mesh & Plasticity

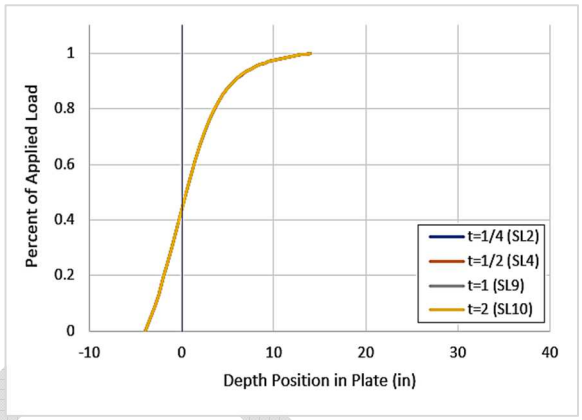

(b) Web thickness

Figure 4.9 (a) Effect of Magnitude of Load, Mesh Size, & Plasticity, and (b) Effect of web thickness; Note, curves are overlapping in both plots

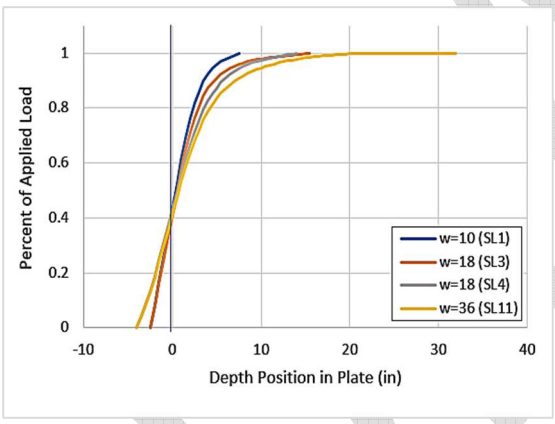

(a) Web depth

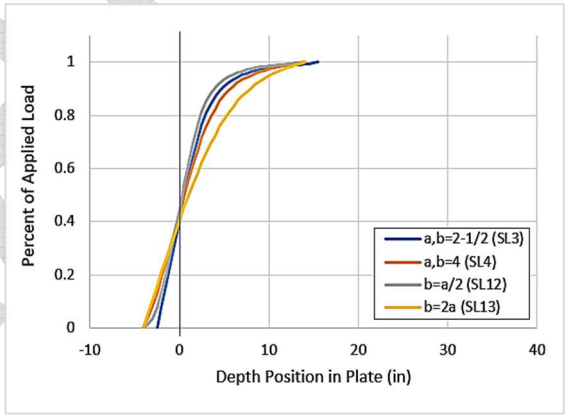

(b) Fastener position

Figure 4.10 (a) Effect of web depth, and (b) Effect of fastener hole position

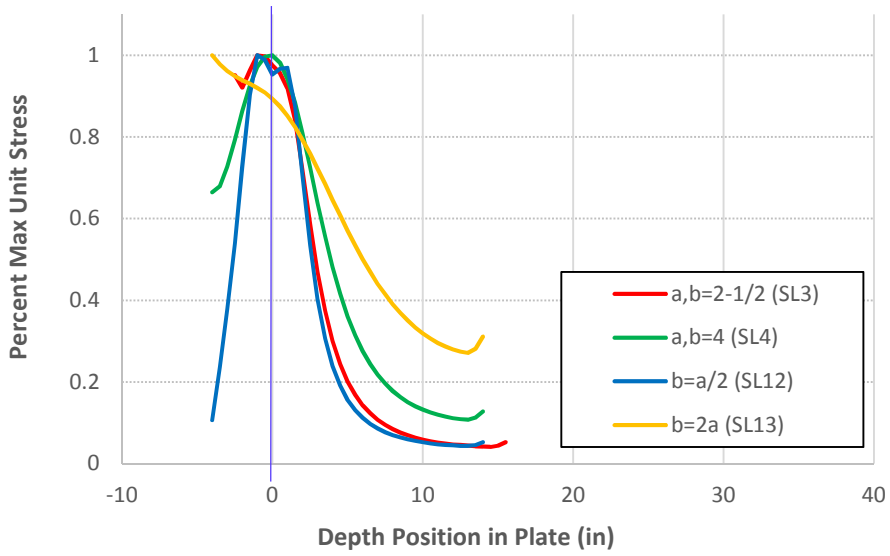

Figure 4.11 Depth into plate to maximize stress range calculation

Based on these findings, a method to calculate the fatigue stress range in a web plate after failure of an adjacent angle was developed. This is shown in equation 4.1. The method has been designated the "40-over-fastener" rule referring to 40% of the redistributed load carried within the portion of the web plate approximately equal to the depth of the fastener. Equation 4.1 simply adds the original net section stress in the web plate from the unfaulted state to the stress resulting from the additional load the plate "picks up" from the failed angle, accounting for shear lag effect.

This stress amplification in the web plate is a linear-elastic calculation and is local to the site of assumed failure. It is intended only for fatigue stress range calculations in the faulted state. For strength checks where there may be local redistribution of forces due to plate slip, local yielding, etc., it can be shown that it would be overly conservative to apply this amplification.

$$f_{AFN} = \frac{P_u}{A_N} + \frac{0.4P_{u-L}}{l_f t_p} \tag{4.1}$$

Where:

$\boldsymbol{A_N}$ = Net section area of the entire member in the unfaulted state (in^2).
$\boldsymbol{f_{AFN}}$ = Factored total net section stress in the faulted state (ksi).

l_f = Fastener edge distance calculated from the center of the fastener hole to the edge of the plate, perpendicular to the force (in). For staggered, or zig-zag fastener patterns, l_f is taken as the smallest edge distance.

P_{u-L} = Total factored tensile load in a single angle assumed to fail (kip).

P_u = Total factored tensile load in the member in the unfaulted state (kip).

t_p = Thickness of the full-depth web plate (in).

Equation 4.1 was applied to all geometries listed in Table 4.1 having a model ID beginning with "A", which are models with failed angles, and were compared to results for models with the same geometries, but having a failed web plate. Two failed angle cases were found to control the maximum stress result, models A4 and A13. When compared with the FEMs, Equation 4.1 slightly overestimated the stress range in the plate by approximately 12-15% in both cases, demonstrating reasonable conservatism. In FEM A4, the gross area of the angles equaled 1.29 times the gross area of the web plate to which they were attached. These proportions would be unusual in-service, but not impossible. The large gross area of the angle simply meant more load redistributed into the web plate resulting in the controlling stress range. The second case was for a built-up I-section (FEM A13). The I-section was governed by angle failure for three reasons worth noting. First, redistributed load from the failed web plate case was shared by four angles, rather than just two as it would be for a built-up channel. Second, failure of the web plate resulted in no bending stress amplification in the angles due to symmetry of the angles around the plate. And third, the I-section had a staggered fastener pattern that placed the fasteners relatively close to the plate edge increasing the result of the "40-over-fastener" calculation. These cases suggest that while the majority of cases will be governed by the hypothetical failure of the web plate within the member, certain circumstances warrant performing the 40-over-fastener calculation to ensure the governing stress range resulting from the faulted state is not missed. It stands to reason therefore, that all built-up I-sections should have the failed angle scenario checked, as well as any built-up channel case where there is only one plate and where the combined gross area of two angles is equal to or greater than 1.3 times the gross area of the plate to which they are in direct contact. This would not include built-up box sections where an angle is in direct contact with more than one plate.

4.2.4. Shear Lag Effects Resulting from Failed Plates in Multi-Component Members

Shear lag effects in tension components connected by fasteners have been researched previously (Easterling *et al.*, 1993; AASHTO 2016; AISC 2017). Factors found in Table 6.8.2.2-1 of AASHTO (2016) reduce the effective area of the connected components, which increases the stress calculation in the connected member. The following section explains development of the shear lag factor, Ξ_{VL}, for built-up

axial multi-component members in the *faulted state*. Because the member is in a faulted stated, the existing AASHTO and AISC shear lag factors cannot be directly applied. The shear lag evaluation method described below utilizes an amplification factor that is applied to the stress calculation, rather than a reduction factor applied to the area. While the intention and mathematical effect are similar, the application and results are different.

During the development of the shear lag factor, Ξ_{VL}, it was realized that Case 2 of AASHTO (2016) Table 6.8.2.2-1 agreed well with results from the present study for built-up channels, comprised of a single full-depth web plate and two angles, when *L* (length of the connection) was assumed to equal two fastener spaces and the angle neutral axis, $\bar{x}$, was used. Two fastener spaces would be the distance between the first engaged fasteners to either side of a failure plane (in other words equal to 2 times the fastener spacing). However, there were exceptions once additional components were introduced to the member geometries, such as partial-depth web plates or additional full-depth web plates. Furthermore, Case 1 from AASHTO (2016) applies an area reduction factor of 1.0 for plates connected by fasteners. However, results from the current study disagreed in the context of built-up axial tension members comprised of many components, in which one is failed. The causes for which have not been specifically researched, but are likely due to the interplay of multiple plates and angles fastened together into the same connection and the added shear lag effects associated with one of the components being completely failed.

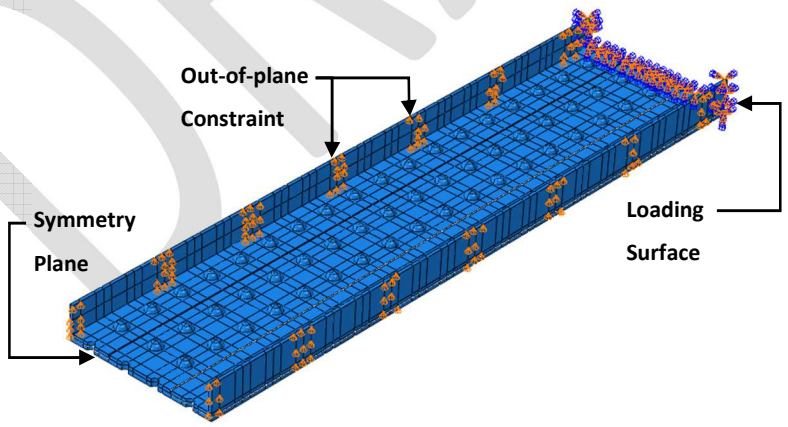

Figure 4.12 Example of boundary conditions applied to models

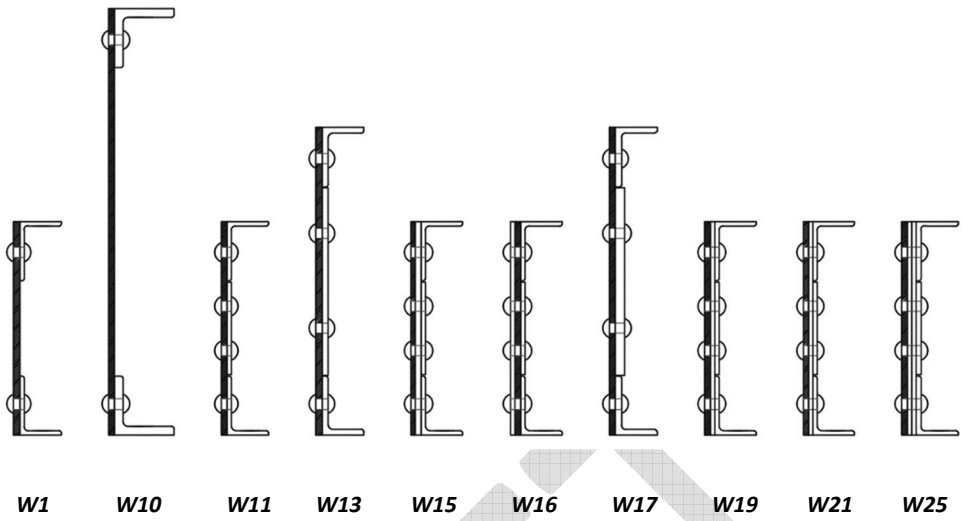

Figure 4.13 Geometries used to study shear lag resulting from failed plates

Given that the existing shear lag calculation procedure does not fully capture the behavior that takes place in multi-component members in which a component has failed, the following segment of the parametric study was conducted to investigate shear lag in tensile members with failed components. Figure 4.12 illustrates the set of boundary conditions that were applied to several FEMs. Boundary conditions were applied to simulate a symmetry plane at the location of the failure, and fixed conditions were applied at the loading plane (released axial displacement during the load step), and out-of-plane displacement of the angle outstanding legs was constrained every 12 inches along the length. The out-of-plane constraints removed bending effects in the stress solutions isolating stress amplification to the effects of shear lag. Figure 4.13 illustrates the geometries studied, ranging from 18 to 36 inches tall, 1 to 4 web plates, and 3/8 to 3/4-inch plate and angle thicknesses. The failed components are hatched in black. Table 4.3 lists the models and each component in the analysis. A nominal theoretical net section stress in the faulted state, σ_{AFN_NOM}, was calculated by dividing the applied load by net area of the member in the faulted state. The faulted net area was simply the net area of the member in the unfaulted state, less the net area of the failed component.

Table 4.3 Component stress results used for shear lag factor

Model ID	Component Failed	Component Evaluated	σ_{AFN_NOM} (ksi)	σ_{AFN_FEA} (ksi)	Ratio
W1	1/2" Full-Depth Web PL	Angle	5.55	6.25	**1.13**
W10	1/2" Full-Depth Web PL	Angle	5.10	5.86	**1.15**
W11	1/2" Full-Depth Web PL	Angle	4.68	4.92	1.05
		Partial-Depth Web PL		5.36	**1.15**
W13	1/2" Full-Depth Web PL	Angle	4.10	4.63	**1.13**
		Partial-Depth Web PL		4.00	0.98
W15	3/8" Ext. Full-Depth Web PL	Angle	3.32	2.98	0.90
		Partial-Depth Web PL		3.06	0.92
		Int. Full-Depth Web PL		3.81	**1.15**
W16	1/2" Int. Full-Depth Web PL	Angle	3.78	3.70	0.98
		Partial-Depth Web PL		4.20	**1.11**
		Ext. Full-Depth Web PL		4.02	1.06
W17	1/2" Full-Depth Web PL	Angle	3.71	4.97	**1.34**
		Partial-Depth Web PL		3.58	0.96
W19	1/2" Ext. Full-Depth Web PL	Angle	3.78	3.47	0.92
		Partial-Depth Web PL		3.52	0.93
		Int. Full-Depth Web PL		4.49	**1.19**
W21	3/8" Ext. Full-Depth Web PL	Angle	3.53	3.41	0.91
		Partial-Depth Web PL		3.13	0.92
		Int. Full-Depth Web PL		4.62	**1.17**
W25	1/2" Ext. Full-Depth Web PL	Angle	3.39	3.21	0.91
		Partial-Depth Web PL		3.26	0.92
		Int. Full-Depth Web PL		4.32	**1.27**
Average of Maximum for each Member:					**1.18**

Table 4.3 also presents the results from the finite element analysis, listed under σ_{AFN_FEA}. This was found by integrating the nodal forces of the area in question and dividing by the net area of the same. The area integrated for angles was the connected leg, including the thickness of the outstanding leg. The entire component net section was integrated for the plates. The final column in the table is *Ratio*. *Ratio* refers the quotient of the σ_{AFN_FEA} to the σ_{AFN_NOM}, indicating the level of local stress increase in the components due to shear lag. The maximum shear lag ratio from each member was averaged, equaling a value of 1.18. Finally, the average was conservatively rounded to the nearest tenth, making it 1.2.

4.2.5. Effect of Number of Plates on Multi-Component Members

The number of plates in the cross-section was studied for its effect on the stress in remaining components due to bending. Figure 4.14 illustrates the set of boundary conditions that were applied to several of the FEMs listed in Table 4.1. The selected models were evaluated once with the boundary conditions shown on the left side of Figure 4.14, and then again with the boundary conditions shown on the right side. The boundary conditions on the left show the out-of-plane constraints applied, while on the right these were removed; all other displacement boundary conditions remained the same. In an

actual bridge, members are connected to another half of identical geometry with lattice or batten plates providing some level of out-of-plane stiffness that does not exist in the model shown on the right. Due to the variety of geometry that exists on bridges in service, it was necessary to envelop the bending effects in the analysis, and develop a reasonable and conservative stress amplification factor which accounts for these effects. Figure 4.15 illustrates the geometries studied. All cases utilized 18-inch tall built-up channels with 1 – 4 plates in which the exterior plate was failed, as indicated by the black hatch.

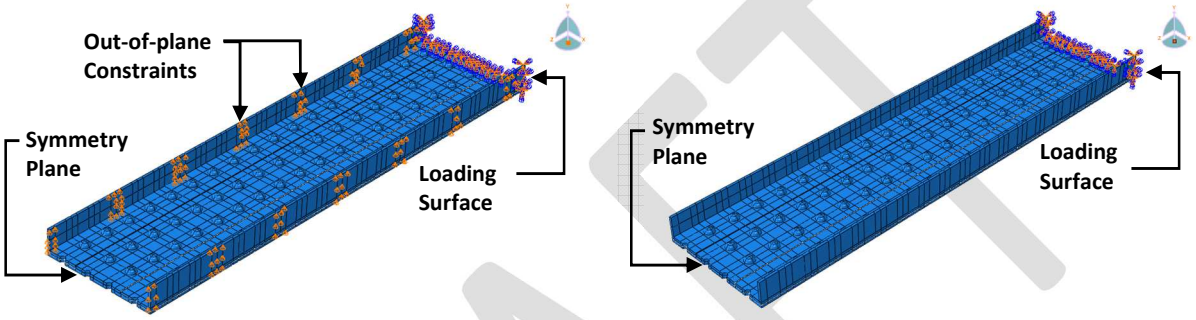

Figure 4.14 Example of boundary conditions applied to models, (Left) with out-of-plane constraint and (Right) without out-of-plane constraint

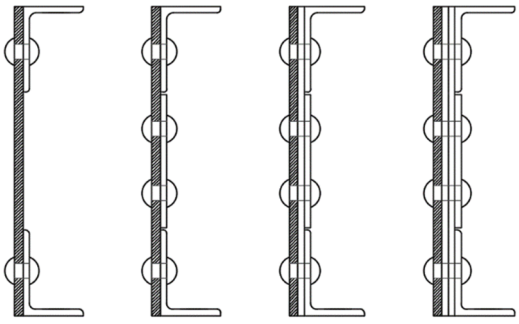

Figure 4.15 Geometries used to analyze effect of the number of plates

Area ratios between failed components and remaining and adjacent components, as well as component thickness were all varied and studied for an effect on bending using geometries listed in Table 4.1. No clear relationship could be observed based on thickness or area ratios between the failed and the

adjacent components. However, the number of plates in the member did show clear correlation with the magnitude of the local bending stress amplification. Interestingly, this parameter (i.e., the number of cover plates) was also observed by Hebdon *et al*. (2015) for built-up flexural members. However, unlike for flexural members, the more plates present in an axial member, the lower the stress amplification observed. This was because increasing the number of plates reduced the local effects due to out-of-plane bending when a single component failed; meaning that the overall effect of a single plate failing in a cross section comprised of many plates was reduced when compared to a cross section where there was only a single web plate to begin with. Table 4.4 lists results from the analysis showing the net section stresses from the braced and unbraced FEMs. Only components in direct contact with the failed component are reported because the bending effect was found to be greatest in these components. The final column, *Ratio*, is the quotient of *Unbraced* σ_{AFN} to *Braced* σ_{AFN} representing the stress increase in the component. By deriving the bending factor from a ratio of the stress resulting from the braced and unbraced model of identical geometry, the shear lag effects were identical between them and therefore became effectively cancelled. Hence, this ratio isolated the effects of shear lag from localized bending in the adjacent component(s).

Table 4.4 Component stress results used for bending factor

Model ID	No. of Plates	Component Failed	Component Evaluated	Unbraced σ_{AFN} (ksi)	Braced σ_{AFN} (ksi)	Ratio
W1	1	1/2" Full-Depth Web PL	Angle	7.96	6.25	1.27
W10	1	1/2" Full-Depth Web PL	Angle	7.58	5.86	1.29
W11	2	1/2" Full-Depth Web PL	Angle	6.08	4.92	1.24
			Partial-Depth Web PL	6.01	5.36	1.12
W13	2	1/2" Full-Depth Web PL	Angle	5.65	4.63	1.22
			Partial-Depth Web PL	4.32	4.00	1.08
W15	3	3/8" Ext. Full-Depth Web PL	Int. Full-Depth Web PL	4.15	3.81	1.09
W16	3	1/2" Int. Full-Depth Web PL	Angle	3.79	3.70	1.03
			Partial-Depth Web PL	4.20	4.20	1.00
			Ext. Full-Depth Web PL	4.21	4.02	1.05
W19	3	1/2" Ext. Full-Depth Web PL	Int. Full-Depth Web PL	5.16	4.49	1.15
W21	3	3/8" Ext. Full-Depth Web PL	Ext. Full-Depth Web PL	4.62	4.13	1.12
W25	4	1/2" Ext. Full-Depth Web PL	Int. Full-Depth Web PL	4.00	3.60	1.15

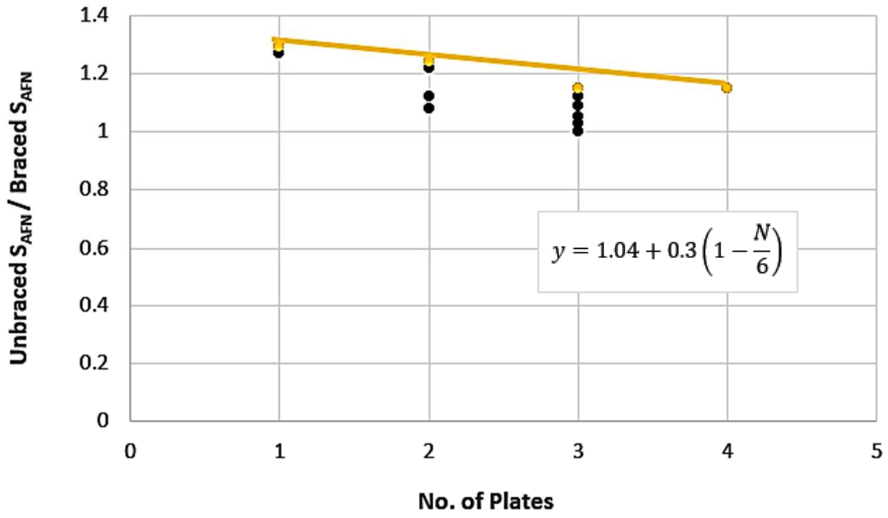

Figure 4.16 Ratios of Unbraced to Braced longitudinal after-fracture net section stress

Figure 4.16 plots all *Ratio* data from Table 4.4 as a function of the number of plates in each member. A line was conservatively fit to the upper bound data points using linear regression analysis. Equation 4.2 is the equation of that line, which can be used to account for the local stress increase due to bending after failure of a single component.

$$\Xi_B = 1.04 + 0.3\left(1 - \frac{N}{6}\right) \tag{4.2}$$

Where:

$\boldsymbol{\Xi_B}$ = Fatigue stress range amplification factor accounting for localized bending effect in a built-up multi-component axial member in the faulted state.

$\boldsymbol{N}$ = Number of plates in the member.

The correlation was such that increasing the number of plates reduced the bending amplification. As stated, this was intuitive since by increasing the number of plates within a given cross-sectional area, the impact of any one of those plates failing is reduced. Hence, preferred detailing for new designs would be to fabricate with the largest number of plates feasible. Also, bending effects were found to be localized near the failure plane. As a result, moments at the fixed boundary plane were near zero for all cases, meaning gusset connections would not experience increased demands resulting from a failed component within multi-component members. In the absence of better design guidance, a few internally redundant

tie member designs have been performed by others where an out-of-plane moment was calculated assuming that when a single component failed the component was removed (along the entire length of the member) from the analysis, which resulted in an asymmetric cross section and eccentric load at the connections. The eccentricity was assumed to equal the distance from the unfaulted member centroid to the new centroid of the faulted member cross section. Based on outcomes from this parametric study, it was clear that this type of design assumption was exceedingly conservative and would result in notable moments that must be resisted at the connections, which in turn would drive up member and connection sizes in order to accommodate those demands. However, for multi-component built-up axial members, the integration of weak-axis member stiffness along the length is essentially unaffected by the extremely short length over which the component is broken. Over short distances, typically within just a couple or three fastener spaces, the redistribution of load has re-equilibrated and the full cross section of the member was again engaged in carrying load. This behavior resulted in localized bending effects centered on the failure location, which were resolved within the member without adding moment demands at the connections. The small moments generated were a function of the load being transferred out of the broken component across the distance between the component centroids, rather than the member centroids. However, when tested, this did not always prove to be an accurate method for calculating a resulting moment. To put the magnitude of the moments into context, a typical resulting moment at the failure plane in the finite element models ranged from about 4 kip-in (for a single web plate geometry) down to less than 1 kip-in (for multi-web plate geometries). This concept may become even clearer when considering the effects resulting from the position of the failed plate discussed in Section 4.2.6, where it is explained that when a broken plate sheds load into adjacent components on both sides of it, the bending effect is cancelled and stress amplification from bending goes away. The bottom line is that this aspect of the analysis has been streamlined to a factor that inherently accounts for these affects and is simply a function of the number of plates, making the analysis all the more convenient for the evaluating engineer.

Additionally, the multi-component bending stress amplification factor, Ξ_B, was developed using half of the member cross-section for models of built-up channels. Equation 4.2 was found to work equally well with box sections with top and bottom flange plates when the plate count was made on half of the cross-section. In other words, each of the flange plates would be counted as 1/2 plate. A few examples are provided in Figure 4.17. Dashed lines indicate the portion of a generic member that contributes to the plate count. Full-depth as well as partial-depth plates are counted. Angle legs, lacing bars, and batten plates are not counted. Flange plates with hand holes are counted. For example, the plate count, *N*, for

Figure 4.17(c) is 4. This is attained by counting 1/2 for each of the top and bottom flange plates (or 1 together), 1 for each of the two full-depth web plates and 1 for the partial-depth web plate that fills between the angle legs.

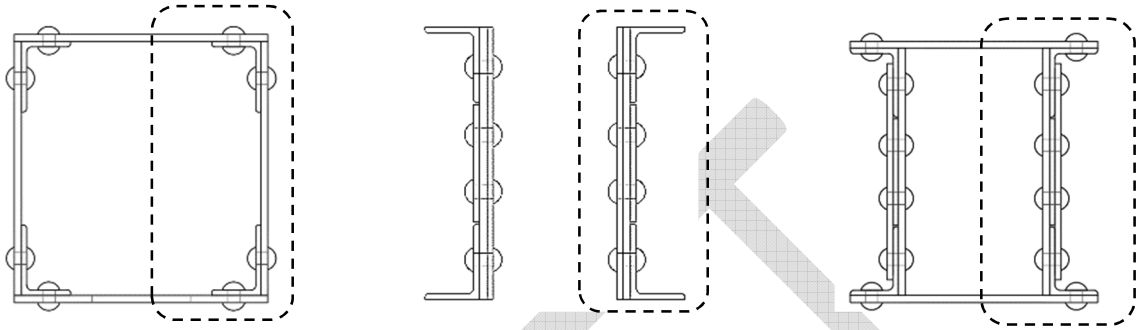

(a) N=2 ***(b) N=3*** ***(c) N=4***

Figure 4.17 Examples of plate counts, N, for bending factor, Ξ_B

4.2.6. Effect of Plate Position on Multi-Component Members

Results from parametric studies discussed above indicated that position of the failed plate within the cross-section may affect the outcome. For this reason, models W19 – W23 were created and analyzed. Cross-sections of these models are shown in Figure 4.18 with hatch marks on the component that was failed in the analysis. Model W19 was identical to geometry of model W16, except that the thicker interior web plate was moved to the exterior position and the thinner exterior web plate was moved to the interior position. Model W23 increased the size of the exterior plate to twice the thickness of the adjacent plate. Otherwise, all failed plate thicknesses were maintained equal between model geometries.

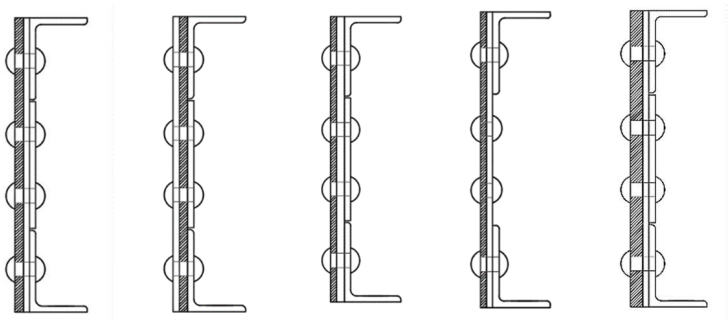

Figure 4.18 Geometries used to analyze plate position effects

It was found that when the failed plate was positioned with components on both sides (meaning the failed plate was an "interior" plate), there was nearly no bending effect in the adjacent components. For example, stress for W16 was overestimated by 28% using the bending and shear lag factors. However, when the failed plate was moved to the exterior position in model W19, the results were overestimated by only 4%. Results for model W20 were overestimated by 27% using the bending stress amplification factor. However, when the failed plate was moved to the exterior in model W21, results were overestimated by only 9%. The same was seen for results of model W22, where the partial-depth web plate was removed. Finally, the failed exterior full-depth web plate in model W19 was made two times thicker in model W23. In this case, bending and shear lag factors slightly underestimated the results by 4% suggesting that if the exterior plate is much thicker than the adjacent plate, the bending effect is slightly increased, but not proportionally to the increase of plate thickness.

Even though bending effects were reduced when the failed component was positioned between other components, the analysis for fatigue stress range must be based on the worst-case scenario for the member. This means that if a member has two web plates for example, and the interior plate is thicker than the exterior plate, the member must be checked for at least two cases. First, the case for failure of the thinner exterior plate including bending and shear lag effects. Then the case for failure of the interior plate where larger load redistribution will occur, but without bending amplification. In summary, either case could control the calculation and should be checked.

4.2.7. Validation Exercise: Simplified Analysis of Multi-Component Members

Results for bending and shear lag factors explained above were applied to all geometries listed in Table 4.1 with Model IDs beginning with "W". Additionally, the "40-over-fastener" rule was applied to all geometries listed with Model IDs beginning with "A". The controlling case, or the case resulting in the largest stress in any component, is reported in Table 4.5 and is compared to the FEA results. Only the controlling component is listed, meaning the component within the member that was found to have the largest stress resulting from failure of another component. This was always an adjacent component in direct contact with the failed component.

Moreover, research into the behavior of axial tension members showed that each half of the built-up member essentially carried the redistributed load independently of the other half; meaning the load from the failed component was locally redistributed, even when top and bottom flange plates were present, such as for a box section. Portions of the box section flange plates participated in load redistribution, however, opposite webs and angles did not. For this reason, the net area used to calculate the nominal axial stress in the faulted state, σ_{AFN_NOM}, only includes the half of the member possessing the assumed failed component, less the area of the failed component. Examples of these areas are shown in Figure 4.17. Furthermore, since each half of the unfaulted member carries half of the full axial load, the full axial load is divided by two when calculating σ_{AFN_NOM}, as seen in Equation 4.3.

σ_{AFN_FEA} in Table 4.5 is the stress obtained from FEA by integrating nodal forces in the area of interest, divided by the net area. The appropriate shear lag factor, Ξ_{VL}, and bending factor, Ξ_B, are also listed in the table. Ξ_B was calculated using Equation 4.2 and the plate counting method shown in Figure 4.17. The after-failure net section stress, f_{AFN}, was calculated using Equation 4.3.

$$f_{AFN} = \Xi_B \Xi_{VL} \sigma_{AFN\_NOM} = \Xi_B \Xi_{VL} \frac{P_u}{2A_{AFN}} \tag{4.3}$$

Where:

$\boldsymbol{A_{AFN}}$ = Net section area of the member in the faulted state. This is equal to the area indicated in **Figure 4.17**, minus the net area of the failed component (in^2).
$\boldsymbol{f_{AFN}}$ = Factored total net section stress in the faulted state (ksi).
$\boldsymbol{P_u}$ = Total factored applied tensile load (kip).
$\boldsymbol{\Xi_B}$ = Stress amplification factor for bending effect.
$\boldsymbol{\Xi_{VL}}$ = Stress amplification factor for shear lag effect.
$\boldsymbol{\sigma_{AFN\_NOM}}$ = The total factored tensile load divided by the net section area of the member in the faulted state (ksi).

The after-failure net section stress, f_{AFN}, was divided by σ_{AFN_FEA} to quantify error between them. This is shown in the last column of Table 4.5. Results agreed well with the finite element models when also incorporating plate position effects. Fourteen percent of the cases examined were slightly underestimated with the largest underestimation being 6%. The largest overestimate was 23%, and the second largest was 15%. The average underestimate was 3.7% and the average overestimate was 8%.

Finally, the method was applied to FEM W26, which was created using design drawings for the largest tension chord on the Liberty Bridge over the Monongahela River in Pittsburgh, PA, to determine if the proposed method would work on a very large member not included in the full parametric study used to develop the criteria. The cross-section of the chord is shown in Figure 4.19. The illustration on the left shows the failed component in black. The image on the right was taken from the finite element model where longitudinal stress contours are plotted and displacements are amplified 200x for illustrative purposes. Table 4.5 contains the results for the analysis showing that the method predicted the fatigue stress range for the large failed exterior plate of the Liberty Bridge within 4% of the finite element solution, which shows the adequacy of the developed procedures in characterizing load re-distribution in multi-component built-up members.

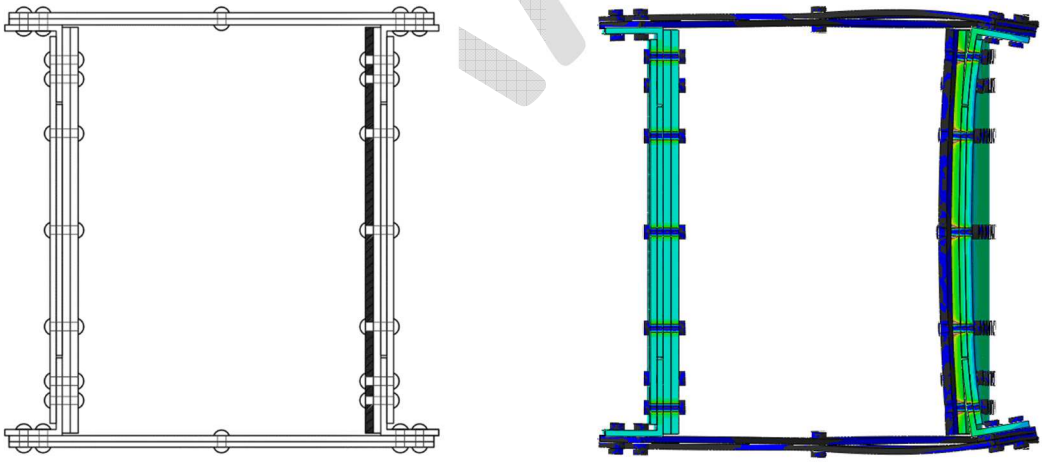

Figure 4.19 Liberty Bridge (FEM W26) cross-section; (Left) Illustration showing failed component in black, (Right) Longitudinal stress contours with displacements amplified 200x for illustration

Table 4.5 Stress amplification results for all multi-component models

Model ID	Type	Components Failed	Controlling Component	σ_{AFN_NOM} (ksi)	σ_{AFN_FEA} (ksi)	Ξ_{VL}	Ξ_B	f_{AFN} (ksi)	f_{AFN} / σ_{AFN_FEA}
W1/A1		Web, Angle	Angle	5.55	7.96		1.29	8.60	1.08
W2/A2		Web, Angle	Angle	5.55	7.96		1.29	8.60	1.08
W3/A3		Web, Angle	Angle	8.86	13.27		1.29	13.72	1.03
W4/A4		Web, Angle	Angle[1]	4.00	5.43		1.29	6.19	1.14
W5/A5		Web, Angle	Angle	8.86	13.88		1.29	13.72	0.99
W6/A6		Web, Angle	Angle	5.55	8.03		1.29	8.60	1.07
W7/A7		Web, Angle	Angle	5.55	7.76		1.29	8.60	1.11
W8/A8		Web, Angle	Angle	4.39	5.53		1.29	6.80	1.23
W9/A9		Web, Angle	Angle	5.07	7.71		1.29	7.85	1.02
W10/A10		Web, Angle	Angle	5.10	7.58		1.29	7.89	1.04
W11/A11		Web, Angle	Angle	4.68	6.08		1.24	6.97	1.15
W12		Web	Angle	5.57	8.24		1.29	8.63	1.02
W13		Web	Angle	4.10	5.65		1.24	6.10	1.08
W14		Web	Angle	4.22	5.65		1.24	6.28	1.11
W15	Channel	Ext. Web	Int. Full-Depth Web	3.32	4.15		1.19	4.74	1.14
W16		Int. Web	Partial-Depth Web	3.78	4.20	1.2	1.0[3]	5.39	1.08
W17		Web	Angle	3.71	5.47		1.24	5.53	1.01
W18		Web	Angle	5.55	8.20		1.29	8.60	1.05
W19		Ext. Web	Int. Full-Depth Web	3.78	5.16		1.19	5.39	1.04
W20		Int. Web	Int. Partial-Depth Web	3.53	3.96		1.0[3]	4.23	1.06
W21		Ext. Web	Int. Full-Depth Web	3.53	4.62		1.19	5.04	1.09
W22		Int. Web	Ext. Full-Depth Web	3.71	4.06		1.0[3]	4.45	1.09
W23		Ext. Web	Int. Full-Depth Web	4.46	6.61		1.19	6.36	0.96
W24		Rolled Channel	Full-Depth Web	7.04	9.76		1.24	10.47	1.07
W25		Ext. Web	Full-Depth Web	3.39	4.96		1.14	4.64	0.94
W26		Ext. Web	Int. Full-Depth Web	3.03	4.00		1.14	4.15	1.04
W27	Box	Web	Angle	3.74	5.45		1.24	5.56	1.02
W28		Web	Angle	3.74	5.83		1.24	5.56	0.95
W29	I-section	Web, Angle	Angle[2]	3.93	4.32		1.0[3]	4.71	1.09

Notes:

1. The angle failure case controlled the stress range in the faulted state for W4, which was 5.5 ksi using the "40 over fastener" rule. However, the calculation (with stress amplification factors) for the web failure case slightly exceeded it. Results in this table are from the web failure case.
2. The angle failure case controlled the stress range in the faulted state for W29. Result for the "40 over fastener" calculation was 5.0 ksi.
3. Failed component was positioned with redundant components on both sides making the bending factor go to 1.0

4.3. Methods Used for Parametric Study of Angle-Only Members

Localized behavior resulting from a single failed angle in members comprised primarily of only angles was examined using the Abaqus FEA software. Several three-dimensional member geometries were created and evaluated using linear elastic, static implicit analysis in which large deformation effects (finite strain theory) were included. All geometries were subjected to a gross-section axial tensile stress of 2 ksi away from the failure site using surface traction on the undeformed cross-section. 8-node linear continuum hexahedral elements with reduced integration and hourglass control (Abaqus designation C3D8R) were used with a structured hexahedral mesh. The global size of the mesh was 1/2 inch with higher density around the fastener holes and a minimum of four elements through the thickness of each component. Similar to the multi-component member parametric study, the mesh size of the fasteners approximately matched the mesh size used at the fastener hole edges. The typical mesh for the members and fasteners are as seen in Figure 4.1.

A linear elastic-isotropic plastic material model was defined for the fasteners, batten plates and angles having a modulus of elasticity of 29,000 ksi and Poisson's Ratio of 0.3; although strains never reached yield. Preload clamping force was assigned for each rivet of 5 kips, when needed. Based on work by Bonachera Martin (2014), the model was assigned general hard contact normal behavior and penalty tangential behavior with a friction coefficient of 0.25. This was also used in Hebdon's work. It was realized that due to the uniform bearing of the fasteners, the results were insensitive to preload and friction parameters, but they sometimes assisted with model convergence by disallowing rotation and slippage of the rivets. Hence, friction and fastener preload were utilized when needed to ease convergence of the analysis.

All fasteners were modeled as rivets, being sized to fill the entire hole, which was 7/8-inch in diameter. This forced the load transfer mechanism between components to be fastener bearing, which increases the bearing stresses at the edges of the holes. This is appropriate for riveted connections, which act primarily in shear. Based on results during the multi-component parametric study, models for the angle-only members were also created using half-symmetry boundary conditions at the location of the assumed failure saving computational cost.

Parameters included in the study of angle-only members were:

- Fixed and pinned boundary conditions
- Angle thickness

- Angle moment of inertia
- Number of fasteners connecting the angles together
- Centerline spacing of the fastener groups
- Gap between angles, *g* (four-angle members only)
- Spacer and batten plate thickness

Figure 4.20 Simple-span pony truss showcasing several angle-only member types

Similar to the multi-component members, there are probably as many geometric combinations for angle-only members as there are bridges that possess them. Hence, many of the parameters were evaluated by bounding the effect of the parameter. That is, if a parameter was determined to have an effect, it was explored further, if it did not, it was removed from further consideration. The study included several geometries made from 2 angles, aptly called "two-angle members", as well as several geometries comprised of 4 angles, suitably referred to as "four-angle members". Angle-only members typically are found on light trusses, such as short-span highway trusses, like that shown in Figure 4.20. More commonly they are used for hanger or diagonal members, but can also be used as tension chord members, such as the pony truss pictured in Figure 4.20. Angle-only members will generally be tied together using

intermittent batten plates (for four-angle members), spacer plates (for two-angle members), or lattice bars. Intermittent batten or spacer plates were used in this study, as well as one case where no spacer plate was used on a two-angle member geometry and the angles were riveted directly to each other. Figure 4.21 shows an example of a four-angle member where the batten plates can be seen spaced at approximately 2-ft. increments. While batten plates were used for the present parametric study, the behavior and methods derived from this study can also be used to evaluate members connected with lacing. The batten plates did not play a role in after-fracture load redistribution behavior. The angle-only member geometries evaluated in the parametric study ranged from 1/2 to 1 inch thick angles with leg lengths between 3-1/2 and 5 inches. Spacing between the angles varied for the two-angle members from 0 to 3 inches, and between 1 and 9 inches for four-angle members. Spacer plate thickness for two-angle members ranged from 0 to 3/8 inches. Batten plate thickness for four-angle members ranged from 3/8-inch to 7/8-inch. Table 4.6 provides all geometric combinations evaluated.

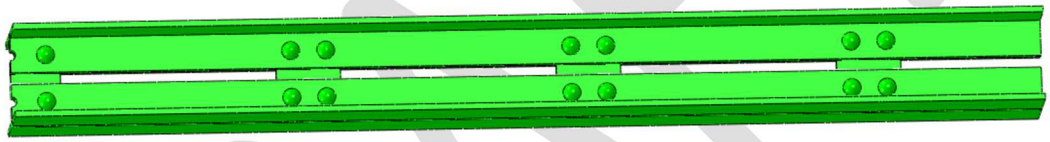

Figure 4.21 Side view of four-angle member showing intermittent batten plates

Table 4.6 Geometries for angle-only member models (dimensions are in inches)

Model ID	No. of Angles	Angle Thickness	Adj. Angle Leg Size	Outstand. Angle Leg Size	I_{faying}[1] (in^4)	Spacer or Batten Thickness	Fastener Group Spacing	No. of Fasteners per Group	Angle Gap, *g*
AM1	2	1/2	3-1/2	5	10	3/8	24	3	N/A
AM2	2	1/2	3-1/2	5	10	3/8	36	1	N/A
AM3	2	1/2	3-1/2	5	10	3/8	72	1	N/A
AM4	2	1/2	3-1/2	5	10	3/8	36	5	N/A
AM5	2	1/2	3-1/2	5	10	3/8	108	5	N/A
AM6	2	1	3-1/2	5	19.8	3/8	36	5	N/A
AM7	2	1/2	3-1/2	5	10	No spacer	36	3	N/A
AM8	2	3/4	3-1/2	5	13.9	3/8	36	5	N/A
AM9	2	1/2	3-1/2	3-1/2	3.63	3/8	36	5	N/A
AM10	2	1/2	3-1/2	5	10	3/8	163.5	3	N/A
AM11	2	1/2	3-1/2	5	10	3/8	163.5	3	N/A
AM12	2	1/2	3-1/2	5	10	3/8	163.5	3	N/A
AM13	4	1/2	3-1/2	5	10	3/8	24	3	1
AM14	4	1/2	3-1/2	3-1/2	3.63	3/8	24	3	1
AM15	4	3/4	3-1/2	5	13.9	3/8	36	5	1
AM16	4	1	3-1/2	5	19.8	3/8	36	5	1
AM17	4	1/2	3-1/2	5	10	3/8	24	3	9
AM18	4	1/2	3-1/2	5	10	3/8	24	3	4
AM19	4	1/2	3-1/2	5	10	3/8	24	3	3
AM20	4	1/2	3-1/2	5	10	3/8	108	3	1
AM21	4	1/2	3-1/2	5	10	3/8	24	3	2
AM22	4	1/2	3-1/2	5	10	3/8	50	3	1
AM23	4	1/2	3-1/2	5	10	7/8	24	3	4

Notes:

1. This is the moment of inertia for a single angle, relative to the direction of bending in the faulted state. This may be the weak or strong axis of the angle depending on the orientation of the angles within the structure.

4.4. Results for Parametric Study of Angle-Only Members

The following sections provide discussion and results for the finite element analysis parametric study that focused on angle-only members. As was observed for multi-component members discussed previously, load redistribution in angle-only members resulted in local stress amplifications due to shear lag and bending effects. Figure 4.22 provides an illustration of the localized behavior. A cross-section is shown from a built-up two-angle and four-angle member. The image plots longitudinal stress in the cross-section (in and out of the page). Any value at or below the remotely applied stress of 2 ksi is blacked out to help highlight stress amplification (note that this also includes compressive stresses). Red indicates a location of highest tensile stress concentration and blues are the lowest magnitude tensile stresses. Areas which are gray indicate stresses above 10 ksi. It can be seen that stresses are highest near fastener holes and through the thickness, nearest the failed component. Stress amplification above the theoretical axial stress of the faulted net cross-section was found to be caused by shear lag in the load transfer and local bending near the failure plane. These effects are discussed in greater detail in the following sections.

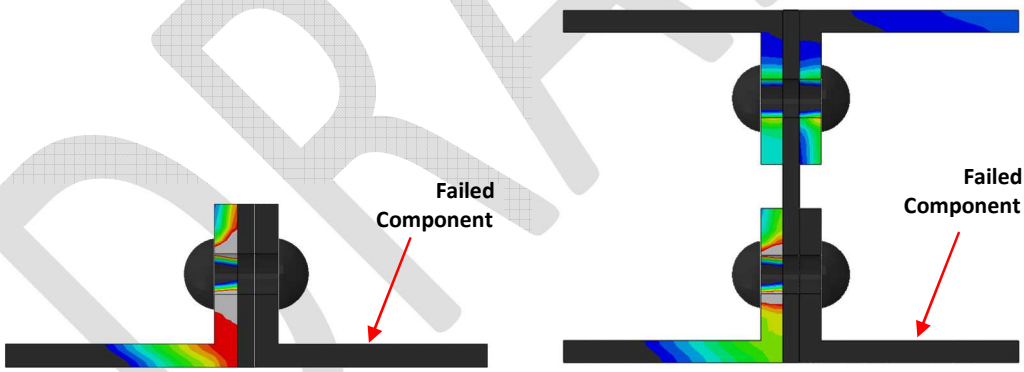

Figure 4.22 Examples of stress concentrations for two-angle and four-angle members

4.4.1. Effect of Boundary Conditions on Angle-only Members

The effect of boundary conditions for angle-only members with a failed component was evaluated by applying fixed and pinned boundary conditions on models of identical geometry. The boundary conditions were applied at the loading surface away from the failure plane. It was found that the effect of fixed vs. pinned boundary conditions was negligible, and in most cases nonexistent—meaning the

outputs were the same. Figure 4.23 illustrates an example of this showing two identical geometries that were evaluated, one with fixed and one with pinned boundary conditions; the solutions matched. Consequently, few models were repeated with pinned boundary conditions (the majority were evaluated with fixed boundary). However, several geometries were evaluated with both boundary conditions as a "spot check" to ensure that the effect remained insignificant throughout the study.

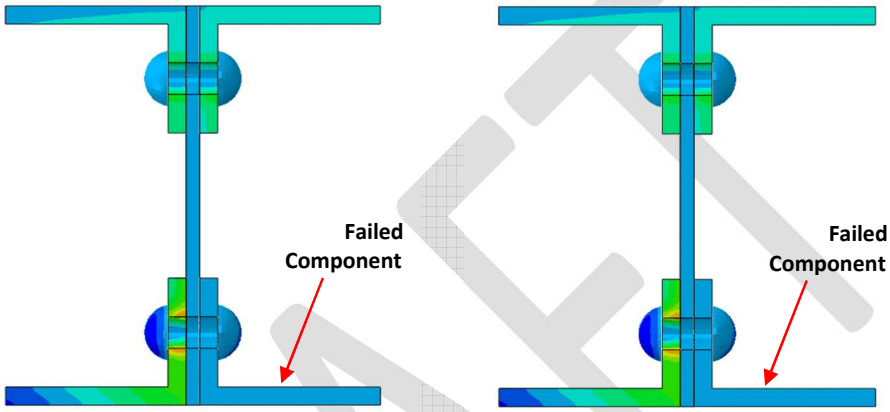

Figure 4.23 Side-by-side comparison results for fixed (Left) vs. pinned (Right) boundary conditions

The level of fixity at the angle-only member connections of a real bridge will likely vary from bridge to bridge, however, because angle-only members are relatively compliant members, it would be estimated that relative to the connections where multiple diagonals, floorbeams, and hangers come together at gusset plates, angle-only members would behave as if the boundary was fixed. This is meaning to say that determining the amount of fixity on an actual bridge is not necessary for angle-only members due to their relative flexibility, which is the primary conclusion from comparing boundary conditions within the parametric study.

4.4.2. Effect of Fastener Group Size on Angle-only Members

Fastener groups refers to the grouping of fasteners at a location where multiple angles are tied together by a batten plate or lattice bar. Fastener groups on angle-only members typically are two to three fasteners per location on actual bridges with battened angle-only members, or a single fastener at connection points for laced members. This parametric study looked at the effect that the number of fasteners in a single group would have on the bending and shear lag stress amplifications. The number of

fasteners in a group ranged from one fastener to five fasteners, as is shown in Figure 4.24. It was thought that conceptually a single fastener may have lower shear lag effects with higher bending effects, while the opposite could be true for five fastener groups where load transfer would occur over shorter distances increasing the effects of shear lag and reducing the effects of local bending. However, this parameter was found to have a negligible effect. The models evaluated had the same shear lag amplification and the bending factor only differed by less than 2%. The spacing between the groups was also considered, the results for which are discussed in Section 4.4.5.2.

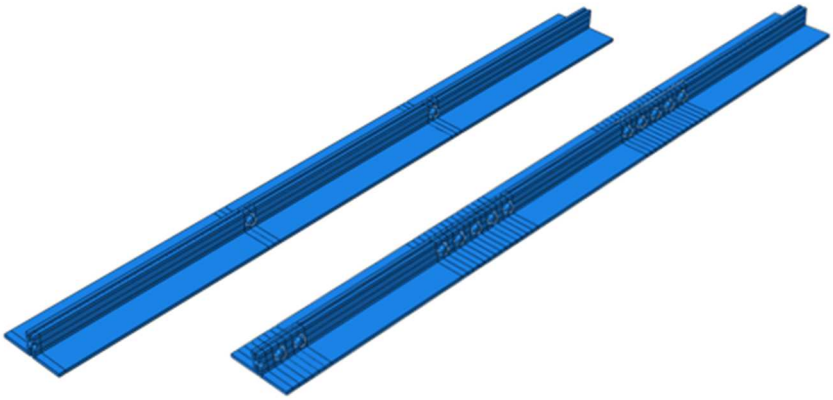

Figure 4.24 Two models showing range of fastener group sizes from 1 to 5 rivets

4.4.3. Effect of Spacer and Batten Plate Thickness on Angle-only Members

Generally a 3/8-inch plate was used for spacers and batten plates on bridges to separate the angles in a two-angle member or tie together the angle pairs of a four-angle member. These plates are intermittently spaced and are not load carrying components. However, it was studied to understand if varying the thickness of the plates, which increases the distance between load bearing components, would affect the shear lag-based or bending stress amplification. Two different cross sections for each of the two-angle and four-angle members were considered, representing differences in spacer and batten plate thicknesses of more than 2x. The cross sections are sketched in Figure 4.25 with the failed component hatched in black. Angle sizes were maintained consistent between members, varying only the distance between angles. AM2 had a 3/8-inch spacer plate and AM7 had no spacer plate. AM18 had a 3/8-inch batten plate and AM23 had a 7/8-inch batten plate.

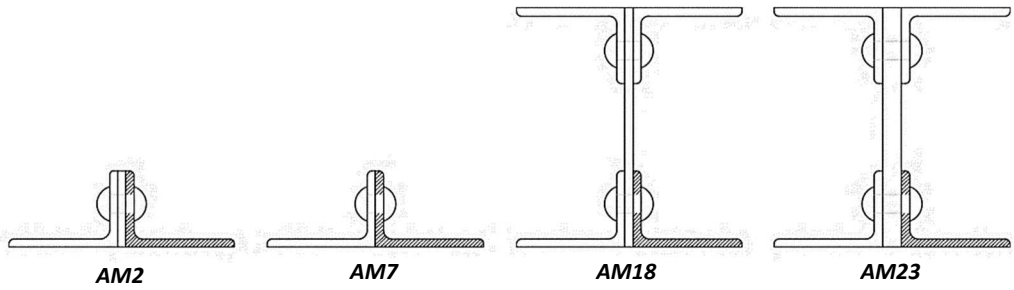

Figure 4.25 Geometries used to study thickness effect of the batten and spacer plates

It was found that more than doubling the batten or spacer plate thickness resulted in negligible stress output differences, on the order of less than 1%. The shear lag factor differed less than 2% between these models and the bending factor less than 1%. Therefore, the thickness of the plate or lattice bar has no impact on after-fracture net section stress and can be ignored.

4.4.4. Parameters Affecting Shear Lag in Angle-only Members

It was discussed in Section 4.2.4 that existing AASHTO and AISC shear lag procedures do not fully capture the behavior that takes place in mechanically built-up members in which a component has failed. The following segment of the parametric study was conducted to investigate shear lag in angle-only members with a failed component. Figure 4.27 illustrates the set of boundary conditions that were applied to several FEMs. Similar to analysis of the multi-component members, boundary conditions were applied to simulate a symmetry plane at the location of the failure, and fixed conditions were applied at the loading plane (released axial displacement during the load step of the analysis), and out-of-plane displacement of the angle outstanding legs was constrained at every fastener group along the length. The out-of-plane constraints removed bending effects in the stress solutions isolating stress amplification to the effects of shear lag.

Figure 4.28 illustrates the geometries studied for two-angle members, ranging from 1/2 to 1-inch thick angles, 3-1/2 to 5-inch angle legs, and 0 to 3/8-inch spacer plates. Figure 4.29 illustrates the geometries studied for four-angle members, ranging from 1/2 to 1-inch thick angles, 3-1/2 to 5-inch angle legs, 3/8 to 7/8-inch batten plates, and 1 to 9-inch gaps between angle pairs. The failed components are hatched in black. AM13, AM20 and AM22 appear to have the same geometry in Figure 4.29. This is true except for the centerline spacing of the fastener groups, S_{FG}, which was varied between these models

from 24 inches for AM13, to 50 inches and 108 inches for AM 22 and AM20, respectively. Table 4.7 lists the models and each component in the analysis.

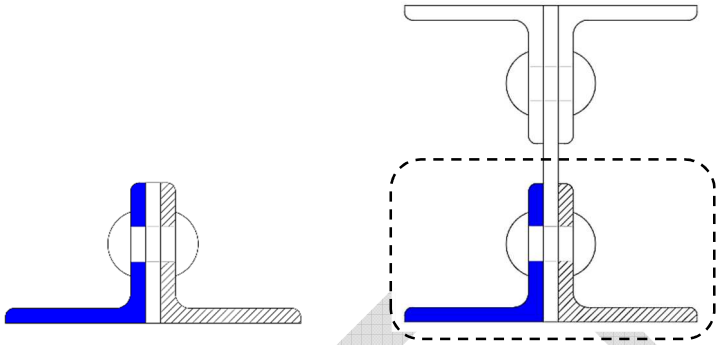

Figure 4.26 Net section areas used to calculate the nominal after-fracture net section stress, σ_{AFN_NOM}, shown in solid blue

A nominal theoretical net section stress in the faulted state, σ_{AFN_NOM}, was calculated by dividing the applied load by net area of the member in the faulted state. The faulted net area was simply the net area of the member in the unfaulted state, less the net area of the failed component. Figure 4.26 illustrates the net areas used for this calculation. For two-angle members the entire load in the member was divided by the net area of the faulted member, which is highlighted in solid blue (the failed angle is hatched in black diagonal lines). For four-angle members, the load in the member was halved before dividing by the faulted net area, which is highlighted in solid blue on the right side of Figure 4.26, within the dashed line. This was done because each pair of angles carried half of the entire load independently of the other half of the member, even in the faulted condition. This same type of behavior was observed for multi-component members.

Table 4.7 contains the results from the finite element analysis, listed under σ_{AFN_FEA}. This was found by integrating the nodal forces of the area in question and dividing by the net area of the same. The area integrated for angles was the connected leg, including the thickness of the outstanding leg. The final column in the table is *Ratio*. *Ratio* refers the quotient of the σ_{AFN_FEA} to the σ_{AFN_NOM}, indicating the level of local stress increase in the components due to shear lag. The shear lag ratio from each member was averaged for the two types of angle-only members. The two-angle member average shear lag factor equaled 1.28. The average shear lag factor for four-angle members was 1.26. Finally, the average was conservatively rounded to the nearest tenth for both cases, making them each 1.3.

Although the averages for the two types of members were very similar, the range of shear lag factor results, as well as the standard deviation for each, differed notably. The range of values for the two-angle member was from 1.19 to 1.31, equaling a span of 0.12 (9% of the average). The range of values for the four-angle member was from 1.12 to 1.71, equaling a span of 0.59 (45% of the average). The standard deviation for two-angle members was 0.04 and for four-angle members it was 0.16. This was not altogether unwarranted when considering that four-angle members have a wider range of parameters than two-angle members. Based on these results, it was expected that application of the shear lag factor in evaluating two-angle geometries would provide a reasonably accurate result. However, for four-angle members the potential existed that the stress amplification resulting from shear lag effects could be unreasonably over or underestimated if a constant shear lag value were to be used for all geometries. The potential inaccuracy was resolved by combining the stress amplification effects of shear lag and bending for four-angle members and normalizing by the computed average shear lag factor. This process is discussed in greater detail in Section 4.4.5.2.

Qualitatively, it was observed that the four-angle members with angle gap dimensions of 1 inch resulted in a lower shear lag factor, averaging closer to 1.15. As the geometries became taller (increasing the gap between angle pairs), it was noted that the shear lag factors increased. The average shear lag factor for geometries with angle gap dimensions greater than 1 inch more closely resembled that of two-angle members, with the tallest geometry, AM17, equaling the two-angle shear lag factor average exactly. This behavior was logical considering that as the angle pairs became farther apart, the behavior approached that of two independent two-angle members. This was not the case, however, for bending factors, which are discussed below. The greatest shear lag effect resulted for geometry having a larger centerline spacing of the fastener groups, S_{FG}. It was primarily the larger S_{FG} geometries that increased the overall shear lag factor average, as well as the range of results. S_{FG} is explained further in Section 4.4.5.2.

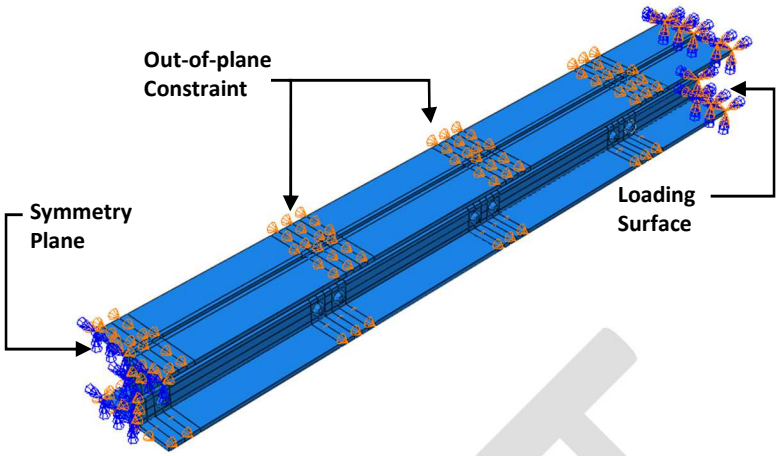

Figure 4.27 Example of boundary conditions applied to models

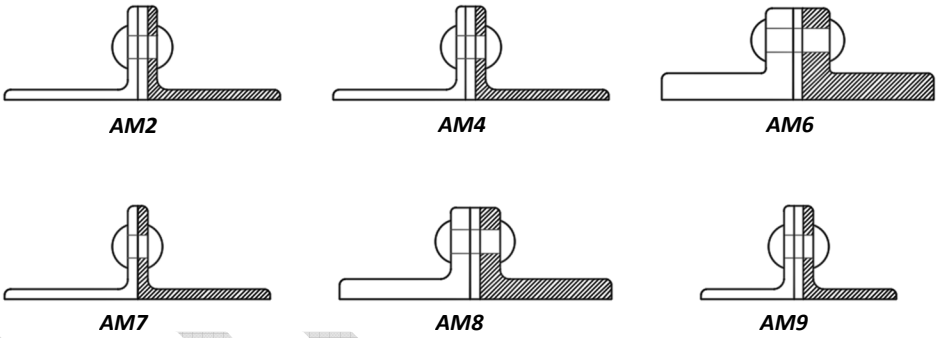

Figure 4.28 Geometries used to study shear lag effect in two-angle members

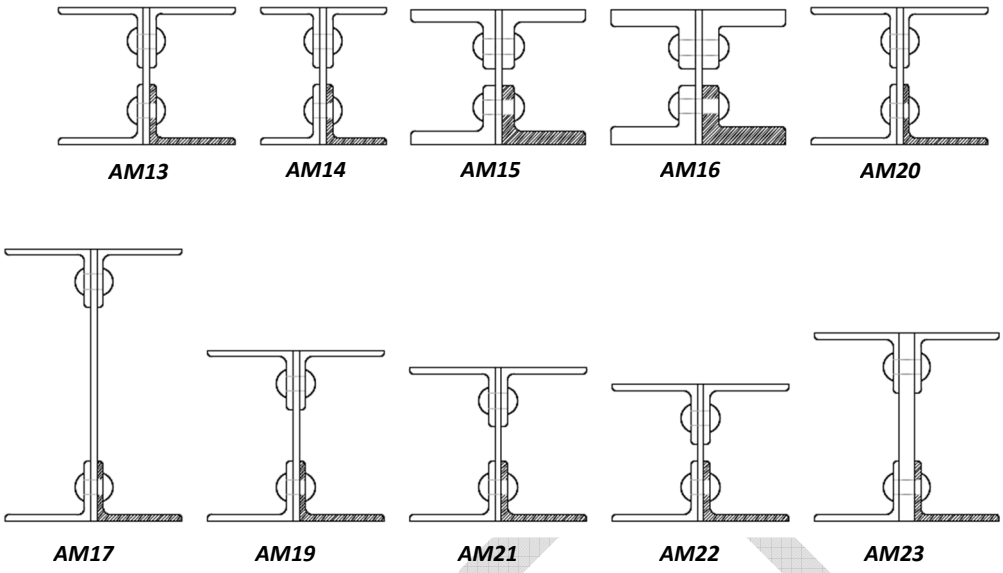

Figure 4.29 Geometries used to study shear lag effect in four-angle members

Table 4.7 Component stress results used for shear lag factor for angle-only members

Model ID	No. of Angles	Component Failed	Component Evaluated	σ_{AFN_NOM} (ksi)	σ_{AFN_FEA} (ksi)	Ratio
AM2	2	1 angle	Adjacent angle	4.49	5.81	**1.29**
AM4	2	1 angle	Adjacent angle	4.49	5.79	**1.29**
AM6	2	1 angle	Adjacent angle	4.53	5.85	**1.29**
AM7	2	1 angle	Adjacent angle	4.49	5.87	**1.31**
AM8	2	1 angle	Adjacent angle	4.51	5.78	**1.28**
AM9	2	1 angle	Adjacent angle	4.62	5.52	**1.19**
AM13	4	1 angle	Adjacent angle	4.49	5.30	**1.18**
AM14	4	1 angle	Adjacent angle	4.62	5.20	**1.12**
AM15	4	1 angle	Adjacent angle	4.51	5.21	**1.16**
AM16	4	1 angle	Adjacent angle	4.53	5.10	**1.13**
AM17	4	1 angle	Adjacent angle	4.49	5.74	**1.28**
AM19	4	1 angle	Adjacent angle	4.49	5.48	**1.22**
AM20	4	1 angle	Adjacent angle	4.49	7.70	**1.71**
AM21	4	1 angle	Adjacent angle	4.49	5.42	**1.21**
AM22	4	1 angle	Adjacent angle	4.49	6.01	**1.34**
AM23	4	1 angle	Adjacent angle	4.49	5.56	**1.24**
Average of Maximum for two-angle Member:						**1.28**
Average of Maximum for four-angle Member:						**1.26**

4.4.5. Parameters Affecting Local Bending in Angle-only Members

Figure 4.30 shows a typical example of each of the two and four-angle members evaluated as part of the parametric study. The figure shows section cuts that were taken at the failure plane. Longitudinal stresses are plotted on the deformed shape with the undeformed shadow shapes for reference. The deformations have been amplified 15x in order to exaggerate them for visual clarity. Figure 4.30 is meant to illustrate the general behavior of the angle-only members in the faulted condition. Deflections were always toward the failed component, which was a result of the local load redistribution around the failure plane. The load path out of the failed component, into the adjacent component, and then back into the failed component formed a locally eccentric load path in the connected angle leg that when put into tension attempted to straighten, bending the member toward the failure plane. In the case of the two-angle members (left side of Figure 4.30) this generally resulted in lateral deflections, but sometimes also produced a slight rotation of the member. A torsional-like rotation was more defined in the four-angle members, such as seen on the right side of Figure 4.30. This was caused by the asymmetry of the faulted cross section where locally at the failure plane the out-of-plane flexure caused by the load redistribution was being resisted by three asymmetric angles that together made up an asymmetric cross section.

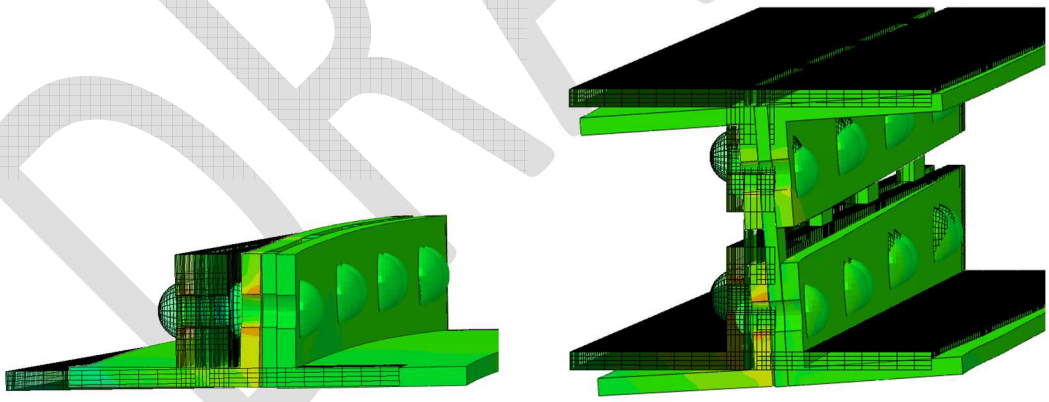

Figure 4.30 FEM images showing the bending in angle-only members resulting from failure of a single angle (deformation amplified 15x)

The controlling stress range in the member was always located in the connected leg of the angle adjacent to the failed angle where the contours of yellow and orange can be observed. This was also the case for two-angle members. While this comparison of member behavior between the two and four-

angle members is somewhat qualitative, it is meant to demonstrate that the response to a failed angle differed and it was found that bending factors were better correlated to different parameters, as is explained in the following sections.

4.4.5.1. Effect of Angle Thickness and Moment of Inertia

The thickness of the angles was investigated and initially found that as the angles became thicker, the bending effect increased. This was logical considering that by simply making the angle thicker, more gross area equated to more load that must be redistributed around the failure plane, which produced larger bending effects in the member. Thick angles also meant larger eccentricities between adjacent angle legs, which would also increase bending effects. This correlation was found to be true for two-angle and four-angle members. However, once differing moments of inertia were introduced while maintaining thickness constant, the correlation to thickness no longer held; meaning members having angles of the same thickness, but with different moments of inertia were found to have different results. Hence, angle thickness parameter was no longer considered. The moment of inertia of a single angle provided a good correlation for all cases of the two-angle members, but not as significant of a correlation for four-angle members resulting in a separate bending factor for each type of angle-only member. The single angle moment of inertia for two-angle members is referred to as I_L and is described in greater detail below. Table 4.8 lists the geometries used to develop the two-angle member bending factor. The final column of this table, *Ratio*, is the quotient of *Unbraced* σ_{AFN} to *Braced* σ_{AFN}, representing the stress increase in the finite element solution over the nominal calculated net section stress. By deriving the bending factor from a ratio of the stress resulting from the braced and unbraced model of identical geometry, the shear lag effects were identical between them and therefore became effectively cancelled. Hence, this ratio isolated the effects of localized bending in the adjacent component.

Table 4.8 Component stress results used for bending factor for two-angle members

Model ID	No. of Angles	I_L[1] (in^4)	Batten g/t Ratio	Component Failed	Component Evaluated	Unbraced σ_{AFN} (ksi)	Braced σ_{AFN} (ksi)	Ratio
AM2	2	10	-	1 angle	Adjacent angle	9.30	5.81	**1.60**
AM4	2	10	-	1 angle	Adjacent angle	9.17	5.79	**1.58**
AM6	2	19.8	-	1 angle	Adjacent angle	10.36	5.85	**1.77**
AM7	2	10	-	1 angle	Adjacent angle	9.33	5.87	**1.59**
AM8	2	13.9	-	1 angle	Adjacent angle	9.87	5.78	**1.71**
AM9	2	3.63	-	1 angle	Adjacent angle	8.23	5.52	**1.49**

Notes:

1. This is the moment of inertia for a single angle relative to the direction of bending in the faulted state. This may be the weak or strong axis of the angle depending on the orientation of the angles within the structure.

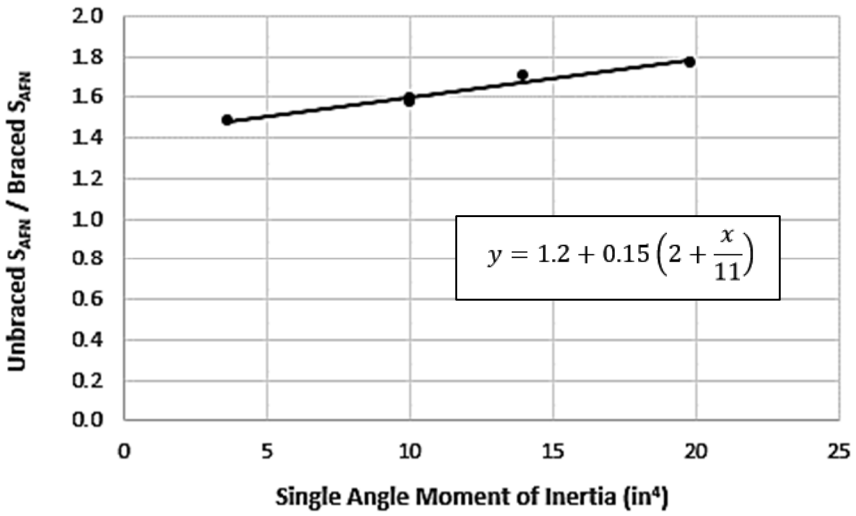

Figure 4.31 Ratios of Unbraced to Braced longitudinal after-fracture net section stress for two-angle Members

Figure 4.31 plots all *Ratio* data from Table 4.8 as a function of the moment of inertia of the remaining intact angle for the two-angle members. A line was fit to the data points using linear regression analysis. Note that all data points are present, but several plotted on top of each other. Equation 4.4 is the equation of the line, which can be used to account for the local stress increase due to bending after failure of an angle in two-angle members.

$$\Xi_B = 1.2 + 0.15\left(2 - \frac{I_L}{11in^4}\right) \quad (4.4)$$

Where:

$\boldsymbol{\Xi_B}$ = Fatigue stress range amplification factor accounting for localized bending effect in a built-up two-angle axial member in the faulted state.

$\boldsymbol{I_L}$ = Moment of inertia for a single angle relative to the direction of bending in the faulted state (in^4).

The moment of inertia used in Equation 4.4 is that of a single angle relative to the principal axis of the intact angle in the direction of bending in the faulted state. This may be the weak or strong axis of the angle, depending on the orientation of the angles within the structure. This is not the moment of inertia of the angle relative to any member centroidal axis. For example, consider Figure 4.32 where the same angles are arranged in different orientations in the two member cross sections. When an angle fails (failed angles are hatched in black), the intact angle will deflect in the direction of the failed angle. This was described previously referencing Figure 4.30. In this case, the members would both be expected to deflect out-of-plane to the right hand side of the page. The principal axis of bending for both cases would be the blue Y-Y axis, which correlates to the strong axis of bending for the case on the left and the weak axis of bending for the case on the right. When using Equation 4.4 to calculate the bending stress amplification, the orientation of the angles within the member should be considered so that the correct moment of inertia is input.

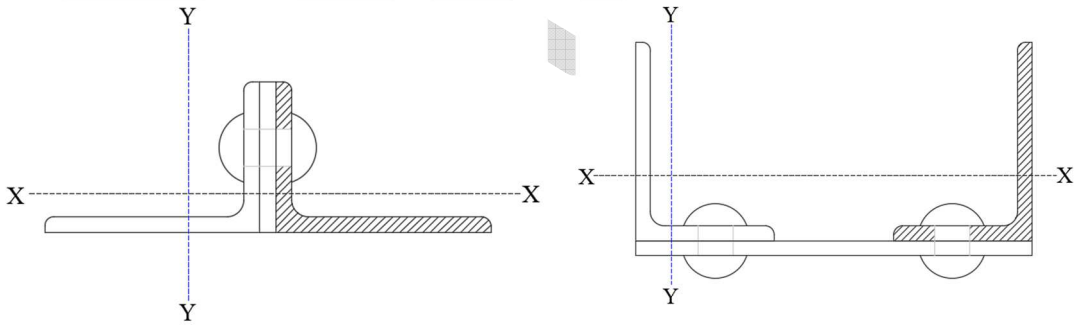

Figure 4.32 Illustrations of principal axes of angles used to determine the bending factor as a function of the intact angle moment of inertia

4.4.5.2. Effect of Angle Gap and Fastener Group Spacing

The dimensions of angle-only members referred to herein as the angle gap and fastener group spacing were studied for their effects on stress outputs in the faulted state. Figure 4.33 is a typical four-angle member depicting the angle gap, *g*, and fastener group spacing, S_{FG} parameters. Clearly the angle gap parameter would not be considered for two-angle members. The angle gap is the length of exposed batten plate between angle legs of the two angle pairs. S_{FG} is the longitudinal distance between the *centerlines* of the intermittent groups of fasteners that are used to tie the angle pairs together via batten plates; not to be confused with the distance between the end of one fastener group and the beginning of another. S_{FG} was found to have no effect on the bending factor for two-angle members, likely due to the characteristic flexibility of this type of member. For example, Model AM3 doubled the fastener group spacing of AM2 and model AM5 tripled the fastener group spacing of AM4, each without affecting the outcomes. S_{FG} was found, however, to affect the bending factor for four-angle members. The angle gap, *g*, was also found to correlate well with the bending factors of four-angle members. Table 4.9 lists the pertinent geometries varied on the models used to investigate these parameters, as well as the outcomes. The second-to-final column of the table, *Ratio*, is the quotient of *Unbraced* σ_{AFN} to *Braced* σ_{AFN}, representing the stress increase in the component without the effect of shear lag. The final column of the table is explained below.

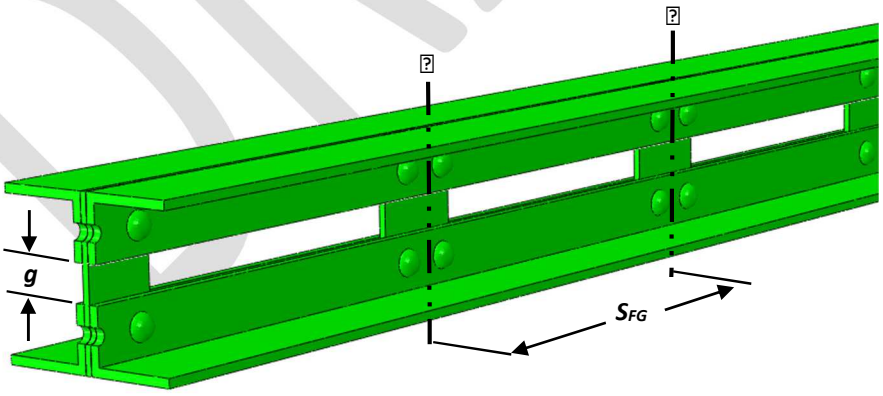

Figure 4.33 Illustration showing the four-angle member dimensions, g and S_{FG}

Table 4.9 Component stress results used for bending factor for four-angle members

Model ID	No. of Angles	Angle Gap, *g*(in)	S_{FG} (in)	Component Failed	Unbraced σ_{AFN} (ksi)	Braced σ_{AFN} (ksi)	Ratio	Normalized Ratio
AM13	4	1	24	1 angle	7.75	5.30	**1.46**	**1.33**
AM14	4	1	24	1 angle	7.05	5.20	**1.36**	**1.17**
AM15	4	1	36	1 angle	7.22	5.21	**1.38**	**1.23**
AM16	4	1	36	1 angle	6.76	5.10	**1.32**	**1.15**
AM17	4	9	24	1 angle	9.18	5.74	**1.60**	**1.57**
AM19	4	3	24	1 angle	8.34	5.48	**1.52**	**1.43**
AM20	4	1	108	1 angle	8.83	7.70	**1.15**	**1.51**
AM21	4	2	24	1 angle	8.07	5.42	**1.49**	**1.38**
AM22	4	1	50	1 angle	8.23	6.01	**1.37**	**1.41**

It was reported in Section 4.4.4 that the range of shear lag values for the four-angle member was from 1.12 to 1.71, equaling a span of 0.59 (45% of the average), and that the standard deviation was 0.16. It was estimated that due to a small range over which the two-angle member shear lag factors fell, evaluating other two-angle geometries using a constant shear lag value would be expected to provide a reasonably accurate result. Yet, for four-angle members the potential existed that the stress amplification resulting from shear lag effects could be unreasonably over or underestimated—if a constant shear lag value were to be used for all geometries. In order to maintain a constant shear lag value and variable bending factor, similar to approaches developed for two-angle and multi-component built-up members, the bending amplification factor was normalized by the average shear lag factor. This was done by taking the bending factor for each geometry, which is the ratio of the *Unbraced* σ_{AFN} to *Braced* σ_{AFN}, times the respective shear lag factor, all of which was divided by the average four-angle member shear lag factor of 1.3. This calculation is shown in Equation 4.5 and the results are reported in Table 4.9 under *Normalized Ratio*.

$$Normalized\ Bending\ Amplification = \frac{\left(\frac{Unbraced\ S_{AFN}}{Braced\ S_{AFN}}\right) \cdot \Xi_{VL}}{\Xi_{VL\_AVG}} \tag{4.5}$$

In the final calculation of the after-fracture net section stress, the shear lag and bending factors are multiplied together. Thus, normalizing the bending factors in this way simply performed this multiplication of factors preemptively, and then normalized to a common shear lag value. The normalized bending factors were plotted with respect to the angle gap, *g*. This is shown in Figure 4.34. Regression

analysis was used to fit a line to the maximum data values and an equation was derived for that line, which can be seen on the same figure. The correlation of bending to the angle gap dimension was such that as the angle gap became larger, the bending factor increased. This was similar to shear lag results, where it was seen that when *g* became sufficiently large the outcomes approached that for two-angle members suggesting that the angle pairs of the four-angle members had become effectively independent of each other. At the largest *g* values evaluated, the bending factor became very similar quantitatively to the two-angle member factors. This behavior persisted even when the batten plate for the four-angle member was more than doubled in thickness.

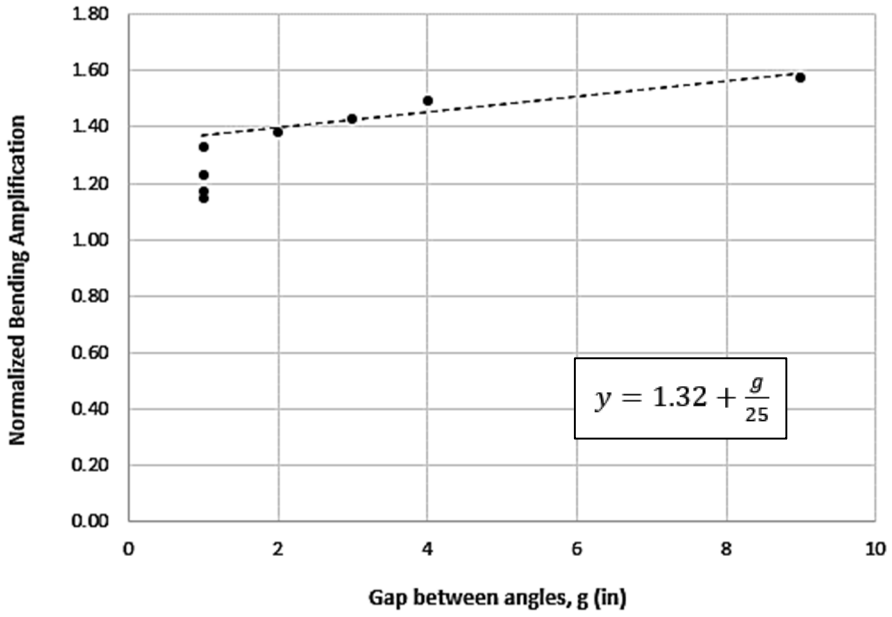

Figure 4.34 Normalized ratios of unbraced to braced longitudinal after-fracture net section stress for four-angle members

Once the bending factors were derived as a function of *g*, it was realized that the net section stresses for members having the largest fastener group spacing were still being underestimated by as much as 15%. This margin may be acceptable, especially when considering the level of conservatism that is involved with this entire methodology that uses lower bound resistance and upper bound demands at several steps throughout the faulted state fatigue life estimation. Nevertheless, a reasonable and simple adjustment to the four-angle member bending factor that accounts for S_{FG} was derived. This was done by taking the bending factor for an angle gap of 1 inch and fastener group spacing of 24 inches, considered

the baseline geometry for this comparison, and subtracting them from all other bending factors of similar geometry and varying fastener group spacing. These data were plotted in Figure 4.35 where the vertical axis is the normalized bending factor minus the baseline factor for spacing of 24 inches and the horizontal axis is the adjusted fastener group spacing—which is the S_{FG} minus the baseline 24 inches. The slope of the line was used to derive the adjustment to the bending factor as a function of fastener group spacing greater than 24 inches.

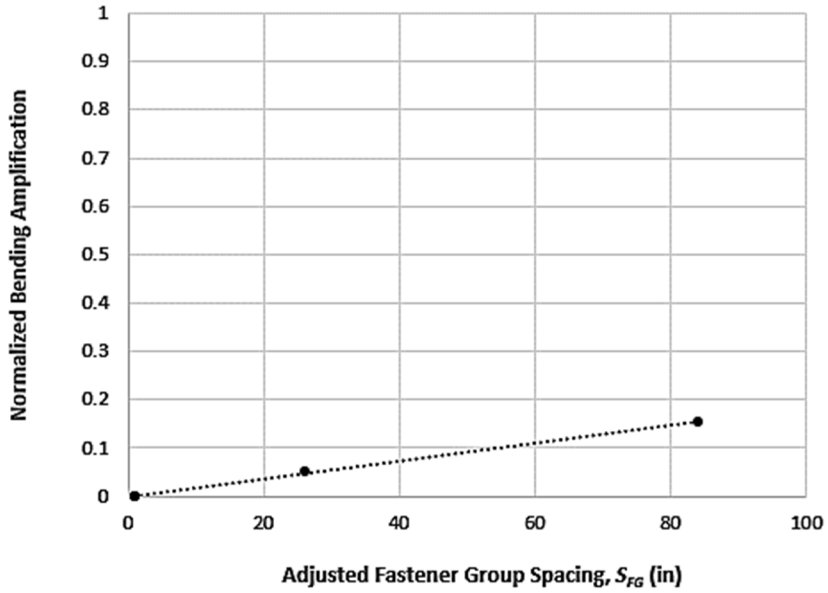

Figure 4.35 Effect of fastener group spacing on four-angle members

The slope of the line shown in Figure 4.35 was found to equal approximately 1/500. This adjustment can simply be added to the bending factor developed from the angle gap, g. Equation 4.6a and 4.6b show the final bending factor equations for four-angle members, accounting for the angle gap and fastener group spacing.

If $S_{FG} \leq 24$ inches, then

$$\Xi_B = 1.32 + \frac{g}{25in} \tag{4.6a}$$

If $S_{FG} > 24$ inches, then

$$\Xi_B = 1.32 + \frac{g}{25in} + \frac{(S_{FG} - 24in)}{500in} \quad (4.6b)$$

Where:

$\boldsymbol{\Xi_B}$ = Fatigue stress range amplification factor accounting for localized bending effect in a built-up four-angle axial member in the faulted state.

$\boldsymbol{S_{FG}}$ = Fastener group spacing taken as the longitudinal distance between centerlines of the intermittent groups of fasteners that are used to tie the angle pairs together via batten plates (in). (See Figure 4.33).

$\boldsymbol{g}$ = Angle gap taken as the length between angle legs of two angle pairs that make up a four-angle member (in). (See Figure 4.33).

4.4.6. Validation Exercise: Simplified Analysis of Angle-only Members

Results for bending and shear lag factors explained above were applied to all angle-only member geometries listed in Table 4.6. The resulting after-fracture net section stress for each case was compared to the corresponding FEA results. The controlling resultant stress range was always the adjacent angle in direct contact with the failed component. More specifically, the angle *leg* in direct contact with the failed angle was found to carry between 85 and 100 percent of the redistributed load, for the fatigue loads applied.

Due to the fact that all redistributed load was carried by the neighboring angle, the net area of a four-angle member used to calculate the nominal axial stress in the faulted state, σ_{AFN_NOM}, only included the half of the member possessing the assumed failed component, less the area of the failed component. An example of this is shown in Figure 4.26. Equation 4.3 is used for the calculation of σ_{AFN_NOM} for four-angle members. Since each half of the unfaulted four-angle member carried half of the full axial load, the full axial load was divided by two. Equation 4.7 was used for the calculation of σ_{AFN_NOM} for two-angle members, which does not divide the full axial load in half.

σ_{AFN_FEA} in Table 4.10 was the stress obtained from FEA by integrating nodal forces in the area of interest, divided by that same net area. The appropriate shear lag factor, Ξ_{VL}, and bending factor, Ξ_B, were also listed in the table. Ξ_B was calculated using Equation 4.4 for two-angle members and Equation 4.6 for four-angle members. The after-failure net section stress, f_{AFN}, was calculated using Equation 4.7 for two-angle members and Equation 4.3 for four-angle members.

$$f_{AFN} = \Xi_B \Xi_{VL} \sigma_{AFN\_NOM} = \Xi_B \Xi_{VL} \frac{P_u}{A_{AFN}} \quad (4.7)$$

Where:

$\boldsymbol{A_{AFN}}$ = Net section area of the member in the faulted state. This is equal to the area indicated in **Figure 4.17**, minus the net area of the failed component (in^2).
$\boldsymbol{f_{AFN}}$ = Factored total net section stress in the faulted state (ksi).
$\boldsymbol{P_u}$ = Total factored applied tensile load (kip).
$\boldsymbol{\Xi_B}$ = Stress amplification factor for bending effect.
$\boldsymbol{\Xi_{VL}}$ = Stress amplification factor for shear lag effect.
$\boldsymbol{\sigma_{AFN\_NOM}}$ = The total factored tensile load divided by the net section area of the member in the faulted state (ksi).

The after-fracture net section stress, f_{AFN}, was divided by σ_{AFN_FEA} to quantify error between them. This is shown in the last column of Table 4.10. Results agreed well with the finite element models when also incorporating S_{FG} effects in four-angle members. Thirteen percent of cases were slightly underestimated with the largest underestimation being only 3%. The largest overestimate was 21%, and the second largest was 16%. The average underestimate was 1.7% and the average overestimate was 5.1%.

Finally, the method was applied to FEM AM12 & AM18 to attempt the proposed factors on typical member geometries not included in any portion of the parametric study used to develop the amplification factors. The cross-section of AM12 is shown in Figure 4.36 and AM18 in Figure 4.37. The illustrations on the left show the failed component in black. The images on the right of each figure were taken from the finite element models where longitudinal stress contours were plotted and displacements were amplified for illustrative purposes. Table 4.10 contains the results for the analyses showing that the method predicted the fatigue stress range for AM12 and AM18 to within 1% of the finite element solution, which shows the adequacy of the developed procedures in characterizing load re-distribution in angle-only built-up members.

Table 4.10 Stress amplification results for all angle-only member models

Model ID	No. of Angles	σ_{AFN_NOM} (ksi)	σ_{AFN_FEA} (ksi)	Ξ_{VL}	Ξ_{B}	f_{AFN} (ksi)	f_{AFN} / σ_{AFN_FEA}
AM1	2	4.49	9.84	1.3	1.64	9.55	0.97
AM2	2	4.49	9.30	1.3	1.64	9.55	1.03
AM3	2	4.49	9.30	1.3	1.64	9.55	1.03
AM4	2	4.49	9.17	1.3	1.64	9.55	1.04
AM5	2	4.49	9.17	1.3	1.64	9.55	1.04
AM6	2	4.53	10.36	1.3	1.77	10.42	1.01
AM7	2	4.49	9.33	1.3	1.64	9.55	1.02
AM8	2	4.51	9.87	1.3	1.69	9.90	1.00
AM9	2	4.62	8.23	1.3	1.55	9.31	1.13
AM10	2	4.19	8.15	1.3	1.55	8.47	1.04
AM11	2	4.19	8.15	1.3	1.55	8.47	1.04
AM12	2	4.49	8.53	1.3	1.55	8.47	0.99
AM13	4	4.49	7.75	1.3	1.35	7.86	1.02
AM14	4	4.62	7.05	1.3	1.35	8.09	1.16
AM15	4	4.51	7.22	1.3	1.35	7.89	1.12
AM16	4	4.53	6.76	1.3	1.35	7.93	1.21
AM17	4	4.49	9.18	1.3	1.56	9.11	1.07
AM18	4	4.49	8.53	1.3	1.43	8.33	1.01
AM19	4	4.49	8.34	1.3	1.40	8.17	1.01
AM20	4	4.49	8.83	1.3	1.35	8.97	1.01
AM21	4	4.49	8.07	1.3	1.37	8.02	1.01
AM22	4	4.49	8.23	1.3	1.35	8.37	1.00
AM23	4	4.49	8.73	1.3	1.37	7.97	0.99

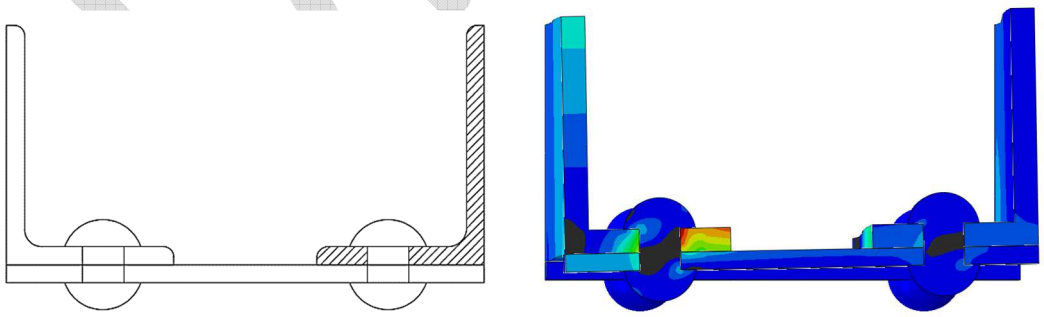

Figure 4.36 FEM AM12 cross-section; (Left) Illustration showing failed component in black hatch, (Right) Longitudinal stress contours in faulted state

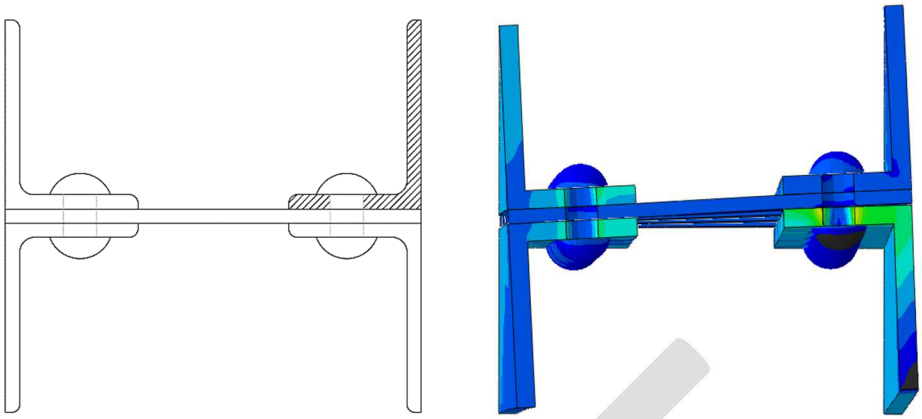

Figure 4.37 FEM AM18 cross-section; (Left) Illustration showing failed component in black hatch, (Right) Longitudinal stress contours with displacements amplified 10x for illustration

4.5. Methods Used for Parametric Study of Two-Channel Members

Global behavior of two-channel type members resulting from a single failed component was examined using Abaqus software suite. This parametric study differed from the multi-component and angle-only member studies in that rather than localized behaviors at individual fasteners near failure planes where load transfer between components was the primary source of stress amplification, global behaviors resulting in second order moments were the primary cause of stress increase in the unbroken component.

4.5.1. Two-Channel Member FEM Calibration and Specifications

Finite element models for the two-channel member parametric study were calibrated using lab benchmark test data from Specimen 6 and 7, the Winona Bridge tension chord specimens. Following FEM calibration, numerous three-dimensional member geometries were created and evaluated using linear elastic, static implicit analysis in which large deformation effects (finite strain theory) were included. The geometries studied included stay-plated members and double-latticed members with the intersection of the lattice bars connected. All geometries were subjected to concentrated axial tensile loads away from the failure site using reference points and kinematic coupling constraints. Plates and channels were modeled using four-node doubly curved shell elements with reduced integration and hourglass control (Abaqus designation S4R) and a structured quadrilateral mesh. The global size of the mesh size was 1/2 inch with five integration points through the thickness of the shells (Simpson integration rule). Lattice

bars were modeled using two-node linear beam elements (Abaqus designation B31) with a 1-1/2-inch mesh size. A shell element mesh convergence study was performed halving the mesh density (1-inch elements), and then doubling the mesh density (1/4-inch elements) at locations adjacent to the failure sites. It was found that the results were insensitive to the mesh size up to at least 1 inch. However, the 1/2-inch element size facilitated the integration of nodal forces at locations of interest without significant increase in computational cost. Figure 4.38 is zoomed in on a gusset plate connection on the 60-foot long Winona Bridge specimen showing a typical mesh for the models. The geometries of the rivets were not explicitly modeled, although non-linear connector elements were initially utilized, which were calibrated to single fastener shear test data obtained from Ocel (2013), he stress outcomes did not change significantly in comparison to simpler approaches, and hence the use of connector elements was not carried forward into the parametric study. Rather, plates and channels were connected using surface-to-surface tie constraints. Lattice bars were connected to channel flanges and at center points of lattice bar intersections using kinematic tie coupling constraints that allowed rotation about what would be the fastener longitudinal axis.

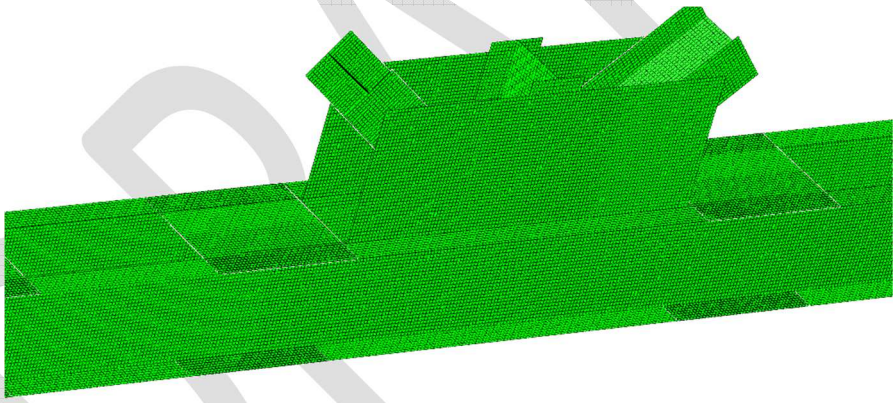

Figure 4.38 Typical 1/2-inch shell element mesh used for FEM validation and two-channel member parametric study

For the benchmark FEM, an elastic-plastic isotropic material was defined for the channels and plates having a yield strength of 40.5 ksi—equal to the actual cover plate yield strength of Specimen 6 and 7 (material test results are presented in Section 3.1.9.1). The modulus of elasticity was defined as 29,000 ksi and a Poisson's Ratio of 0.3. Following calibration of the shell element models, the material definition was simplified to linear-elastic for the parametric study.

Data collected during the laboratory testing of Specimen 6 and 7 were compared to the benchmark finite element model to calibrate the model parameters and ensure accurate solutions. Strain, load, and displacement sensors used during the experimental testing provided data for comparison. Figure 4.39 and Figure 4.40 show load-displacement curves for each of the specimens compared to load-displacement results obtained from the benchmark FEM. While the load-displacement relationship was not necessarily the output of interest for purposes of the parametric study, it was considered a useful indicator of overall behavior and response to load in comparison of the laboratory test results to the FEM results. Figure 4.39 plots data for Specimen 7, where the member was cut at location "B", between the gusset plate and end stay plate. Several elastic load cycles were applied, followed by two large load cycles resulting in permanent plastic deformation. It can be seen in Figure 4.39 that the FEM results compared relatively well with the laboratory results, particularly within the linear-elastic range up to about 400 kips. The FEM load-displacement curve showed reasonable non-linear behavior, as well. The same can be said for Figure 4.40 comparing FEM results to Specimen 6, which was cut at location "A"—the mid-panel point centered between truss nodes. The goal of this process was to simplify the FEM as much as possible while achieving reasonable and acceptable accuracy that could be carried forward into the parametric study of two-channel members. The divergence at peak loads seen in the plots is attributed to the modeling simplifications regarding rivets. For example, at peak loads the physical test experienced some slip at rivets very approximate to the location of failure, slip at bolted connections used to attach the specimen to the load frame, in-plane rotational slip of the stay plate pair closest to the member cut, as well as fastener hole deformation at extreme loads. These sources of additional axial displacement would not be captured by the simplified FEM, but were not considered necessary for the parametric study either, which focused on linear-elastic behavior that would be used for fatigue-based stress range calculations and subsequent fatigue life estimates.

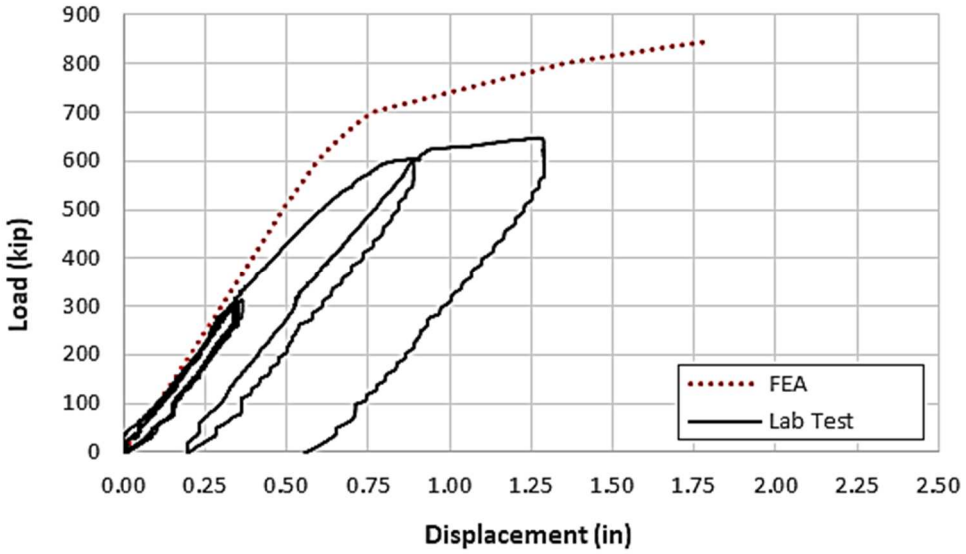

Figure 4.39 Benchmark data comparing FEA results to lab test data for Specimen 7 in faulted condition with severed member at mid-panel (Cut "A", Figure 3.24)

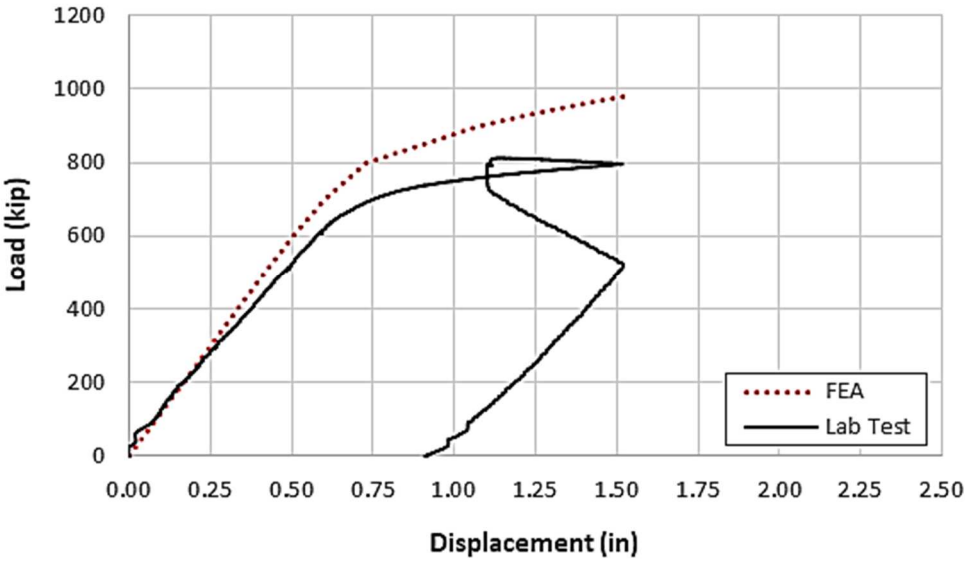

Figure 4.40 Benchmark data comparing FEA results to lab test data for Specimen 6 in faulted condition with severed member at mid-panel (Cut "B", Figure 3.24)

Strain gages were placed at several cross sections along the full length of the specimens, as shown in the gage plans in Appendix C. The benchmark FEM generated longitudinal stress results within 10% or

less of laboratory results at all critical areas, such as near the points of severed members, and within 15% or less of all other measured data. Figure 4.41(a) shows a cross-sectional view of the benchmark FEM at the site of the "failure" of Specimen 7. Symbols are sketched at approximate locations where the strain gages were installed, corresponding to the stress plots in Figure 4.41(b)-(d). Figure 4.41(b)-(d) plot stress on the vertical axes and transverse position on the component on the horizontal axes. Dashed lines are also sketched on Figure 4.41(a), corresponding to the path across which the stress outputs were obtained from the FEM. Figure 4.41(b) shows longitudinal normal stress across the width of the cover plate. The triangle indicates the location of the strain gage, which was centered between the edges of the cover plate, as well as between the adjacent stay plates, directly across from the severed half of the member. Figure 4.41(c) shows longitudinal normal stress across the width of the channel flange. Two strain gages were installed on the flange, one (diamond) was located 1-1/2 inches from the edge of the flange and the other (circle) was 1/2 inch from the edge. Both of these gages were centered between the adjacent stay plates directly across from the severed half of the member. Figure 4.41(d) plots longitudinal normal stress across the width of the channel web. The square indicates the location of the strain gage, which was directly opposite the strain gage installed on the cover plate. The applied load was 300 kips. All FEM results in this location were within 10% or less of laboratory measurements and considered acceptable. Figure 4.42 shows a side view of the same FEM, where the severed half can be seen, along with the stress hotspots at the corners of the stay plates. The strain gage symbols have also be placed on Figure 4.42 to illustrate their approximate positions. Note that the cover plate gage (triangle) is out of view. Stresses carried by the intact half of the member included the full axial load applied to the member, as well as secondary flexural stresses resulting from load redistribution around the discontinuity. Stay plates functioned as load paths for the redistribution carrying load through in-plane shear, helping resist opening of the severed half of the member. This caused the intact member to displace inward (toward the severed member). Out-of-plane displacements of the FEM at the location of "failure" matched laboratory specimen measurements to within 5% at peak loads.

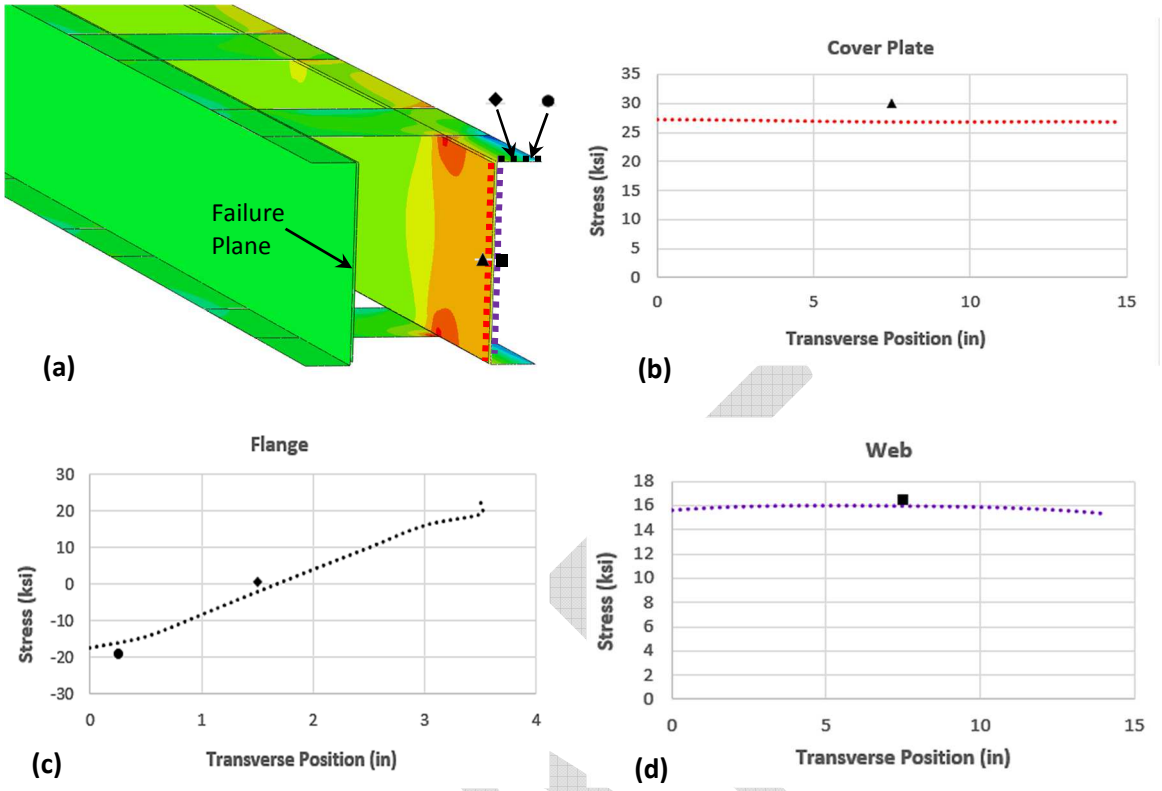

Figure 4.41 Benchmark data comparing FEA results to measured data at the location of failure

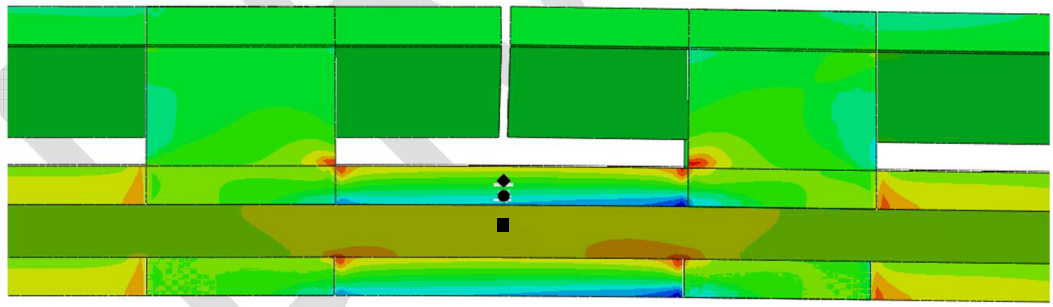

Figure 4.42 Benchmark FEM showing location of the severed half and stress hotspots at load equal to 300 kips

Pinned and fixed boundary conditions were also applied to the FEM in an effort to understand the effect it may have on the benchmark results. It was found that boundary conditions had a negligible effect likely due to benefits attributed to the member being continuous, meaning more than a single panel

length. Boundary conditions and their effect on resulting stress within the context of the parametric study are discussed further in Section 4.5.3.

The benchmark shell element model, as described in herein, was found to be acceptably accurate, particularly within the linear-elastic range. Stresses and displacements at locations of highest interest were found to be within 10% of that measured in the laboratory tests and therefore the procedures used to construct the benchmark FEA were used as the basis for FEMs used in the parametric study of two-channel members.

4.5.2. Geometric Parameters Varied for Two-Channel Members

The parametric study was divided into four subgroups: continuous stay-plated, continuous laced, non-continuous stay-plated, and non-continuous laced. Each of these subgroups was studied for effects of equivalent applicable parameters, but were divided into subgroups due to the differences in after-fracture load redistribution behavior.

The modern AASHTO LRDF Bridge Design Specification is silent on the sizing and spacing of stay plates and lattice bars for built-up tension members. It does provide guidance on the design of built-up compression members, including single-angle members. Many existing built-up members, however, were constructed long before the modern design specification. The earliest AASHTO design specification that could be referenced for this work was *The Standard Specifications for Highway Bridges* adopted by AASHO in 1935 (later changed to AASHTO in 1973). Later AASHO specifications also had the same or similar requirements. It provided design guidance for built-up tension and compression members. It states that separate segments of tension members composed of shapes may be connected by stay plates or end stay plates and lacing. End stay plates were required to be sized the same as compression members. Intermediate stay plates were required to be sized at a minimum of three-quarters of that specified for compression member intermediate stay plates. This would require the following:

- End stay plates for tension members must be a minimum of 1.25 times the distance between the inner lines of rivets connecting them to the flanges.
- Intermediate stay plates for tension members would be a minimum of 0.75 x 1.25 times the distance between the inner lines of rivets connecting them to the flanges, equaling 0.9375 times the distance between the inner line of rivets connecting them to the flanges.
- Thickness of all stay plates must not be less than 1/50 of the distance between inner rivet lines connecting them to flanges.

Finally, the clear distance between stay plates was limited to no more than 36 inches. Lacing bars could be flats or shapes and were limited to a minimum width that was based on the diameter of the rivets connecting them to the member flanges. For example, a minimum of 2-1/2 inch wide flat bar would be required for a 7/8-inch diameter rivet. Thickness of the bars was set at a minimum of 1/40 of the distance between connections for single lacings, and 1/60 for double lacing, but not less than 5/16 inch. The angle between the lacing bars and the longitudinal axis of the member was limited to "approximately 45 degrees" for double lacing and 60 degrees for single lacing. Double lacing was required for any member whose distance between connecting lines of rivets was equal to or greater than 15 inches. Finally, two rivets were required to connect each end of a lacing bar if the flanges were 5 inches or wider.

As a point of comparison, the current AREMA Chapter 15 provides guidance on design of these elements, as well. It states that built-up members shall be connected by stay plates or lacing bars with end stay plates. It goes on to specify that tension members shall have stay plates sized to a minimum of two-thirds the lengths specified for stay plates on primary compression members. This would require the following:

- End stay plates for tension member must be a minimum of 0.67 x 1.25 x the distance between the lines of connection to the outer flanges, equaling 0.833 times the distance between lines of connection to the outer flanges.
- Intermediate stay plates shall not be less than three-quarters of the end stay plate size. This means the tension member intermediate stay plates would be 0.67 x 0.75 times the distance between lines of connection to the outer flanges, equaling 0.5 times the distance between lines of connection to the outer flanges. Thus, intermediate stay plates would be sized at about 60% of the length of end stay plates on tension members.
- Thickness of all stay plates must not be less than 1/50 of the distance between lines of connection to the outer flanges for main members, or 1/60 for bracing members.

Lacing bars for tension members where the distance between connection lines in the flanges is greater than 15 inches and a bar less than 3-1/2 inches wide is used, the lacing shall be double and connected at the intersections. The angle and thickness of the lacing bars was similar to the requirements of the 1935 AASHTO Standard Specifications. AREMA Chapter 15 also requires a similar minimum bar width and double fastener requirements for flanges of 5 inches or wider.

The parametric study included a mix of models that followed the requirements of the 1935 AASHTO Standard Specification, a few geometries that would not have met the minimums, and many geometries that would have exceeded the minimums. While it is likely that most bridges would have been built to the minimal design requirements, it cannot be said conclusively that some were not. Furthermore, it cannot be said that the minimums would have been different for bridges designed using earlier specifications or dissimilar guidelines that were not available for reference for the current study. It was also preferred to develop a simplified method of analysis that would be inclusive of all possible designs, including those that were designed per the 1935 AASHTO provisions and those designed per the AREMA provisions, albeit the differences between the two specifications are marginal.

4.5.2.1. Parameters Evaluated for Two-Channel Members

Due to the size of the table, the specific combinations of geometric parameters have been tabulated in Appendix A. Table A.1 lists geometries for continuous stay-plated two-channel members. Table A.2 shows geometries for continuous laced two-channel members. Table A.3 contains the parameters studied for non-continuous stay-plated two-channel members and Table A.4 is for non-continuous laced two-channel members. Many of the parameters evaluated for the two main types of members, stay-plated and laced, were similar. However, there were several parameters unique to the each type of two-channel member. The parameters evaluated for stay-plated members included:

- Boundary conditions (Fixed vs. Pinned),
- Channel section,
- Channel spacing,
- Panel length – referring to the distance between two adjacent gusset joint centerlines,
- Stay plate thickness,
- Stay plate length,
- Stay plate clear spacing,
- Gusset plate thickness (for non-continuous only),
- Location of failures (Next to the gusset vs. centered between gussets at mid-panel).

The laced members were modeled with end stay plates. Based on results for the stay-plated members, the thickness and length parameters of the end stay plates were not varied. Additionally, results for the stay-plated members also showed that gusset plate thickness for the non-continuous

members had negligible effect and therefore was not varied for the laced members. The parameters considered for laced members included:

- Boundary conditions (Fixed vs. Pinned),
- Channel section,
- Channel spacing,
- Panel length – referring to the distance between two adjacent gusset joint centerlines,
- Lacing bar thickness,
- Lacing bar length,
- Lacing bar spacing – referring to the distance between connecting rivets to the channel flange, which determined the lacing angle relative to the channel,
- Location of failures (Next to the gusset vs. centered between gussets at mid-panel).

Boundary conditions were found to have a significant effect on results, which is discussed in greater detail in Section 4.5.3. Three sizes of rolled channels were considered, however not all sections were considered for all combinations of parameters. They were the C15x50, C15x40, and C8x11.5, which are sketched to scale in Figure 4.43 to give a sense of relative sizes. C15x50 is the largest rolled channel section currently available, so it was selected to learn if parametric effects varied between it and the next size smaller. C15x40 was chosen because it appeared to be the most commonly used channel section for main tension chords in legacy bridges. This was the channel size used to construct the Winona Bridge from which two test specimens, Specimen 6 and 7, were obtained for the present research. It was necessary to consider channel section size effects, if any. The C8x11.5 was selected as a channel that is most likely representative of the smallest size rolled channel used on bridges for any tension member, such as diagonals and hangers. While this size channel would not likely be found on railroad bridges, it would be very possible for shorter-span highway bridges.

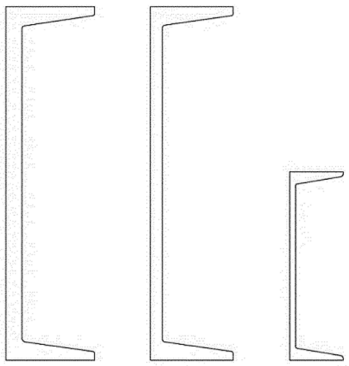

Figure 4.43 Channel sections included in the parametric study

Panel lengths were varied from 20-ft. to 40-ft. for continuous and non-continuous members of both stay-plated and laced types. The thickness of the tie elements, such as stay plates and lattice bars, varied from 1/8-inch up to 3/4-inch for lattice bars, and from 3/8-inch up to 7/8-inch for stay plates. Spacing of the tie elements was also examined, varying from 1/2 the depth of the channel to two times the depth of the channel for lattice bar spacing, and from 18 inches up to 148 inches for stay plate clear distances. Gusset plates were modeled for the non-continuous members, as is explained further in Section 4.5.3. The thickness of the gussets were modeled at 3/8 and 7/8-inch. Finally, the location of the failure within a member was also examined for the effect on results. Two locations were studied for all geometries, which included one at the mid-panel location centered between the gusset connections, and the other was adjacent to gusset plates located between the end stay plate and the gusset connection. This was considered for the continuous as well as the non-continuous types.

4.5.2.2. Definition of Eccentricity Parameter, e

Figure 4.44 illustrates the dimension "*e*" used in the post processing of data from the parametric study. 2*e* represents the distance between the centroids of individual channels that make up a two-channel member; or in other words the channel spacing. Hence, *e* would simply be half of 2*e*, or the distance from the unfaulted *member centroid* to the centroid of an individual channel. The figure demonstrates how the eccentricity for two members that are comprised of the same size of channels with the same web-to-web spacing, but in reversed orientation, would be calculated and may differ from each other. The parametric study included channels in both orientations. All results discussed in the following used the appropriate theoretical $P \cdot e$ to normalize the second order moment resulting from failure of a single channel; where *P* was the total load in the member. In this way, a simplified method to calculate the resulting moments in two-channel members as a percentage of $P \cdot e$ was developed.

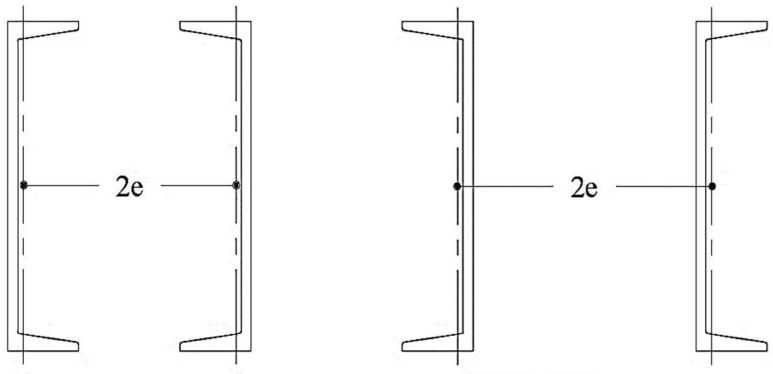

Figure 4.44 Illustrations showing eccentricity "e" used in development of the simplified evaluation method for two-channel members

4.5.3. Rotational Stiffness of Joints for Continuous and Non-Continuous Two-Channel Members

Boundary conditions proved to be the most influential parameter affecting the resulting second order moments on non-continuous two-channel members in the faulted condition. Boundary conditions were inconsequential to continuous members. Figure 4.45 plots some data for several models where the length of stay plates parameter was being evaluated, which is used here only to illustrate this principle. The vertical axis plots the resulting moment normalized by *P·e*, or the percent of *P·e.* The horizontal axis plots the length of the stay plate over the depth of the channel. Varying boundary conditions were applied to each geometry, including a non-continuous member with pinned ends, a non-continuous member with fixed ends, a three-span continuous member with pinned ends, and a three-span continuous member with fixed ends. The dashed lines represent the continuous members. The percent *P·e* for the non-continuous member with pinned boundary conditions differed as much as ten times more than the same geometry with fixed boundaries. Figure 4.45 also shows that results for continuous members were very similar to fixed members and that boundary conditions on the continuous member ends had negligible effect on outcomes. This plot demonstrates that the rotational stiffness of the member connections has a large impact on results. Continuity of the channels through the connections provided rotational constraint that approached fixed boundary conditions. No additional rotational constraints were placed in the models at the interior gusset connections of the three-span member; however, they did have displacement constraints conservatively simulating constraints that would exist on an actual bridge to prevent out-of-plane displacement, while allowing rotation.

Primary and secondary members, including chords, floorbeams, diagonals, lateral braces, sway braces, and bearings, tie into panel points on a truss that are connected together using gusset plates. Chords or diagonal members that carry tensile loads will restrain the joint against rotation. The slender members of lateral bracing may act in tension to restrain against rotation of the gusset connection. Sway bracing members are stiffly designed against buckling limit states and therefore can add significant resistance to joint rotation. Floorbeams, often with connections as deep as the floorbeam themselves, increase rotational constraint of the connection. In some cases bearings that are fixed, or even expansion bearings designed to only displace longitudinally offer further resistance to rotation for the gusset connections. The combined restraint provided by all of these members is difficult to estimate without finite element analysis of each individual bridge and member geometry, which would not be feasible for most bridge owners, nor was it the desired outcome of this research. However, the effect of the rotational stiffness on the internal redundancy of two-channel members was apparent. It was clear that pinned conditions would not exist in actual bridges. However, it would be difficult to justify perfectly fixed conditions, as well.

Two-channel members typically are deeply connected into gusset plates; often they would be trimmed such that they fit tightly into the connection to within a few inches of the other intersecting primary members. An example of this is shown in Figure 4.46, which shows a removed railroad deck truss joint with diagonal two-channel members connected into the gusset plates. Due to the rotational stiffness of the connection as a whole, for reasons previously stated, it was estimated that most of the rotation that a two-channel member would experience would most likely be due to local flexure of the gusset plates near or at the edges of the gusset plates and that the plates themselves would behave as fixed toward the center of the connection. This concept was modeled by tying the channels to a set of gusset plates and then applying fixed boundary conditions to the edges of the gusset plates. By doing this, generous flexibility of the gusset plate was allowed while simultaneously providing a reasonable level of rigidity that may be present due to intersecting members within the joint.

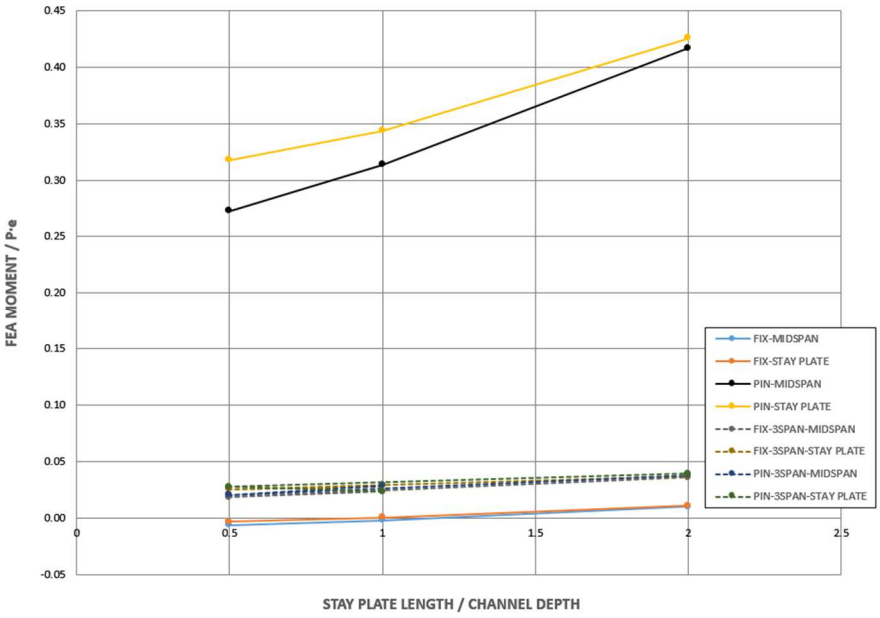

Figure 4.45 FEM results demonstrating effect of boundary conditions and member continuity

Hence, a parametric study was carried out to determine how best to model the boundary conditions of the non-continuous members without over estimating joint rotational stiffness. The parameters considered in the study included the effective portion of the gusset plate, the member embedment depth into the gusset plate, the gusset length beyond the member, and the gusset plate thickness. Figure 4.47 shows an illustration of these parameters. Two different effective areas of gusset were examined, a simple rectangular shape shown on the left and a Whitmore Section-like shape, shown on the right. The member embedment depth was evaluated looking at depths ranging from half the channel depth to two times the channel depth. The gusset plate length beyond the member, labeled *L* on the figure, also ranged from half the channel depth up to two times the channel depth.

Figure 4.46 Example of deeply set two-channel diagonal members connected into a gusset plate

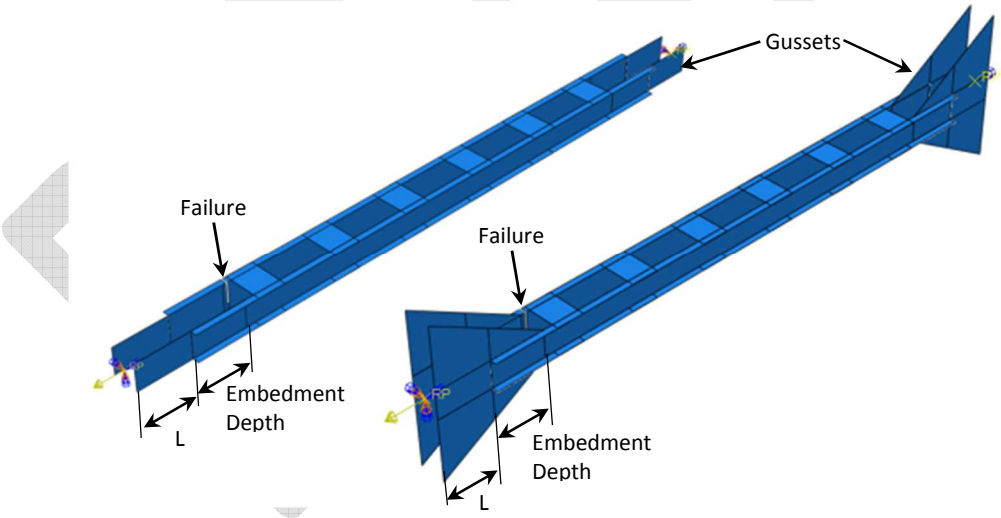

Figure 4.47 Example of FEMs used to study gusset connection parameters (Left) Rectangular Gusset, (Right) Whitmore Gusset

Figure 4.48 plots the results of the rotational stiffness parametric study. Green dots represent values resulting from mid-panel failures. Black dots represent values resulting from failures near the gusset connections, such as those shown in Figure 4.47. The rectangular and Whitmore-like effective gusset

plate shapes are both represented. The chart on the left plots the percent of *P·e* on the vertical axis and the member embedment depth into the gusset plate, normalized by the channel depth, on the horizontal axis. The chart on the right plots the same vertical axis and the gusset plate length, *L*, on the horizontal axis normalized by the channel depth. By quadrupling the embedment depth, the percent *P·e* only increased by 2% for failures near the gusset plate and by less than 1% for mid-panel failures. By quadrupling the gusset plate length, *L*, the percent *P·e* increased by less than 1% for both failure locations. The final parameter considered was the thickness of the gusset plates. Gusset plates of 3/8-inch thick are the thinnest plates used in bridges. The thickest plate is unknown, and would not vary much from 3/8 inch for legacy bridges, but for new designs thicker gussets plates could be used, particularly on long span trusses. For these reasons it was necessary to understand if the thickness of the gusset plates would influence the finite element solution. Several non-continuous models were analyzed varying only the gusset plate thickness from 3/8-inch to 7/8-inch. It was found that results differed by 3% or less and therefore was concluded that the gusset plate thickness was not an essential geometric parameter.

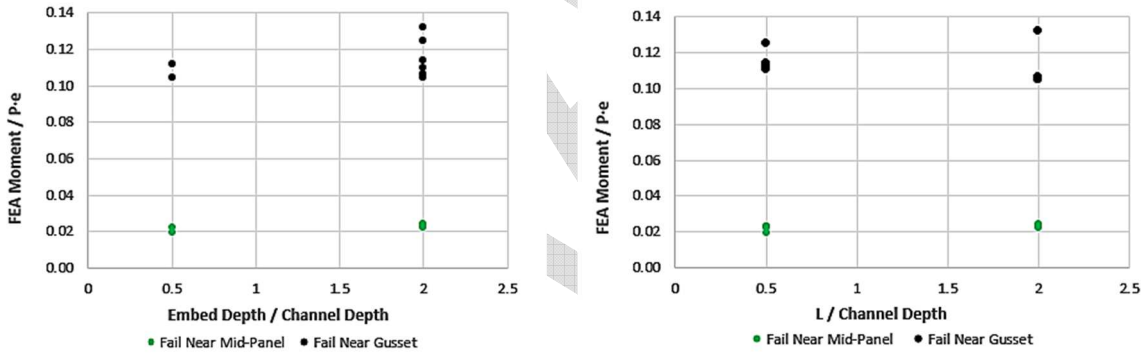

Figure 4.48 FEA results showing effects of the member embedment length (Left) and gusset length, L (Right) (See Figure 4.47)

The non-continuous member boundary condition study concluded that outcomes were insensitive to the shape of the gusset assumed to be engaging in rotational constraint, the member embedment depth, the gusset plate length *L*, and the gusset plate thickness. As a result, non-continuous FEMs were modeled in the comprehensive parametric study using 3/8-inch thick rectangular gusset plates with embedment depths and gusset plate lengths equal to the channel depth.

Finally, when percent *P·e* results in Figure 4.48 are compared back to Figure 4.45 it can be seen that by adding the gusset plates to the non-continuous members, percent *P·e* falls between results for pinned and fixed boundary conditions, more closely resembling that of fixed boundary conditions, and comparable to the continuous members. It is believed that this method of analysis reasonably and conservatively simulated typical boundary conditions on actual bridges for the non-continuous two-channel members, which was found to significantly affect the internal redundancy evaluation.

4.6. Results for Parametric Study of Two-Channel Members

The largest resulting second order moments were always located in the intact member directly across from the location of failure. The largest of these moments nearly always resulted from a failure between the gusset plate and end stay plate, particularly for stay-plated members. Figure 4.49 shows the plan view of several FEMs with exaggerated deflections to illustrate general global behavior. Two were failed at the mid-panel, (a) and (b), and two were failed between the gusset plate and end stay plate, (c) and (d). Overall global behavior was relatively similar between these two member types when they had failures at the same location. Mid-panel failures allowed moment distribution along the length of the intact channel via lattice bars or stay plates helping to distribute load more gradually around the failure. Gusset-end stay plate failures, however, forced much of the resulting moment to be resisted by the intact channel within a smaller localized area. Deflections across the remainder of the member were relatively gradual, as can be seen in Figure 4.49(c) and (d).

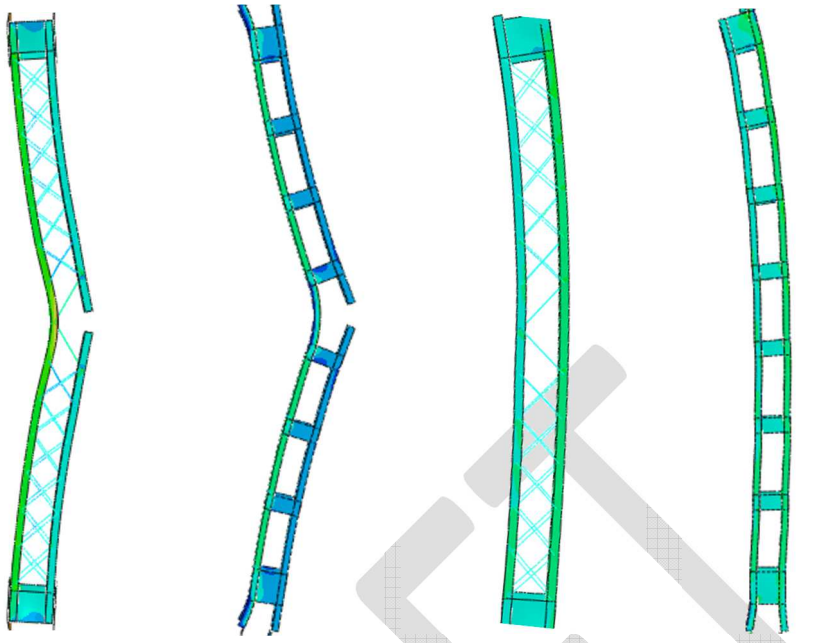

Figure 4.49 Non-continuous FEM results with deformations amplified 50x for clarity, (a) Laced with mid-panel failure, (b) Stay-plated with mid-panel failure, (c) Laced with end failure near gusset, (d) Stay-plated with end failure near gusset

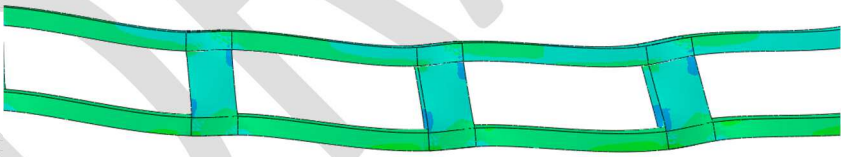

Figure 4.50 Close-up of stay-plated member with deformations amplified 50x showing reverse curvature of the channels

Moments integrated at the mid-panel of members with gusset-end stay plate failures were found to be very small compared to the moment at the end stay plate near the failure. Stay-plated members were also observed to experience localized reverse curvature at the edges of the stay plates that produced hot spots of stress and amplified moments. All moments reported in the following sections were taken near the edges of stay plates, when applicable, in order to capture the largest resultant moment. Figure 4.50

illustrates the reverse curvature of stay-plated members in which deformations are amplified with a very large load applied in order to make the structural behavior obvious. The opening of the fracture plane was resisted through in-plane shear in the stay plates. Laced members also benefited from in-plane shear resistance provided by end stay plates.

The size of the channel was found to have negligible effect on the outcomes. This makes sense when considering that loads were proportioned to the area of the member and that second order effects resulting from load redistribution were a function of eccentricity created when half the member was severed. Thus, a smaller channel carried proportionally smaller loads and would be proportionally spaced, as well, causing similar behavior but on a smaller scale. This means that when the results were plotted as a ratio of the second order moment (caused by the load redistribution) to the theoretical moment, $P \cdot e$ (where P is the load and e is the member eccentricity explained in Section 4.5.2.2), the results for the larger and smaller channel sections were nearly indistinguishable. This was the result for both continuous and non-continuous members.

In addition to channel size, the spacing between channel pairs was also examined. This parameter ranged from a spacing equal to half the depth of the channel up to two times the depth of the channel. When resulting second order moments were normalized by the theoretical moment, $P \cdot e$, then it appeared that as the spacing increased the resulting moment was reduced. However, when the second order moments were not normalized, and absolute magnitudes were compared for geometries ranging in channel spacing, then it became clear that channel spacing had minimal effect on the results. The larger theoretical moment was simply reducing the ratio of FEA moment to theoretical moment, due to the larger eccentricity, e. This conclusion goes against the assumption that some have had toward two-component members, and even some designs for multi-component members, that when one of the components fails, the resulting second order moment is equal to the original load times the faulted member eccentricity. The present parametric study found that such an assumption would be overly conservative for any two-channel geometry; and as the spacing between components increased, that assumption would become increasingly overly conservative.

The panel length, which refers to the distance taken from centerline of a panel point to centerline of the next panel point for continuous members or the length of the channels themselves for non-continuous members, was found to have minimal effect on the after-fracture moment. Due to the localized curvature of the channels at the edges of stay plates that generated hotspots in the intact channel, longer spans having similar clear distances between stay plates were observed to have negligible effect. For laced

members, there were marginal increases in the resulting moments with longer spans. For example, doubling the span in some cases increased the after-fracture moment by a mere 2%.

Thickness and length of the stay plates had negligible effect on the results. The thickness of the plates ranged from 3/8 to 7/8 inch. The lengths of the plates ranged from half the depth of the channel to two times the depth of the channel. This range included a mixture of end and intermediate stay plates that would have violated and exceeded known minimum design provisions. However, the results were insensitive to these changes in stay plate parameters. The design provisions also state that each plate must be fastened to the flanges of primary components with a minimum of three rivets. This type of connection would offer in-plane rotational constraint engaging the stay plates in resisting opening of the failed component, transferring load around the discontinuity. The connection was modeled using surface-to-surface tie constraints between shell elements, which constrained displacements and rotational degrees of freedom. Hence, modeled rotational constraint would be similar to real-world, though slightly stiffer since slip at the highest loads on a riveted connection would not be allowed with the tie constraint such as was observed to occur on Specimen 6 in the laboratory test. The consequence of stiffer stay plate connections is larger localized transferal of moment into the intact channel, which means any minimal error in the FEM results caused by stiffer stay plate connections would be conservative in nature. However, it is important to keep in mind that laboratory testing of the Winona Bridge chord, Specimen 6 and 7, showed that slip at the stay plates did not occur until near peak loads were reached, well beyond original design loads, and only for Specimen 6 when cut near the gusset connection. Specimen 7 showed no evidence of yielding and very minor evidence of slip at completion of testing in the stay plates adjacent to the failure location. The effectiveness of the stay plates in load redistribution is directly dependent upon the rotational constraint. This implies that stay plates have a minimum length to remain effective, but anything equal to or greater than half the depth of the channels to which they are attached with a minimum of three fasteners will effectively redistribute load. End stay plates were found to slightly reduce moments near the gusset connections for laced members, but did not affect the moment at the mid-panel location for mid-panel failures.

The number of stay plates within a given panel length was also studied. When clear distances were maintained constant and the number of stay plates was increased, this forced a longer panel length, for which the number of stay plates had no effect on results. However, if the panel length was maintained constant and the number of stay plates was increased, this forced smaller and smaller clear distances between the plates. The result was a slight increase in second order moments resulting from members

having more stay plates within a given length. This is illustrated in Figure 4.51 where results for pinned, fixed, and continuous models have been plotted together as a function of the number of stay plates within a fixed panel length. The solid lines are single-span members and the dashed lines are 3-span continuous members. The legend indicates the boundary condition and the location where the moment was integrated in the FEM. The location of failure was mid-panel for all of the models shown in this figure. The effect was that as the number of stay plates increased, the stiffness of the member increased. This was most notable for pinned boundary conditions, with only marginal increases for fixed and continuous members. Smaller clear distances between stay plates resulted in stiffer sections of channel between the stiffening elements (the stay plates), which transferred slightly more load and consequently increased moments.

Lacing bar thickness, length, and spacing were examined for their effect on laced two-channel members. Lattice bars sizes ranged from 1/8 to 3/4 inch thick. Lattice fastener spacing ranged from half of the channel spacing to two times the channel spacing. Design provisions limit the lattice spacing to about 45 degrees, which would be equal to the channel spacing. Design provisions also called for a lattice thickness-to-length ratio of about 1/60. The parametric study varied this ratio from 1/169 to 1/28. It was found that these parameters all had negligible effects. One model was also analyzed in which the lattice bars were completely removed so that it only had the end stay plates. When the failure was at the mid-panel location of the member, the resulting moment at the location of the failure was reduced by about half compared to the same geometry with lattice bars, but the moment at the end stay plate was unaltered. When the failure was located between the end stay plate and the gusset connection of the member without lattice bars, the resulting moment at the mid-panel location was unchanged and the moment at the location of failure was nearly doubled, going from 5% to about 9% of $P \cdot e$. This behavior suggests that while the lattice may support some limited load redistribution, they are not critical to performance of the member in the faulted condition. This also suggests that even though the parametric study focused on double lattice with fastened intersections, less robust systems of lattice, such as single lattice, would not be expected to affect results significantly. This comparison suggests that the simplified method of analysis resulting from the parametric study can be used for laced members of all kinds, whether double or single lattice configurations.

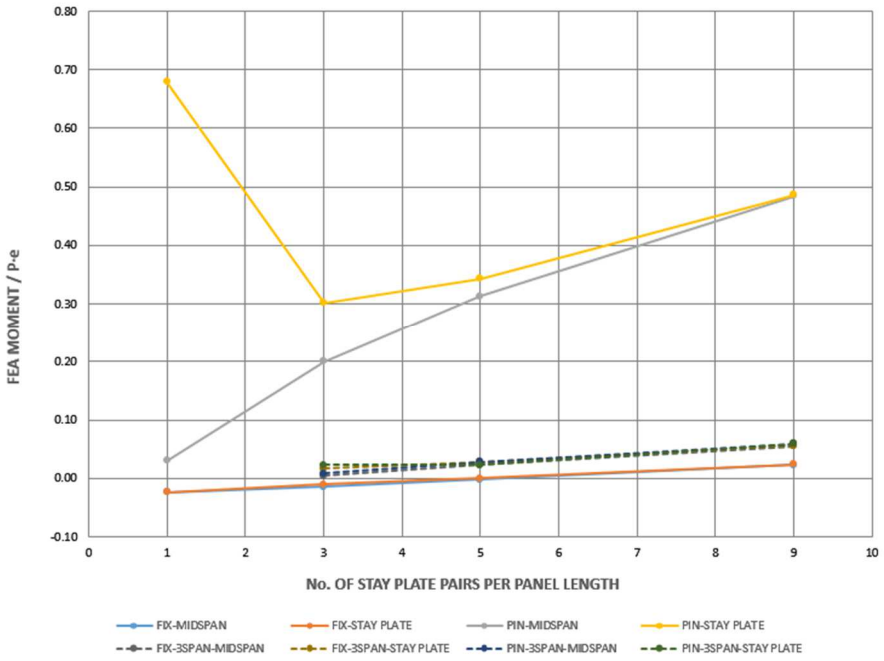

Figure 4.51 Plot showing the increase in moment resulting from more stay plates

The final parameter studied was the location of the failure. This was not necessarily geometric, but affected the response of the members and magnitude of the solution. It included the mid-panel location and between the end stay plate and the gusset plate connections. Figure 4.52 shows four examples, one from each of the locations for each type of member. Figure 4.52(a) shows failure between the end stay plate and gusset plate on a laced member. Figure 4.52(b) shows failure between the end stay plate and gusset plate on a stay-plated member. Figure 4.52(c) shows the mid-panel failure for a laced member where the two lattice bars that would have connected into the location of the failure have been removed to facilitate convergence of the finite element solution. This was done for all laced member mid-panel failure models. Figure 4.52(d) shows a typical mid-panel failure for the stay-plated members. The resulting moment in laced members was not significantly affected by the location of the failure. This means that the resulting moment was always largest at the location of failure, however, the magnitude was not necessarily larger for mid-panel failures versus failures near the gusset plate. The same cannot be said for stay-plated types, as it was found that failures near the gusset connection for both continuous and non-continuous stay-plated members resulted in moments that were two or three times larger than for the same geometry failed near the mid-panel length. There were a few exceptions to this observation, so most models were analyzed two times, once with a failure at each location to ensure the worst-case

scenario was captured for a given geometry. Plots of the percent of *P·e* in the following sections include results for both failure locations, which is the primary source of the data scatter.

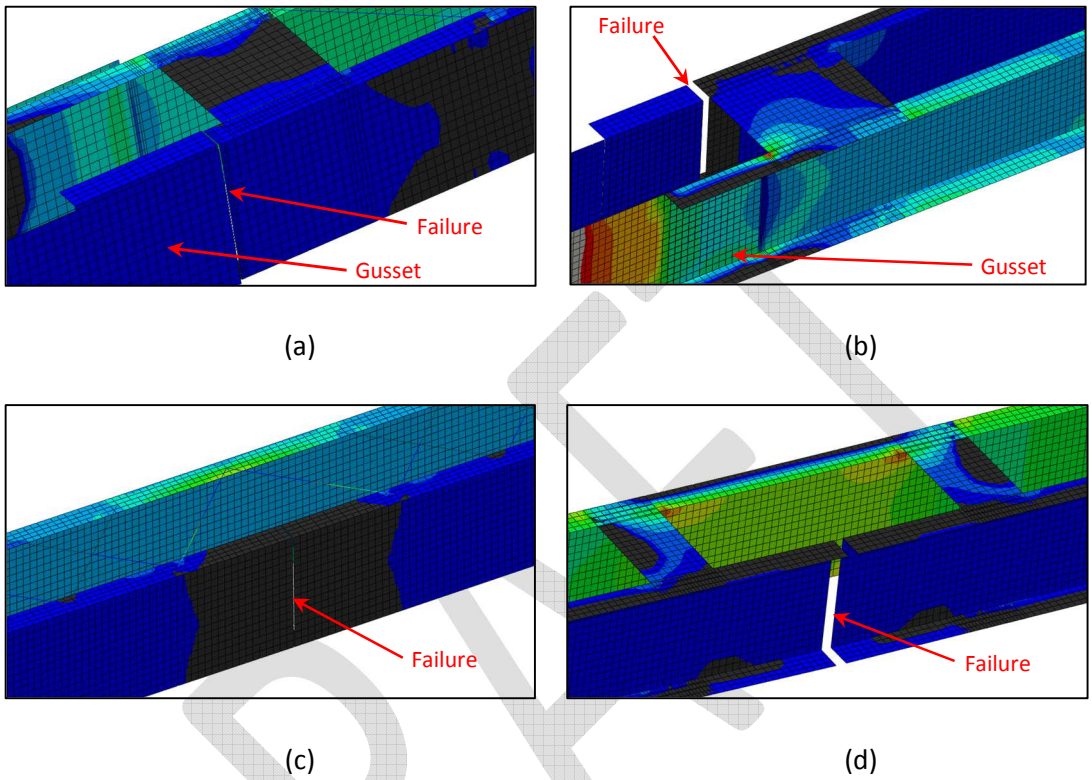

Figure 4.52 Images depicting failure locations for stay-plated and laced two-channel members

4.6.1. Results for Continuous Stay-Plated Two-Channel Members

Figure 4.53 compiles the results for all continuous stay-plated models analyzed. The vertical axis is the finite element analysis moment divided by the theoretical moment, *P·e*. The horizontal axis is a combination of geometric properties used to correlate the results. The correlation includes the number of stay plate pairs (meaning a pair of plates located at the top and bottom of the member at the same cross section) within a single panel length, which includes the two end stay plate pairs and all intermediate stay plate pairs on the section of the member being evaluated, times the ratio of the channel depth to the channel spacing.

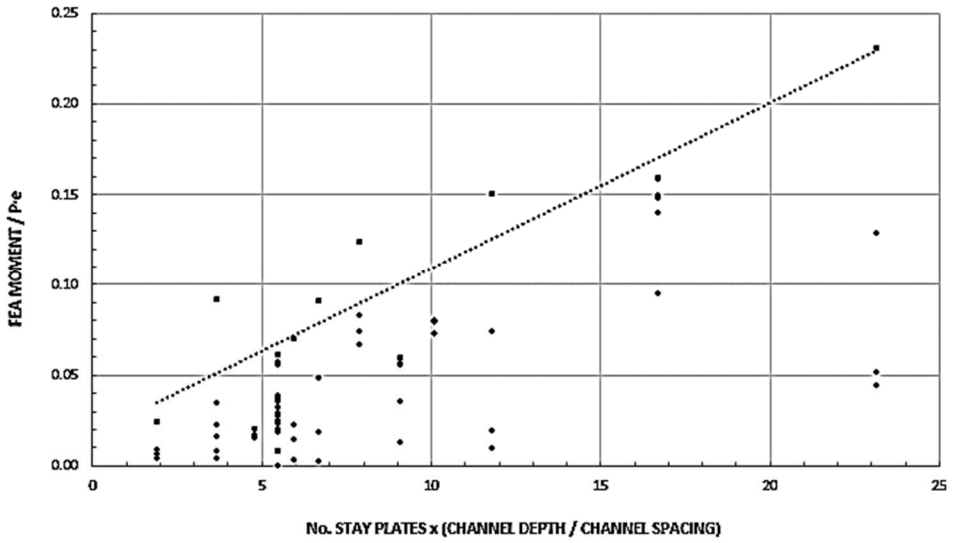

Figure 4.53 Plot of results for continuous stay-plated two-channel members

Regression analysis was used to conservatively fit a line to the maximum values. Approximately 5% of the data exceeded the limit defined by the line, which was considered acceptable. The line is defined by Equation 4.8, which can be used to calculate the second order moment resulting from a failed channel in a continuous stay-plated two-channel member.

$$M_{AF} = \frac{P_u e}{120}\left[\frac{N_{SP} d_{CH}}{2e} + 3\right] = \frac{P_u N_{SP} d_{CH} + 6P_u e}{240} \tag{4.8}$$

Where:

$\boldsymbol{M_{AF}}$ = After-fracture moment resulting from failure of a channel in a two-channel member (kip-in).

$\boldsymbol{P_u}$ = Total factored axial load (kips).

$\boldsymbol{e}$ = Distance measured from the centroid of the unfaulted two-channel member to the centroid of the intact channel in the faulted state (in; See Figure 4.44).

$\boldsymbol{N_{SP}}$ = Number of stay plate pairs (1 pair equals the top and bottom stay plates at the same cross section) within the span of the member between the panel points.

$\boldsymbol{d_{CH}}$ = Depth of the channels (in).

The resulting moment is inserted into equation 4.12 to calculate the after-fracture net section stress used to determine the remaining fatigue life. All results for continuous stay-plated members have also been tabulated in Appendix B.

4.6.2. Results for Continuous Laced Two-Channel Members

Figure 4.54 compiles the results for all continuous laced models analyzed. The vertical axis is the finite element analysis moment divided by the theoretical moment, $P \cdot e$. The horizontal axis is a combination of geometric properties used to correlate the results. The correlation parameters includes the length (inches) from the centerline of a panel point to the centerline of the next panel point, times the ratio of the channel depth to the channel spacing.

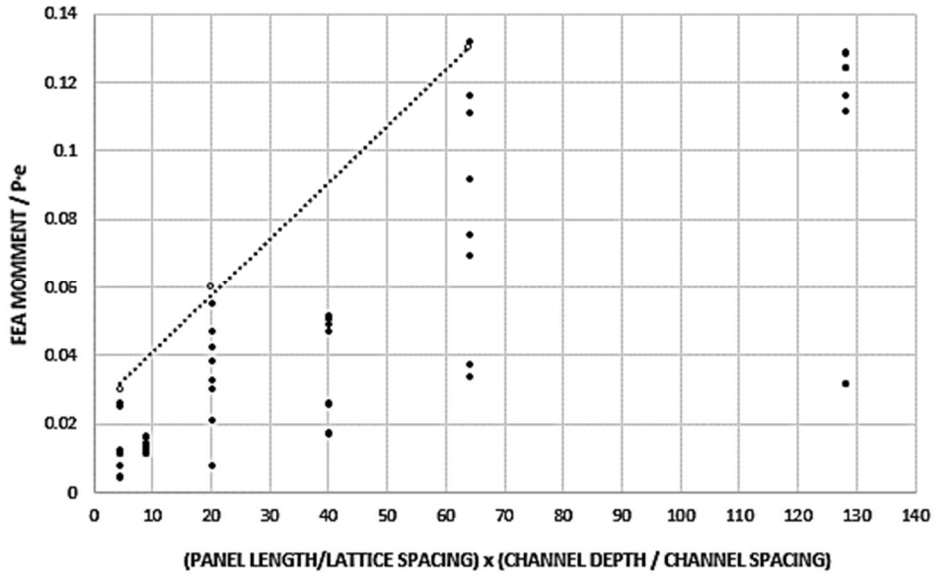

Figure 4.54 Plot of results for continuous laced two-channel members

Regression analysis was used to conservatively fit a line to the maximum values. Less than 5% of the data exceeded the limit defined by the line, which was considered acceptable. The line is defined by Equation 4.9, which can be used to calculate the second order moment resulting from a failed channel in a continuous laced two-channel member. The lattice bar configuration factor, γ_{LB}, accounts for the fact that single lattice bars will have twice the spacing of comparable double lattice bars. Equation 4.9 was derived using double lattice bar spacing. Based on results for members where the lattice was removed, the simplified method can be extended to single lattice configurations, as well. Thus, the lattice bar

configuration factor reduces the spacing of single lattice bar members to an equivalent double lattice bar spacing such that the moment is not incorrectly doubled for single lattice members. Finally, as can be seen in Figure 4.54 the maximum moment reaches a plateau of less than fourteen percent of *Pe*. Equation 4.9 limits the moment to 0.15*Pe*, which is slightly above the maximum value observed for the continuous laced members.

$$M_{AF} = \frac{P_u e}{590}\left[\frac{L_{PL} d_{CH}}{\gamma_{LB} S_{LB} 2e} + 14\right] = \frac{P_u L_{PL} d_{CH} + 28 P_u e \gamma_{LB} S_{LB}}{1180 \gamma_{LB} S_{LB}} \leq 0.15 P_u e \qquad (4.9)$$

Where:

$\boldsymbol{M_{AF}}$ = After-fracture moment resulting from failure of a channel in a two-channel member (kip-in).
$\boldsymbol{P_u}$ = Total factored axial load (kips).
$\boldsymbol{e}$ = Distance measured from the centroid of the unfaulted two-channel member to the centroid of the intact channel in the faulted state (in; See Figure 4.44).
$\boldsymbol{L_{PL}}$ = Length of the panel measured between the centerlines of two panel points (in).
$\boldsymbol{S_{LB}}$ = Spacing of the lattice bars measured longitudinally between centerlines of fasteners connecting the lattice bars to a channel flange (in).
$\boldsymbol{d_{CH}}$ = Depth of the channels (in).
$\boldsymbol{\gamma_{LB}}$ = Lattice bar configuration factor; 1.0 for double lattice, 0.5 for single lattice.

The resulting moment is inserted into equation 4.12 to calculate the after-fracture net section stress used to determine the remaining fatigue life. All results for continuous laced members have also been tabulated in Appendix B.

4.6.3. Results for Non-Continuous Stay-Plated Two-Channel Members

Figure 4.55 compiles the results for all non-continuous stay-plated models analyzed. The vertical axis is the finite element analysis moment divided by the theoretical moment, *P·e*. The horizontal axis is a combination of geometric properties used to correlate the results. It is the number of stay plate pairs (meaning a pair of plates located at the top and bottom of the member at the same cross section) along the entire length of the member, which includes the two end stay plate pairs and all intermediate stay plate pairs on the section of the member being evaluated, times the ratio of the channel depth to the channel spacing.

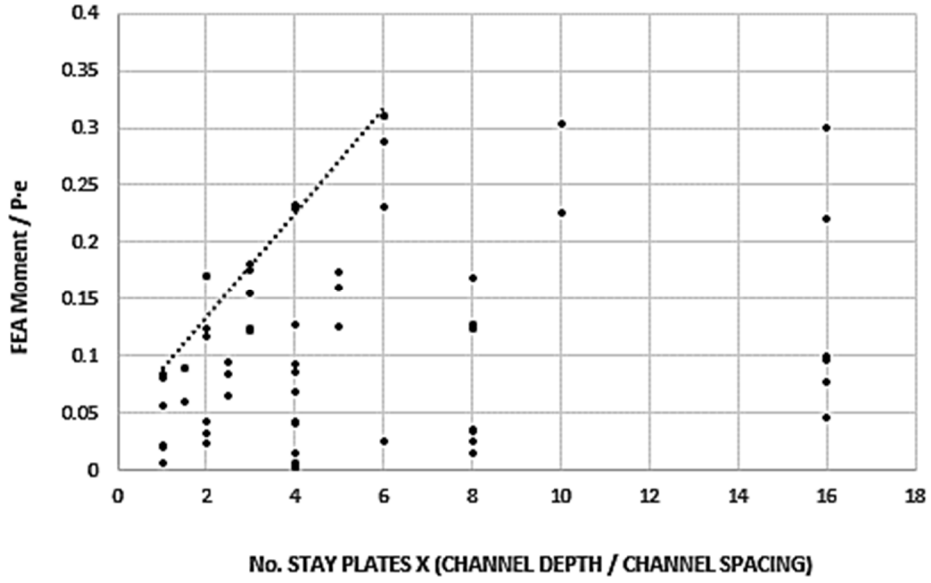

Figure 4.55 Plot of results for non-continuous stay-plated two-channel members

Regression analysis was used to conservatively fit a line to the maximum values. Less than 5% of the data exceeded the limit defined by the line, which was considered acceptable. The line is defined by Equation 4.10, which can be used to calculate the second order moment resulting from a failed channel in a non-continuous stay-plated two-channel member. The moment is limited to 0.35*Pe*, which is slightly above the maximum value observed for the continuous laced members, as can be seen in Figure 4.55.

$$M_{AF} = \frac{P_u e}{22}\left[\frac{N_{SP} d_{CH}}{2e} + 1\right] = \frac{P_u N_{SP} d_{CH} + 2P_u e}{44} \leq 0.35Pe \qquad (4.10)$$

Where:

$\boldsymbol{M_{AF}}$ = After-fracture moment resulting from failure of a channel in a two-channel member (kip-in).

$\boldsymbol{P_u}$ = Total factored axial load (kips).

$\boldsymbol{e}$ = Distance measured from the centroid of the unfaulted two-channel member to the centroid of the intact channel in the faulted state (in; See Figure 4.44).

N_{SP} = Number of stay plate pairs (1 pair equals the top and bottom stay plates at the same cross section) within the span of the member between the panel points.

d_{CH} = Depth of the channels (in).

The resulting moment is inserted into equation 4.12 to calculate the after-fracture net section stress used to determine the remaining fatigue life. All results for non-continuous stay-plated members have also been tabulated in Appendix B.

4.6.4. Results for Non-Continuous Laced Two-Channel Members

Figure 4.56 compiles the results for all non-continuous laced models analyzed. The vertical axis is the finite element analysis moment divided by the theoretical moment, *P·e*. The horizontal axis is a combination of geometric properties used to correlate the results. It is the length in inches of the channels, including the depth into the gusset plate at each end of the member, times the ratio of the channel depth to the channel spacing.

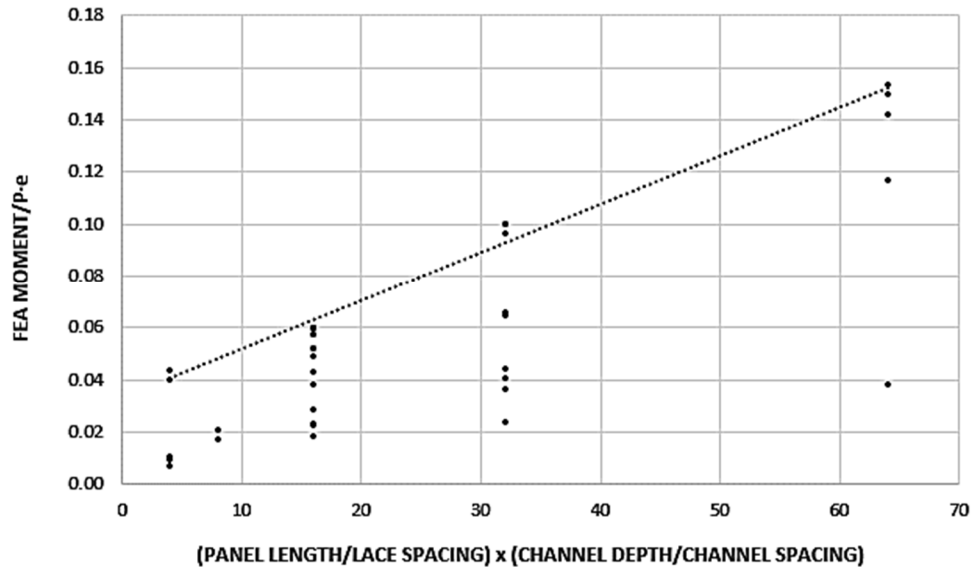

Figure 4.56 Plot of results for non-continuous laced two-channel members

Regression analysis was used to conservatively fit a line to the maximum values. Five percent of the data exceeded the limit defined by the line, which was considered acceptable. The line is defined by

Equation 4.11, which can be used to calculate the second order moment resulting from a failed channel in a non-continuous laced two-channel member. The lattice bar configuration factor, γ_{LB}, accounts for the fact that single lattice bars will have twice the spacing of comparable double lattice bars. Equation 4.11 was derived using double lattice bar spacing. Based on results for members where the lattice was removed, the simplified method can be extended to single lattice configurations, as well. Thus, the lattice bar configuration factor reduces the spacing of single lattice bar members to an equivalent double lattice bar spacing such that the moment is not incorrectly doubled for single lattice members.

$$M_{AF} = \frac{P_u e}{550}\left[\frac{L_{PL} d_{CH}}{\gamma_{LB} S_{LB} 2e} + 20\right] = \frac{P_u L_{PL} d_{CH} + 40 P_u e \gamma_{LB} S_{LB}}{1100 \gamma_{LB} S_{LB}} \quad (4.11)$$

Where:

$\boldsymbol{M_{AF}}$ = After-fracture moment resulting from failure of a channel in a two-channel member (kip-in).
$\boldsymbol{P_u}$ = Total factored axial load (kips).
$\boldsymbol{e}$ = Distance measured from the centroid of the unfaulted two-channel member to the centroid of the intact channel in the faulted state (in; See Figure 4.44).
$\boldsymbol{L_{PL}}$ = Length of the panel measured between the centerlines of two panel points (in).
$\boldsymbol{S_{LB}}$ = Spacing of the lattice bars measured longitudinally between centerlines of fasteners connecting the lattice bars to a channel flange (in).
$\boldsymbol{d_{CH}}$ = Depth of the channels (in).
$\boldsymbol{\gamma_{LB}}$ = Lattice bar configuration factor; 1.0 for double lattice, 0.5 for single lattice.

The resulting moment is inserted into equation 4.12 to calculate the after-fracture net section stress used to determine the remaining fatigue life. All results for non-continuous laced members have also been tabulated in Appendix B.

4.6.5. Application of Parametric Study Findings for Two-Channel Members

The following sections describe implementation of the after-fracture moments, previously explained, in order to calculate the after-fracture net section stress resulting from failure of a channel in a two-channel member. A validation exercise is completed and further guidance is given for proper application of the simplified method.

4.6.5.1. After-fracture Net Section Stress Calculation

Following calculation of the after-fracture moment that results from failure of one of the two channels, Equation 4.12 is used to calculate the after-fracture net section stress. The equation combines the axial net section stress and second order flexural stress. The axial net section stress is simply the total factored load carried by the member in the unfaulted state, divided by the after-fracture net section. The flexural stress is the after-fracture moment calculated using one of equations 4.8 – 4.11, as applicable for the member type, times the distance from the neutral axis to the point of interest, *c*, divided by the weak axis moment of inertia, I_y.

$$f_{AFN} = \frac{P_u}{A_{AFN}} + \frac{M_{AF}c}{I_y} \tag{4.12}$$

Where:

$\boldsymbol{A_{AFN}}$ = Net section area of the member in the faulted state. This is equal to the net area of a single channel (in^2).
$\boldsymbol{f_{AFN}}$ = Factored total net section stress in the faulted state (ksi).
$\boldsymbol{P_u}$ = Total factored applied tensile load (kip).
$\boldsymbol{I_y}$ = Principle axis moment of inertia about the weak axis of a single channel (in^4).
$\boldsymbol{c}$ = Distance from the centroid of the channel to the surface of stress calculation (in).
$\boldsymbol{M_{AF}}$ = After-fracture moment resulting from failure of a channel in a two-channel member (kip-in).

The flexural stress calculation requires the input of the variable, *c*, which is the distance from the channel weak orientation neutral axis to the spot on the channel for which the stress calculation is being made. Failure of a channel will result in the intact channel bending inward toward the failed channel, or toward the center of the member. This means that the highest combination of tensile axial and flexural stress will result at the interior surface of the intact channel. The stress should be estimated for the location of fasteners that are closest to the center of the member because they would likely be the most fatigue prone detail subjected to the greatest tensile stress range. For the case of the Winona Bridge Specimen 6, shown in Figure 4.57 where the channels were oriented with the flanges pointing away from the center of the member, this would be the inward surface of the cover plate where fasteners holes were located. Generally speaking, though, two-channel members will only have fasteners in the flanges used for connection to lattice bars or stay plates. Therefore, the flexural stress would be calculated for the

centerline position of the fasteners in the channel flanges. If the channels were oriented with flanges pointed outward, this could mean that the fastener holes may be subjected to compressive flexural stresses.

Finally, Equations 4.8 through 4.12 are intended for use in the calculation of strength limit states, as well as fatigue. The residual dead load that redistributes following failure of a single channel will generate a residual secondary moment that is combined with the increased axial load demands on the remaining channel. Then the same equations are used for the factored live loads in order to estimate after-fracture net section stress range leading to evaluation of fatigue life.

4.6.5.2. Validation Exercise: Simplified Analysis of Two-Channel Members

Data collected on the Winona Bridge chord, Specimen 6, were used to validate the simplified analysis method for continuous stay-plated two-channel members. The Winona Bridge test specimen data were used to calibrate the finite element models utilized to perform the parametric study for two-channel members. However, the geometries used to develop the simplified method of analysis did not specifically include the Winona Bridge tension chord. This means it was reasonable to use the experimental data collected on the Winona Bridge specimens to validate the simplified method. Moreover, the experimental data was preferred for a validation process because it was a physical measurement of stresses in a true bridge member, rather than an assumed and idealized geometry analyzed using finite element.

Although Specimen 6 was not two-channel member, it was treated as such by severing an entire half of the member. If the Winona Bridge chord, or one similar to it, were being evaluated in reality, it would be treated as a multi-component member due to the fact that the rolled channels each had redundant web plates that would prevent an entire half of the cross section from fracturing. Furthermore, prior to cutting of the channel on Specimen 6, the redundant web plate (or cover plate) was cut and the specimen was loaded measuring load, displacement and stress. It was observed that no second order moment was generated in the member, as it was for the case when an entire half of the member was severed. This observation supports the categorization of a member configured similar to the Winona Bridge tension chord as a “multi-component member” where load redistribution was managed within the portion of the member containing the failure component. However, solely for the purpose of validating the two-channel member simplified analysis methods, this member was treated as if there were only two components where one entire half has fractured leaving half of the original cross section to carry the full axial load and

secondary moment resulting from load redistribution. Final conclusions from the FEM-based parametric study confirm that this approach was reasonable and effective.

Figure 4.57 shows the cross-sectional view of Specimen 6 at the location of the severed channel and cover plate. The channel and cover plate that were cut have been hatched with black lines. Strain gages are sketched on the intact cross section with blue rectangles at the exact locations they were installed on the test specimen, but are not to scale. Each gage is labeled with the channel identity prescribed to them during the experimental testing. Gage A11 was centered in the net section between the two rows of rivets that stitched the cover plate to the rolled channel. Gage A13 was directly opposite of A11 on the outward surface of the channel web. The eccentricity of the member, *e*, was calculated based on the composite section of the channel and redundant web plate. The weak orientation neutral axis is shown, labeled "*NA*", which was positioned very closely to the outward surface of the channel web. Stay plates were located in the foreground and background of the location of the cross section shown, but have been removed for clarity.

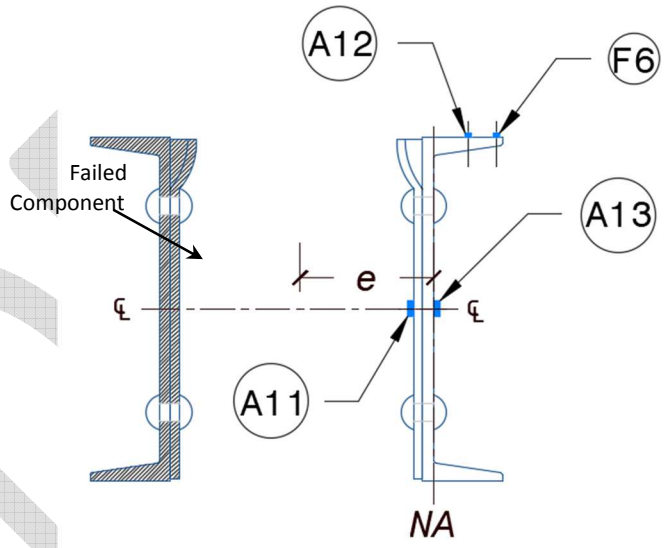

Figure 4.57 Cross sectional view of Winona Bridge Specimen 6, cut location "A", showing exact locations of strain gages used for validation example

Table 4.11 lists the member properties that were used for the validation exercise. A_{AFN} was the after-fracture net section area, N_{SP} was the number of stay plate pairs within a panel length, *e* was the distance from the centroid of the member in the unfaulted state to the centroid of the member in the faulted state, d_{CH} was the depth of the channels, c_{A11} was the distance from the centroid (neutral axis) of the member

in the faulted state to the location of gage A11, c_{A13} was the distance from the centroid (neutral axis) of the member in the faulted state to the location of gage A13, and I_y was the weak axis moment of inertia for the remaining half of the member.

Table 4.11 After-fracture properties for Specimen 6

Member Property	Units	Value
A_{AFN}	in^2	15.91
N_{SP}	-	8
e	in	5.96
d_{CH}	in	15
c_{A11}	in	0.845
c_{A13}	in	-0.03
I_y	in^4	12.8

Table 4.12 contains the results for the simplified method of analysis, as well as the measured stresses collected during two loading cycles, Test 9 and Test 10, for Specimen 6. P was the total axial load applied to the member, which is presented in increments of 50 kips. M_{AF} was the after-fracture moment calculated using Equation 4.8 for continuous stay-plated two-channel members. f_{bend} was the stress in the member due to the after-fracture moment, M_{AF}, calculated for the position of strain gage A11. f_{axial} was the after-fracture net section axial stress calculated by dividing P by the after-fracture net section area, A_{AFN}. f_{AFN} was the total after-fracture net section stress calculated using Equation 4.12, or simply adding f_{bend} to f_{axial}. The final two columns contain the experimental results measured with strain gage A11, located on the inward surface of the redundant web plate (see Figure 4.57).

Table 4.12 Validation results for Specimen 6, gage A11 located on cover plate

Load, P (kip)	M_{AF} (kip-in)	f_{bend} (ksi)	f_{axial} (ksi)	f_{AFN} (ksi)	Test 9, Gage A11 (ksi)	Test 10, Gage A11 (ksi)	Test Average (ksi)	Percent Error
50	32.4	2.1	3.1	5.3	5.1	5.2	5.2	1.9%
100	64.9	4.3	6.3	10.6	11.1	9.3	10.2	3.8%
150	97.3	6.4	9.4	15.9	15.8	15.3	15.6	1.9%
200	129.8	8.6	12.6	21.1	21.3	20.8	21.1	0%
250	162.2	10.7	15.7	26.4	25.3	24.7	25.0	5.3%
300	194.7	12.9	18.9	31.7	30.2	30.0	30.1	5%

Table 4.13 contains the results for the simplified method of analysis, as well as the measured stresses collected during two loading cycles, Test 9 and Test 10, for Specimen 6. *P* was the total axial load applied to the member. M_{AF} was the after-fracture moment calculated using Equation 4.8 for continuous stay-plated two-channel members. f_{bend} was the stress in the member due to the after-fracture moment, M_{AF}, calculated for the position of strain gage A13. f_{axial} was the after-fracture net section axial stress calculated by dividing *P* by the after-fracture net section area, A_{AFN}. f_{AFN} was the total after-fracture net section stress calculated using Equation 4.12, or simply adding f_{bend} to f_{axial}. The final two columns contain the experimental results measured with strain gage A13, located on the outward surface of the channel web. As can be seen on Figure 4.57, gage A13 was installed very close to the weak direction neutral axis of the member in the faulted state, which is why the flexural stress component was nearly zero at all load steps.

Table 4.13 Validation results for Specimen 6, gage A13 located on the channel web

Load, *P* (kip)	M_{AF} (kip-in)	f_{bend} (ksi)	f_{axial} (ksi)	f_{AFN} (ksi)	Test 9, Gage A13 (ksi)	Test 10, Gage A13 (ksi)	Test Average (ksi)	Percent Error
50	32.4	-0.1	3.1	3.0	3.8	2.5	3.2	-6.6%
100	64.9	-0.2	6.3	6.1	5.6	4.9	5.3	13.1%
150	97.3	-0.2	9.4	9.2	8.1	10.0	9.1	1%
200	129.8	-0.3	12.6	12.3	11.3	10.9	11.1	9.7%
250	162.2	-0.4	15.7	15.3	13.9	13.3	13.6	11.1%
300	194.7	-0.5	18.9	18.4	17.0	16.5	16.7	9.2%

Comparing results from strain gage A11 for Test 9 and Test 10 to f_{AFN} in Table 4.12 yields:

- The largest over estimation from the simplified method was 14% (1.3 ksi) for Test 10 at the 100 kip load step,
- The greatest under estimate was 5% (-0.5 ksi) for Test 9 at the 100 kip load step,
- The combined average error for all of Test 9 was an over estimation of 1%,
- And the combined average error for Test 10 was an over estimate of 6%.

Results shown in Table 4.12 would be used to determine the after-fracture net section stress and establish the remaining fatigue life of the member. However, to extend the validation exercise further, the data set collected for strain gage A13 on the channel web was also compared to the simplified method of analysis.

Weighing results from strain gage A13 for Test 9 and Test 10 against f_{AFN} in Table 4.13 yields:

- The greatest over estimation from the simplified method was 25% (1.2 ksi) for Test 10 at the 50 kip load step,
- The largest under estimate was 19% (-0.7 ksi) for Test 9 at the 150 kip load step,
- The average error for all of Test 9 was an over estimation of 5%,
- And the average error for Test 10 was an over estimation of 13%.

The two experimental test results can also be averaged and then compared to the simplified method solutions. For stress at the location of gage A11:

- The largest over estimate becomes 5.3% (1.4 ksi) at the 250 kip load step,
- There was no under estimation,
- The error at the peak load was a 5% (1.6 ksi) over estimation,
- And the combined average error was a 3% over estimation.

For stress at the location of gage A13:

- The largest over estimate became 13.1% (0.8 ksi) at the 100 kip load step,
- The largest under estimation became -6.6% (-0.2 ksi) at the 50 kip load step,
- The error at the peak load was a 9.2% over estimation,
- And the combined average error was an 6.2% over estimation.

It was anticipated that results from the simplified method for the location of gage A13 could have larger margins of error due to the fact that it was located very close to the estimated neutral axis of bending. However, overall the results agreed well. The simplified method was able to predict the after-fracture net section stress for the controlling fatigue detail to within acceptable margins of error at multiple load steps.

4.6.5.3. Guidance for Use of Closed-form Solution for Two-Channel Members

The simplified method of analysis was developed taking into account failures at mid-panel and near the gusset connections capturing the largest resulting moments for the geometries analyzed. This means that a single after-fracture moment calculation and net section stress calculation need to be performed

for each member. There is no need to repeat this calculation multiple times for different cross sections of the same member. Figure 4.58 and Figure 4.59 illustrate two typical types of trusses where two-channel members could be used. Figure 4.58 shows a generic three-span continuous deck truss structure. Figure 4.59 depicts a generic single-span through-truss structure. Each figure has been highlighted with red and blue lines. The red lines indicate members that would be analyzed using either Equation 4.8 (stay-plated) or 4.9 (laced) for continuous members. The blue lines designate members that would be evaluated using either Equation 4.10 (stay-plated) or 4.11 (laced) for non-continuous members. Members that are *not* highlighted, or which appear black, are compression members that would not need to be evaluated for internal redundancy. Reversal zones that are subjected to both tensile and compressive live load stresses would also need to be evaluated. Notice that the terminating bottom chord of each truss is evaluated using equations for non-continuous members. Due to the lack of continuity beyond the abutment at each end of a truss, the last panel must be analyzed using equations developed for non-continuous members.

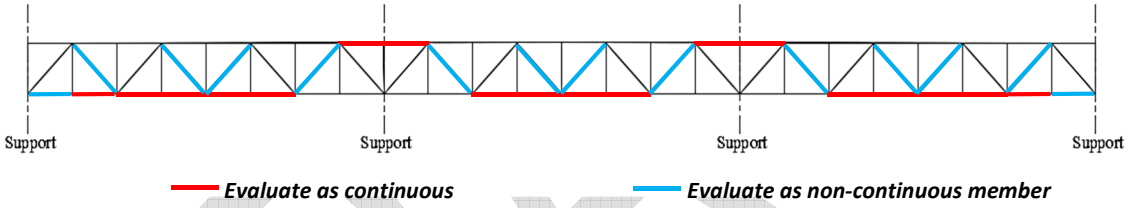

Figure 4.58 Sketch illustrating correct application of equations 4.8 – 4.11on continuous trusses

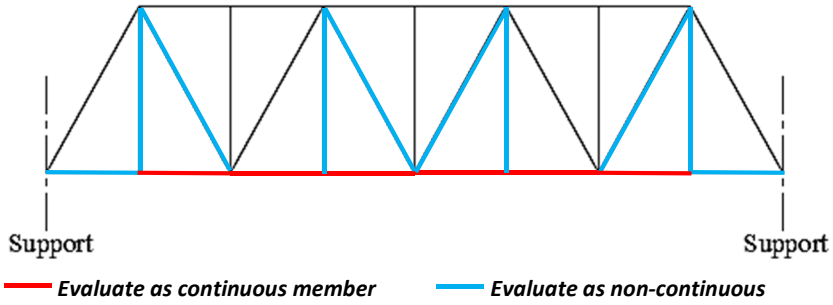

Figure 4.59 Sketch illustrating correct application of equations 4.8 – 4.11 on simple span trusses

5. SUMMARY AND CONCLUSIONS

The objectives of this research were to determine if mechanically-fastened steel built-up axially-loaded tension members are resistant to complete cross-sectional fracture when an individual component suddenly fractures and if so, to develop simplified methods of analysis for post-fracture load redistribution behavior for calculation of remaining fatigue life. The ability to resist complete member failure and perform at a predetermined level of reliability in the faulted condition is referred to as internal member redundancy (IMR). The term coined herein to describe the capacity of these members to arrest fracture at the boundary between fastened components is *cross-boundary fracture resistance* (CBFR). Extremely demanding fracture tests were performed on five full-scale specimens, including one with a tack weld placed in the fracture path. Two additional full-scale specimens removed from a 1940's era built-up riveted deck truss were partially failed and tested to calibrate finite element models for two-channel members. Comprehensive finite element model-based parametric studies were carried out investigating the load redistribution behavior and resulting stress amplification for multi-component, angle-only, and two-channel type axial members. Simplified closed-form solutions were developed for members of any geometry that fall within these broad categories of built-up axially-loaded tension members.

The simplified methods of analysis for axial members found herein are intended to build upon existing redundancy research. For the complete assessment of member-level redundancy of axial member, load factors developed by Connor *et al*. (2018) for the Redundancy II load case would be used to factor axial loads. Fatigue categories codified in AASHTO (2017) would be used to establish the estimated fatigue life in the unfaulted state. Fatigue categories developed by Hebdon *et al*. (2015) would be used to estimate fatigue life in the faulted condition. A fatigue life methodology that includes Case I (infinite fatigue life in the unfaulted state) and Case II (finite fatigue life in the unfaulted state) scenarios advanced by Hebdon *et al*. (2015) would be applied in the process of establishing axial IRM special inspection intervals. The basic procedure for evaluating axial member internal redundancy would go as follows:

1. Identify the type of member being evaluated, whether multi-component, angle-only, or two-channel member. Other types of mechanically-fastened built-up axially-loaded tension members were not presently researched and therefore would require adequate, independent finite element analysis.

2. Calculate the fatigue life in the unfaulted state based on the live load stresses and AASHTO fatigue detail categories that are appropriate for the member. Bolted members will be Category B and riveted members will be Category D. Category C is not used when evaluating riveted members in the unfaulted condition even though it is allowed by the AASHTO Manual for Bridge Evaluation, as is explained by Hebdon *et al*. (2015). The reasoning is that widespread cracking in the components is undesirable for member-level redundancy. Determining the fatigue life based on Category D resistance will help ensure members with very low risk of existing fatigue damage move forward in the evaluation of internal redundancy and those at higher risk are screened from the process.
3. The strength limit states are checked using appropriate Redundancy II load factors (Connor *et al*., 2018). Members must meet strength requirements in the faulted condition before moving forward in the IRM evaluation process. The stress amplification factors are set equal to 1.0. Closed-form solutions developed herein are used to calculate the strength demands.
4. Compute the after-fracture net section stress. Use the stress amplification factors and other pertinent equations for the simplified analysis described herein based on the type of member.
5. Estimate the fatigue life of the axial member in the faulted condition.
6. A special inspection interval is established based on the governing (*i.e*., shortest) fatigue life of the member in the faulted condition. Proposed guide specifications are currently being considered by appropriate governing committees that will clarify this process and help guide suitable inspection intervals.
7. Once a member has been evaluated and determined to be an internally redundant member (IRM), redesignation of the member from fracture critical member (FCM) to IRM would be completed, provided it is allowed by governing policy and regulation.

The IRM evaluation process is intended to combine the probability of detection (POD) of fatigue cracks on steel bridges with the fatigue damage tolerance of mechanically-fastened built-up members. Preliminary results from ongoing POD research at Purdue University suggests that the steel bridge industry has unknowingly been relying on internal redundancy of mechanically-fastened built-up members for a long time. In other words, due to the difficulty of finding small cracks in components of built-up members, it is more likely that traditional arms-length inspections of fracture-critical members

will find broken components instead. More candidly stated, this research provides the industry with quantitative analysis for the purpose of establishing rational inspection intervals for built-up axial members that are realistic about what can be reliably found during inspections and for what duration undiscovered damage can be safely tolerated due to internal member redundancy of the mechanically-fastened built-up member.

5.1. Summary of Principal Findings

The following is a succinct summary of principal findings for the present research.

5.1.1. Summary of Fracture Resistance

1. Cross-boundary fracture resistance (CBFR) is the capacity to resist complete cross-sectional fracture by arresting a running fracture at the boundary between components. Mechanically-fastened built-up axial members were found to possess CBFR sufficient to survive harsh fracture tests when certain limits on component proportions were met and there was positive remaining fatigue life at the time the fault occurred.
2. Toughness was not an essential property for mechanically-fastened built-up axial members to resist full member fracture because of CBFR.
3. It is believed to be a very unlikely possibility that a tack weld would be intercepted by a running fracture. However, should it happen, this research concluded that the tack weld would not provide a crack propagation path into adjacent components.

5.1.2. Summary of Multi-component Member Load Redistribution Behavior

1. Between 80% and 100% of load in a failed component was redistributed into the adjacent component(s) in direct contact with the failed component, even when other components not in contact with the failed component were present.
2. Typically, in a member comprised of angles and plates, the failure of a plate produced the largest stress range in remaining components due to the proportionately larger load being redistributed. Only two cases were found where a failed angle could govern the after-fracture net section stress calculation:
    a. Built-up I-sections

b. Built-up channels where the combined gross area of two angles is greater than or equal to 1.3 times the gross area of the plate to which they are in direct contact.

3. Boundary conditions had negligible effects due to highly localized load redistribution.
4. Shear lag effects in adjacent components were found to amplify stress by 20% on average above the calculated net section stress in the faulted condition.
5. Localized bending of adjacent components was found to increase stress concentrations by as much as 30%, being inversely proportional to the number of plates within the member; *i.e.*, the more plates within the member, the lower the effect of local bending resulted.
6. Position of the failed plate within the member had a notable influence on the local bending effect, such that failed interior plates effectively resulted in zero bending amplification.
7. Equations 4.1, 4.2, and 4.3 were developed to calculate after-fracture net section stress for multi-component axially-loaded members.

5.1.3. Summary of Angle-only Member Load Redistribution Behavior

1. Between 80% and 100% of load in a failed angle was redistributed into the attached angle leg of the adjacent angle.
2. Boundary conditions had negligible effects due to relatively high flexibility of the angle-only members.
3. The number of fasteners within intermittent fastener groups was found to have no effect on results. The thickness of the batten plate (for four-angle members) or spacer plate (for two-angle members) also produced no effect.
4. Shear lag effects in adjacent angles were found to amplify stress by 30% on average above the calculated net section stress in the faulted condition.
5. Bending effects in two-angle members were best correlated using the moment of inertia of the intact angle. Bending effects in four-angle members were best correlated using the angle gap distance combined with the fastener group spacing.
6. Equations 4.4 for two-angle members, 4.6a and 4.6b for four-angle members, and 4.7 were developed to calculate after-fracture net section stress for angle-only type axially-loaded members.

5.1.4. Summary of Two-channel Member Load Redistribution Behavior

1. Stay-plated members were studied independently of laced members due to differences in load redistribution behavior.
2. Load redistribution behavior of two-channel members was less localized than for angle-only and multi-component members. Rather than local stress amplification factors, the parametric study developed methods for calculating the resulting after-fracture moment that is combined with axial load to calculate stress in the faulted condition.
3. Due to the global behavior of two-channel members, boundary conditions were found to have a very significant effect on results. Rotational stiffness of the joints strongly influenced results forcing the parametric study to look at continuous and non-continuous members separately. A reasonably conservative approach for simulating boundary conditions of non-continuous members was done by attaching gusset plates with fixed ends. Gusset plate thickness, member embedment depth into the gusset plates, and the gusset plate length parameters yielded negligible effects on results.
4. Location of failures between end stay plates and gusset plate connections for continuous and non-continuous members nearly always resulted in the largest after-fracture moment.
5. Channel size, channel spacing, stay plate size, and lattice bar sizes had minimal to no effect on results.
6. Length of the member had negligible effect on results for both member types.
7. Equations 4.8 for continuous stay-plated two-channel members, 4.9 for continuous laced two-channel members, 4.10 for non-continuous stay-plated two-channel members, and 4.11 for non-continuous laced two-channel members were developed to calculate after-fracture secondary moment for two-channel type axially-loaded members. Equation 4.12 is used to calculate the after-fracture net section stress.

5.2. Recommendations for Future Work

1. There are many types of built-up axial members used on a broad range of truss types and sizes. Multi-component, angle-only, and two-channel members make up a majority of those members. However, there are others that exist which could not be included in this research that would be good to study. One example is a two-component member made up of WT sections laced together to form a built-up I-section. A study of the remaining “odds

and ends" members would further enhance the present research and expand the reach of the simplified methods of analysis for bridge owners.

2. A conservative approach was taken in this research whereby it was assumed that all of the load in a member stays within the member after fracture occurs. Load shedding in built-up members having only two components where upon fracture of one component the axial stiffness of the member is significantly reduced, diminishes the after-fracture demands on a member in the faulted state. When axial load demands are reduced, consequently the secondary after-fracture moment is too. A study to develop a simplified method to determine how much load would remain in the faulted two-component member following failure of a single component could further improve upon the estimated fatigue life in the faulted state.
3. Built-up tie-girders are traditionally classified as fracture-critical members. The Hastings Bridge demonstrated internal redundancy when a web plate failed. Extending this research to include a simple closed-form solution for built-up tie-girders would further enhance the present research and expand the reach of the simplified methods of analysis for bridge owners.
4. There remain many historic steel bridges that possess multi-eyebar members, particularly within the railroad inventories. Load redistribution behavior of these members will be dependent upon joint rotational stiffness, similar to two-channel members, but likely even more so. A study of multi-eyebar member load redistribution behavior that develops a simplified method of analysis for this type of member would further enhance the present research and expand the reach of the simplified methods of analysis for bridge owners.

LIST OF REFERENCES

AASHTO. (2017). *AASHTO LRFD Bridge Design Specifications*. *Transportation* (7th Ed.). Washington DC, USA.

AASHTO (2016). *AASHTO Manual for Bridge Evaluation*. (2nd Edition). Washington, DC, USA.

American Welding Society (AWS). (2015). AWS D1.5:2015 Bridge Welding Code. Miami, FL.

Baker, K. A., and Kulak, G. L. (1982). *Fatigue Strength of Two Steel Details*. Structural Engineering Report No. 105. Department of Civil Engineering, University of Alberta, Edmonton, Alberta.

Bowman, M. D., Fu, G., Zhou, Y. E., Connor, R. J., & Godbole, A. A. (2012). *NCHRP Report 721: Fatigue Evaluation of Steel Bridges*. Washington DC, USA.

Brown, J. D., Lubitz, D. J., Cekov, Y. C., Frank, K. H., & Keating, P. B. (2007). *Evaluation of Influence of Hole Making Upon the Performance of Structural Steel Plates and Connections*. Austin, TX.

Cha, H., Lyrenmann, L., Connor, R. J., and Varma, A. H. (2014). *Experimental and Numerical Evaluation of the Postfracture Redundancy of a Simple Span Truss Bridge*. Journal of Bridge Engineering. American Society of Civil Engineers. DOI: 10.1061/(ASCE)BE.1943-5592.0000622.

Collette, Q. (2014). *Riveted Connections in Historical Metal Structures (1840 - 1940)*. Vrije University Brussel. DOI: 10.13140/2.1.3157.2801.

Connor, R. J., Bonachera Martin, F. J., Korkmaz, C., Varma, A. H., and Lai, Z. (2018). *NCHRP Report 883: Fracture-Critical System Analysis for Steel Bridges*. Washington, D.C.

Connor, R. J. and Lloyd, J. B. (2017). *NCHRP 20-07/Task 387 Report: Maintenance Actions to Address Fatigue Cracking in Steel Bridge Structures*. Washington, D.C., USA.

Connor, R. J., Dexter, R., & Mahmoud, H. (2005). *NCHRP Synthesis 354: Inspection and Management of Bridges with Fracture-Critical Details* (p. 84). Washington DC, USA.

DiBattista, J. D. and Kulak, G. L. (1995). Fatigue of Riveted Tension Members. Structural Engineering Report N. 211, University of Alberta. Edmonton, Alberta.

Diggelmann, L. M., Connor, R. J., & Sherman, R. J. (2013). *Evaluation of Member and Load-Path Redundancy on the US-421 Bridge Over the Ohio River*. Washington DC, USA.

Federal Aid Highway Act. , Pub. L. No. 90-495 (1968).

FHWA. (2012). *Memorandum: Clarification of Requirements for Fracture Critical Members*.

FHWA. (1995). *Recording and Coding Guide for the Structure Inventory and Appriasial of the Nation's Bridges*. Report No. FHWA-PD-96-001.

Fisher, J. W., Yen, B. T., & Wang, D. (1990). *Fatigue Strength of Riveted Bridge Members*. Journal of Structural Engineering, *116*(11), 2968. doi:10.1061/(ASCE)0733-9445(1990)116:11(2968)

Fisher, J. W., Yen, B. T., Wang, D., & Mann, J. E. (1987). *NCHRP Report 302 - Fatigue and Fracture Evaluation for Rating Riveted Bridges*. Transportation Research Board. Washington DC, USA.

Hebdon, M. H., Korkmaz, C., Martín, F. J., & Connor, R. J. (2015). *Member-level redundancy of built-up steel girders subjected to flexure.* West Lafayette, IN: Purdue University. https://doi.org/10.5703/1288284316728

Hebdon, M. H., Bonachera Martin, F. J., Korkmaz, C., and Connor, R. J. (2017a). *Fracture Resilience of Steel Built-up Members Subjected to Flexure*. Journal of Bridge Engineering, American Society of Civil Engineers (ASCE). Doi: 10.1061/(ASCE)BE.1943-5592.0001059.

Hebdon, M. H., Bonachera Martin, F. J., Korkmaz, C., and Connor, R. J. (2017b). *Load Redistribution and Remaining Fatigue Life of Steel Built-up Members Subjected to Flexure Following a Component Failure*. Journal of Bridge Engineering, American Society of Civil Engineers (ASCE). Doi: 10.1061/(ASCE)BE.1943-5592.0001087.

Judy, S. (2013). *FDOT Scrambles to Make Repairs to Mathews Bridge*.[online]. Engineering News Record (ENR). Available from: <https://www.enr.com/articles/12001-fdot-scrambles-to-make-repairs-to-mathews-bridge>. [Accessed June 2018].

Kulak, G. L. , Fisher, J. W., and Struik, J. H. (2001). Guide to Design Criteria for Bolted and Riveted Joints. American Institute of Steel Construction (AISC). Chicago, IL.

Lwin, M. M. (2012). *Clarification of Requirements for Fracture Critical members*. Memorandum HIBT-10 to Directors of Field Services, Federal Lands Highway Division Engineers, and Division Administrators. Federal Highway Administration (FHWA), Washington, D. C.

Martin, F. J. B. (2014). *Detailed Finite Element Analysis and Preliminary Study of the Effects of Friction and Fastener Pre-Tension on the Mechanical Behavior of Fastened Built-Up Members*. Purdue University, West Lafayette, IN.

Mekker, M. M., Remias, S. M., McNamara, M. L., and Bullock, D. M. (2015). *Characterizing Interstate Crash Rates Based on Traffic Congestion Using Probe Vehicle Data*. Transportation Research Board. Washington, D.C. Available at: < http://docs.trb.org/prp/16-1194.pdf>

National Bridge Inspection Standards. (1971). *Federal Register*, *36*(81), 7851–7852.

National Bridge Inspection Standards. (1988). *Federal Register*, *53*, 32611.

Niemann, T. L. (1999). Hastings Bridge Fracture Investigation. In *The International Bridge Conference*. Pittsburgh, PA.

Ocel, J. M. (2013). NCHRP Web-Only Document 197: *Guidelines for the Load and Resistance Factor Design and Rating of Riveted and Bolted Gusset-Plate Connections for Steel Bridges*. Transportation Research Board. Washington DC, USA.

Out, J., Fisher, J., & Yen, B. (1984). Fatigue strength of weathered and deteriorated riveted members, October 1984.(DOT/OST/P-34/85/016) 138p, (October).

RCSC Committee A.1. (2014). *Specifications for Structural Joints Using High Strength Bolts*. Research Council on Structural Connections. Chicago, IL.

Reemsnyder, H. S. (1975). *Fatigue Life Extension of Riveted Connections*. J. Structural Division, ASCE, 101(12), 2591-2608.

Rice, J. (2017). *Large Fracture in Steel Truss Closes Deleware River Bridge*.[online]. Engineering News Record (ENR). Available from: <https://www.enr.com/blogs/11-mid-atlantic-monitor/post/41308-large-fracture-closes-delaware-river-bridge>. [Accessed June 2018].

Zhou, Y. E. (1994). *Fatigue Strength Evaluation of Riveted Bridge Members*. Lehigh University.

APPENDIX A. TWO-CHANNEL MEMBER GEOMETRIES

Table A.1 Geometries for continuous stay-plated two-channel models

Model ID	Section	SP Length / Channel Depth	No. SP[1]	SP Thickness (in)	Panel Length (ft)	CS / CD	End BC	Failure Location[2]
C-SP1	15x40	1	6	3/8	20	1	Fix	Mid-Panel
C-SP2	15x40	1	6		20	1	Pin	Mid-Panel
C-SP3	15x40	1	6		20	1	Fix	Gusset
C-SP4	15x40	0.5	6		20	1	Fix	Mid-Panel
C-SP5	15x40	0.5	6		20	1	Pin	Mid-Panel
C-SP6	15x40	2	6		20	1	Fix	Mid-Panel
C-SP7	15x40	2	6		20	1	Pin	Mid-Panel
C-SP8	15x40	2	6		20	1	Fix	Gusset
C-SP9	15x40	1	4		20	1	Fix	Mid-Panel
C-SP10	15x40	1	4		20	1	Pin	Mid-Panel
C-SP11	15x40	1	4		20	1	Fix	Gusset
C-SP12	15x40	1	10		20	1	Fix	Mid-Panel
C-SP13	15x40	1	10		20	1	Pin	Mid-Panel
C-SP14	15x40	1	10		20	1	Fix	Gusset
C-SP15	15x40	1	6		40	1	Fix	Mid-Panel
C-SP16	15x40	1	6		40	1	Pin	Mid-Panel
C-SP17	15x40	1	6		40	1	Fix	Gusset
C-SP18	15x40	1	10		20	0.5	Fix	Mid-Panel
C-SP19	15x40	1	10		20	0.5	Pin	Mid-Panel
C-SP20	15x40	1	10		20	0.5	Fix	Gusset
C-SP21	15x40	1	10		20	2	Fix	Mid-Panel
C-SP22	15x40	1	10		20	2	Fix	Gusset
C-SP23	15x40	1	10		20	2	Pin	Mid-Panel
C-SP24	15x40	1	4		20	0.5	Fix	Mid-Panel
C-SP25	15x40	1	4		20	0.5	Fix	Gusset
C-SP26	15x40	1	4		20	2	Fix	Mid-Panel
C-SP27	15x40	1	4		20	2	Fix	Mid-Panel
C-SP28	8x11.5	1	4		20	1	Fix	Mid-Panel
C-SP29	8x11.5	1	6		20	1	Fix	Mid-Panel
C-SP30	8x11.5	0.5	6		20	0.5	Fix	Mid-Panel
C-SP31	8x11.5	2	6		20	2	Fix	Mid-Panel
C-SP32	8x11.5	1	4		20	1	Fix	Gusset
C-SP33	8x11.5	1	6		20	1	Fix	Gusset
C-SP34	8x11.5	0.5	6		20	0.5	Fix	Gusset
C-SP35	8x11.5	2	6		20	2	Fix	Gusset

Notes: SP = Stay plate; BC Boundary condition; CD = Channel Depth (in.); CS = Channel Spacing, or 2*e* (in.)
1. Number of stay plates within a single panel length (between two gusset connections)
2. Mid-Panel refers to a location centered on the member mid-way between gusset connections

Table A.2 Geometries for continuous laced two-channel models

Model ID	Section	LS (in)	Lattice Bar Width (in)	Lattice Bar Thickness (in)	Panel Length (ft)	CS / CD	End BC	Failure Location
C-L1	15x40	12	2	3/8	40	1	Fix	Mid-Panel
C-L2	15x40	12			40	1	Pin	Mid-Panel
C-L3	15x40	12			40	1	Fix	Gusset
C-L4	15x40	12			40	1	Pin	Gusset
C-L5	15x40	12			20	1	Fix	Mid-Panel
C-L6	15x40	12			20	1	Pin	Mid-Panel
C-L7	15x40	12			20	1	Fix	Gusset
C-L8	15x40	12			20	1	Pin	Gusset
C-L9	15x40	7.5			40	0.5	Fix	Mid-Panel
C-L10	15x40	7.5			40	0.5	Pin	Mid-Panel
C-L11	15x40	7.5			40	0.5	Fix	Gusset
C-L12	15x40	7.5			40	0.5	Pin	Gusset
C-L13	15x40	7.5			20	0.5	Fix	Mid-Panel
C-L14	15x40	7.5			20	0.5	Pin	Mid-Panel
C-L15	15x40	7.5			20	0.5	Fix	Gusset
C-L16	15x40	7.5			20	0.5	Pin	Gusset
C-L17	15x40	27			40	2	Fix	Mid-Panel
C-L18	15x40	27			40	2	Pin	Mid-Panel
C-L19	15x40	27			40	2	Fix	Gusset
C-L20	15x40	27			40	2	Pin	Gusset
C-L21	15x40	27			20	2	Fix	Mid-Panel
C-L22	15x40	27			20	2	Pin	Mid-Panel
C-L23	15x40	27			20	2	Fix	Gusset
C-L24	15x40	27			20	2	Pin	Gusset
C-L25	15x40	7.5			20	0.5	Fix	End Gusset
C-L26	15x40	12			20	1	Pin	End Gusset

Notes: PL = Panel length (in.); LS = Lacing spacing (in.); CD = Channel Depth (in.); CS = Channel Spacing, or 2*e* (in.); BC = Boundary condition

Table A.3 Geometries for non-continuous stay-plated two-channel models

Model ID	Section	Gusset Thickness (in)	No. SP[1]	SP Clear Distance (in)	SP Thickness (in)	Panel Length (in)	CS / CD	End BC	Failure Location[2]
N-SP1	15x50	3/8	2	36	3/8	56	0.5	Fixed Gusset Plate	Gusset
N-SP2	15x50	3/8	2	36		74	1		Gusset
N-SP3	15x50	3/8	2	36		112	2		Gusset
N-SP4	15x50	3/8	3	36		97	0.5		Gusset
N-SP5	15x50	3/8	3	36		119	1		Gusset
N-SP6	15x50	3/8	3	36		165	2		Gusset
N-SP7	15x50	3/8	5	36		179	0.5		Gusset
N-SP8	15x50	3/8	5	36		209	1		Gusset
N-SP9	15x50	3/8	5	36		271	2		Gusset
N-SP10	15x50	3/8	8	36		302	0.5		Gusset
N-SP11	15x50	3/8	8	36		344	1		Gusset
N-SP12	15x50	3/8	8	36		430	2		Gusset
N-SP13	15x50	7/8	2	36		56	0.5		Gusset
N-SP14	15x50	7/8	3	36		97	0.5		Gusset
N-SP15	15x50	7/8	3	36		119	1		Gusset
N-SP16	15x50	7/8	5	36		209	1		Gusset
N-SP17	15x50	7/8	5	36		271	2		Gusset
N-SP18	15x50	7/8	8	36		430	2		Gusset
N-SP19	15x50	3/8	8	36		326	1		Gusset
N-SP20	15x50	3/8	2	36		56	1		Gusset
N-SP21	15x50	3/8	4	36		110	1		Gusset
N-SP22	15x50	3/8	8	36		218	1		Gusset
N-SP23	15x50	3/8	8	36		218	1		Gusset
N-SP24	15x50	3/8	3	148.5		344	1		Gusset
N-SP25	15x50	3/8	2	36		56	0.5		Mid-Panel
N-SP26	15x50	3/8	2	36		74	1		Mid-Panel
N-SP27	15x50	3/8	2	36		112	2		Mid-Panel
N-SP28	15x50	3/8	4	36		164	1		Mid-Panel
N-SP29	15x50	3/8	3	148.5		344	1		Gusset
N-SP30	15x50	3/8	6	36		254	1		Mid-Panel
N-SP31	15x50	3/8	3	146		326	1		Gusset
N-SP32	15x50	3/8	8	36		302	0.5		Mid-Panel
N-SP33	15x50	3/8	8	36		344	1		Mid-Panel
N-SP34	15x50	3/8	8	36		430	2		Mid-Panel
N-SP35	8x11.5	3/8	2	36		46	0.5		Gusset
N-SP36	8x11.5	3/8	2	36		56	1		Gusset
N-SP37	8x11.5	3/8	2	36		76	2		Gusset
N-SP38	8x11.5	3/8	3	36		85	0.5		Gusset
N-SP39	8x11.5	3/8	3	36		97	1		Gusset
N-SP40	8x11.5	3/8	3	36		121	2		Gusset
N-SP41	8x11.5	3/8	5	36		163	0.5		Gusset
N-SP42	8x11.5	3/8	5	36		179	1		Gusset
N-SP43	8x11.5	3/8	5	36		211	2		Gusset
N-SP44	8x11.5	3/8	8	36		280	0.5		Gusset
N-SP45	8x11.5	3/8	8	36		302	1		Gusset
N-SP46	8x11.5	3/8	8	36		346	2		Gusset
N-SP47	8x11.5	3/8	2	36		46	0.5		Mid-Panel
N-SP48	8x11.5	3/8	2	36		56	1		Mid-Panel
N-SP49	8x11.5	3/8	2	36		76	2		Mid-Panel
N-SP50	8x11.5	3/8	8	36		280	0.5		Mid-Panel
N-SP51	8x11.5	3/8	8	36		302	1		Mid-Panel
N-SP52	8x11.5	3/8	8	36		346	2		Mid-Panel

Notes: SP = Stay plate; BC Boundary condition; CD = Channel Depth (in.); CS = Channel Spacing, or 2*e* (in.)

1. Number of stay plates within a single panel length;

2. Mid-Panel refers to a location centered on the member mid-way between gusset connections

Table A.4 Geometries for non-continuous laced two-channel models

Model ID	Section	LS (in)	Lattice Bar Width (in)	Lattice Bar Thickness (in)	Panel Length (ft)	CS / CD	End BC	Failure Location
N-L1	15x40	15	2	3/8	20	1	Fixed Gusset Plate	Mid-Panel
N-L2	15x40	30		3/4	20	2		Mid-Panel
N-L3	15x40	7.5		1/8	20	0.5		Mid-Panel
N-L4	15x40	30		5/8	20	1		Mid-Panel
N-L5	15x40	7.5		5/16	20	1		Mid-Panel
N-L6	15x40	15		3/8	40	1		Mid-Panel
N-L7	15x40	15		3/4	20	1		Mid-Panel
N-L8	15x40	15		1/8	20	1		Mid-Panel
N-L9	15x40	15		3/8	20	1		Mid-Panel
N-L10	15x40	-		-	20	1		Mid-Panel
N-L11	15x40	15		3/8	20	1		Gusset
N-L12	15x40	30		3/4	20	2		Gusset
N-L13	15x40	7.5		1/8	20	0.5		Gusset
N-L14	15x40	30		5/8	20	1		Gusset
N-L15	15x40	7.5		5/16	40	1		Gusset
N-L16	15x40	15		3/8	20	1		Gusset
N-L17	15x40	15		3/4	20	1		Gusset
N-L18	15x40	-		-	20	1		Gusset

Notes: PL = Panel length (in.); LS = Lacing spacing (in.); CD = Channel Depth (in.); CS = Channel Spacing, or 2*e* (in.); BC = Boundary condition

APPENDIX B. TABULATED RESULTS FOR TWO-CHANNEL MEMBERS

Table B.1 Moment ratio results for continuous stay-plated two-channel members

Model ID	Failure Location	No. SP x (CD/CS)	FEA Moment @ Adjacent Stay Plate (kip-in)	FEA Moment @ Midpoint of Adjacent Stay Plates (kip-in)	*P·e* (kip-in)	Ratio @ Stay Plate	Ratio @ Midpoint
C-SP1	Mid-Panel	5.45	58.0	48.3	2062.5	0.03	0.02
C-SP2	Mid-Panel	5.45	48.5	59.6	2062.5	0.02	0.03
C-SP3	Gusset	5.45	114.5	126.5	2062.5	0.06	0.06
C-SP4	Mid-Panel	5.45	52.3	38.2	2062.5	0.03	0.02
C-SP5	Mid-Panel	5.45	56.5	41.9	2062.5	0.03	0.02
C-SP6	Mid-Panel	5.45	77.0	74.3	2062.5	0.04	0.04
C-SP7	Mid-Panel	5.45	80.9	78.1	2062.5	0.04	0.04
C-SP8	Gusset	5.45	78.4	16.5	2062.5	0.04	0.01
C-SP9	Mid-Panel	3.64	34.3	8.6	2062.5	0.02	0.00
C-SP10	Mid-Panel	3.64	47.7	17.8	2062.5	0.02	0.01
C-SP11	Gusset	3.64	188.9	72.5	2062.5	0.09	0.04
C-SP12	Mid-Panel	9.09	117.1	115.1	2062.5	0.06	0.06
C-SP13	Mid-Panel	9.09	122.9	121.7	2062.5	0.06	0.06
C-SP14	Gusset	9.09	73.9	27.2	2062.5	0.04	0.01
C-SP15	Mid-Panel	5.45	66.2	17.4	2062.5	0.03	0.01
C-SP16	Mid-Panel	5.45	66.9	17.7	2062.5	0.03	0.01
C-SP17	Gusset	5.45	117.9	0.9	2062.5	0.06	0.00
C-SP18	Mid-Panel	16.67	168.2	166.6	1125.0	0.15	0.15
C-SP19	Mid-Panel	16.67	179.7	178.2	1125.0	0.16	0.16
C-SP20	Gusset	16.67	157.7	106.6	1125.0	0.14	0.09
C-SP21	Mid-Panel	4.76	63.8	63.1	3937.5	0.02	0.02
C-SP22	Gusset	4.76	81.5	69.1	3937.5	0.02	0.02
C-SP23	Mid-Panel	4.76	63.7	62.9	3937.5	0.02	0.02
C-SP24	Mid-Panel	6.67	54.5	20.9	1125.0	0.05	0.02
C-SP25	Gusset	6.67	102.2	3.5	1125.0	0.09	0.00
C-SP26	Mid-Panel	1.90	26.7	36.3	3937.5	0.01	0.01
C-SP27	Mid-Panel	1.90	94.7	17.4	3937.5	0.02	0.00
C-SP28	Mid-Panel	7.85	34.1	27.6	412.1	0.08	0.07
C-SP29	Mid-Panel	11.77	30.7	4.0	412.1	0.07	0.01
C-SP30	Mid-Panel	23.12	27.0	9.3	209.9	0.13	0.04
C-SP31	Mid-Panel	5.94	18.6	2.9	816.5	0.02	0.00
C-SP32	Gusset	7.85	51.2	30.6	412.1	0.12	0.07
C-SP33	Gusset	11.77	62.0	8.1	412.1	0.15	0.02
C-SP34	Gusset	23.12	48.5	10.9	209.9	0.23	0.05
C-SP35	Gusset	5.94	57.2	12.0	816.5	0.07	0.01

*Note: *Ratios* are the FEA results divided by the theoretical moment *P·e* at the respective location

Table B.2 Moment ratio results for continuous laced two-channel members

Model ID	Failure Location	(PL/LS) x (CD/CS)*	FEA Moment @ Mid-Panel (kip-in)	FEA Moment @ End Stay Plate (kip-in)	*P·e* (kip-in)	Ratio @ Mid-Panel	Ratio @ End Stay Plate
C-L1	Mid-Panel	40	92.1	48.1	1822.5	0.05	0.03
C-L2	Mid-Panel	40	94.7	47.4	1822.5	0.05	0.03
C-L3	Gusset	40	32.1	85.5	1822.5	0.02	0.05
C-L4	Gusset	40	31.4	90.0	1822.5	0.02	0.05
C-L5	Mid-Panel	20	86.1	100.5	1822.5	0.05	0.06
C-L6	Mid-Panel	20	77.7	70.0	1822.5	0.04	0.04
C-L7	Gusset	20	15.0	55.6	1822.5	0.01	0.03
C-L8	Gusset	20	38.3	60.0	1822.5	0.02	0.03
C-L9	Mid-Panel	128	114.2	110.5	887.5	0.13	0.12
C-L10	Mid-Panel	128	114.4	110.5	887.5	0.13	0.12
C-L11	Gusset	128	28.4	103.2	887.5	0.03	0.12
C-L12	Gusset	128	28.4	98.9	887.5	0.03	0.11
C-L13	Mid-Panel	64	117.1	98.5	887.5	0.13	0.11
C-L14	Mid-Panel	64	103.3	61.5	887.5	0.12	0.07
C-L15	Gusset	64	30.0	66.9	887.5	0.03	0.08
C-L16	Gusset	64	33.1	81.5	887.5	0.04	0.09
C-L17	Mid-Panel	8.89	60.1	46.5	3700.0	0.02	0.01
C-L18	Mid-Panel	8.89	62.1	46.2	3700.0	0.02	0.01
C-L19	Gusset	8.89	42.0	49.8	3700.0	0.01	0.01
C-L20	Gusset	8.89	42.1	53.7	3700.0	0.01	0.01
C-L21	Mid-Panel	4.44	46.3	98.1	3700.0	0.01	0.03
C-L22	Mid-Panel	4.44	42.4	94.5	3700.0	0.01	0.03
C-L23	Gusset	4.44	19.3	29.0	3700.0	0.01	0.01
C-L24	Gusset	4.44	15.6	42.5	3700.0	0.00	0.01
C-L25	End Gusset	64	-	199.8	887.5	-	0.23
C-L26	End Gusset	20	-	147.7	1822.5	-	0.08

*Note: PL = Panel length (in.); LS = Lacing spacing (in.); CD = Channel Depth (in.); CS = Channel Spacing, or 2*e* (in.)
Ratios are the FEA results divided by the theoretical moment *P·e* at the respective location

Table B.3 Moment ratio results for non-continuous stay-plated two-channel members

Model ID	Failure Location	CD / CS*	FEA Moment @ Gusset (kip-in)	FEA Moment @ Mid-Panel	*P·e* (kip-in)	Ratio @ Gusset	Ratio @ Mid-Panel
N-SP1	Gusset	2	389.8	-	1675.8	0.23	-
N-SP2	Gusset	1	386.5	-	3329.6	0.12	-
N-SP3	Gusset	0.5	368.9	-	6637.1	0.06	-
N-SP4	Gusset	2	388.3	-	1675.8	0.23	-
N-SP5	Gusset	1	406.5	-	3329.6	0.12	-
N-SP6	Gusset	0.5	398.1	-	6637.1	0.06	-
N-SP7	Gusset	2	379.8	-	1675.8	0.23	-
N-SP8	Gusset	1	419.5	-	3329.6	0.13	-
N-SP9	Gusset	0.5	434.1	-	6637.1	0.07	-
N-SP10	Gusset	2	370.8	-	1675.8	0.22	-
N-SP11	Gusset	1	414.2	-	3329.6	0.12	-
N-SP12	Gusset	0.5	449.3	-	6637.1	0.07	-
N-SP13	Gusset	2	481.8	-	1675.8	0.29	-
N-SP14	Gusset	2	483.1	-	1675.8	0.29	-
N-SP15	Gusset	1	513.8	-	3329.6	0.15	-
N-SP16	Gusset	1	530.7	-	3329.6	0.16	-
N-SP17	Gusset	0.5	558.0	-	6637.1	0.08	-
N-SP18	Gusset	0.5	573.1	-	6637.1	0.09	-
N-SP19	Gusset	1	413.8	-	3329.6	0.12	-
N-SP20	Gusset	1	409.9	-	3329.6	0.12	-
N-SP21	Gusset	1	422.7	-	3329.6	0.13	-
N-SP22	Gusset	1	424.3	-	3329.6	0.13	-
N-SP23	Gusset	1	424.3	-	3329.6	0.13	-
N-SP24	Gusset	1	409.5	-	3329.6	0.12	-
N-SP25	Mid-Panel	2	104.3	136.8	3329.6	0.04	0.03
N-SP26	Mid-Panel	1	1.2	142.5	3329.6	0.04	0.00
N-SP27	Mid-Panel	0.5	44.3	35.8	6637.1	0.01	0.01
N-SP28	Mid-Panel	1	25.9	46.2	3329.6	0.01	0.01
N-SP29	Gusset	1	409.5	-	3329.6	0.12	-
N-SP30	Mid-Panel	1	55.8	81.4	3329.6	0.02	0.02
N-SP31	Gusset	1	405.2	-	3329.6	0.12	-
N-SP32	Mid-Panel	2	129.0	167.0	1675.8	0.10	0.08
N-SP33	Mid-Panel	1	81.8	111.8	3329.6	0.03	0.02
N-SP34	Mid-Panel	0.5	20.3	39.9	6637.1	0.01	0.00
N-SP35	Gusset	2	66.4	-	209.9	0.32	-
N-SP36	Gusset	1	70.2	-	412.1	0.17	-
N-SP37	Gusset	0.5	68.2	-	816.5	0.08	-
N-SP38	Gusset	2	65.2	-	209.9	0.31	-
N-SP39	Gusset	1	72.4	-	412.1	0.18	-
N-SP40	Gusset	0.5	73.2	-	816.5	0.09	-
N-SP41	Gusset	2	63.7	-	209.9	0.30	-
N-SP42	Gusset	1	71.9	-	412.1	0.17	-
N-SP43	Gusset	0.5	76.9	-	816.5	0.09	-
N-SP44	Gusset	2	62.9	-	209.9	0.30	-
N-SP45	Gusset	1	69.7	-	412.1	0.17	-
N-SP46	Gusset	0.5	76.3	-	816.5	0.09	-
N-SP47	Mid-Panel	2	1.29	8.9	209.9	0.04	0.01
N-SP48	Mid-Panel	1	12.9	10.0	412.1	0.02	0.03
N-SP49	Mid-Panel	0.5	17.5	16.1	816.5	0.02	0.02
N-SP50	Mid-Panel	2	9.6	20.2	209.9	0.10	0.05
N-SP51	Mid-Panel	1	5.7	15.0	412.1	0.04	0.01
N-SP52	Mid-Panel	0.5	3.7	2.4	816.5	0.00	0.00

*Note: CD = Channel Depth (in.); CS = Channel Spacing, or 2*e* (in.)

Ratios are the FEA results divided by the theoretical moment *P·e* at the respective location

Table B.4 Moment ratio results for non-continuous laced two-channel members

Model ID	Failure Location	(PL/LS) x (CD/CS)*	FEA Moment @ Mid-Panel (kip-in)	FEA Moment @ End Stay Plate (kip-in)	*P·e* (kip-in)	Ratio @ Mid-Panel	Ratio @ End Stay Plate
N-L1	Mid-Panel	16	119.0	79.6	2062.5	0.06	0.04
N-L2	Mid-Panel	4	27.6	41.6	3937.5	0.01	0.01
N-L3	Mid-Panel	64	172.8	159.6	1125.0	0.15	0.14
N-L4	Mid-Panel	8	68.5	82.6	3937.5	0.02	0.02
N-L5	Mid-Panel	32	133.2	91.8	2062.5	0.06	0.04
N-L6	Mid-Panel	32	206.4	84.4	2062.5	0.10	0.04
N-L7	Mid-Panel	16	123.1	89.2	2062.5	0.06	0.04
N-L8	Mid-Panel	16	58.7	101.5	2062.5	0.03	0.05
N-L9	Mid-Panel	16	118.7	199.7	2062.5	0.06	0.10
N-L10	Mid-Panel	-	54.8	81.8	2062.5	0.03	0.04
N-L11	Gusset	16	47.2	107.5	2062.5	0.02	0.05
N-L12	Gusset	4	37.5	171.9	3937.5	0.01	0.04
N-L13	Gusset	64	43.4	131.8	1125.0	0.04	0.12
N-L14	Gusset	8	40.9	108.8	1125.0	0.04	0.10
N-L15	Gusset	32	49.9	135.9	2062.5	0.02	0.07
N-L16	Gusset	32	48.4	108.0	2062.5	0.02	0.05
N-L17	Gusset	16	38.7	123.6	2062.5	0.02	0.06
N-L18	Gusset	-	50.7	185.0	2062.5	0.02	0.09

*Note: PL = Panel length (in.); LS = Lacing spacing (in.); CD = Channel Depth (in.); CS = Channel Spacing, or 2*e* (in.)
Ratios are the FEA results divided by the theoretical moment *P·e* at the respective location

APPENDIX C. SPECIMEN GAGE PLANS

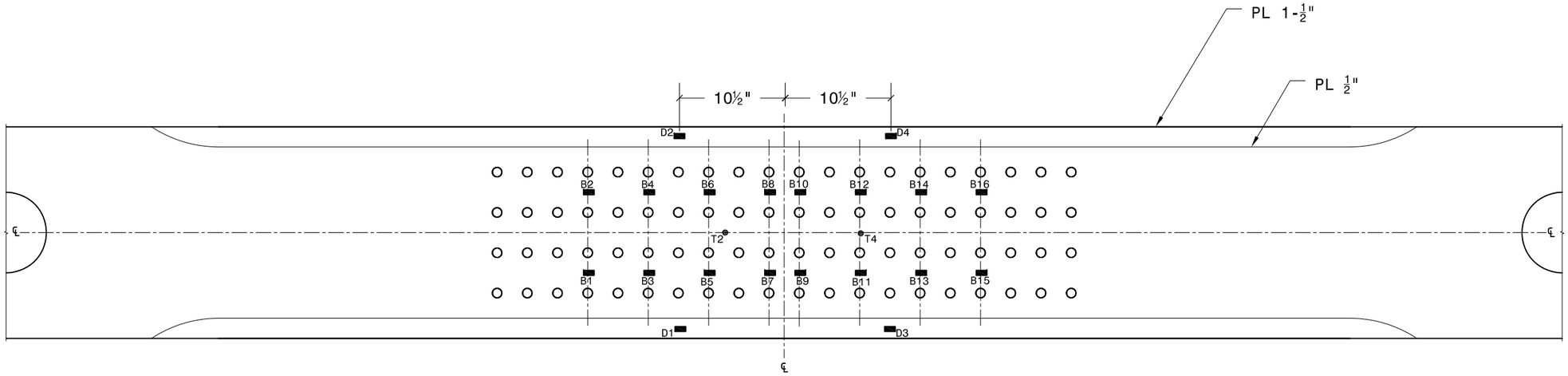

UP

1/1 SPECIMEN 2 EAST SIDE

SCALE: 1" = 1'-0"

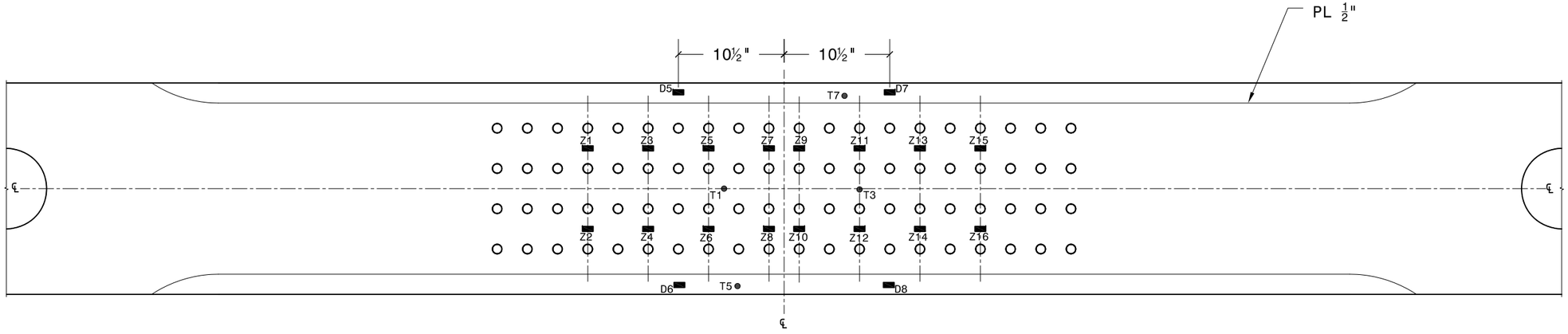

UP

2/1 SPECIMEN 2 WEST SIDE

SCALE: 1" = 1'-0"

BOWEN LABORATORY
PURDUE UNIVERSITY

1040 SOUTH RIVER ROAD
WEST LAFAYETTE, IN 47906
P: 765-494-2227 F: 765-494-9886

PROJECT:

POOLED FUND TPF-5(238)

SHEET NOTES:

- Thermocouple
- Strain gage

REVISIONS:

NO.	DATE	BY

DESIGNED BY: JL

DRAWN BY: JL

CHECKED BY:

DATE:

PROJECT NO.: TPF-5(253)

SHEET TITLE:

BUILT-UP SPECIMEN 1 & 2 GAGE PLANS

SHEET NO.: 1 of 1

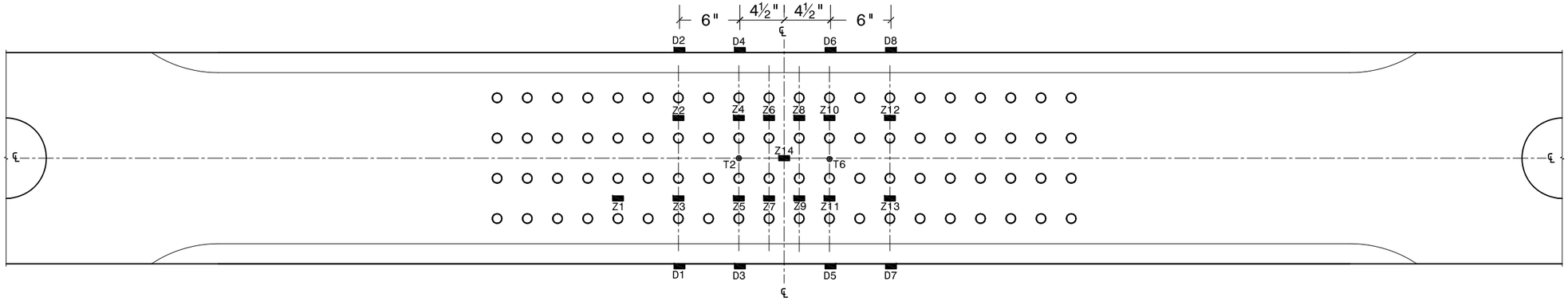

UP

1/1 SPECIMEN 3 & 4 EAST SIDE

SCALE: 1" = 1'-0"

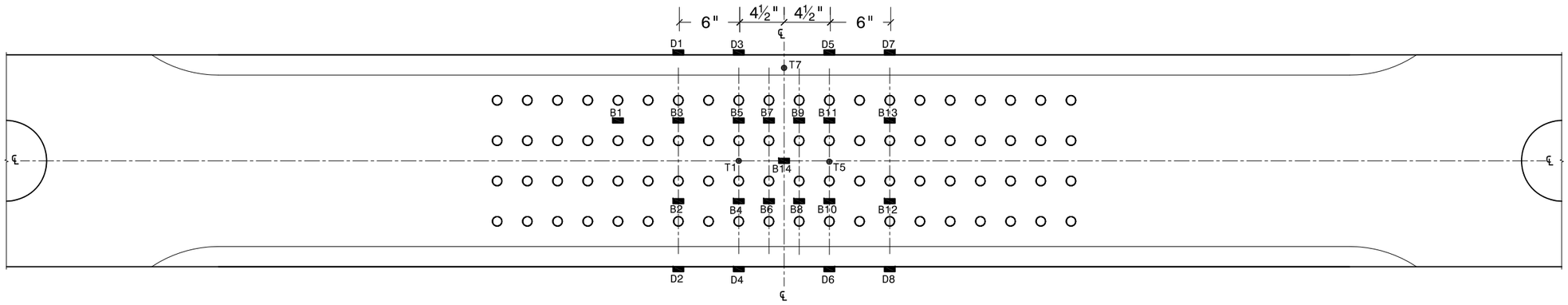

UP

2/1 SPECIMEN 3 & 4 WEST SIDE

SCALE: 1" = 1'-0"

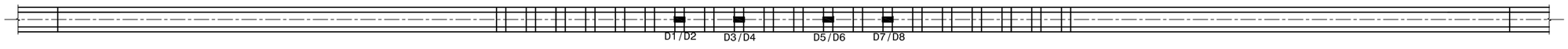

UP

3/1 TYPICAL CENTER PLATE GAGE INSTALLATION

SCALE: 1" = 1'-0"

BOWEN LABORATORY
PURDUE UNIVERSITY

1040 SOUTH RIVER ROAD
WEST LAFAYETTE, IN 47906
P: 765-494-2227 F: 765-494-9886

PROJECT:

POOLED FUND TPF-5(238)

SHEET NOTES:

- Thermocouple
- Strain gage

REVISIONS:

NO.	DATE	BY

DESIGNED BY: JL
DRAWN BY: JL
CHECKED BY:
DATE:
PROJECT NO.: TPF-5(253)
SHEET TITLE:

BUILT UP SPECIMENS 3 AND 4

SHEET NO.:

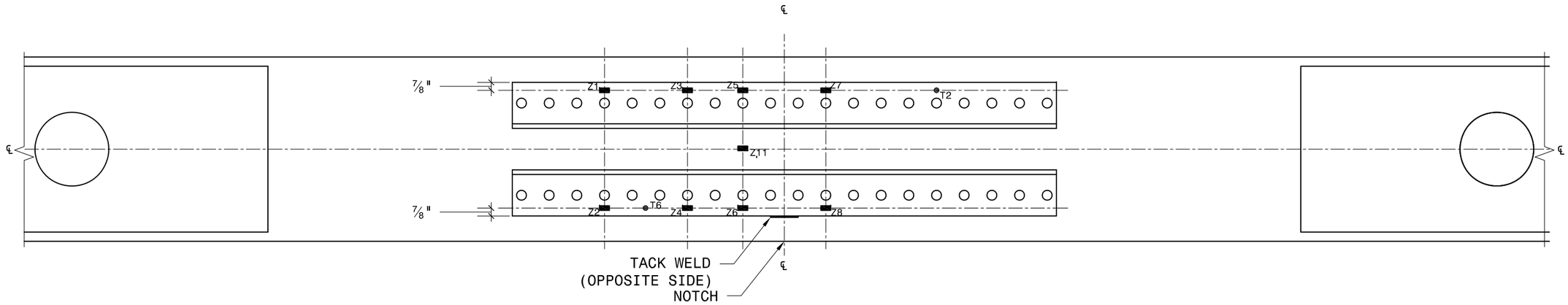

UP — 1/1 SPECIMEN 5 EAST SIDE

SCALE: 1" = 1'-0"

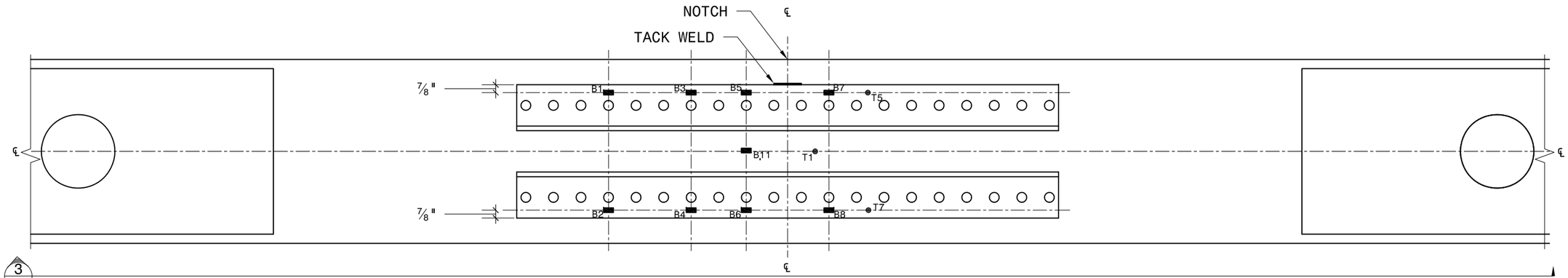

UP — 2/1 SPECIMEN 5 WEST SIDE

SCALE: 1" = 1'-0"

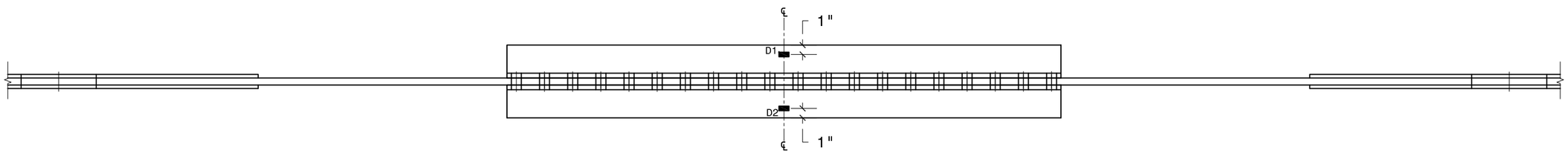

UP — 3/1 SPECIMEN 5 NORTH SIDE

SCALE: 1" = 1'-0"

BOWEN LABORATORY
PURDUE UNIVERSITY

1040 SOUTH RIVER ROAD
WEST LAFAYETTE, IN 47906
P: 765-494-2227 F: 765-494-9886

PROJECT:

POOLED FUND TPF-5(238)

SHEET NOTES:

- Thermocouple
- Strain gage

REVISIONS:

NO.	DATE	BY

DESIGNED BY: JL
DRAWN BY: JL
CHECKED BY:
DATE:
PROJECT NO.: TPF-5(253)
SHEET TITLE:

BUILT UP SPECIMEN 5

SHEET NO.: 1 of 1

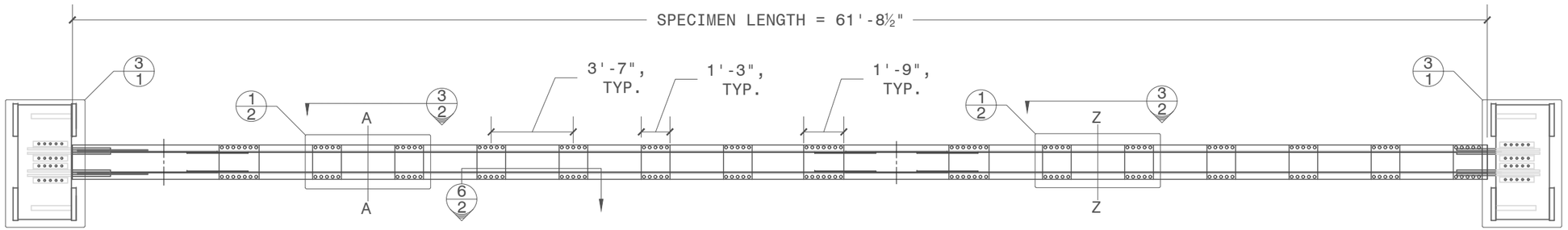

1/1 PLAN VIEW
SCALE: 3/16" = 1'-0"

LOAD (SOUTH)

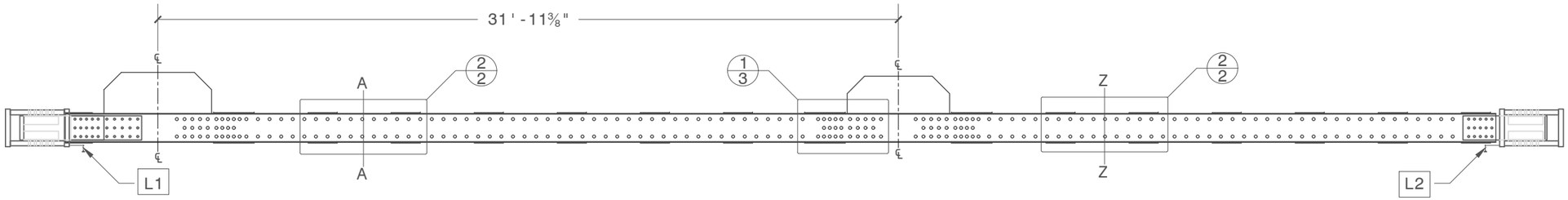

2/1 ELEVATION VIEW
SCALE: 3/16" = 1'-0"

LOAD (SOUTH)

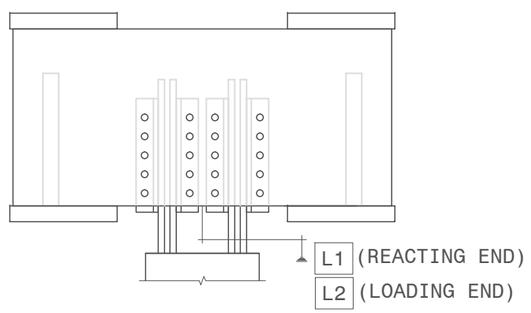

3/1 STRING POTENTIOMETERS
SCALE: 3/4" = 1'-0"

BOWEN LABORATORY
PURDUE UNIVERSITY

1040 SOUTH RIVER ROAD
WEST LAFAYETTE, IN 47906
P: 765-494-2227 F: 765-494-9886

PROJECT:
Winona Truss Test Gage Plans

SHEET NOTES:

L1 Displacement sensor channels

A1 Strain gage channels

REVISIONS:

NO.	DATE	BY

DESIGNED BY: JBL
DRAWN BY: JBL
CHECKED BY:
DATE: 2017
PROJECT NO.:
SHEET TITLE:

SPECIMEN 6 OVERVIEW

SHEET NO.: 1 of 4

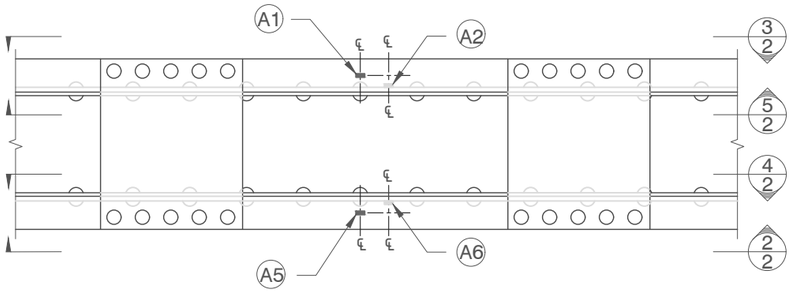

1/2 PLAN VIEW, TYP.
SCALE: 3/4" = 1'-0"

LOAD (SOUTH)

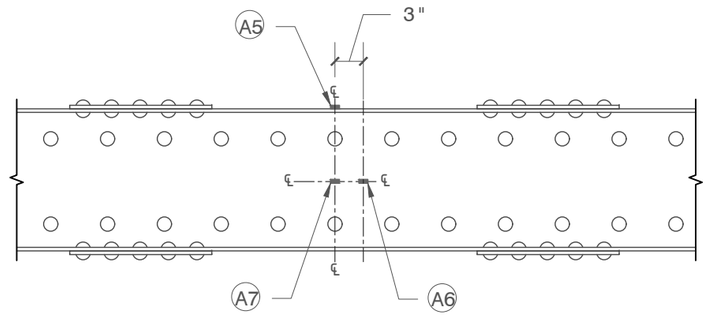

2/2 WEST EXT. ELEVATION
SCALE: 3/4" = 1'-0"

LOAD (SOUTH)

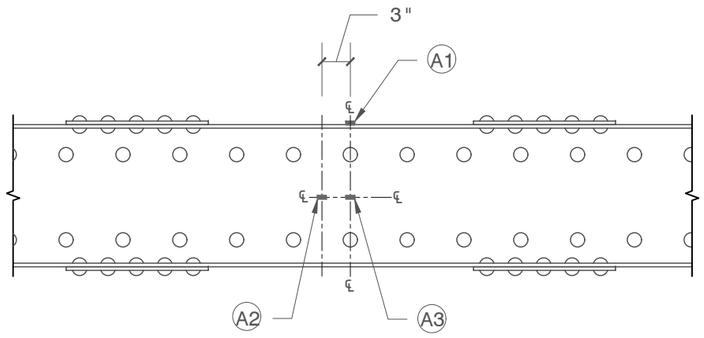

3/2 EAST EXT. ELEVATION
SCALE: 3/4" = 1'-0"

LOAD (SOUTH)

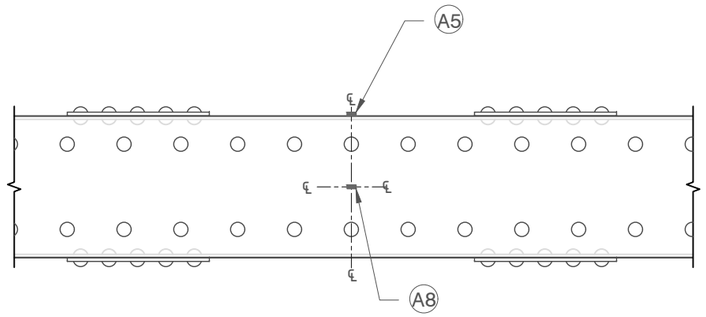

4/2 WEST INT. ELEVATION
SCALE: 3/4" = 1'-0"

LOAD (SOUTH)

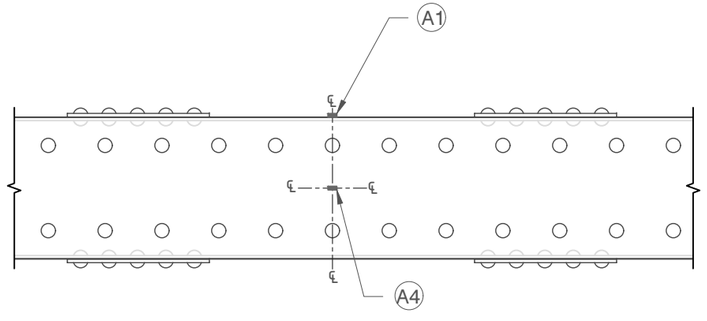

5/2 EAST INT. ELEVATION
SCALE: 3/4" = 1'-0"

LOAD (SOUTH)

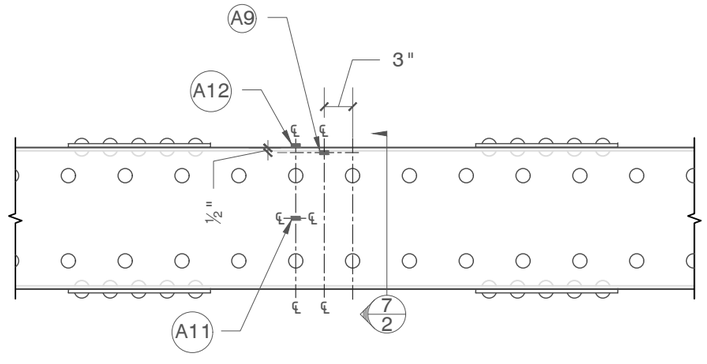

6/2 WEST INT. ELEVATION
SCALE: 3/4" = 1'-0"

LOAD (SOUTH)

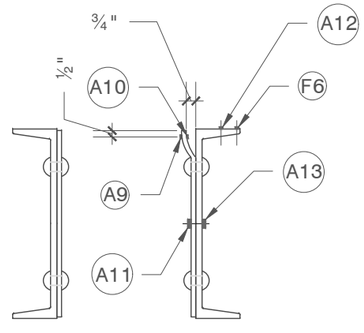

7/2 WEST CHANNEL CROSS-SECTION
SCALE: 1" = 1'-0"

BOWEN LABORATORY
PURDUE UNIVERSITY

1040 SOUTH RIVER ROAD
WEST LAFAYETTE, IN 47906
P: 765-494-2227 F: 765-494-9886

PROJECT:
Winona Truss Test Gage Plans

SHEET NOTES:

L1 Displacement sensor channels

A1 Strain gage channels

REVISIONS:

NO.	DATE	BY

DESIGNED BY: JBL
DRAWN BY: JBL
CHECKED BY:
DATE: 2017
PROJECT NO.:
SHEET TITLE:

SPECIMEN 6 GAGE PLACEMENT DETAILS

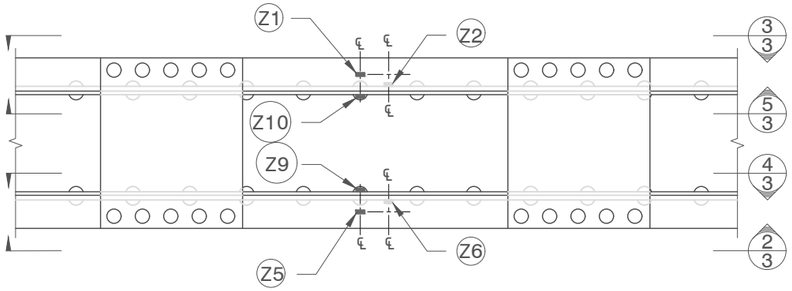

1/3 PLAN VIEW, TYP.
SCALE: 3/4" = 1'-0"

LOAD (SOUTH)

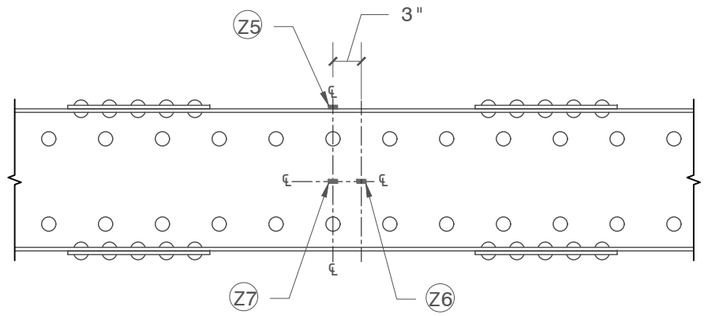

2/3 WEST EXT. ELEVATION
SCALE: 3/4" = 1'-0"

LOAD (SOUTH)

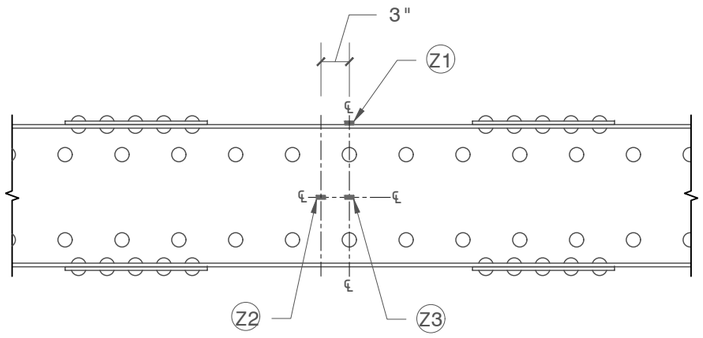

3/3 EAST EXT. ELEVATION
SCALE: 3/4" = 1'-0"

LOAD (SOUTH)

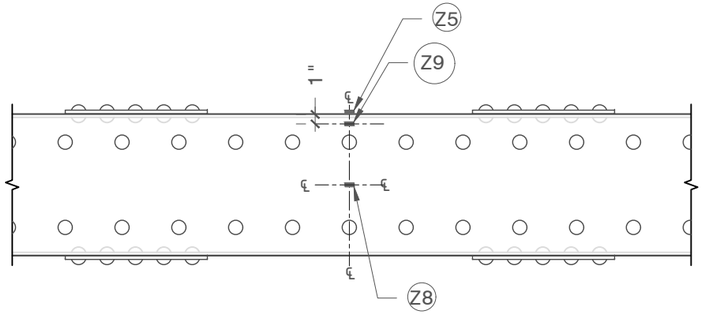

4/3 WEST INT. ELEVATION
SCALE: 3/4" = 1'-0"

LOAD (SOUTH)

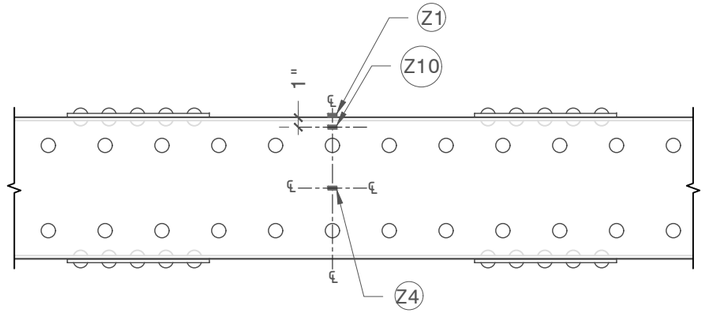

5/3 EAST INT. ELEVATION
SCALE: 3/4" = 1'-0"

LOAD (SOUTH)

BOWEN LABORATORY
PURDUE UNIVERSITY

1040 SOUTH RIVER ROAD
WEST LAFAYETTE, IN 47906
P: 765-494-2227 F: 765-494-9886

PROJECT:
Winona Truss Test Gage Plans

SHEET NOTES:

L1 Displacement sensor channels

A1 Strain gage channels

REVISIONS:

NO.	DATE	BY

DESIGNED BY: JBL
DRAWN BY: JBL
CHECKED BY:
DATE: 2017
PROJECT NO.:
SHEET TITLE:

SPECIMEN 6 GAGE PLACEMENT DETAILS

SHEET NO.: 3 of 4

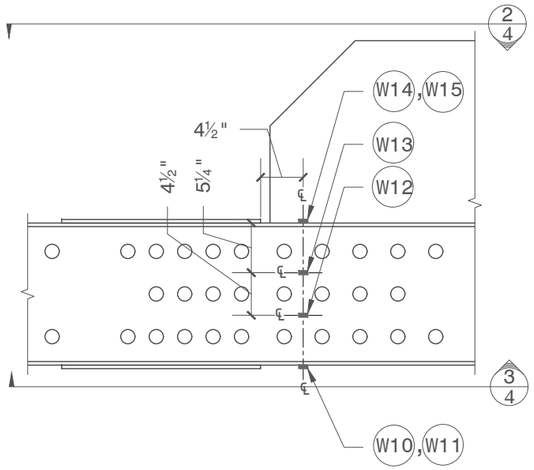

1/4 WEST EXT. ELEVATION
SCALE: 3/4" = 1'-0"

LOAD (SOUTH) →

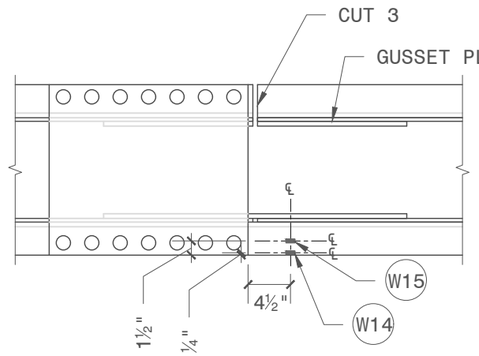

2/4 TOP PLAN VIEW
SCALE: 3/4" = 1'-0"

LOAD (SOUTH) →

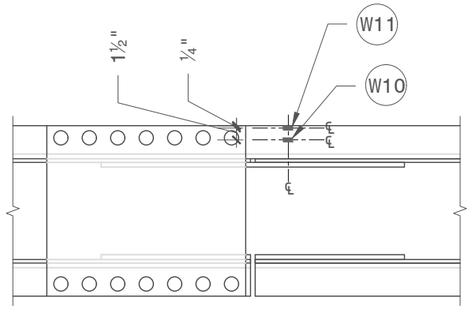

3/4 BOTTOM PLAN VIEW
SCALE: 3/4" = 1'-0"

LOAD (SOUTH) →

BOWEN LABORATORY
PURDUE UNIVERSITY

1040 SOUTH RIVER ROAD
WEST LAFAYETTE, IN 47906
P: 765-494-2227 F: 765-494-9886

PROJECT:
Winona Truss Test Gage Plans

SHEET NOTES:

L1 Displacement sensor channels

A1 Strain gage channels

REVISIONS:

NO.	DATE	BY

DESIGNED BY: JBL
DRAWN BY: JBL
CHECKED BY:
DATE: 2017
PROJECT NO.:
SHEET TITLE:

SPECIMEN 6 GAGE PLACEMENT DETAILS

SHEET NO.: 4 of 4

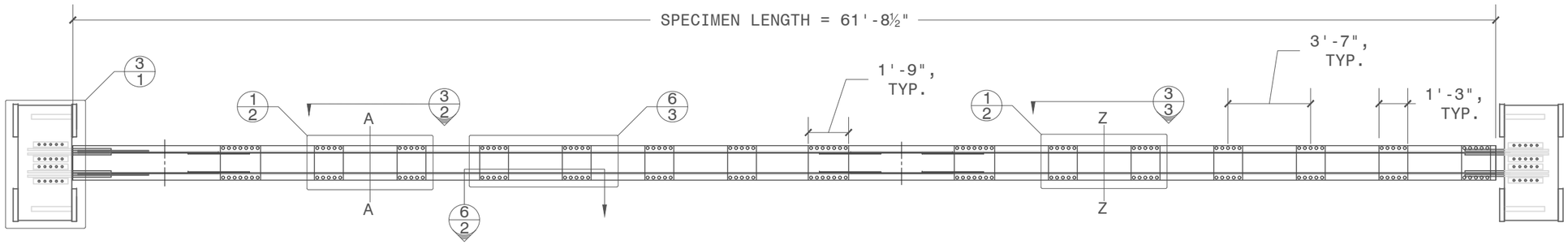

1 / 1 PLAN VIEW

SCALE: 3/16" = 1'-0"

LOAD (SOUTH) →

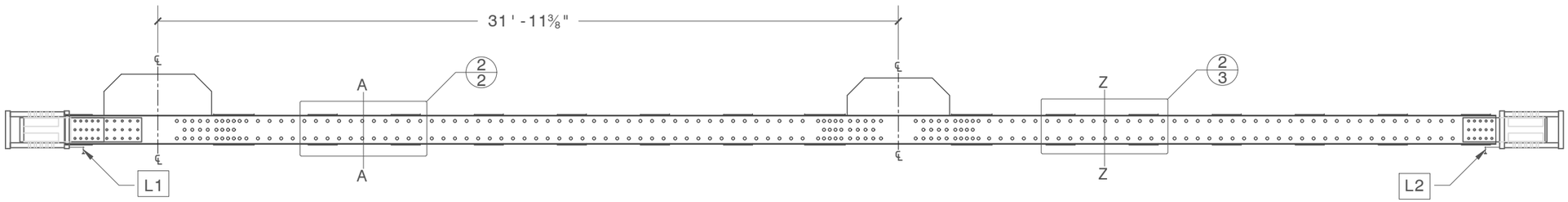

2 / 1 ELEVATION VIEW

SCALE: 3/16" = 1'-0"

LOAD (SOUTH) →

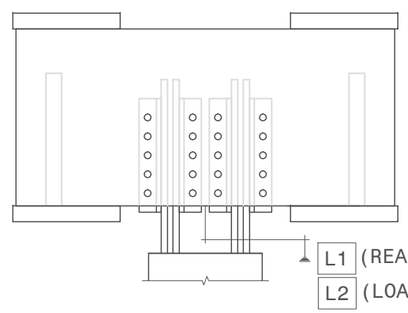

3 / 1 STRING POTENTIOMETERS

SCALE: 3/4" = 1'-0"

BOWEN LABORATORY
PURDUE UNIVERSITY

1040 SOUTH RIVER ROAD
WEST LAFAYETTE, IN 47906
P: 765-494-2227 F: 765-494-9886

PROJECT:

Winona Truss Test Gage Plans

SHEET NOTES:

L1 Displacement sensor channels

A1 Strain gage channels

REVISIONS:

NO.	DATE	BY

DESIGNED BY: JBL
DRAWN BY: JBL
CHECKED BY:
DATE: 2017
PROJECT NO.:
SHEET TITLE:

SPECIMEN 7 OVERVIEW

SHEET NO.: 1 of 3

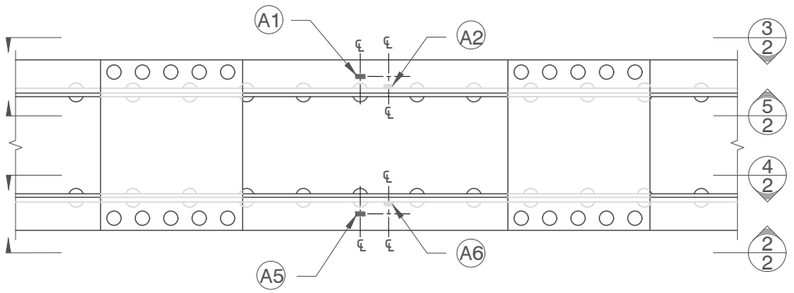

1/2 PLAN VIEW, TYP.
SCALE: 3/4" = 1'-0"

LOAD (SOUTH)

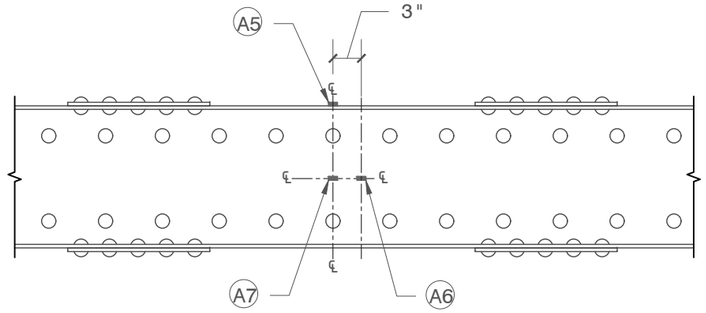

2/2 WEST EXT. ELEVATION
SCALE: 3/4" = 1'-0"

LOAD (SOUTH)

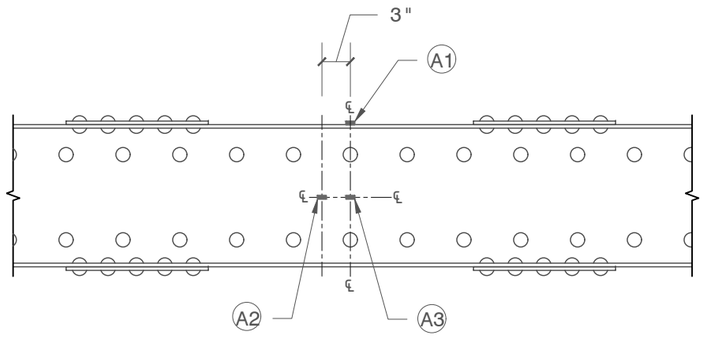

3/2 EAST EXT. ELEVATION
SCALE: 3/4" = 1'-0"

LOAD (SOUTH)

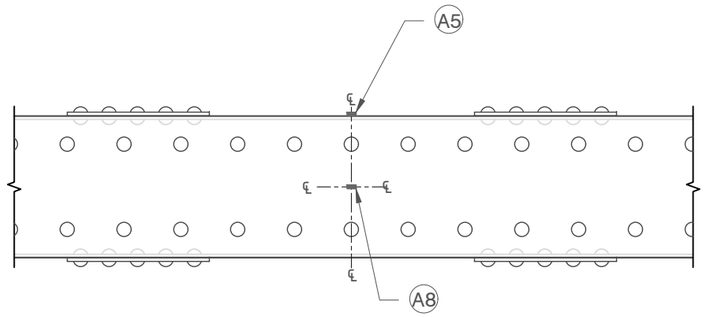

4/2 WEST INT. ELEVATION
SCALE: 3/4" = 1'-0"

LOAD (SOUTH)

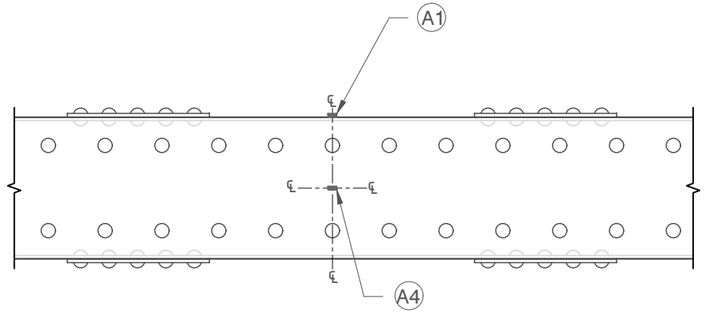

5/2 EAST INT. ELEVATION
SCALE: 3/4" = 1'-0"

LOAD (SOUTH)

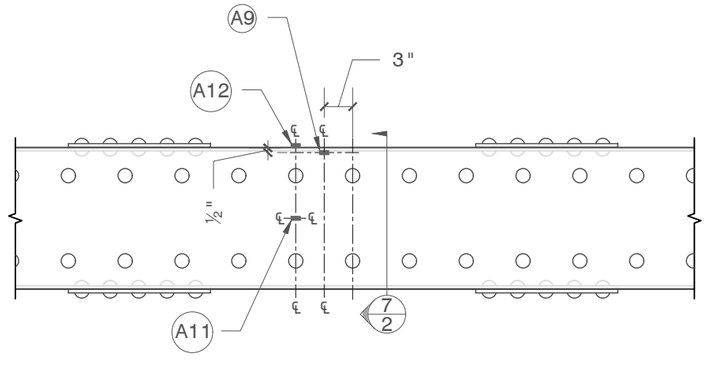

6/2 WEST INT. ELEVATION
SCALE: 3/4" = 1'-0"

LOAD (SOUTH)

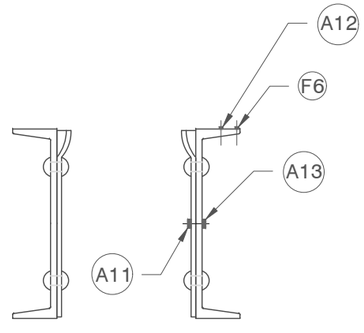

7/2 WEST CHANNEL CROSS-SECTION
SCALE: 1" = 1'-0"

BOWEN LABORATORY
PURDUE UNIVERSITY

1040 SOUTH RIVER ROAD
WEST LAFAYETTE, IN 47906
P: 765-494-2227 F: 765-494-9886

PROJECT:
Winona Truss Test Gage Plans

SHEET NOTES:

L1 Displacement sensor channels

A1 Strain gage channels

REVISIONS:

NO.	DATE	BY

DESIGNED BY: JBL
DRAWN BY: JBL
CHECKED BY:
DATE: 2017
PROJECT NO.:
SHEET TITLE:

SPECIMEN 7 GAGE PLACEMENT DETAILS

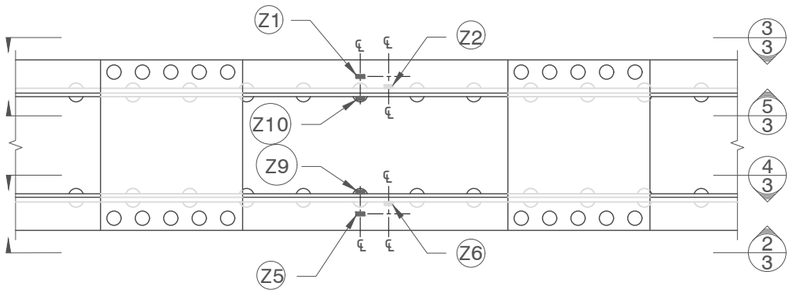

1/3 PLAN VIEW, TYP.
SCALE: 3/4" = 1'-0"

LOAD (SOUTH)

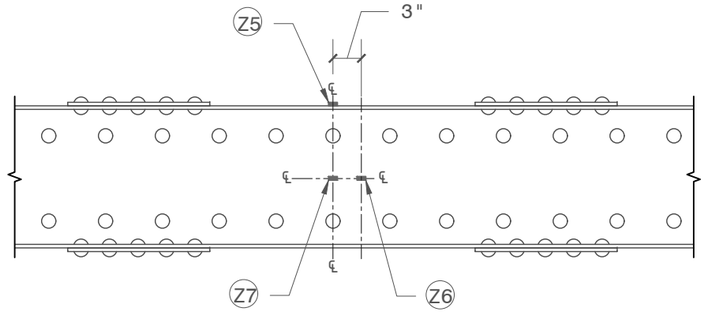

2/3 WEST EXT. ELEVATION
SCALE: 3/4" = 1'-0"

LOAD (SOUTH)

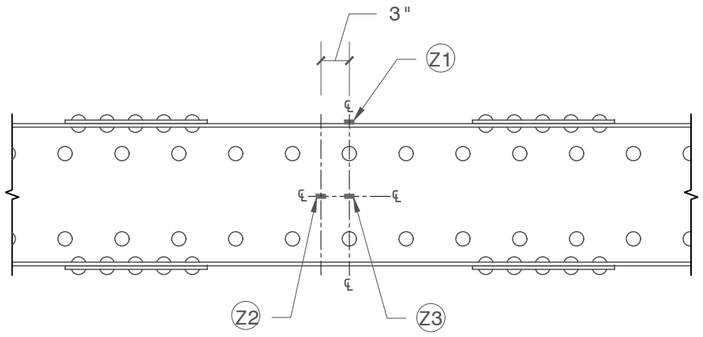

3/3 EAST EXT. ELEVATION
SCALE: 3/4" = 1'-0"

LOAD (SOUTH)

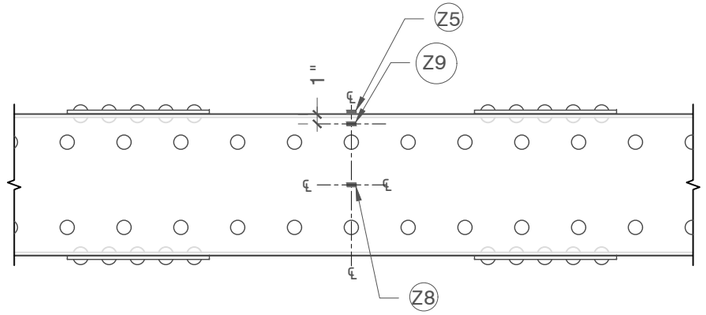

4/3 WEST INT. ELEVATION
SCALE: 3/4" = 1'-0"

LOAD (SOUTH)

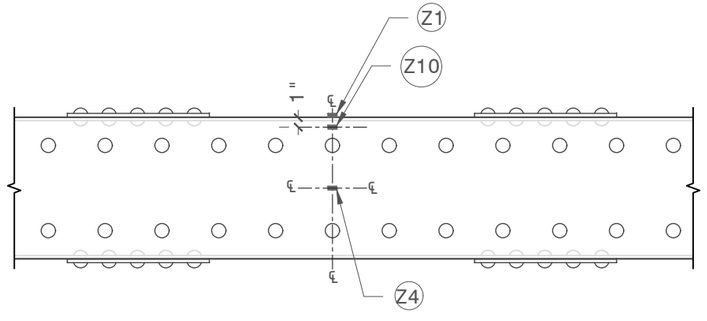

5/3 EAST INT. ELEVATION
SCALE: 3/4" = 1'-0"

LOAD (SOUTH)

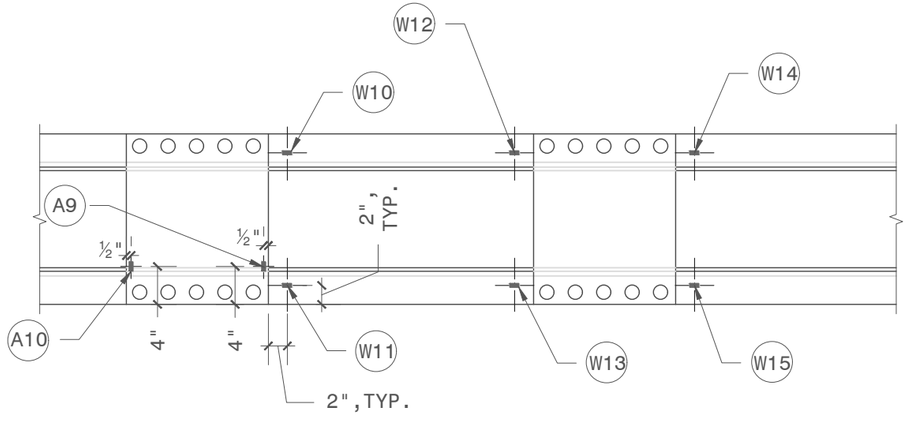

6/3 PLAN VIEW
SCALE: 3/4" = 1'-0"

LOAD (SOUTH)

BOWEN LABORATORY
PURDUE UNIVERSITY

1040 SOUTH RIVER ROAD
WEST LAFAYETTE, IN 47906
P: 765-494-2227 F: 765-494-9886

PROJECT:

Winona Truss Test Gage Plans

SHEET NOTES:

L1 Displacement sensor channels

A1 Strain gage channels

REVISIONS:

NO.	DATE	BY

DESIGNED BY: JBL
DRAWN BY: JBL
CHECKED BY:
DATE: 2017
PROJECT NO.:
SHEET TITLE:

SPECIMEN 7 GAGE PLACEMENT DETAILS

APPENDIX D. SPECIMEN FABRICATION DRAWINGS

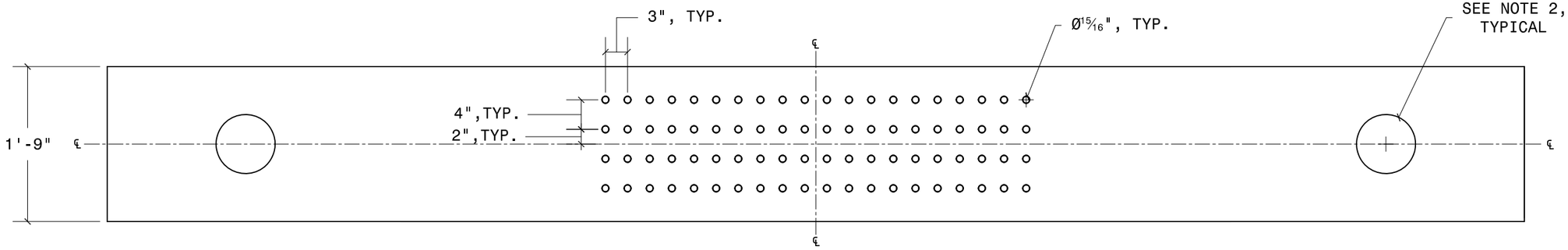

1 / 1 SPECIMEN 1, 2, 3 & 4 CENTER PLATE

SCALE: 3/4" = 1'-0"

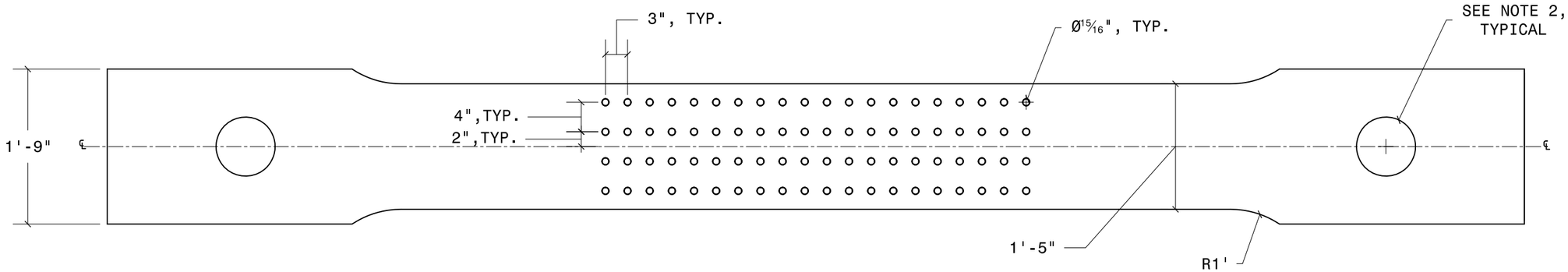

2 / 1 SPECIMEN EXTERIOR PLATES

SCALE: 3/4" = 1'-0"

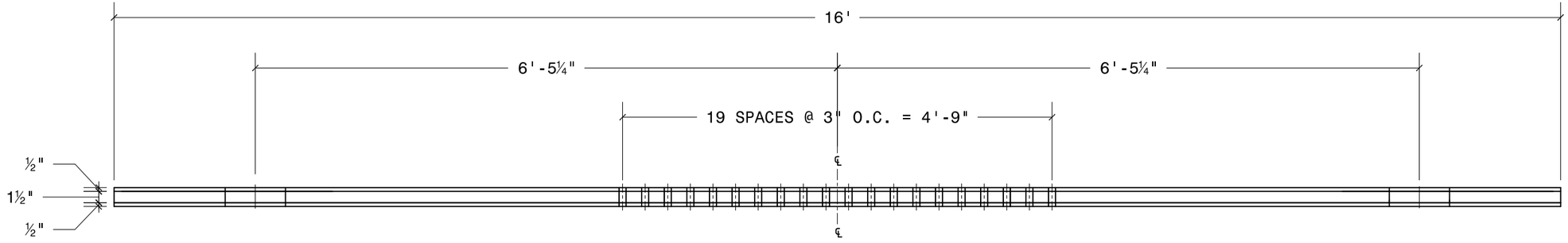

3 / 1 SPECIMEN ASSEMBLED ELEVATION

SCALE: 3/4" = 1'-0"

BOWEN LABORATORY
PURDUE UNIVERSITY

1040 SOUTH RIVER ROAD
WEST LAFAYETTE, IN 47906
P: 765-494-2227 F: 765-494-9886

PROJECT:

POOLED FUND TPF-5(238)

SHEET NOTES:

1. (2) SPECIMENS SHALL BE FABRICATED FROM PLATE MATERIAL PROVIDED BY AND DELIVERED TO FABRICATOR'S SHOP BY PURDUE UNIVERSITY.

2. PIN HOLE DIAMETER = 8.020" +0.020"/-0.000"

3. HOLE PLACEMENT SHALL BE BASED ON 1/2" PLATE TEMPLATE PROVIDED BY PURDUE UNIVERSITY.

4. TEMPLATE PLATE AND SPECIMEN PLATES HOLES SHALL BE MATCHED TO EACH OTHER.

4. ANY TACK WELDS USED DURING FABRICATION TO HOLD THE TEMPLATE PLATE IN PLACE SHALL BE GROUND SMOOTH UPON COMPLETION OF THE WORK.

5. TWO NEW SPECIMENS AND THE 1/2" TEMPLATE PLATE SHALL BE DELIVERED TO BOWEN LAB UPON COMPLETION OF FABRICATION.

REVISIONS:

NO.	DATE	BY

DESIGNED BY: JL

DRAWN BY: JL

CHECKED BY:

DATE:

PROJECT NO.: TPF-5(253)

SHEET TITLE:

BUILT-UP SPECIMENS 1, 2, 3 AND 4

SHEET NO.:

1 of 1

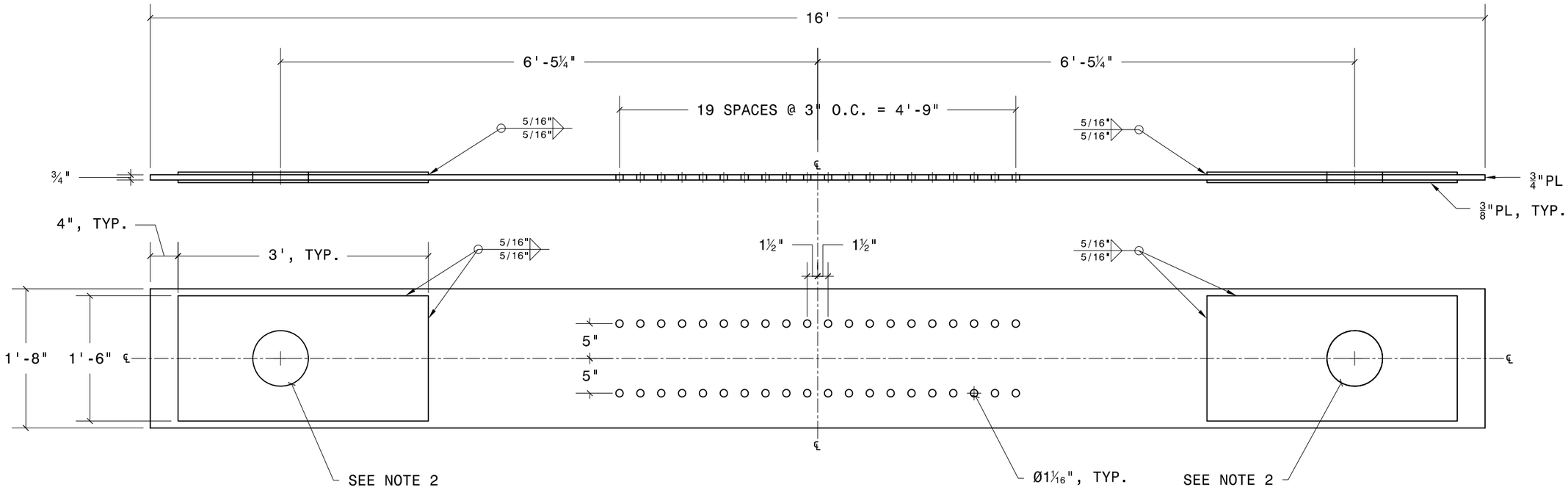

1 / 1 CENTER PLATE
SCALE: 3/4" = 1'-0"

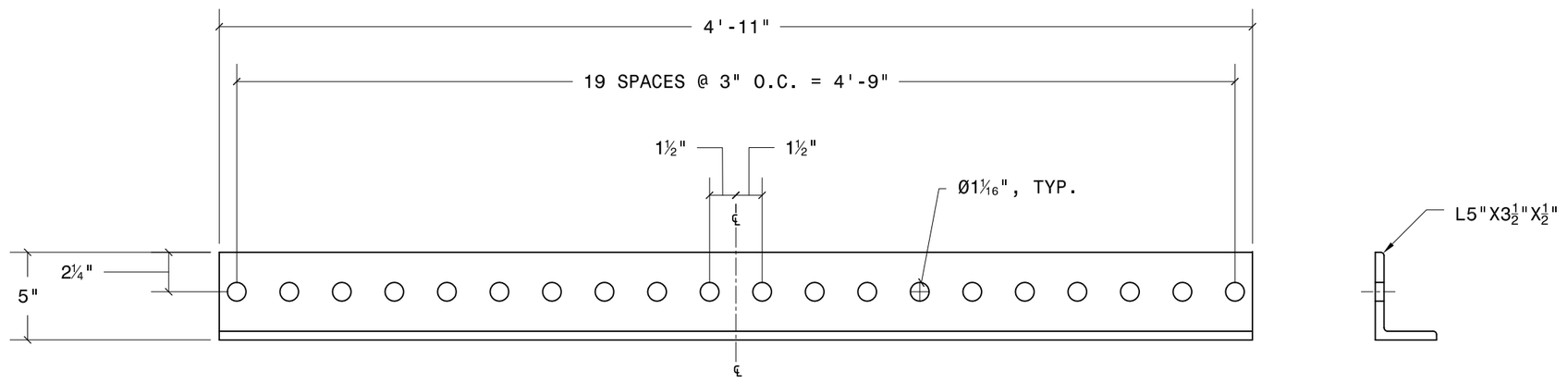

2 / 1 REDUNDANCY ANGLES
SCALE: 1" = 1'-0"

BOWEN LABORATORY
PURDUE UNIVERSITY

1040 SOUTH RIVER ROAD
WEST LAFAYETTE, IN 47906
P: 765-494-2227 F: 765-494-9886

PROJECT:
POOLED FUND TPF-5(238)

SHEET NOTES:

1. (1) CENTER PLATE AND (4) REDUNDANCY ANGLES SHALL BE FABRICATED FROM MATERIAL PROVIDED BY THE FABRICATOR

2. PIN HOLE DIAMETER = 8.020" +0.020"/-0.000"

3. BOLT HOLE PATTERN FOR THE REDUNDANCY ANGLES MUST MATCH THE CENTER PLATE.

5. THE CENTER PLATE AND THE REDUNDANCY ANGLES SHALL BE DELIVERED TO BOWEN LAB UPON COMPLETION OF FABRICATION.

REVISIONS:

NO.	DATE	BY

DESIGNED BY: JL
DRAWN BY: JL
CHECKED BY:
DATE:
PROJECT NO.: TPF-5(253)
SHEET TITLE:

BUILT UP SPECIMEN 5

SHEET NO.:
1 of 1

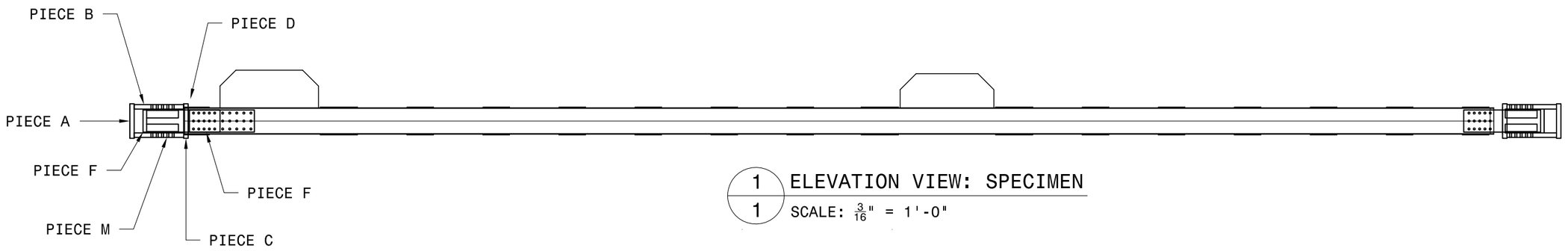

1/1 ELEVATION VIEW: SPECIMEN

SCALE: 3/16" = 1'-0"

2/1 ELEVATION VIEW: COLUMNS

SCALE: 3/16" = 1'-0"

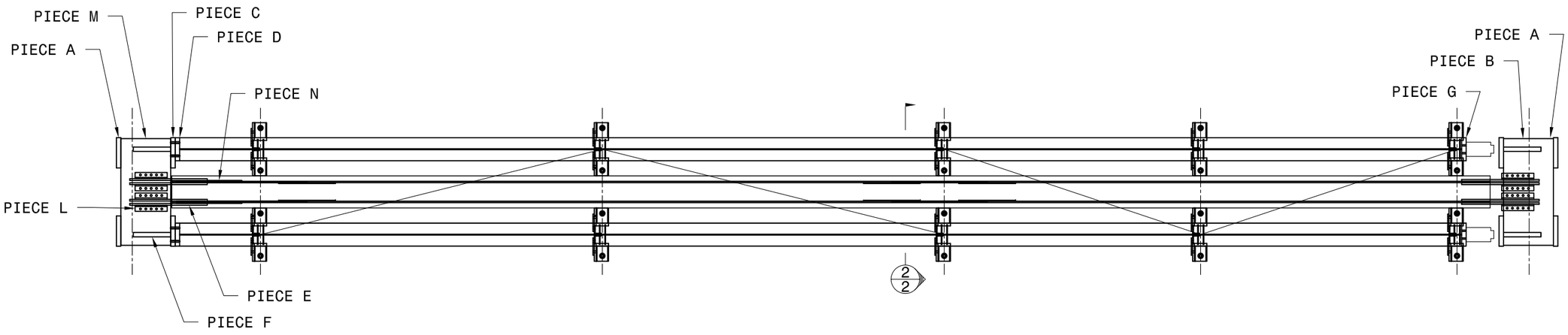

3/1 PLAN VIEW

SCALE: 3/16" = 1'-0"

BOWEN LABORATORY
PURDUE UNIVERSITY

1040 SOUTH RIVER ROAD
WEST LAFAYETTE, IN 47906
P: 765-494-2227 F: 765-494-9886

PROJECT:

Winona Truss Test

SHEET NOTES:

REVISIONS:

NO.	DATE	BY

DESIGNED BY: JBL
DRAWN BY: JBL
CHECKED BY:
DATE: 2017
PROJECT NO.:
SHEET TITLE:

Specimen 6 & 7 General Test Setup

SHEET NO.: 1 of 5

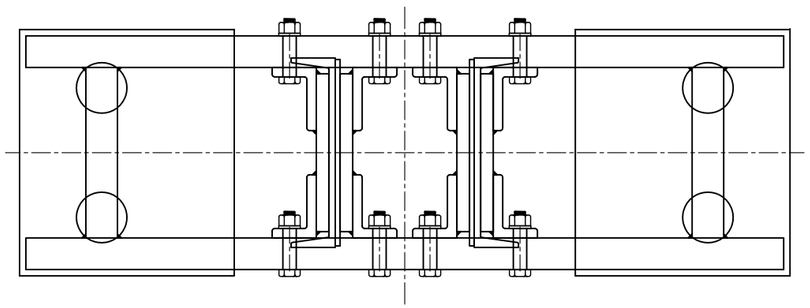

1/2 ELEVATION: LOAD BEAM
SCALE: 1" = 1'-0"

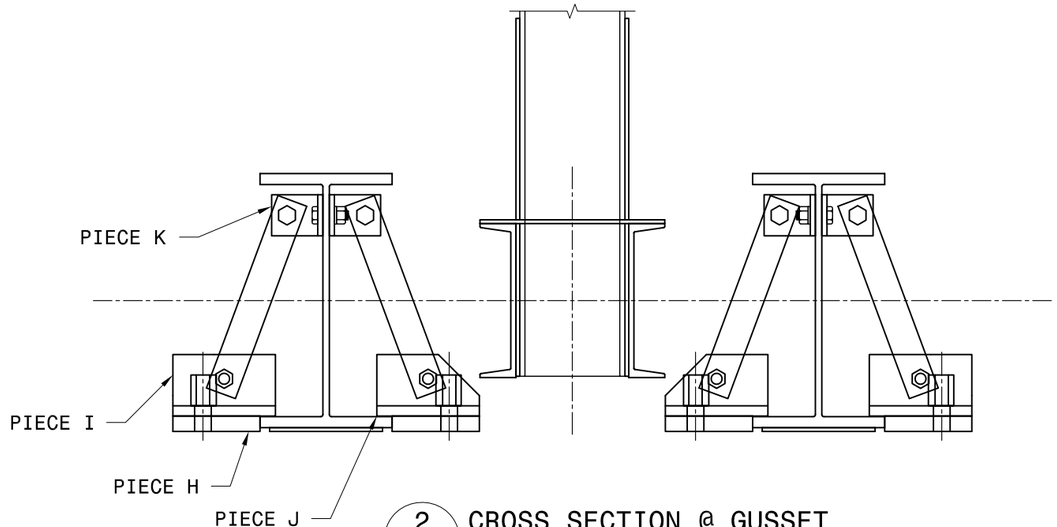

2/2 CROSS SECTION @ GUSSET
SCALE: 1/2" = 1'-0"

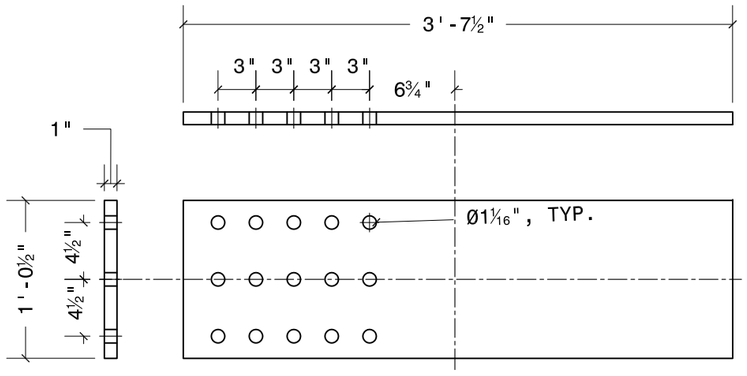

3/2 PIECE E (x8)
SCALE: 1" = 1'-0"

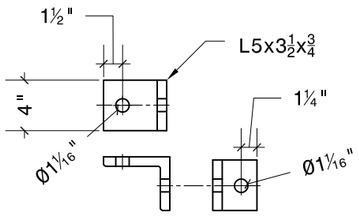

4/2 PIECE K (x12)
SCALE: 1" = 1'-0"

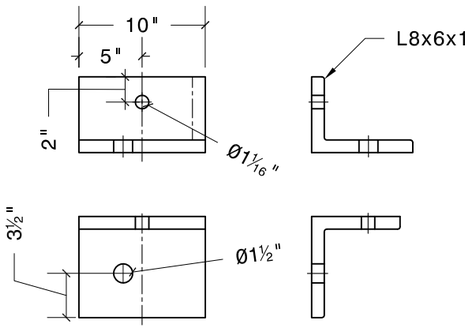

5/2 PIECE I (x10)
SCALE: 1" = 1'-0"

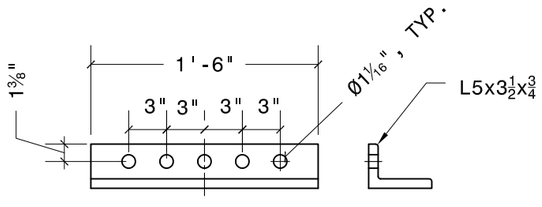

8/2 PIECE L (x16)
SCALE: 1" = 1'-0"

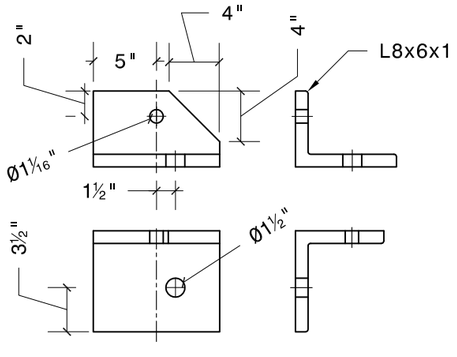

6/2 PIECE J (x10)
SCALE: 1" = 1'-0"

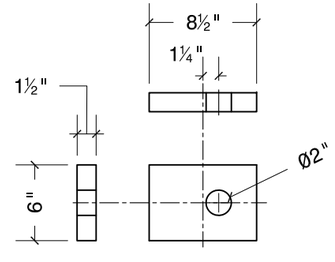

7/2 PIECE H (x20)
SCALE: 1" = 1'-0"

BOWEN LABORATORY
PURDUE UNIVERSITY

1040 SOUTH RIVER ROAD
WEST LAFAYETTE, IN 47906
P: 765-494-2227 F: 765-494-9886

PROJECT:
Winona Truss Test

SHEET NOTES:
(1) SHEAR STUDS WILL BE INSTALLED BY PURDUE UNIVERSITY.

REVISIONS:

NO.	DATE	BY

DESIGNED BY: JBL
DRAWN BY: JBL
CHECKED BY:
DATE: 2017
PROJECT NO.:
SHEET TITLE:
Specimen 6 & 7 : PLATES

SHEET NO.:

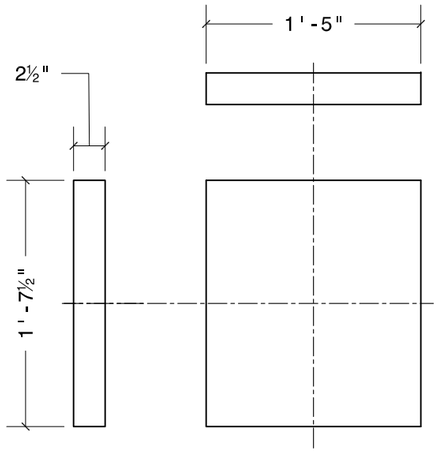

1 / 3 PIECE A (x6)
SCALE: 1" = 1'-0"

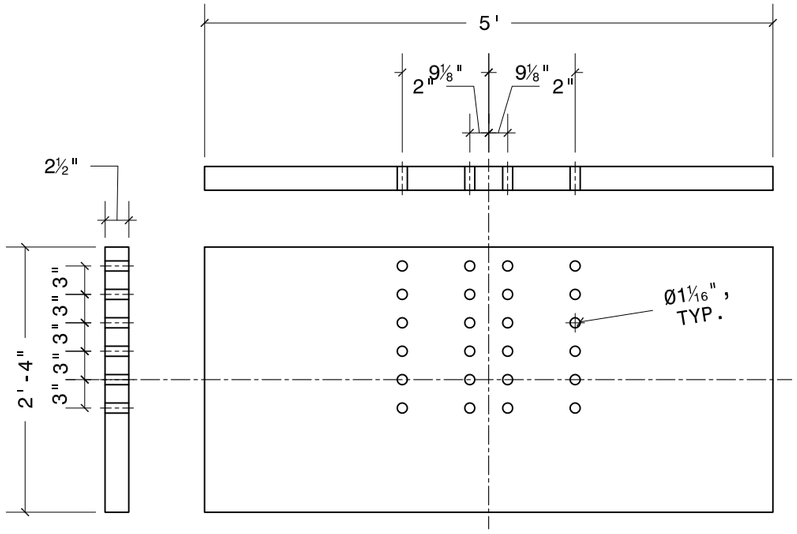

2 / 3 PIECE B (x2)
SCALE: ¾" = 1'-0"

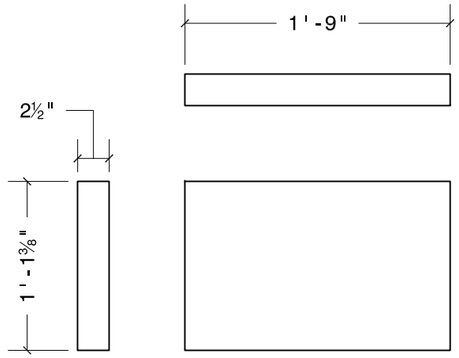

6 / 3 PIECE F (x4)
SCALE: 1" = 1'-0"

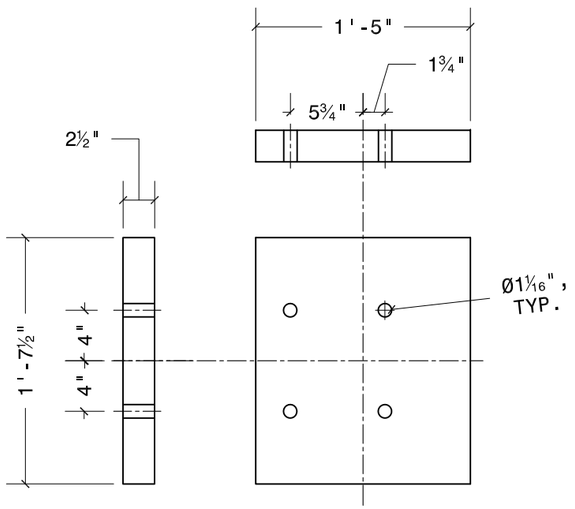

3 / 3 PIECE C (x2)
SCALE: 1" = 1'-0"

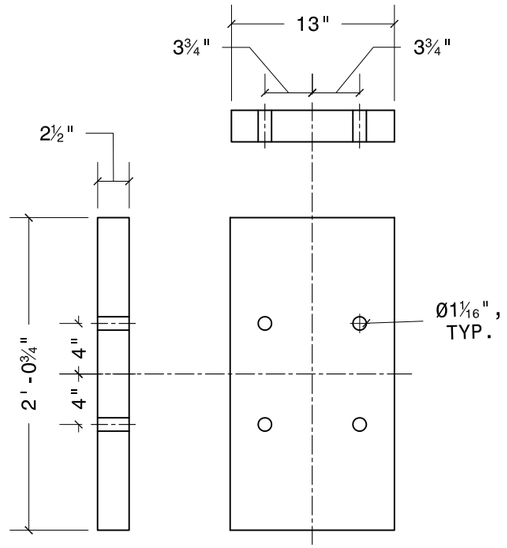

4 / 3 PIECE D (x2)
SCALE: 1" = 1'-0"

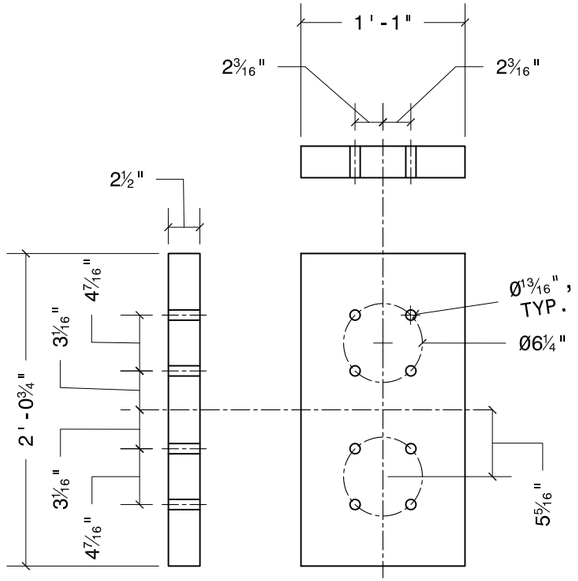

5 / 3 PIECE G (x2)
SCALE: 1" = 1'-0"

BOWEN LABORATORY
PURDUE UNIVERSITY

1040 SOUTH RIVER ROAD
WEST LAFAYETTE, IN 47906
P: 765-494-2227 F: 765-494-9886

PROJECT:
Winona Truss Test

SHEET NOTES:

REVISIONS:

NO.	DATE	BY

DESIGNED BY: JBL
DRAWN BY: JBL
CHECKED BY:
DATE: 2017
PROJECT NO.:
SHEET TITLE:

Specimen 6 & 7 : PLATES

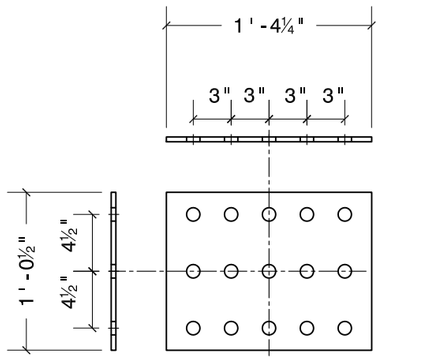

1/4 PIECE O (x2)

SCALE: 1" = 1'-0"

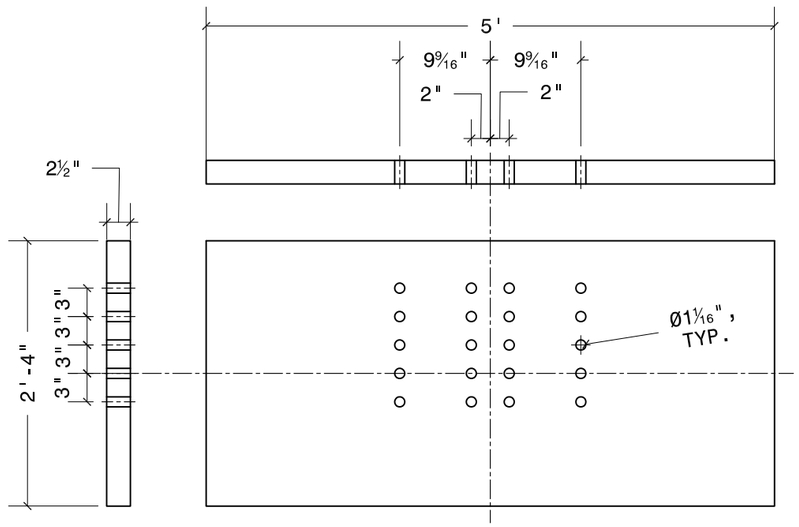

2/4 PIECE M (x2)

SCALE: ¾" = 1'-0"

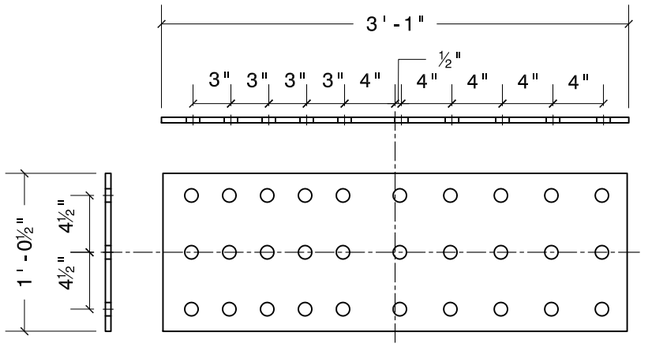

3/4 PIECE N (x2)

SCALE: ¾" = 1'-0"

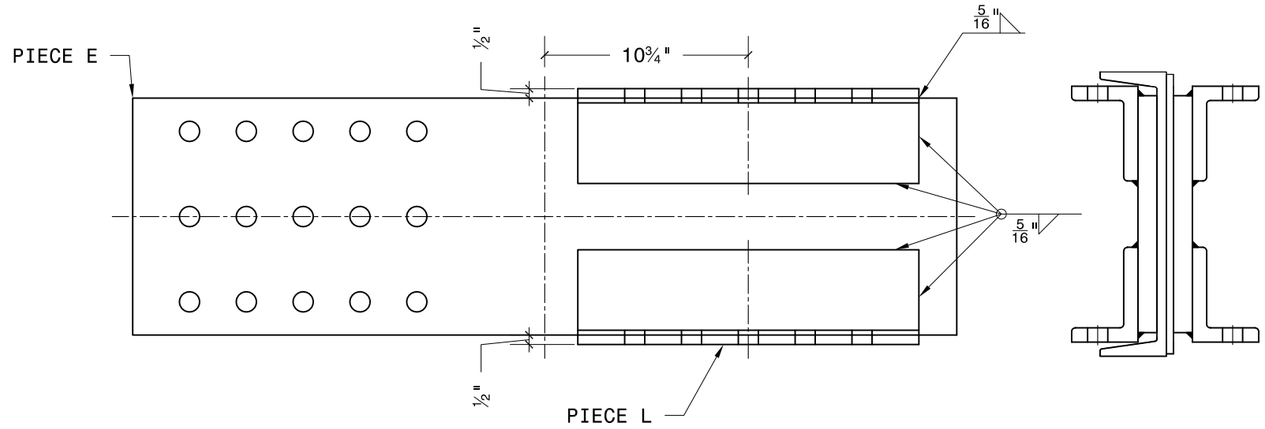

4/4 LOADING ANGLE DETAIL

SCALE: 1-1/2" = 1'-0"

BOWEN LABORATORY
PURDUE UNIVERSITY

1040 SOUTH RIVER ROAD
WEST LAFAYETTE, IN 47906
P: 765-494-2227 F: 765-494-9886

PROJECT:

Winona Truss Test

SHEET NOTES:

REVISIONS:

NO.	DATE	BY

DESIGNED BY: JBL
DRAWN BY: JBL
CHECKED BY:
DATE: 2017
PROJECT NO.:
SHEET TITLE:

Specimen 6 & 7 : PLATES

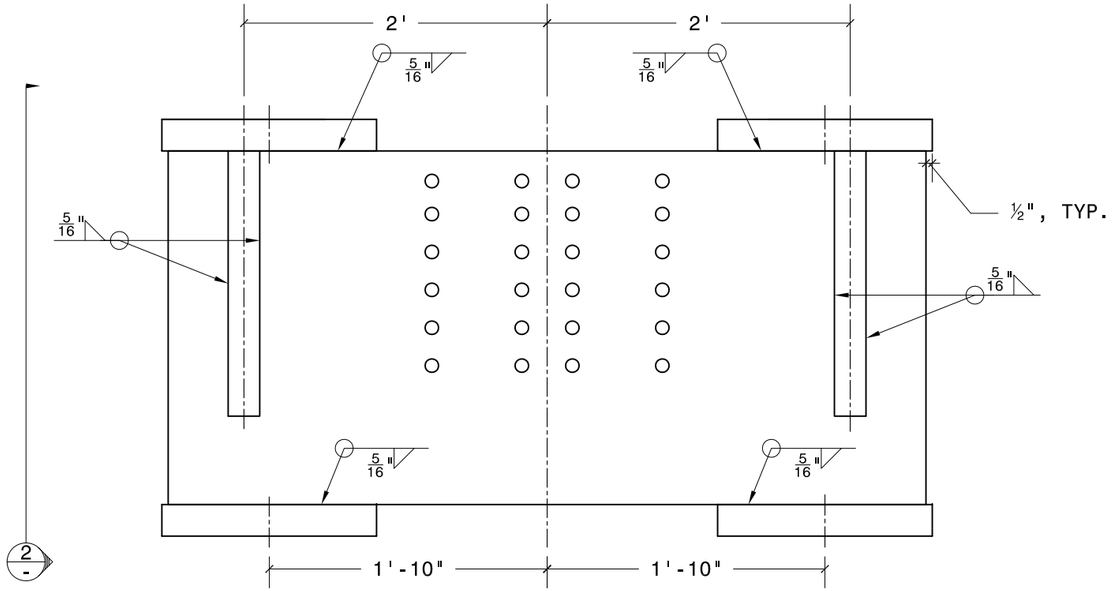

1 / 5 LOADING BEAM WELD DETAIL
SCALE: 1" = 1'-0"

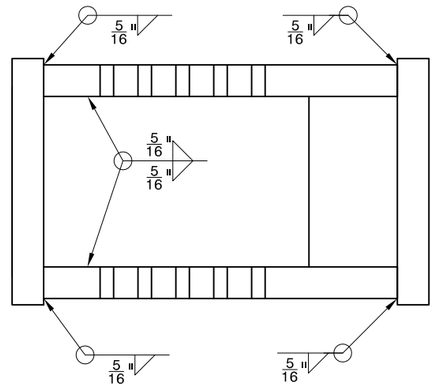

2 / 5 LOADING BEAM WELD DETAIL
SCALE: 1" = 1'-0"

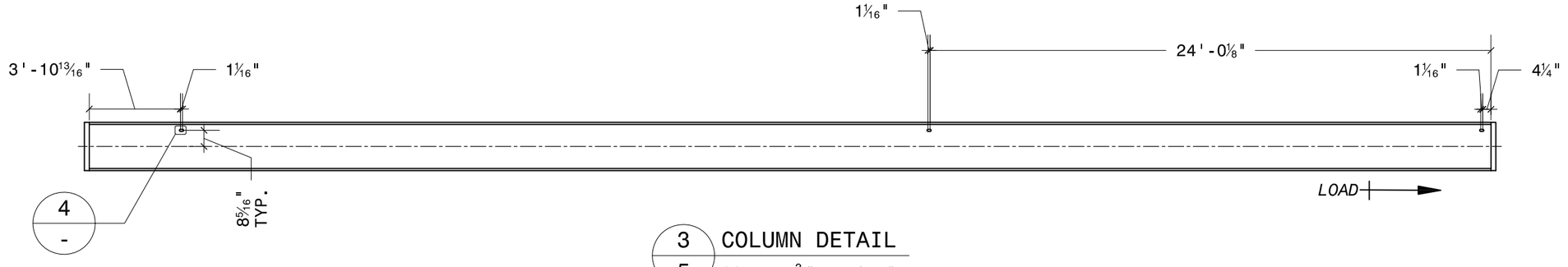

3 / 5 COLUMN DETAIL
SCALE: 3/16" = 1'-0"

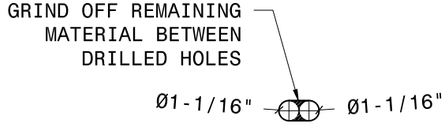

4 / 5 SLOTTED HOLE DETAIL
SCALE: 1-1/2" = 1'-0"

BOWEN LABORATORY
PURDUE UNIVERSITY

1040 SOUTH RIVER ROAD
WEST LAFAYETTE, IN 47906
P: 765-494-2227 F: 765-494-9886

PROJECT:
Winona Truss Test

SHEET NOTES:

REVISIONS:

NO.	DATE	BY

DESIGNED BY: JBL
DRAWN BY: JBL
CHECKED BY:
DATE: 2017
PROJECT NO.:
SHEET TITLE:
Specimen 6 & 7 : PLATES

SHEET NO.:
5 of 5